Surface Engineering of Magnesium Alloys: Surface Modification to Improve Corrosion Resistance

A Dissertation

Presented to

the faculty of the School of Engineering and Applied Science

University of Virginia

in partial fulfillment

of the requirements for the degree

Doctor of Philosophy

by

Michael A. Melia

May

2018

APPROVAL SHEET

The dissertation
is submitted in partial fulfillment of the requirements
for the degree of
Doctor of Philosophy

AUTHOR

The dissertation has been read and approved by the examining committee:

Professor Jim M. Fitz-Gerald
Advisor

Professor John R. Scully

Professor Sean Agnew

Professor Nick Birbilis

Professor Patrick Hopkins

Accepted for the School of Engineering and Applied Science:

Craig H. Benson, Dean, School of Engineering and Applied Science

May
2018

Surface Engineering of Magnesium Alloys:

Surface Modification to Improve Corrosion Resistance

A Dissertation Defense

Presented to the Faculty of the School of Engineering and Applied Science

University of Virginia

In Partial Fulfillment of the Requirements for the Degree of

Doctor of Philosophy in Materials Science and Engineering

By

Michael A. Melia

February 14th, 2018

Research advisors:

James M. Fitz-Gerald, Associate Professor of Materials Science and Engineering at the University of Virginia.

Professor John R. Scully, Interim Department Chair of the Materials Science and Engineering Department at the University of Virginia.

Committee chair:

Professor Sean Agnew, Professor of Materials Science and Engineering at the University of Virginia.

Committee members:

Professor Patrick Hopkins, Associate Professor of Mechanical and Aerospace and Engineering at the University of Virginia.

Professor Nick Birbilis, Woodside Innovation Chair and Head of the Department of Materials Science and Engineering at the Monash University.

Acknowledgements:

First I would like to thank my advisors, Jim Fitz-Gerald and John Scully, for their endless insight and support regarding my research and giving me the tools to thrive and grow as a scientist. Whether it was the often unscheduled daily meetings with Professor Fitz-Gerald or the monthly meetings with Professor Scully, the discussions and ideas from those meetings led to the constant growth and development of my projects and are why this thesis work was successful and spanned numerous topics. I would also like to thank my committee members for dedicating their time and support in this crucial step in my career.

Thank you to the students from the MSE department for their assistance on various characterization techniques and openness for scientific discussion in particular Taylor Cain, Matt Steiner, Matt Schneider, Marybeth Parker, Piyush Khullar, and the entire Fitz-Gerald and Scully groups. I would also like to thank the numerous undergraduate and high school students I had the privilege of advising and mentoring throughout my time at UVA. A special thanks to David Florian, Michael Purzycki, Bruce Briglia, and Liam Agnew for being an integral part of my thesis work, performing many of my experiments, as well as my development as a mentor and teacher.

Most importantly, I want to thank the constant support from my family and my girlfriend LeighAnn Larkin, for dealing with my periods of insanity and random tangents into the depths of my research, always there to listen and politely nod.

I would like to thank the primary funding source for this work the U.S. Army Research Laboratory under agreement number W911NF-14-2-0005 with Dr. Joe Labukas as project manager. The U.S. Government is authorized to reproduce and distribute reprints for Governmental purposes notwithstanding any copyright notation thereon. The views and conclusions contained herein are those of the authors and should not be interpreted as necessarily representing the official policies or endorsements, either expressed or implied, of the U.S. Government. I would also like to thank the Arconic/Alcoa Undergraduate research grants and the Virginia Space Grant Consortium (VSGC) for awarding a number of our undergraduate students funding which supported them to pursue summer research in the Fitz-Gerald lab and allowed me to pursue additional directions of my research.

Abstract

Magnesium (Mg) and its alloys have been the topic of intense research over the past 15 years as the automotive and aeronautic industries strive to increase fuel efficiency by reducing the weight of vehicles. Widespread implementation is currently limited by the poor intrinsic corrosion resistance of Mg and its alloys stemming from the lack of a passivating film and their high susceptibility to galvanic corrosion. Poor intrinsic corrosion of Mg alloys is often attributed to heterogeneous microstructures containing electrochemically noble secondary phases which promote the preferential dissolution of the Mg matrix. The research herein is aimed at the mitigation of localized corrosion which stems primarily from the secondary phases present in Mg alloys by non-equilibrium surface processing.

The initial thrust of the research was intended to describe controlling factors for localized corrosion (micro-galvanic couples) which occur during full immersion of specific Mg alloys (AZ31B-H24, AZ91D, and AM60B) in NaCl solutions. A focus was placed on the critical size of an electrochemically noble secondary phase particle required to induce localized corrosion, breakdown of the partially passive film, or the initiation of filiform-like corrosion (FFC). When immersed in a stagnant 0.6 M NaCl solution, the AZ31B alloy exhibited local pitting-like corrosion for the areas surrounding β-$Mg_{17}Al_{12}$ (radius < 250 nm) particles while the initiation of FFC was most often observed in proximity to the larger Al-Mn secondary phase particles (radius > 250 nm). The smaller Al-Mn secondary phase particles (radius < 50 nm) showed minimal contribution to the local corrosion processes.

The second thrust investigated the near surface dissolution of the Al-Mn and Mg-Al secondary phase particles present in the Mg alloys, utilizing a non-equilibrium surface process with a pulsed ultraviolet excimer laser. Analytical calculations showed that after a single laser pulse, and a typical melt time of ~50 ns, secondary phase particles with a radius of 75 nm could be dissolved. However, experiments utilizing scanning electron microscopy (SEM) observed complete dissolution for particles up to a radius of 250 nm, within the resolution of the SEM (~5 nm), and partial dissolution for the larger Al-Mn particles. The additional homogenization afforded by excimer laser processing was explained by the

liquid mixing generated by a plasma pressure wave and the low melting temperature of the β-$Mg_{17}Al_{12}$ particles (T_m = 723 K) which led to complete melting. The laser induced plasma formed above the substrate during processing was found to generate a pressure of ~50 MPa which acted on the melted substrate surface, resulting in material transport of several µm, experimentally shown to be ~3 µm per pulse. This material transport could also push the liquid Mg on top of the larger Al-Mn particles, minimizing the particles impact as local cathodes during corrosion. Overall, when a single laser pulse was applied to AZ31B, the density of secondary phase particles was reduced by approximately an order of magnitude. This reduction in secondary phase particle density led to a reduction in cathodic the half-cell hydrogen evolution reaction (HER) kinetics for all Mg alloys. The laser processing parameters were optimized around this corrosion response ultimately yielding an order of magnitude reduction in cathodic HER kinetics (fluence = 1.5 J/cm^2, pulse per area = 200, pulse overlap = 50%, and Ar pressure = 810 Torr).

The third thrust investigated the full immersion corrosion response for the laser processed Mg alloys in a stagnant 0.6 M NaCl solution. It was determined that the order of magnitude reduction in cathodic kinetics resulted in an order of magnitude increase in polarization resistance (inversely proportional to corrosion rate) for all Mg alloys. The polarization resistance for AZ31B-H24, AM60B, and AZ91D began at 200 Ω-cm^2, 2,000 Ω-cm^2, and 2,000 Ω-cm^2, respectively and after laser processing were increased to 5,000 Ω-cm^2, 23,000 Ω-cm^2, and 28,000 Ω-cm^2, respectively. The open circuit potential (OCP) was more negative for the laser processed Mg alloys, similar to high purity Mg, and observed a gradual increase to values similar to the as-received alloy. The initiation of FFC occurred shortly after the OCP of the laser processed specimen reached the OCP of the as-received specimen, typically after 24 to 60 hours of full immersion. This extension in the time to initiation of FFC is substantial considering the relatively aggressive corrosion environment (full immersion in 0.6 M NaCl), and should observe an additional increase in time to initiation in more applicable corrosion environments, such as field exposures in non-marine environments.

The use of x-ray diffraction (XRD) and Fourier transform infrared (FTIR) spectroscopy determined the corrosion product for all specimen to primarily consist of $Mg(OH)_2$ and a layered double hydroxide (LDH) phase (likely hydrotalcite). LDHs have been observed on Al containing Mg alloys previously; however, the ability for a LDH corrosion product to act as a passive layer is often short lived because the initiation of FFC occurs quickly in aqueous NaCl solutions, dominating the electrochemical response of the alloy. Interestingly, the LDH formed to some extent on all specimens after immersion in the stagnant 0.6 M NaCl solution, regardless of the heterogeneity of the Al containing Mg alloys microstructure. The difference in corrosion product for an as-received and laser processed surface was based on the quantity of $Mg(OH)_2$, with the as-received alloys exhibiting more $Mg(OH)_2$ in comparison to the laser processed specimen, indicative of the higher coverage of FFC on the as-received alloys. That said, the observation of the LDH phase on all specimen may have a wide spread impact on the corrosion analysis of Al containing Mg alloys since the primary corrosion product at short immersion times for these alloys was verified to be the LDH phase which precipitates at a pH of ~8 in contrast to $Mg(OH)_2$ precipitating at a pH of ~10.5.

The fourth thrust of this thesis was centered on the deposition of a multilayered coating composed of $MgO/Mg(OH)_2$ and $Gd(OH)_3$ by pulsed laser deposition onto the AZ31B-H24 surface. The 300 nm thick films were successfully applied and acted as a passive coating, inhibiting the initiation of FFC on the as-received and laser processed AZ31B-H24 alloy for 1 and 72 hours, respectively. Increasing the initiation time of FFC to 72 hours in 0.6 M NaCl is similar to results for hydrotalcite conversion coatings on Mg alloys. The polarization resistance of the laser processed and coated specimen increased to a value of ~100,000 $\Omega\text{-cm}^2$, decreasing with immersion time to ~30,000 $\Omega\text{-cm}^2$ until the initiation of FFC occurred after 72 hours. Initiation of FFC on the laser processed and coated specimens was preceded by a “re-passivation” like phenomenon where local defects in the coating were filled in by the conversion/precipitation of $Mg(OH)_2$.

The fifth and final thrust of this thesis investigated the specimen’s corrosion response to a B117 salt spray exposure as a harsh, accelerated outdoor exposure. A LDH phase was formed on all specimens, similar to the full immersion conditions, with the only detectable corrosion product found on the laser processed specimens being the LDH, signifying the lessened coverage of FFC for the laser processed surfaces. In addition, the LDH phases were found to be in competition for the most thermodynamically stable corrosion product with the carbonate rich phase, hydromagnesite, with experimental results verifying the presence of Al suppressed its formation. Regardless of the corrosion products formed, the laser processed specimens consistently observed slower corrosion rates than their as-received counterparts, albeit with a less dramatic reduction in corrosion rate, only ~3 fold for the salt spray versus ~10 fold for the full immersion experiments.

Table of Contents

List of Figures

List of Tables

List of Symbols

ATR-FTIR – Attenuated total reflection – Fourier transform infrared spectroscopy
AW – Atomic weight of Mg
B – Stern-Geary constant
BSE – Backscattered electron
β_a – Anodic Tafel slope
β_c – Cathodic Tafel slope
CC – Conversion coating
C_{film} – Film capacitance
C_{DL} – Double layer capacitance
CW – Continuous wave
d – Distance away from the secondary phase particle
D – Diffusivity coefficient
DI – Deionized
E_{bkdn} – Breakdown potential
E_{corr} – Corrosion potential
E_{galv} – Galvanic potential
EDS – Energy dispersive spectroscopy
EIS – Electrochemical impedance spectroscopy
F – Faraday's constant
FFC – Filiform-like corrosion
HAZ – Heat affected zone
HER – H_2 evolution reaction
GI-XRD – Grazing incident x-ray diffraction
γ – Adiabatic exponent of processing gas
γ_o – Adiabatic exponent of metal vapor
Λ_b – Heat of vaporization
i – Current density
i_a – Anodic current density
i_c – Cathodic current density
i_{corr} – Corrosion current density
i_{galv} – Galvanic coupled current density
i_o – Exchange current density
I_{galv} – Galvanic current
I_o – Irradiance (from laser fluence)
ICP-OES – Inductively coupled plasma – optical emission spectroscopy
K-K – Kramers-Kronig transform
K_{sp} – Solubility constant
L – Inductance
λ – Wavelength
LDH – Layered double hydroxide
LSC – Laser supported combustion
LP – Laser processed
LPC – Laser processed and coated
ms - Milliseconds
ν_{lat} – Radial velocity of liquid from plasma and recoil pressure
ρ – Density

ρ_o – Gas density
n – Ionic charge
η – Over potential
ns – Nanoseconds
NND – Nearest neighbor distance
NDE – Negative difference effect
OCP – Open circuit potential
OES – Optical emission spectroscopy
PEO – Plasma electrolytic oxidation
PLD – Pulsed laser deposition
PVD – Physical vapor deposition
PPA – Pulse per area
p_o – Processing pressure
$p_{\text{saturated vapor}}$ – Saturated vapor pressure
p_s^{LSC} – Plasma pressure from the laser supported combustion
Δp – Sum of the recoil and plasma pressures minus the ambient pressure
P_{CO_2} – Partial pressure of CO_2
Q_a^{EIS} – Anodic charge associated with the dissolution of Mg
r_{II} – Lateral propagation rate of corrosion filaments in stage II
r_{III} – Lateral propagation rate of corrosion filaments in stage III
r_{particle} – Radius of secondary phase particles
$r_{\text{susceptible}}$ – Radius surrounding a secondary phase particle that is susceptible to corrosion
R – Gas constant
R_3 – Inductor resistance
R_{ct} – Charge transfer resistance
R_{film} – Film resistance
R_{FFC} – Polarization resistance of a single filament
R_p – Polarization resistance
R_s (or ρ) – Solution resistance
SCE – Saturated calomel electrode
SEM – Scanning electron microscopy
SKPFM – scanning kelvin probe force microscopy
SLIM – Simulated laser interactions with materials
SS – Solid solubility
SVET – Scanning vibrating electrochemical technique
T_b – Equilibrium boiling temperature
TEM – Transmission electron microscopy
V_{SCE} – Potential in reference to the saturated calomel electrode
W – Dimensionless particle velocity
XCT – X-ray computed tomography
XRD – X-ray diffraction
Z' – Real impedance
Z" – Imaginary impedance
ZRA – Zero resistance ammeter

Page intentionally left blank.

Chapter 1: Introduction

1.1 Motivation

Mg and its alloys can be rolled, cast, forged, extruded and machined to allow for a variety of structural assembly options, typically added into design schemes to reduce the weight of a non-critical structural component (e.g. radiator and cab supports, light-duty automobile transmission housings) [1,2,3,4,5,6,7]. Automotive and aerospace industries have begun to implement Mg components because of the added fuel efficiency afforded by lighter components, as seen in the plot of **Figure 1.1**. That said, wide spread integration of Mg has been limited by its relatively poor corrosion resistance [2,8].

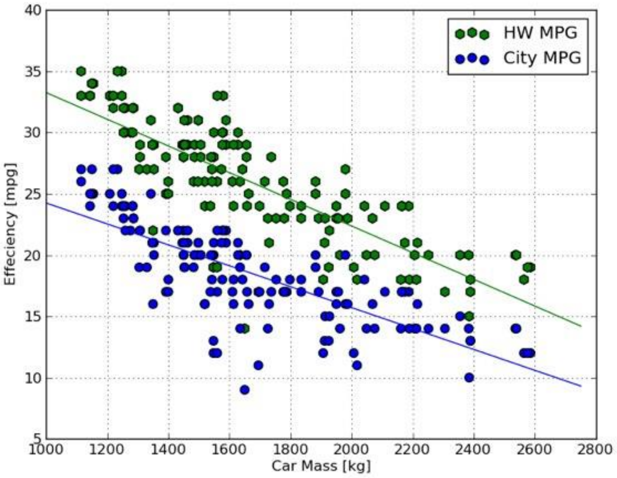

Figure 1.1: Fuel efficiency base on highway (HW) and city driving conditions in miles per gallon (mpg) depending on the automobiles mass. Plot is courtesy of a Wired.com [9].

A significant amount of work has gone into investigating the fundamental mechanisms of Mg corrosion in the past 15 years, including the implementation of advanced scanning electrochemical techniques for *in situ* monitoring of the local corrosion behavior as well as the combination of typical electrochemical measurements with chemical analysis techniques to determine the corrosion behavior of Mg and its alloys [10,11,12]. Much of the application space for Mg alloys would require intermittent exposure to neutral, Cl^- containing aqueous environments, which aggressively corrode Mg [7]. The corrosion susceptibility of Mg alloys stems from the negative electrochemical half-cell reaction potential of Mg, making it energetically favorable to dissociate in water and galvanically couple to more noble materials, a common occurrence in structural design [13,14,15,16,17,18,19,20,21]. The lack of a passivating corrosion product above this half-cell potential, across a wide range of pH values (pH = 0-10.5), is also unfavorable as this adds to the thermodynamic favorability to dissolve Mg with no kinetic barrier [22,23,24].

The common solution to improving a materials intrinsic corrosion response is through alloying with other, more electrochemically stable elements (such as Cr additions to steel) [25]. However, the secondary phases which result from alloying additions to Mg are often more noble than the surrounding Mg matrix, leading to micro-galvanic coupling and the initiation of intense localized corrosion, making the corrosion of such alloys unpredictable [14,18]. The abundance of secondary phases is derived from low solid solubility (SS) of alloying elements with Mg and subsequent chemically heterogeneous microstructures [26,27]. Limited control of these heterogeneous microstructures is possible by traditional processing routes such as casting and forging, which have a limited range of cooling rates [28]. The intense localized corrosion which develops at the micro-galvanic couples is similar to pitting and known as filiform-like corrosion (FFC) [29,30,31,32,33]. To alleviate the low corrosion resistance and susceptibility to localized corrosion, many coatings and paints have been applied and developed for a variety of alloys (e.g. tagnite) [34,35,36]. That said, scratches and flaking of the coatings result in the exposure of a small area of the alloys heterogeneous microstructure which leads to the initiation of FFC when under full immersion conditions in chloride containing solution. Therefore a surface treatment capable of chemically homogenizing the Mg alloys microstructure could suppress the time to initiation of FFC [37,38,39].

1.2 Corrosion of pure Mg

Hundreds of articles have been published in the past 30 years regarding the corrosion response of pure Mg and its alloys [7,8,40,41,42,43,44]. These studies range in complexity from the influence of new coatings and surface treatments to time dependent corrosion morphology changes and studies attempting to explain the negative difference effect (NDE) [7,31,36]. In general, the electrochemical reactions associated with the corrosion of Mg in aqueous solutions are:

$$Mg^0 (s) \rightarrow Mg^{2+} (aq) + 2e^- \text{ (Anodic reaction)} \qquad (\mathbf{1})$$

$$2H_2O (l) + 2e^- \rightarrow 2OH^- (aq) + H_2 (g) \text{ (Cathodic reaction)} \qquad (\mathbf{2})$$

The corrosion of Mg is primarily controlled by the H_2 evolution reaction (HER) rate which only requires H_2O to progress and will be proportional to the area density of exposed cathodic material at the pure Mg or Mg alloy surface [7,13,45]. The influence of other cathodic reactions in aqueous solutions, such as the oxygen reduction reaction, has been shown to have no significant effect on the corrosion of Mg [46]. The noble impurities or secondary phases present in the Mg can act as preferential sites for the cathodic reaction to occur, creating localized corrosion cells known as micro-galvanic couples [47,48]. These galvanic couples lead to localized degradation of the Mg metal and are accompanied by a local increase in pH for the solution near the cathodic particle because the HER generates OH^-, as depicted in **Figure 1.2 a** and **b**. Macroscopic galvanic couples are also a major concern for the electrochemical active Mg, making the design of devices containing Mg components difficult because intense galvanic corrosion can occur if the Mg component is not properly isolated from a component composed of a dissimilar metal [7,49].

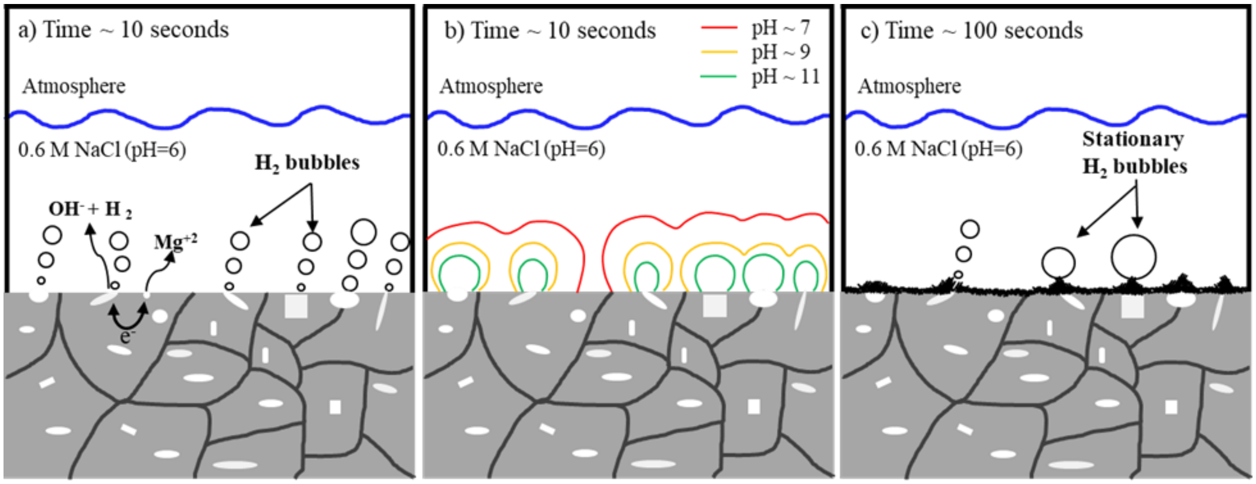

Figure 1.2: A cross-section depiction of expected corrosion activity with respect to time for Mg immersed in stagnant 0.6 M NaCl solution with a number of impurities or secondary phase particles present at the surface. At short times (~10 seconds) micro-galvanic couples form between the secondary phase particles and the surrounding Mg matrix resulting in local dissolution of Mg next to the particles and streams of H_2 gas from the particles as seen in a). An increase in pH is also observed at the surface, b), and develops at a similar time scale, ~10 seconds. At longer times, 100 seconds, the solution near the Mg surface becomes saturated with Mg^{2+} and OH^- ions, exceeding the solubility constant (K_{sp}) for $Mg(OH)_2$ which results in the deposition of a flaky $Mg(OH)_2$ product on the surface, as seen in c). Increased quantity of the $Mg(OH)_2$ is often observed on the secondary phase particles.

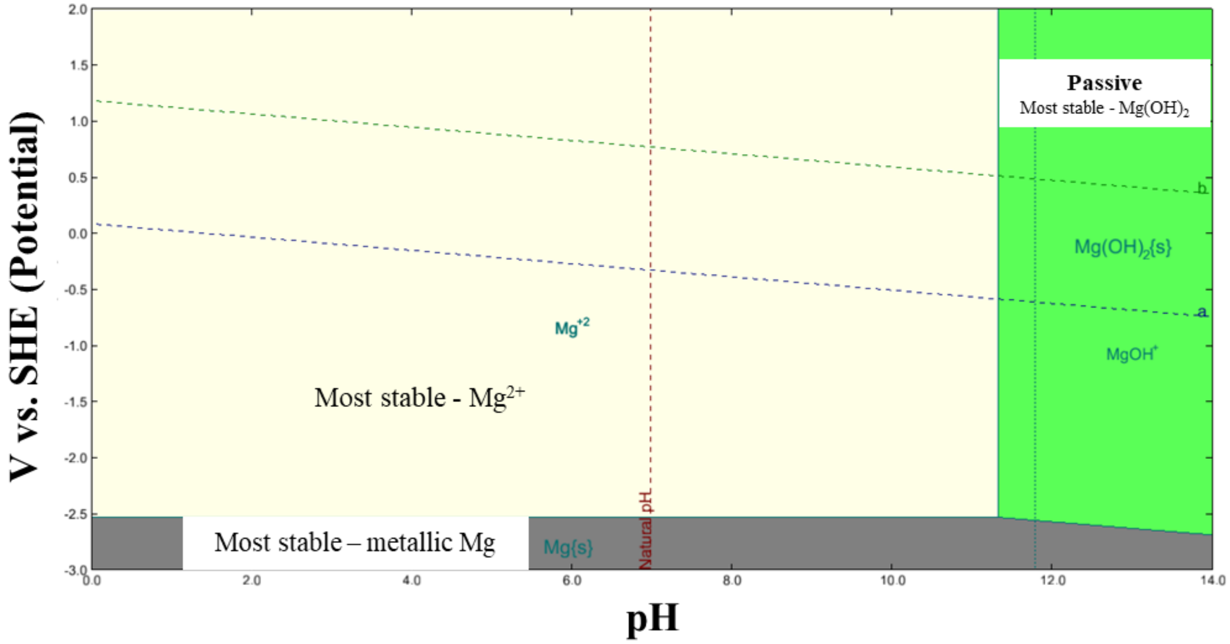

Figure 1.3: A Pourbaix diagram for Mg was generated utilizing the OLI software for immersion of pure Mg in a solution of 0.6 M NaCl. The yellow phase field is where Mg^{2+} is the most stable state, the green phase field is where $Mg(OH)_2$ is the most stable state, and the gray phase field is where Mg metal is the most stable state.

The susceptibility of Mg to corrosion is increased by the lack of thermodynamic stability of the native oxide and resulting corrosion products in aqueous solution, as observed by the Pourbaix diagram in **Figure 1.3** [24]. The stable corrosion product of Mg in most aqueous solutions, $Mg(OH)_2$, is observed to be stable only above a pH of ~10.5, suggesting minimal thermodynamic driving force for it to form in neutral solutions. The majority of corrosion experimentation and desired applications for Mg alloys occur in near neutral solutions containing aggressive ions, typically Cl^- or SO_4^{-2}, where the formation of the stable corrosion product is not expected. However, the OH^- ions produced by the cathodic reaction of Mg corrosion lead to an increase in pH for the electrolyte at the Mg surface, in particular near secondary phases [50]. This local pH rise results in the precipitation of $Mg(OH)_2$ with a flaky and porous morphology, as depicted in **Figure 1.2b and c**. The localized corrosion and natural convection of the solution leads to non-uniform corrosion product formation across the surface and acting as a partially passive film. In addition, the incorporation of aggressive ions into the solution leads to destabilization of the corrosion product and to more intense and accelerated corrosion responses such as the pitting and filiform-like corrosion (FFC) which occurs in Cl^- containing solutions [10,51].

Many of the initial corrosion studies for Mg observe impurity content effects on pure Mg, suggesting the most detrimental and common impurities to be transition metals such as Fe, Ni, and Cu. Small quantities (> 40 ppm) can lead to order of magnitude increases in the Mg corrosion rate, as seen in **Figure 1.4a** [7,13]. This extreme effect on corrosion rate is a function of certain impurity elements ability to support the HER and electrochemical nobility in comparison to Mg. These impurity elements have standard redox potentials substantially less negative than Mg (2 V) and lead to micro-galvanic couples to form with a large driving force for the HER and the subsequent Mg dissolution. E-log(i) measurements performed by Sudholz et al. in 0.1 M NaCl revealing specifically the cathodic kinetics of relevant impurity elements can be found in **Figure 1.4b** along with a E-log(i) measurement of pure Mg [18]. The current density where the impurity E-log(i) measurement intersects with the Mg E-log(i) measurement will give an idea of how severely these two materials will galvanically couple.

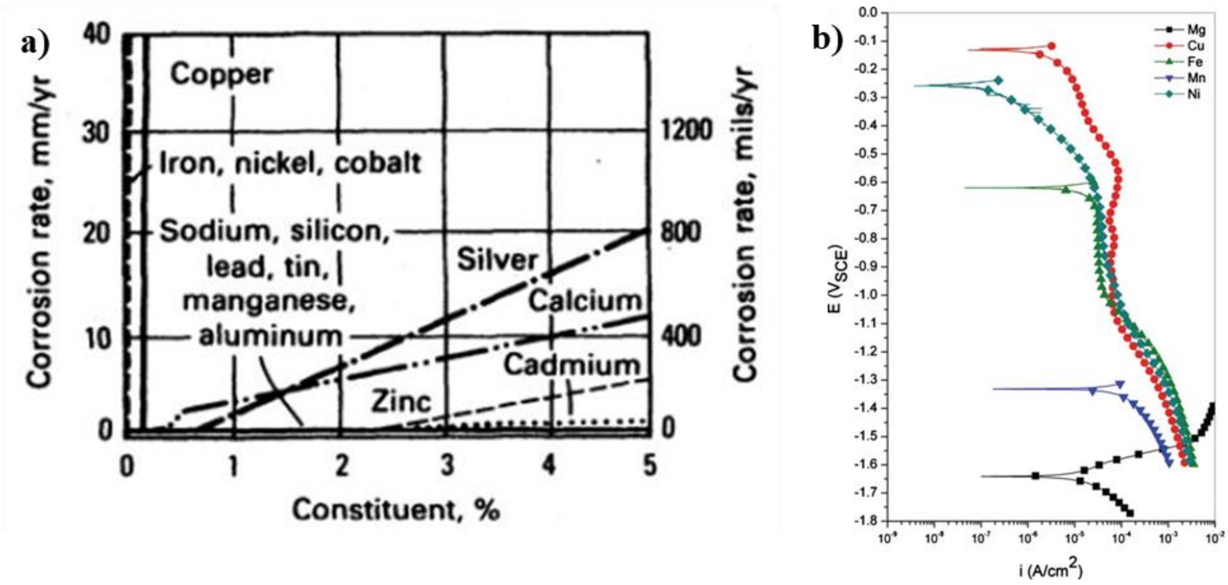

Figure 1.4: a) A replication of the plot originally used by Makar/McNulty to quantify the impact impurity content in pure Mg will influence corrosion rate regardless of corrosion morphology or the materials microstructure [8,13]. b) E-log(i) measurements of common impurity elements found in Mg under full immersion in stagnant 0.1 M NaCl, as well as a E-log(i) measurement of pure Mg, plot is reproduced from Sudholz et al. [18].

The rapid micro-galvanic coupling may be observed in **Figure 1.5** for a commercial purity (CP) Mg specimen after 10 minutes full immersion in stagnant 0.1 M NaCl solution. The agglomerate of flaky corrosion product is indicative of the deposition of $Mg(OH)_2$ at and around a local cathode, in this case one's composed of Si and Fe. The bright region adjacent to the impurity particle is caused by convection induced by H_2 gas evolved at the particle, quickly replacing the Mg^{2+} and OH^- rich solution with fresh 0.1 M NaCl preventing significant $Mg(OH)_2$ deposition and allowing for local degradation. After cleaning the corrosion product from the surface with a chromic acid solution, in **Figure 1.5 b**, the impurity particle was observed along with the local corrosion to the right of the particle.

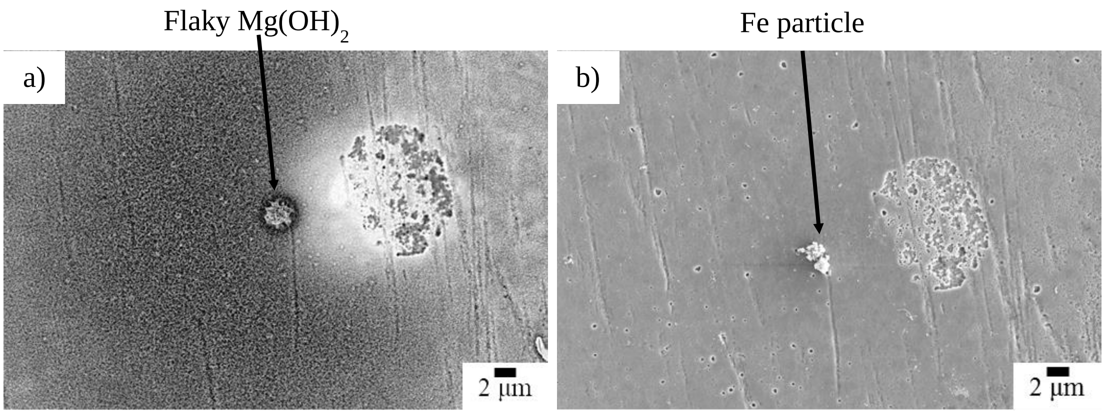

Figure 1.5: a) A backscattered electron micrograph of the corrosion product and local degradation which occurred on a commercial purity Mg sample after 10 minutes of immersion in stagnant 0.1 M NaCl. The agglomeration of flaky $Mg(OH)_2$ in the center of the image is covering an impurity particle rich in Fe. **b)** A secondary electron micrographs of the same area from **a)** after cleaning with a chromic acid solution, revealing the Fe particle and local degradation to the right of the particle.

Impurities are often the initiation sites for a more intense corrosion phenomenon, FFC, a corrosion response commonly observed on organically coated Al and steel alloys, yet is the typical corrosion response for Mg and its alloys in Cl^- containing aqueous solutions [10,11,31,32,33,52,53,54,55]. The scanning vibrating electrochemical technique (SVET) has had success in characterizing the nature in which the thin filaments of corrosion propagate across the Mg surface, with an intense anodic head and cathodic current detected in the trailing tail of each filament [10,12,31]. Sensitivity of the FFC morphology has been rigorously studied by SVET and time dependent optical and electron microscopy studies, revealing an increase in Cl^- concentrations and impurity (Fe) content can shift the morphology from the propagation of individual filaments to “discs” of intense corrosion, behaving similar to clusters of aligned filaments [31]. The addition of inhibiting ions, such as CrO_3^{-4}, has also been shown to limit propagation, even in solutions containing high concentrations of Cl^- [56].

Another influential parameter over the corrosion response of pure Mg is its texture, i.e. grain orientation. There have been two variations in studying the influence of grain orientation on Mg corrosion with most observing the overall corrosion rate change as a result of the materials texture [57,58,59]. Other observations have been made on a variation in how corrosion propagates through individual grains

[60,61,62,63,64,65]. As has been observed with other materials, when the closest packed planes of Mg are exposed to corrosive media, corrosion is observed to be the slowest in comparison to higher index planes [66]. The reason for slowed corrosion rates at low index planes was expected, as lower surface energies are typical for these close packed orientations [62,63]. However, a different response was observed by Bland et al. suggesting that the lower index planes formed a thinner, less protective MgO/Mg$(OH)_2$ corrosion product, hence increasing the corrosion rate for {0001} grains [65]. In addition, grain size as well as deformation (dislocation density) has also been observed to influence corrosion rates [67,68,69].

1.3 General effects of alloying additions on Mg corrosion

The purpose of adding alloying elements is to improve and control processing, casting, forming, mechanical, and degradation (corrosion, wear, etc.) properties [4,7,70,71]. For the corrosion properties of Mg alloys, many of the possible alloying additions have been investigated in binary systems, observing the influence of a single alloying element. One common route to observing corrosion kinetics is through linear polarization measurements where a more positive or negative potential is applied to the alloy (working electrode) at a constant rate versus time (typically 1 mV/sec.). These experiments result in current density measurements with respect to the corrosion potential of the alloy which correlates to the individual anodic (positive potentials) or cathodic (negative potentials) kinetics (reaction rates) [25]. A range of alloying elements have been investigated and summarized in **Figure 1.6** [7,16,20]. This plot presents the two main strategies for slowing the corrosion rate of Mg, through the reduction of the anodic and/or cathodic kinetics. However these results, while helpful, do not account for changes to the microstructure with most effects taken for binary alloys in the as-cast condition and not complete solid solution. They also do not consider the more complex scenarios typical for technologically relevant alloys with more than one alloy addition.

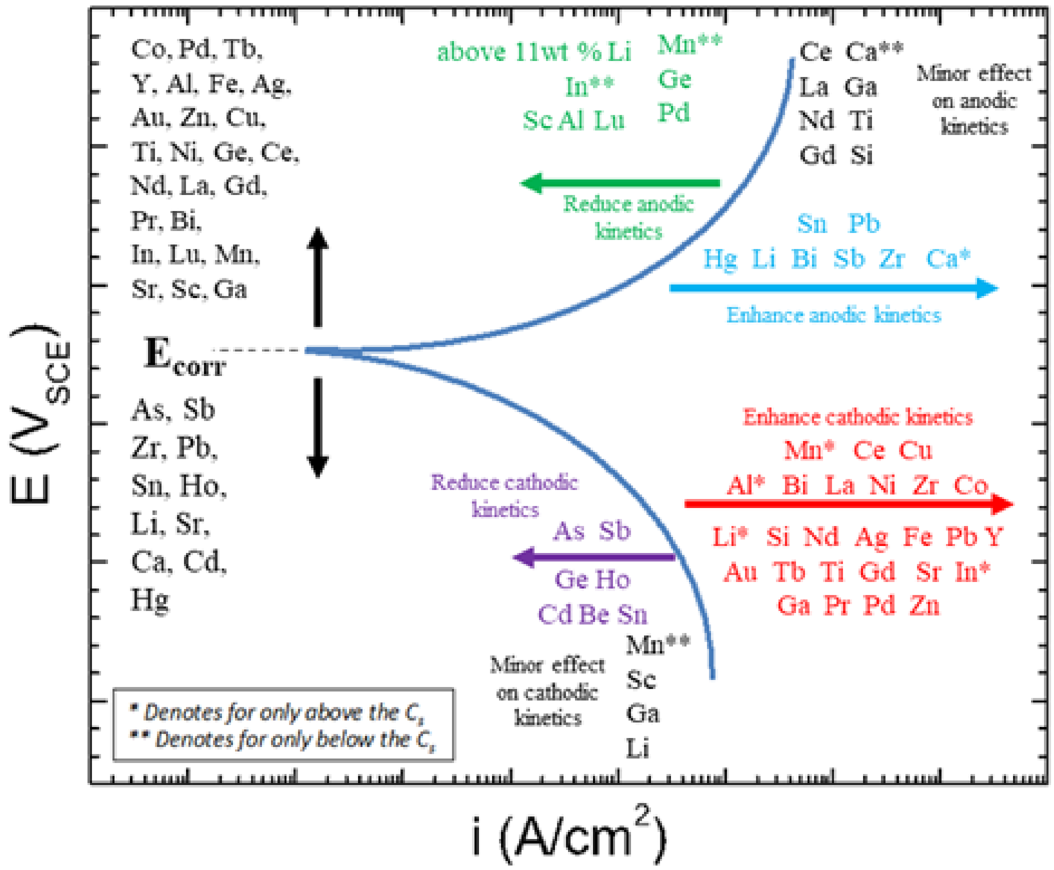

Figure 1.6: Potential versus current density plot with a general indication of how specific alloying elements may individually affect the corrosion potential (E_{corr}), the anodic kinetics (more positive than E_{corr}), and the cathodic kinetics (more negative than E_{corr}). Reproduced with permission from Prof. Birbilis.

The addition of elements that bind with the electrochemically noble impurities and shift their electrochemical potential to something similar to that of Mg will reduce their driving force for micro-galvanic coupling, therefore reduce the HER rate and slowing the corrosion rate of Mg. Additions of Mn to Al containing Mg alloys lead to the encapsulation of Fe impurity particles which shift their electrochemical potential to be more negative than pure Fe, yet still capable of acting as a local cathode [72]. A similar approach was formulated by adding elements that reduce the efficiency of the HER with some success in alloying Mg with As and Ge, effectively poisoning the HER [73,74].

Another strategy of adding alloying elements is to improve the stability of the Mg corrosion product across a wider pH range, thereby reducing the anodic reaction rate. The most common alloy additions for this approach (Al, Nd, Y, other lanthanides) are those which make the oxide/hydroxide corrosion product more thermodynamically stable while not forming an abundance of electrochemically noble secondary phases [7]. A more dramatic improvement to the stability of the corrosion product will also be observed for alloying elements that are capable of being in solid solution with Mg at room temperature; however the terminal solid solubility of many alloying elements is low when added to Mg as seen in **Table 1.1** [7,26,75]. The benefits of solid solution alloying elements with Mg will be a common theme throughout this thesis.

Table 1.1: Categorizing the maximum equilibrium solid solubility achievable for alloying elements when added to Mg in a binary solution.

Binary Systems	**Equilibrium Terminal Solid Solubility Range (at. %)**				
	<0.1	**0.1-1**	**1-5**	**5-25**	**>25**
Mg - X	As, Ba, Ce, Co, Cu, Eu, Fe, Ge, La, Na, Ni, Pd, Pr, Sb, Si, Sr	Au, Ca, Ir, Nd, Th, Mn, Ti	Ag, Bi, Dy, Ga, Gd, Hg, Pu, Sn, Y, Yb, Zn, Zr	Al, Er, Ho, Li, Lu, Pb, Tl, Tm, In, Sc	Cd

1.4 Background on Mg alloy metallurgy and processing

The alloys selected for this study were the wrought Mg alloy AZ31B (provided by Mg Elektron) in the strain hardened and partially annealed H24 condition as a 3 mm thick sheet and AM60B and AZ91D (provided by Meridian) in the as-cast condition, compositions are presented in **Table 1.2**. An explanation of common Mg alloy nomenclature is presented in **Figure 1.7** [3]. Wrought Mg alloys have been found in few commercial applications (most commonly as sacrificial anodes for water heaters) however, AZ31B has been utilized as electric motor frames, oil pans, and ballistic armor plate [1,2,3]. The cast alloys AM60B and AZ91D were selected to show employing laser processing can beneficially impact Mg alloys that are more commonly found in production. Die cast Mg alloys make up 35% of the total uses for Mg, primarily in the automotive industry with a few applications in consumer electronics and power tools.

AZ91D is most commonly utilized in transmission casings and parts of the powertrain in automobiles and as laptop cases in the electronics sector. Due to its high ductility, AM60B can be found in more structurally integral parts of the automobile such as instrument panels, seat frames, inner boot lid sections, and steering components [3,4,76].

Table 1.2: Composition in wt% of AZ31B-H24, AZ91D, and AM60B alloys used in thesis work as determined by ICP-OES analysis.

Element (wt%)	Al	Zn	Mn	Fe	Mg
AZ31B-H24	3.0	1.0	0.33	0.005	Bal.
AZ91D	7.2	0.79	0.19	0.02	Bal.
AM60B	5.9	0.02	0.28	0.01	Bal.

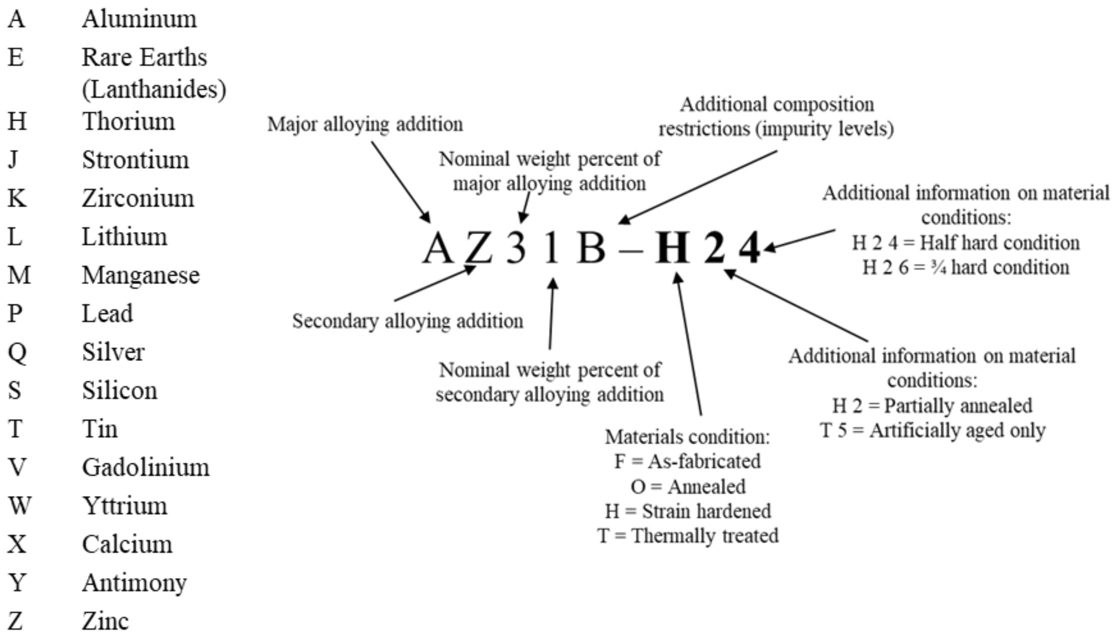

A	Aluminum
E	Rare Earths (Lanthanides)
H	Thorium
J	Strontium
K	Zirconium
L	Lithium
M	Manganese
P	Lead
Q	Silver
S	Silicon
T	Tin
V	Gadolinium
W	Yttrium
X	Calcium
Y	Antimony
Z	Zinc

Figure 1.7: Explanation of the nomenclature used for naming Mg alloys.

a)

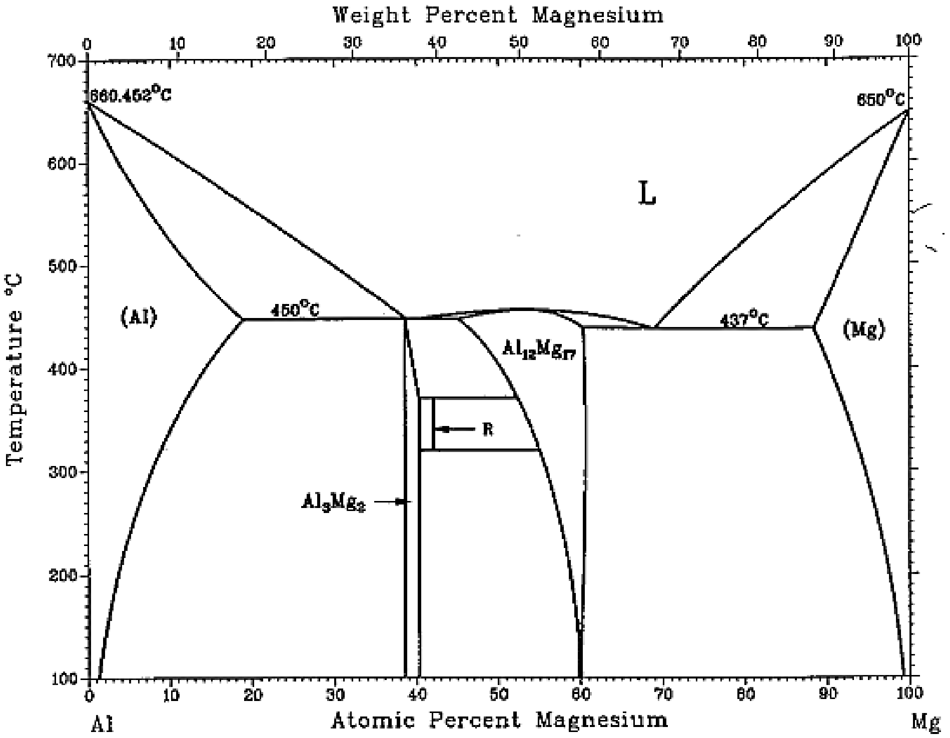
Weight Percent Magnesium
0
10
20
30
40
50
60
70
80
90
100
700
600
500
400
300
200
100
Temperature °C
660.452°C
650°C
L
(Al)
450°C
437°C
(Mg)
$Al_{12}Mg_{17}$
R
Al_3Mg_2
0
10
20
30
40
50
60
70
80
90
100
Al
Atomic Percent Magnesium
Mg

b)

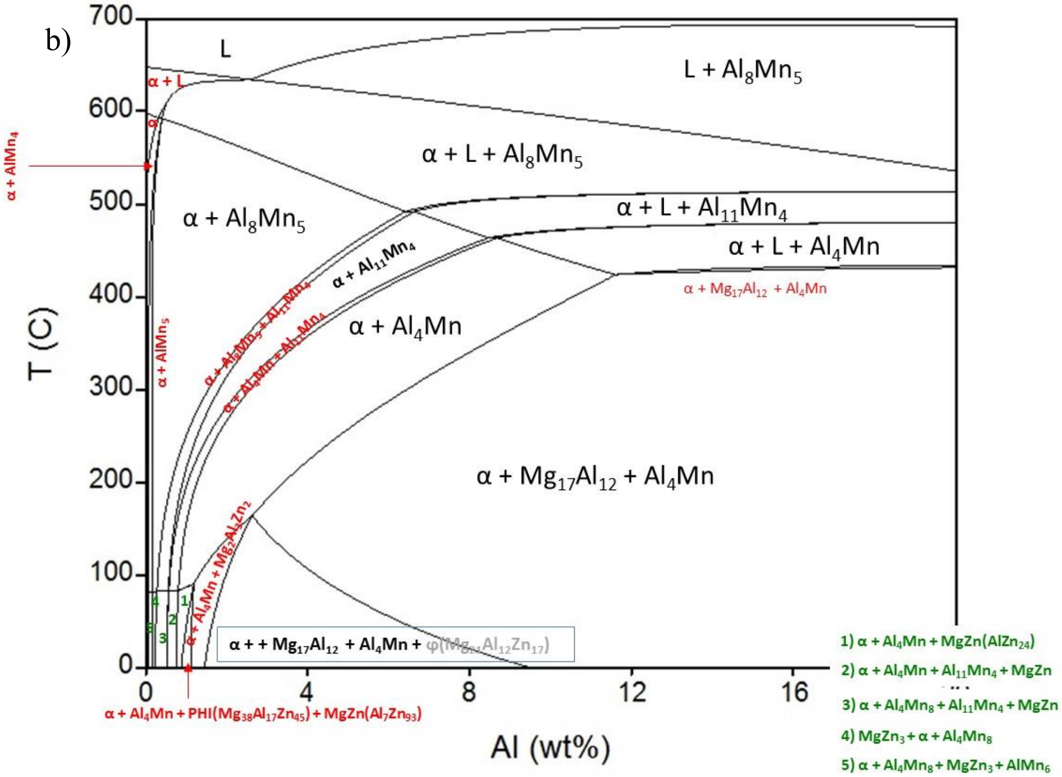
700
600
500
400
300
200
100
0
T (C)
L
$L + Al_8Mn_5$
$\alpha + L$
α
$\alpha + AlMn_4$
$\alpha + L + Al_8Mn_5$
$\alpha + Al_8Mn_5$
$\alpha + L + Al_{11}Mn_4$
$\alpha + L + Al_4Mn$
$\alpha + Al_{11}Mn_4$
$\alpha + Mg_{17}Al_{12} + Al_4Mn$
$\alpha + Al_8Mn_5 + Al_{11}Mn_4$
$\alpha + Al_4Mn + Al_{11}Mn_4$
$\alpha + AlMn_5$
$\alpha + Al_4Mn$
$\alpha + Mg_{17}Al_{12} + Al_4Mn$
$\alpha + Al_4Mn + Mg_2Al_3Zn_2$
4
1
2
5
3
$\alpha + + Mg_{17}Al_{12} + Al_4Mn + \varphi(Mg_{21}Al_{12}Zn_{17})$
0
4
8
12
16
$\alpha + Al_4Mn + PHI(Mg_{38}Al_{17}Zn_{45}) + MgZn(Al_7Zn_{93})$
Al (wt%)
1) $\alpha + Al_4Mn + MgZn(AlZn_{24})$
2) $\alpha + Al_4Mn + Al_{11}Mn_4 + MgZn$
...
3) $\alpha + Al_4Mn_8 + Al_{11}Mn_4 + MgZn$
4) $MgZn_3 + \alpha + Al_4Mn_8$
5) $\alpha + Al_4Mn_8 + MgZn_3 + AlMn_6$

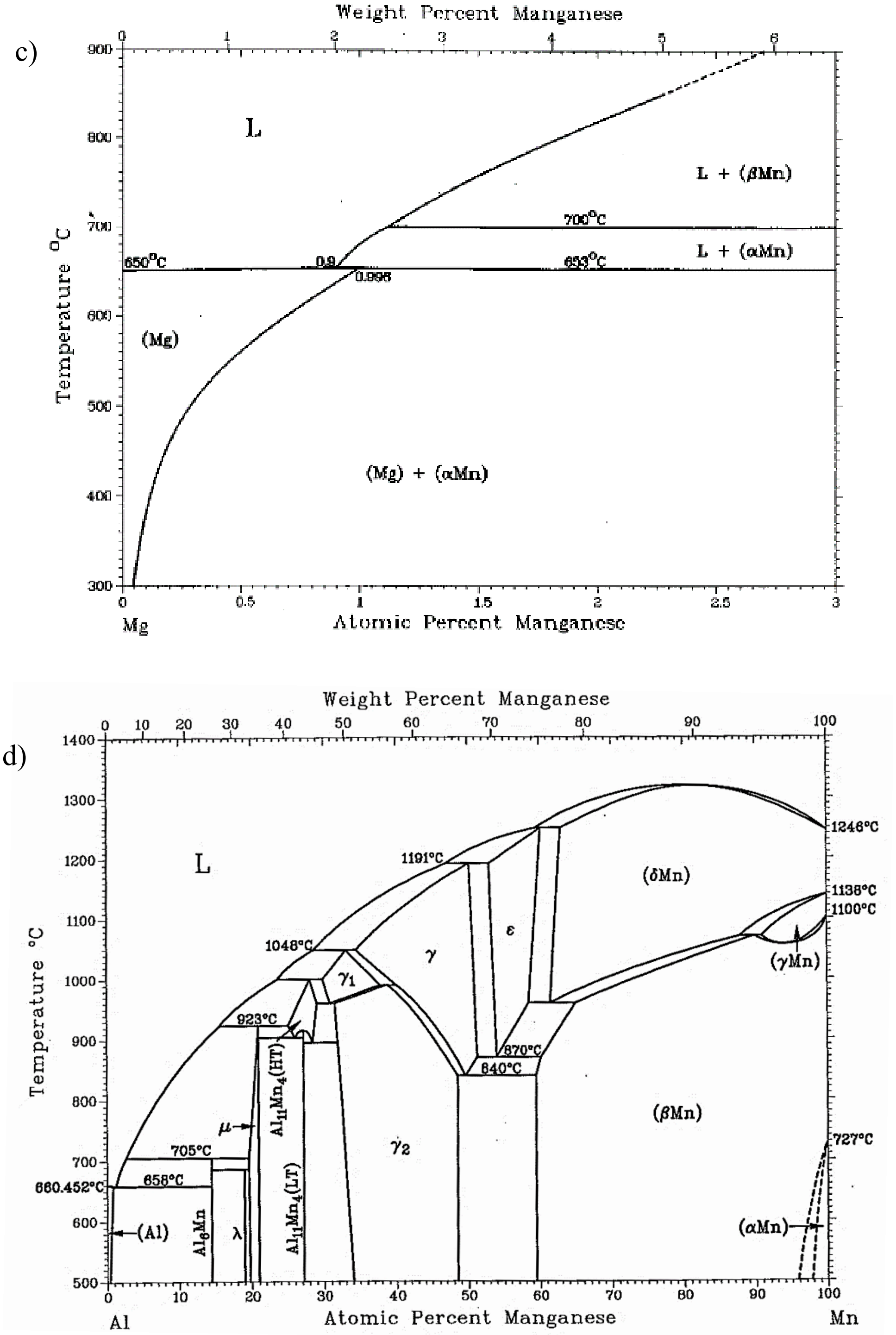

Figure 1.8: Presented here are four phase diagrams for the Mg-Al alloy system: a) Mg-Al, b) a psuedo-binary phase diagram of the Mg - Al - 1 wt% Zn- 0.6 wt% Mn system, c) Mg-Mn, and d) Al-Mn. The pseudo-binary phase diagram is courtesy of Dr. Kateryna Gusieva where the Zn and Mn quantities were kept constant while the Al and Mg quantities were varied [77].

The microstructures which can develop for the Al containing Mg alloys depend heavily on Al content, the cooling rates achieved during casting, and whether or not thermomechanical processing occurred after casting. All alloys considered lie in the eutectic region of the Mg-Al phase diagram, as shown in **Figure 1.8a**, where β-$Mg_{17}Al_{12}$ is the primary secondary phase at equilibrium [77,78]. The small addition of Zn to the AZ31B and AZ91D alloys does little to alter the resulting microstructure, however the phases formed are often influenced [79,80]. Both alloys have shown Zn to become incorporated into the β-$Mg_{17}Al_{12}$, yielding β-$Mg_{17}Al_{(12-x)}Zn_x$, or the possibility of the formation of Φ-Mg_xAl_y,Zn_z phase as shown in the pseudo-binary phase diagram in **Figure 1.8b**. Zinc may also reside in solid solution with the Mg matrix, along with Al at room temperature as shown by phase diagrams and **Table 1.1** [77].

The final common addition to these alloys is Mn which forms no secondary phases and has less than 1 at% solid solubility with Mg as shown in **Figure 1.8c**. During the initial casting stages, the Mn additions encapsulate the Fe impurity particles, surrounding these particles and reducing the electrochemical potential similar to that of Mn [72]. When incorporated in Al containing Mg alloys, the resulting encapsulating phase is typically an Al-Mn compound commonly observed to be the γ-Al_8Mn_5 phase as seen in the pseudo-binary phase diagram in **Figure 1.8b** [81]. These Al-Mn phases which form during casting have melting temperature on the order of 900^oC as seen in the Al-Mn binary phase diagram in **Figure 1.8d** hence subsequent heat treatments do little to control their morphology.

For the materials in the as-cast condition the secondary phase β-$Mg_{17}Al_{12}$ primarily forms as a divorced eutectic at the grain boundaries resulting in a cellular cast microstructure, as seen in **Figure 1.9a**. The volume fraction, connectivity of the β-$Mg_{17}Al_{12}$ cell structure, and general size of the β-$Mg_{17}Al_{12}$ depends on Al content and cooling rate of the casting process, as seen by the lack of connectivity for AM60B, which was formed in an identical manner to the AZ91D but with less Al in **Figure 1.9b**. The Al-Mn phases for the cast alloys are found littered throughout the alloys microstructure as constituent particles typically larger than 500 nm in radius ($r_{particle}$). That said a high magnification micrograph of the AZ91D alloy revealed smaller Al-Mn rich particles randomly dispersed throughout the microstructure, as seen in

Figure 1.9c, typically $r_{particle}$ 100 nm. These smaller Al-Mn particles were also observed for the AM60B material.

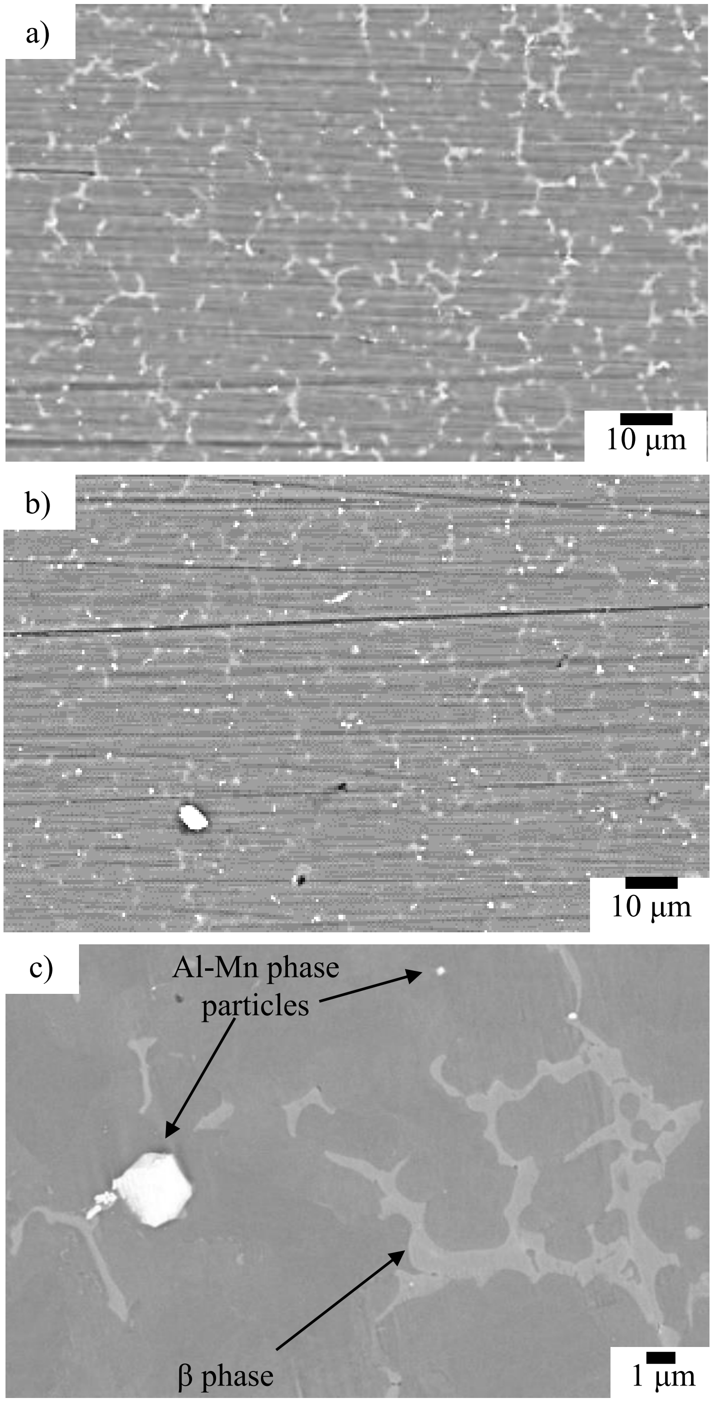

Figure 1.9: Backscattered electron micrographs of the as-cast alloys microstructures at low magnification of a) AZ91D and b) AM60B. A higher magnification micrograph on the AZ91D alloy is presented in c) revealing the general dimensions for secondary phase particles commonly observed.

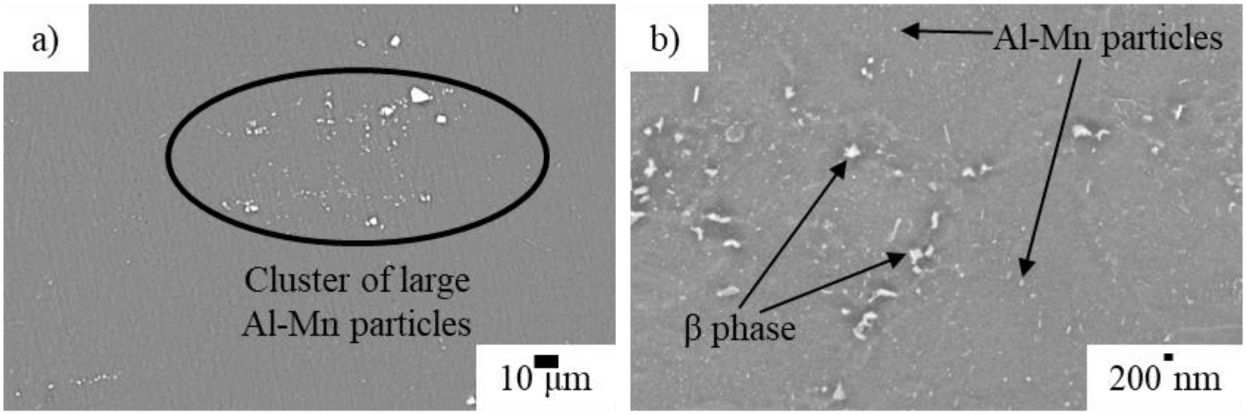

Figure 1.10: Backscattered electron micrographs of the AZ31B-H24 alloy after polishing to colloidal silica and a light nitol etch at low a) and high b) magnification.

For the wrought AZ31B-H24 alloy, the easily observable secondary phase particles at low magnification through backscattered electron microscopy are the Al-Mn phase particles which form during casting and range in size from $r_{particle}$ = 125 to 20,000 nm. A cluster of these Al-Mn particles may be observed in **Figure 1.10a**. The β-$Mg_{17}Al_{12}$ phase present in the AZ31B-H24 is a small volume fraction, enriched in Zn, and forms as particles at the grain boundaries, typically smaller than $r_{particle}$ = 250 nm, as seen in **Figure 1.10b**. An additional phase forms which is dispersed uniformly through a grain in the form of the Al-Mn rich precipitates smaller than $r_{particle}$ = 50 nm. These phases are primarily for strengthening and have been shown to have a minimal effect on corrosion in comparison to the other, electrochemically noble phases and constituent particles present in AZ31B-H24 [18,29].

1.5 The effect of secondary phases on Mg alloy corrosion

For the Mg alloys considered here, the distribution and composition of secondary phase particles present in their respective microstructures control the initiation and propagation of localized corrosion [29,30,31,32,33]. The starting microstructures for all alloys contain similar secondary phases with electrochemically noble potentials in comparison to pure Mg, varying in severity depending on composition, as seen in **Table 1.3** [18,47,48,82,83,84,85]. The secondary phases create micro-galvanic couples between the cathodic particle and its surrounding matrix and will have a number of effects associated with it including: local changes to surface potential, increased Mg matrix dissolution rates near the particle, solution concentration gradients, and local corrosion product formation and degradation [86,87,88]. This section will explore how the phases and particle distributions in the as-cast and wrought alloys microstructure influence the micro-galvanic couples formed at the surface and subsequent initiation of FFC in NaCl solutions.

Table 1.3: Table of corrosion potentials of relevant phases found in Al containing Mg alloys immersed in NaCl solutions.

Phase	**Corrosion potential (E_{corr})**
Pure Fe [18]	-0.60
Al-Fe phase [82]	-0.60
Pure Al [82]	-0.85
Al-Mn phase [82,85]	-0.90
Pure Zn [82]	-1.03
β-$Mg_{17}Al_{12}$ [47,48]	-1.25
Pure Mn [82]	-1.32
$MgZn_2$ [89]	-1.42
α-Mg [83,84]	-1.80

1.5.1 Secondary phase particle morphology influence on corrosion for AZ31B, AM60B, and AZ91D

For the cast alloys, the uniform and abundant distribution of the β-$Mg_{17}Al_{12}$ (or $Mg_{17}Al_{(12-x)}Zn_x$) phase resides along the grain boundaries and leads to the most intense corrosion occurring in the α-Mg matrix, which the β-phase surrounds. The severity of the local Mg corrosion is dependent on the volume fraction of β-$Mg_{17}Al_{12}$ as well as their individual particle spacing/connectivity, it is ultimately determined by the potential difference between the β-phase and α-Mg [90]. It has been found that higher solidification rates during casting yield a higher quantity of Al and Zn in solid solution with the Mg, raising the corrosion potential of Mg an reducing the severity of a micro-galvanic couple between α and β. The resulting local corrosion response comes in the form of filiform-like corrosion which propagates along the surface and into the material [31,32]. That said, if the β-phase exhibits good connectivity then it may act as a barrier to this localized corrosion propagation [90]. This barrier effect prevents the formation of long corrosion filaments as well as limits the depth of localized corrosion penetration [91]. In the wrought AZ31B-H24 alloy, the β-$Mg_{17}Al_{12}$ phase is less abundant in comparison to the alloys with higher Al content, yet it is still found at the grain boundaries, as seen in **Figure 1.10b**. The smaller size of the β phase, ranging from $r_{particle}$ = 20 to 250 nm, suggests the micro-galvanic corrosion with the Mg grains will be less probable and severe.

The area ratio between the anode and cathode of a galvanic couple will dictate the rate of corrosion at the anode. A cathode with a radius of $r_{particle}$ = 20,000 nm is able to support an increased galvanic corrosion current in comparison to one with a $r_{particle}$ = 125 nm. The large Al-Mn phase particles, $r_{particle} \approx 500$ nm or greater, which form during casting in all alloys create a positive electrochemical potential difference from the α-Mg matrix and have been consistently observed to be the primary initiation sites for FFC, in particular for the AZ31B alloy [29]. The Fe enriched Al-Mn particles are especially detrimental as the particles corrosion potential can be increased by a few 100 mV if Fe is present [85]. Local Mg dissolution in the form of pits can be observed at early times of full immersion surrounding the Al-Mn particles for AZ31B-H24, as seen in **Figure 1.11.** The deposition of flaky $Mg(OH)_2$ may also be observed on these particles similar to the Fe impurity particle in **Figure 1.5**, a sign of the local increase in pH at the particle.

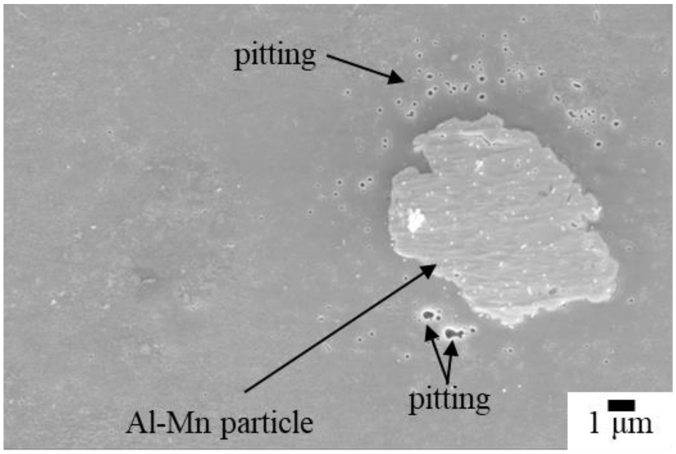

Figure 1.11: Secondary electron micrograph of AZ31B-H24 after polishing to colloidal silica finish (20 nm), corrosion in 0.6 M NaCl for ~10 minutes, and cleaning of the corrosion product with chromic acid. Emphasis is on the pitting that occurs around the Al-Mn particle.

1.5.2 Quantifying the secondary phase particle size effects on micro-galvanic coupling: Galvanic current

The common route to describing a galvanic couple is through the use of E-log(i) measurements, one for the expected anode and one for the expected cathode in the solution of interest, here being 0.6 M NaCl [25]. From these plots the expected cathodic current density and anodic current density behavior of the cathode and anode can be shown across a wide range of potentials and for a specific solution [47]. A schematic of how the galvanic coupled current density (i_{galv}) is determined for an anode (α) and cathode (β) is shown in **Figure 1.12.** The cathodic E-log(i) measurement for β and the anodic E-log(i) measurement for α intersect to determine the i_{galv} acting on the anode ($i_{galv\ on\ anode}$). The extrapolation of the anodic measurement for β and the cathodic measurement for α intersect to determine the i_{galv} acting on the cathode. The accelerated current density on the anode, $i_{galv\ on\ anode}$, is of primary concern for micro-galvanic couples, like the ones observed in Mg and its alloy. The reduced current density observed on the cathode, $i_{galv\ on\ cathode}$, is typically considered to be negligible considering its reduction in comparison to the corrosion current density of β ($i_{corr\ (\beta)}$). In the extreme case for pure Mg coupled with an Fe impurity as was shown for E-log(i) measurements by Sudholz in **Figure 1.4b**, the corrosion potential for Fe is ~ 1 V more noble than Mg [18]. This potential difference is the thermodynamic driving force which causes a galvanic couple to develop and defines the anodic or cathodic behavior of a metal. In addition, the cathodic current density (i_c) of Fe and the anodic current density (i_a) of Mg intersect at a rather low potential, E_{galv} = -1.55 V vs. SCE, because of the low polarizability of Mg. The current density where these two E-log(i) plots intersect is the i_{galv} that will act on the Mg anode. This i_{galv} value may be used to predict the amplified corrosion rate occurring on the Mg anode when galvanically coupled with Fe [25].

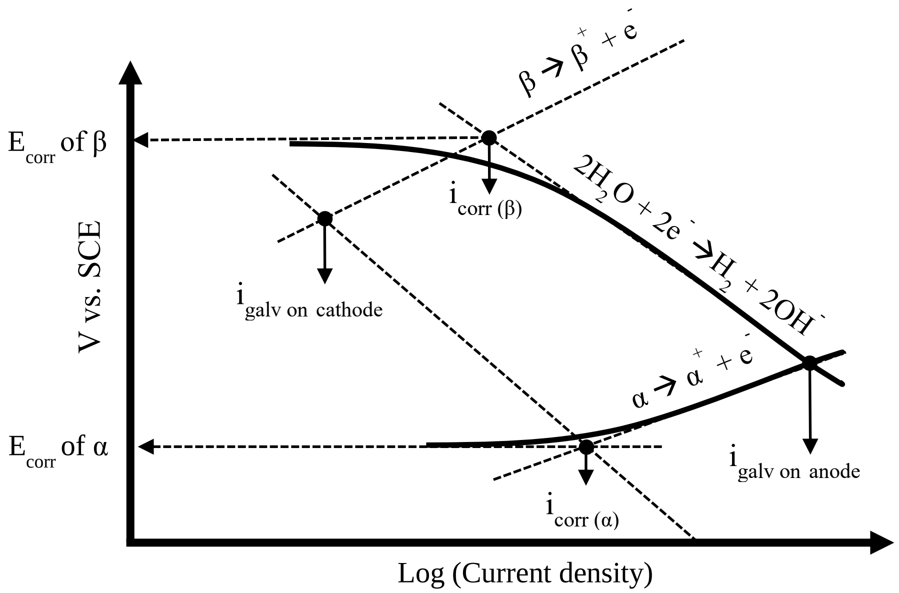

Figure 1.12: Schematic of how to determine the galvanic coupled current density which will act on an anode and cathode. The dotted lines are the Tafel extrapolations for the anodic and cathodic branches of the α and β metal.

In the case of the Al containing Mg alloys, the secondary phases E_{corr} are significantly more negative than pure Fe and the intersection of the Mg i_a is expected to be at smaller values, as observed by Mathieu et al. [47]. Experimental work showing the E-log(i) behavior of all secondary phases present in the Mg alloys is minimal [47,48,85]. However, a general treatment to observe the influence of secondary phase particle size on micro-galvanic coupled current can be observed if Tafel linear extrapolation is used [25]. The Tafel equation assumes a linear relationship between the change in potential and resulting change in current density for a E-log(i) measurement, typically observed for over-potentials of 50 mV away from the E_{corr}. The Tafel equation is presented below [25]:

$$\eta = \beta_x \log\left(\frac{i}{i_0}\right) \qquad \textbf{(3)}$$

where η is the over-potential with respect to E_{corr} of the corroding material (V), β_x is known as the Tafel slope (V/decade), x defines if β is from the anodic ($\beta_{Mg\text{-}anodic}$) or cathodic ($\beta_{particle\text{-}cathodic}$) linearization, i is the current density (A/cm^2), and i_0 is the exchange current density (A/cm^2) also known as the corrosion current density. For the purposes of the treatment herein the $\beta_{Mg\text{-}anodic}$ will be equal to 30 mV per decade of current density as was experimentally observed for high purity Mg and the $\beta_{particle\text{-}cathodic}$ will be equal to

120 mV per decade of current density as was estimated from cathodic E-log(i) measurements performed on the β-phase [47]. Additional assumptions of the exchange current density and E_{corr} of the Mg matrix and the β-phase is required and summarized in **Table 1.4**. The electrochemical nature of the secondary phase particles is known to differ depending on the particles phase but for simplicity an assumption will be made here that all particles of all sizes will have the same characteristics as β from **Table 1.4** [47,48].

Table 1.4: Values used for Tafel extrapolations for a single secondary phase particle embedded in a pure α - Mg matrix. Values from [41,47,48].

	β – $Mg_{17}Al_{12}$	**α - Mg**
E_{corr} (V vs SCE)	-1.25	-1.8
i_{corr} (A/cm^2)	3.0x10^{-6}	1.0x10^{-5}
β_x (mv/decade)	120	30

The treatment here investigates how the size of an individual secondary phase particle will influence the galvanic coupled current acting on the surrounding Mg matrix, the anode. The cathodic particles radii ($r_{particle}$) will be varied based on the AZ31B-H24 alloy, from 5 to 5,000 nm, assuming all particles are circular. The area of Mg matrix surrounding each particle assumed to be corroding will be constant and defined as the distance from the edge of the cathodic particle as $r_{susceptible}$ = 1,000 nm. **Figure 1.13** shows how the E-log(i) plots for the β particle and α matrix will be converted to an E-log(I) plot for a β particle with $r_{particle}$ = 500 nm and $r_{susceptible}$ = 1,000 nm. The determination of the I_{galv}, directly proportional to corrosion rate on the Mg matrix, for a series of cathodic particle radii qualitatively shows the impact of micro-galvanic coupling.

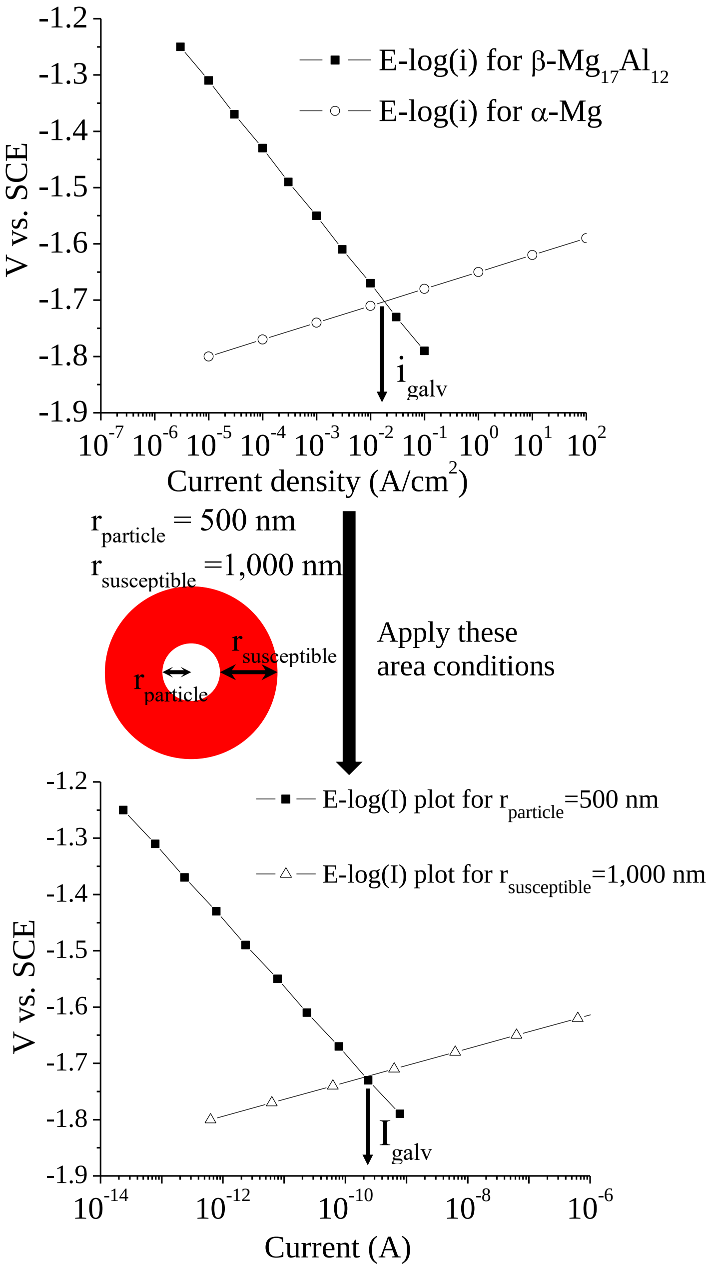

Figure 1.13: Representation of how an E-log(i) (A/cm^2) plot will be converted to an E-log(I) (A) plot so the impact of $r_{particle}$ and $r_{susceptible}$ may be quantified for a variety of micro-galvanic coupling conditions. The red area is assumed to corrode uniformly.

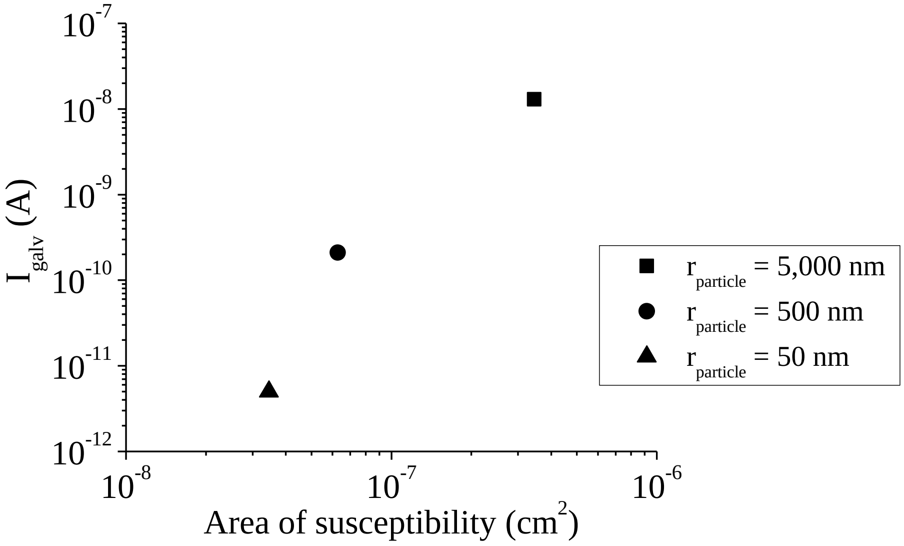

Figure 1.14: I_{galv} values as determined from E-log(I) plots for all secondary phase particle sizes and an $r_{susceptible}$ = 1,000 nm. The susceptible area is presented as a uniformly corroding area (cm^2) rather than $r_{susceptible}$ since the area changes depending on the particle radius.

The I_{galv} values determined for each $r_{particle}$ are summarized in **Figure 1.14**. If there was no intersection of the anodic and cathodic E-log(I) plots, only observed for $r_{particle}$ = 5 nm, then that particle radius is assumed to not support a galvanic couple for a $r_{susceptible}$ = 1,000 nm. That said, if a smaller susceptible area was assumed for the smaller cathodic particles then galvanic corrosion would be possible since less cathodic current is required to support the anodic reaction on a smaller anode. The I_{galv} value is directly proportional to the maximum corrosion current that may be affecting the susceptible region surrounding the cathodic particle when not considering effects from solution resistance [25]. Regardless of the susceptible area, the largest cathodic particle would be capable of supporting a galvanic current almost two orders of magnitude greater than any of the other particle sizes. This suggests the larger secondary phase particles can support rapid corrosion of the surrounding Mg matrix and explains why these larger particles are often the site for FFC initiation [29].

1.5.3 Quantifying the secondary phase particle size effects on micro-galvanic coupling: Susceptible area surrounding cathodic particle

The determination of what the susceptible area of Mg surrounding the cathodic particle will be equally important for the design of an alloy. This susceptible area is commonly described as the area around a cathodic particle where the electrochemical potential gradient imposed by the particle on the surrounding matrix is above a critical value, typically the breakdown potential (E_{bkdn}) of the matrix material. Investigations of the “throwing power” of a cathodic particle formulated by Buchheit [86] and adopted by Jain et al. [87,88] gives an estimation of this susceptible area and how solution resistance (R_s), matrix polarization resistance (R_p), particle E_{corr}, and $r_{particle}$ influence it. A one-dimensional model has been shown capable of estimating the electrochemical potential distribution surrounding a single cathodic secondary phase particle. The electrochemically noble E_{corr} of the cathodic particle will raise the potential on the matrix material, acting as if an anodic potential is being applied to the surrounding matrix material. The equation used to determine the potential distribution on the matrix material surrounding the cathodic particle is given below:

$$E(r) = E_{corr}^{matrix} - \left(E_{corr}^{matrix} - E_{corr}^{particle}\right)\exp\left[-\left(\frac{3\rho}{4R_p r_{particle}}\right)^{\frac{1}{2}} d\right] \quad \textbf{(4)}$$

where E_{corr}^{matrix} is the corrosion potential of the Mg matrix in V vs. SCE, $E_{corr}^{particle}$ is the corrosion potential of the secondary phase in V vs. SCE, ρ is the solution resistivity in Ω.cm, R_p is the polarization resistance of the matrix in $\Omega.cm^2$, $r_{particle}$ is the radius of the secondary phase particle in cm, and d is the distance away from the secondary phase particle in cm. All of the electrochemical properties (E_{corr}^{matrix}, $E_{corr}^{particle}$, R_p, and ρ) considered for the material immersed in stagnant 0.6 M NaCl solution values are found in **Table 1.5**. The values for R_s are for stagnant 0.6 M, 0.1 M, and 0.01 M NaCl solutions. The R_p value was determined by electrochemical impedance spectroscopy of the AZ31B Mg alloy at the anodic potential of -1.3 V vs. SCE.

Table 1.5: Values used to determine "throwing power" of a single cathodic particle and the susceptibility region in NaCl solutions.

ρ (Ω-cm)	25, 100, and 800
d (cm)	varied
$r_{particle}$ (cm)	5×10^{-4} to 5×10^{-7}
$E_{corr}^{particle}$(V vs. SCE)	-1.25
E_{corr}^{matrix}(V vs. SCE)	-1.8
E_{bkdn} (V vs. SCE)	-1.57
R_p (Ω-cm^2)	1

The results are plotted in **Figure 1.15** for varying $r_{particle}$ and R_s with a line representing the E_{bkdn} on each plot. Coinciding with the expectations from the I_{galv} estimations an increase in $r_{particle}$ led to an increase in the distance away from the cathodic particle that will be susceptible to galvanic corrosion. The distance of Mg susceptibility decreased as the R_s increased (or the NaCl concentration decreased).

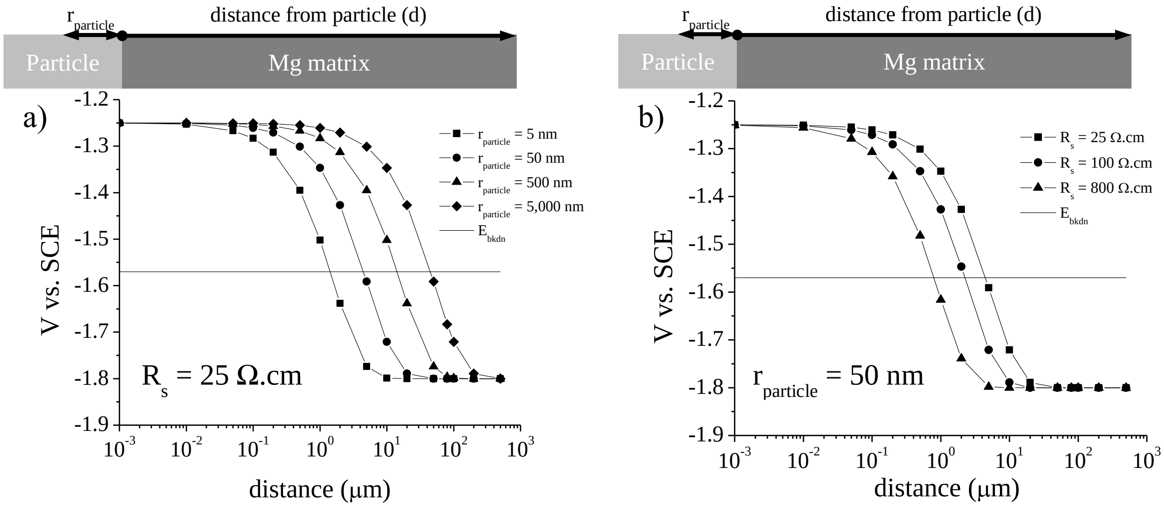

Figure 1.15: Potential versus distance plots of the effective anodic potential the Mg matrix will be susceptible to if adjacent to an electrochemically noble secondary phase particle. The potential gradient is observed to change depending on a) $r_{particle}$ and b) R_s.

The above investigations have revealed the general impact of $r_{particle}$, $r_{susceptible}$, and R_s on the nature of micro-galvanic couples present in a Mg alloy. All trends point to smaller electrochemically noble secondary phase particles leading to alloys which are less susceptible to micro-galvanic corrosion.

However, if many of these smaller particles are in close proximity with one another so that their areas of susceptibility overlap, then substantial localized corrosion will occur. A key to preventing micro-galvanic couples will be to make $r_{particle}$ small enough so it cannot support any level of galvanic activity which from the above treatment appears impossible as a particle with $r_{particle} = 5$ nm can theoretically support such a galvanic couple.

Fortunately, the above scenarios occur at time equals zero on a freshly polished surface with no corrosion product or change to the corroding solution. From the depiction in **Figure 1.2** as well as a number of studies, the pH at the surface of Mg will increase rapidly making it more thermodynamically stable to form a partially protective corrosion product in $Mg(OH)_2$. The formation of this corrosion product as well as the increase in pH will move the I_{galv} to lower values, preventing the possibility of some of the micro-galvanic couples. The small Al-Mn particles ($r_{particle} \sim 10$ nm) found in the grains of AZ31B-H24 were shown to have minimal localized corrosion near them, as indicated by a lack of dark, oxidized regions when observed after 3 hours of immersion in stagnant 0.6 M NaCl by backscattered electron microscopy in **Figure 1.16**. That said, the β-$Mg_{17}Al_{12}$ phase ($r_{particle} = 100$ nm) found at grain boundaries shows substantial darkening, indicative of micro-galvanic coupling. The β phase as well as the large Al-Mn particles will be the primary sites of micro-galvanic coupling as shown experimentally for all Mg alloys. Therefore dissociation of these phases, which typically have a radius greater than 50 nm, through laser processing is a primary goal for improving the corrosion response in this study.

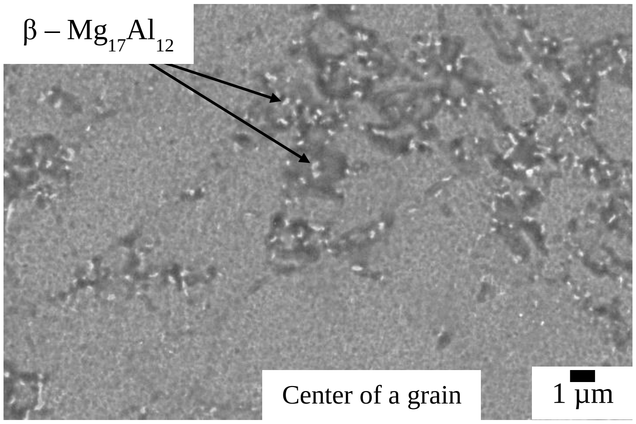

Figure 1.16: Backscattrered electron micrograph of the AZ31B-H24 alloy microstructure after corrosion in stagnant 0.6 M NaCl solution for 3 hours. Bright contrast is from the β phase which reveal local degradation (darkened regions) surrounding all β particles.

1.6 Evolution of the corrosion morphology on Mg alloys in full immersion of stagnant NaCl solutions

One of the primary goals of this dissertation is to control and minimize the impact of FFC through alterations of the alloys microstructure. The previous section explored the potential initiation sites for FFC as expected for the Mg alloys considered, while this section investigates the filaments of corrosion propagation across the alloys surface.

1.6.1 Background on FFC of Mg and Mg alloys

The FFC observed on Mg is unique in that is does not require a coating, is not based on a differential aeration model, and is observed when an alloy surface is exposed to full immersion conditions [32,51,56]. Investigations of the filament formation across pure Mg or Mg alloy surfaces have utilized a number of techniques including scanning vibrating electrode technique (SVET), time lapse optical microscopy, transmission electron microscopy (TEM), scanning electron microscopy (SEM), x-ray computed tomography (XCT), and electrochemical impedance spectroscopy (EIS) [10,12,31,32,33,51,56,92,93,[94]]. Many of the early Mg FFC studies utilized simple approaches, observing the propagation of corrosion filaments in NaCl solutions optically with subsequent SEM and elemental and grain orientation analysis leading to some understanding of how filaments propagate through certain grains better than others

[51,54]. For cast alloys, these early investigations revealed the ability β-phase has to act as a barrier to FFC propagation into the alloy when there is appreciable β-phase connectivity along the grain boundaries. Many studies since then have observed similar phenomena for the FFC propagation on Mg alloys and have reported filament propagation and morphology to be sensitive to an alloys grain structure, local composition, secondary phase distribution, and local solution chemistry [31,32,51,56].

Recent TEM work from McGill University has been used to observe microstructural effects on the propagation of filaments as well as to help verify a propagation mechanism associated with the filaments [32]. Cano et al. observed the intact corrosion product on the Mg matrix and a filament, revealing cracks which propagate through the filamentous corrosion product to the metal and the FFC process to occur underneath an intact film of MgO and $Mg(OH)_2$ [23,32]. The presence of a film during FFC propagation is consistent with the Al and Fe alloys where organic coatings are required for it to occur. The film confines the corrosion activity to linear propagation at the surface as well as the solution chemistry at the head of a filament where the film may act as a diffusion barrier to fresh bulk solution, critical to establishing a differential aeration cell on Al and Fe alloy. In addition, a layer of an electrochemically noble alloying element was shown to form under the previously corroded filament typically developing as a Zn rich layer for the AZ alloys, thought to be the cause of cathodic activation of the filaments [32].

Another recent study on AZ31 by Krebs et al. utilized in-situ 3D x-ray microtomography coupled with SEM to show changes in the FFC morphology with time [33]. The corrosion morphology changes were suggested to develop in three stages; stage I was the time leading up to corrosion initiation, stage II was characterized by shallow filament propagation, and stage III develops after stage II has completely progressed across the exposed surface and consists of deeper penetrating filaments, growing deeper with longer immersion times.

To further elaborate on these stages of corrosion, the research presented in this section analyzed localized corrosion via simultaneous electrochemical measurements as a function of immersion time. This study was conducted on the AZ31B-H24 alloy which was immersed in stagnant NaCl of varying concentrations. Several trends between the electrochemical measurements and time dependent corrosion morphologies are revealed. Real-time video was utilized to show filament propagation, providing unique insights into H_2 evolution and the impact of changing corrosion morphology. The ramifications of local corrosion on corrosion rate are discussed utilizing time dependent EIS coinciding with the filament propagation videos. The presented work also reveals the distinct ability for filaments to propagate during specific stages of corrosion without any clear evidence of H_2 evolution in proximity to the propagating filament.

1.6.2 Experimental approach to filament propagation characterization

The material used was the AZ31B in the strain hardened and partially annealed H24 condition with a grain size of approximately 6 μm, measured using the linear intercept technique. Prior to corrosion testing, specimens were ground to a 1200 grit finish using Buehler® SiC paper in a Struers alcohol-based lubricant with ethanediol, free of water, to minimize surface oxidation. A colloidal silica finish was achieved for specimens used in optical corrosion videography. All tests were started within 30 minutes of the grinding or polishing process.

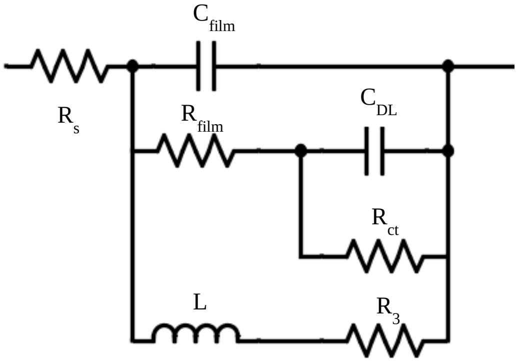

Figure 1.17: Equivalent circuit used for analysis of EIS measurements. R_s is the solution resistance, R_{film} and C_{film} are the resistance and capacitance of the corrosion product, C_{DL} is the capacitance of the electrochemical double layer, R_{ct} is the charge transfer resistance, and L and R_3 are an inductor and accompanying resistance commonly observed on corroding Mg surfaces.

Corrosion experiments were performed in a stagnant 0.6 M NaCl solution, prepared the day of the experiments. Electrochemical measurements were performed in a standard three electrode setup with the ground specimen as the working electrode, Pt mesh as the counter electrode, and a saturated calomel electrode (SCE) utilized as the reference electrode with an electrochemical impedance spectroscopy (EIS) capable Biologic SP-150 potentiostat. Electrochemical measurements were conducted using electrochemical impedance spectroscopy (EIS) performed at the open circuit potential (OCP). An area of 1 cm^2 was exposed to 250 mL of solution for the OCP/EIS measurements. EIS measurements were taken at immersion times dictated by the OCP and resulting morphology, typically at 5 minutes (prior to breakdown of passivity), 30 minutes (after breakdown), and successively at 60/120/240/360/720/ 1,080/1,440 minutes. The EIS measurements were performed over a frequency range of 100,000 Hz to 0.005 Hz at 6 points per decade using an amplitude of ±10 mV. EIS data was analyzed and a global polarization resistance (R_p) was determined using the equivalent circuit, shown in **Figure 1.17**, model and fitting procedure as described in previous work [41,93,95]. A large value of global R_p signifies a low corrosion current density ($i \propto \frac{1}{R_p}$) where the R_p has been shown to be the dominant term in Stern-Geary determined Mg alloy corrosion rates [41].

Observations of the corrosion process were performed with a Dinolite™ digital microscope for macroscopic images, and a Nikon® Optiphot-100 optical microscope for higher magnification. Real time videos of the corrosion process on the optical microscope were captured with an AmScope MU-1000 CMOS camera. *ImageJ*™ was utilized to determine FFC propagation rates across the surface and the filament width from the real time videos acquired using optical techniques. A Zygo® white light interferometer was used to measure filament depths. The change in length of the optically black corrosion filaments (corrosion fronts) was measured every 5 to 10 seconds, yielding a lateral propagation rate, **r** (cm/s), parallel to the specimen surface. After immersion, samples were rinsed with DI water and cleaned via chromic acid (200 g/L CrO_3) per ASTM G-1 to remove the specimen corrosion products [96].The combination of these techniques allowed for corrosion rate determination based on filiform areas, depths, and propagation behavior. All experiments and measurements were replicated a minimum of 4 times.

An estimate of the R_p of a single filament in stage II and III is possible by conversion of the lateral rate of propagation (**r** (cm/s)) determined for each stage to an anodic dissolution rate from the filament head in the form of current density which is proportional to R_p. Faraday's law was rearranged and used to yield a current density based on the propagation rate in the x-z surface plane (y being lateral propagation of a filament):

$$\boldsymbol{i}\left(\frac{\mathbf{A}}{\boldsymbol{cm^2}}\right) = \boldsymbol{r}\left(\frac{\boldsymbol{cm}}{\boldsymbol{s}}\right)\cdot\left(\frac{\boldsymbol{AW}\left(\frac{\boldsymbol{g}}{\boldsymbol{mol}}\right)}{\boldsymbol{n}\left(\frac{\boldsymbol{eq}}{\boldsymbol{mol}}\right)\cdot\boldsymbol{F}\left(\frac{\boldsymbol{C}}{\boldsymbol{eq}}\right)\cdot\boldsymbol{\rho}\left(\frac{\boldsymbol{g}}{\boldsymbol{cm^3}}\right)}\right)^{-1} \qquad \textbf{(5)}$$

Hence a current density for an active head of a single corrosion filament may be determined from the lateral propagation rate measured by optical microscopy where AW is the atomic weight of Mg, n is the charge number that indicates electrons exchanged within a dissolution reaction for Mg (n = 2), F is Faraday's constant, and ρ is the density of Mg. Using the Stern-Geary expression and B = 0.036 V justified from the literature [41,95], the electrochemical polarization resistance of a single filament or corroding front, R_{FFC} (Ω-cm^2), can be determined by the corrosion current density in A/cm^2.

$$\mathbf{R_{FFC}\ (\Omega\text{-}cm^2)} = \frac{\mathbf{B\ (V)}}{\mathbf{i}\ (\frac{\mathbf{A}}{\boldsymbol{cm^2}})} \qquad \textbf{(6)}$$

1.6.3 Evolution of electrochemical behavior of AZ31B at OCP

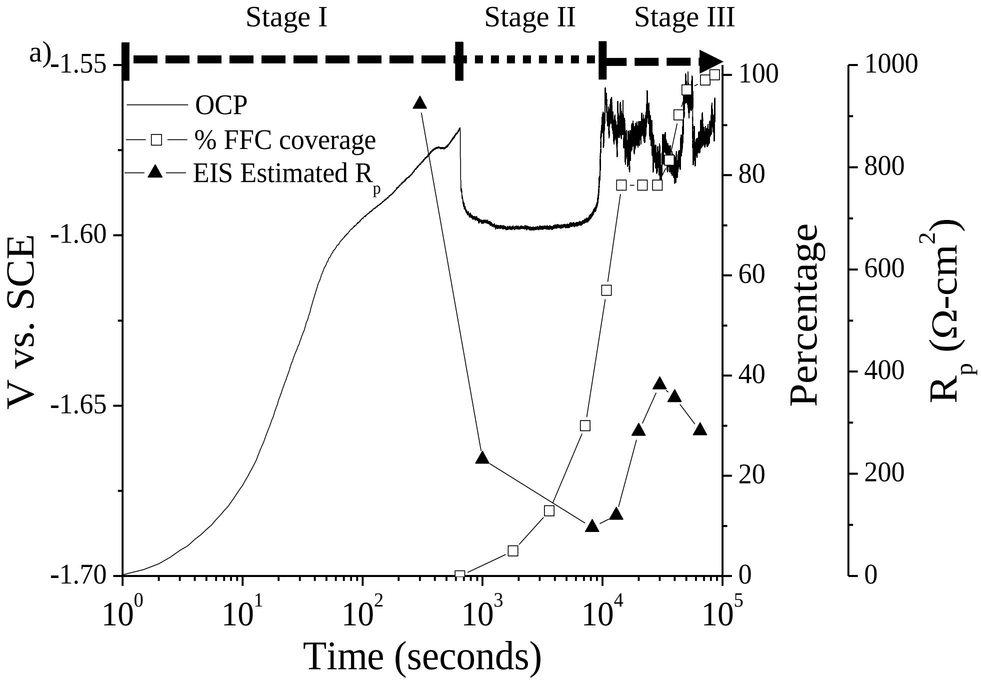

b) Stage I c) Stage II d) Stage III

Figure 1.18: One set of representative data for the OCP, percent coverage of filiform-like corrosion product, and EIS estimated global R_p plotted versus time of the AZ31B-H24 alloy immersed in 0.6 M NaCl is shown in (a). Representative optical images of the different corrosion stages occurring on AZ31B with time are shown in (b) to (d), correlated back with the plot in (a).

The OCP, percent coverage of black filiform-like corrosion product, and global R_p (the parallel R_p of passive areas and local corrosion activity) measured by EIS are plotted as a function of immersion time in **Figure 1.18a**. The OCP, which is close to -1.7 V_{SCE} , increases quickly to a peak at -1.57 V_{SCE} within the first 10 minutes, termed stage I[1]. Stage I signifies an incubation time required prior to initiation of localized corrosion on a nominally passive Mg surface, described in the previous section. The global R_p measured by EIS of stage I was observed to be ~ 900 Ω-cm^2, with the impedance spectra indicating two

---

[1] The use of the terms for each regime of FFC, stage I, II, and III, were adopted from Krebs et al. [33].

distinct capacitive loops, as observed in **Figure 1.19**, and no signs of inductive behavior [41,92,93,95]. This suggests that corrosion of the partially passive native oxide dominates the initial electrochemical response for Mg alloys. Stage I corrosion is shown via the macroscopic time lapse image in **Figure 1.18b.** In this image, large, stable bubbles of H_2 are observed on the surface. Typically the bubbles are attached to the randomly distributed constituent Al-Mn particles on the order of 5 µm in size found throughout the microstructure. The gas bubbles are then observed to decrease in size and evolve as streams of H_2 upon breakdown of the oxide, signifying the initiation of local FFC.

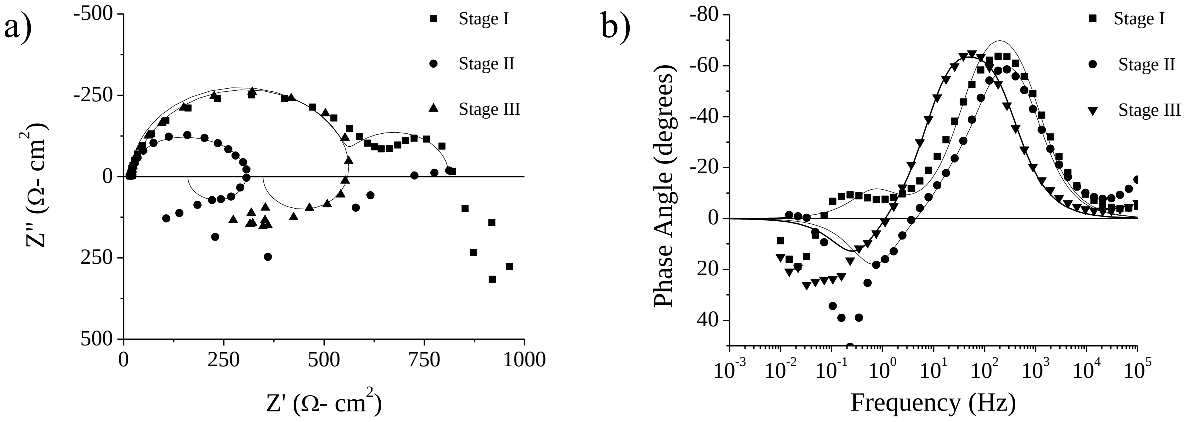

Figure 1.19: Representative impedance spectra for stage I, stage II, and stage III corrosion with raw data shown as symbols and after simulation using the equivalent circuit by King et al. as a line. Data is presented as a Nyquist plot in (a) and as a Bode phase plot in (b).

Breakdown of the native oxide film typically occurred after ~10 minutes of immersion and initiated near one of the large Al-Mn particles, as observed in previous work [29]. This regime of corrosion, termed stage II, is characterized by a stable OCP at -1.59 V_{SCE} (**Figure 1.18a**) and the initiation of thin, individual corrosion filaments that propagate across the surface in an arborescent nature, **Figure 1.18c**. During stage II, the global R_p measured by EIS, was observed directly after the initiation of FFC. The resistance decreased in magnitude to ~ 200 Ω-cm^2 after 1,000 seconds and continued to decrease in magnitude throughout the duration of stage II, reaching a local minimum, indicating a faster dissolution rate with time. Upon initiation of stage II, the global R_p reflects the parallel R_p of active filament heads, inactive filament tails, and passive areas. After completion of stage II, the OCP increased to an average of -1.57 V_{SCE} with severe fluctuations in potential.

The rate of corrosion product coverage was observed to slow at the end of stage II with black corrosion product covering ~78% of the surface (**Figure 1.18a**). Complete coverage of the 1 cm^2 exposed surface with dark corrosion product was observed after ~24 hours of immersion. In general, complete coverage by dark corroded regions is assumed when stage II is completed, however silvery regions persist in between the shallow penetrating filaments [12,92]. The α-Mg, not yet affected by FFC, remains silver in color and has developed a thin, uniform corrosion product at this stage, made of MgO (inner layer) and $Mg(OH)_2$ (porous outer layer) [23,32,94,97]. The black corrosion product is where deep localized corrosion occurs, hence complete coverage of the surface by the localized corrosion morphology should be distinguished from the still, silvery regions, where more uniform and a lower rate of corrosion is taking place.

The final regime of FFC is termed stage III, shown by the macroscopic image in **Figure 1.18d**. For stages II and III, the impedance spectra were similar in nature with the loss of the distinct oxide film capacitance from stage I and the development of inductive behavior. The corrosion product of stage III transitioned to an optically darker corrosion morphology than that observed in stage II. Moreover, the global R_p measured by EIS typically increased to more than double the minimum values determined for stage II. The darker color and shift in R_p in stage III suggests a change in the corrosion mechanism after stage II, governed by changes in the exposed alloy surface and solution chemistry. A thicker corrosion product and rougher surface morphology are associated with this stage of corrosion.

1.6.4 Evolution of localized corrosion morphology of AZ31B at OCP

Further characterization of stages II and III are shown in **Figure 1.20** with videos available online in reference [30]. In **Figure 1.20a**, a corrosion filament is observed in the bottom left of the micrograph showing streams of H_2 bubbles emanating from around the filament head. This H_2 stream continued in **Figure 1.20b** along with propagation of the corrosion filament. However, H_2 evolution at the head of the advancing filament terminated while the filament continued to propagate, as shown in **Figure 1.20 b, c** with an 8 second delta. An outline of the prior location of the filament shown in **Figure 1.20b** is placed on the image in **Figure 1.20c** to illustrate advancement of the filament. In this time frame, this is the first time that an advancing filament has been captured on video without the presence of a H_2 stream emanating at the corrosion front. In addition, filament propagation without H_2 streaming from a filament head was observed at higher frequencies when samples were immersed in more dilute NaCl solutions such as 0.1 M and 0.01 M NaCl [30]. The lack of H_2 evolution at the front of an advancing filament could stem from the time it takes H_2 gas to build up underneath the intact oxide/hydroxide film of the Mg

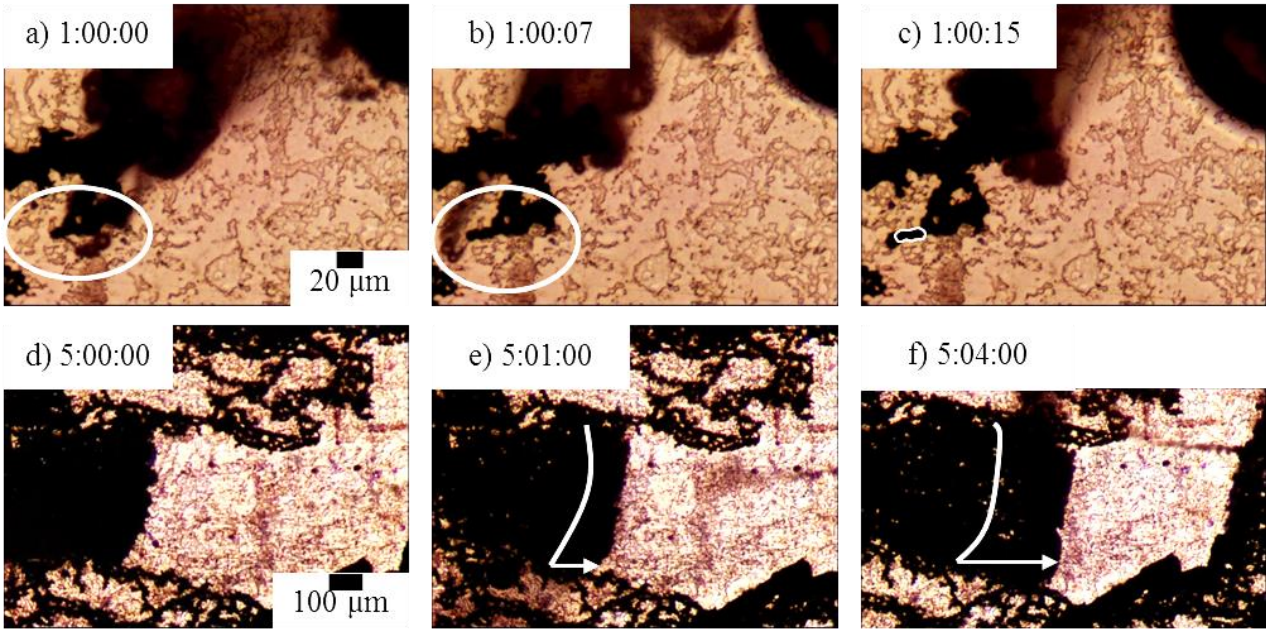

Figure 1.20: A time lapse of 15 seconds for filaments from stage II propagating across the AZ31B specimen, polished to a colloidal finish, after 1 hour of immersion in 0.6 M NaCl is shown in (a) to (c). A time lapse of 240 seconds for a stage III corroding front, propagating across the as-received AZ31B specimen, polished to a colloidal finish, after 5 hours of immersion in 0.6 M NaCl is shown in (d) to (f). A supplemental video is available for both sets of images.

matrix, followed by the rupture of the film and a burst of H_2 gas into the solution. Lower NaCl concentration solutions would observe this more frequently because of slower cathodic kinetics leading to longer times required to reach a critical amount of H_2 gas under the corrosion product. This response would be similar in nature to the rupture of blisters during the pitting corrosion of Al [98,99,100]. However a final burst of H_2 is often not observed when the filament is shown to completely stop propagation as in **Figure 1.20**.

The Mg filament propagation theory put forward by Curioni et al. regarding a “remote anodic current” may explain a filaments ability to shut off without any observable H_2 evolution at the filament head [92,93]. Here a filament has formed a supporting galvanic couple with a cathodic site some distance away from the filament head, leading to an alternate location for H_2 evolution to occur. The lack of H_2 at the filament head would prevent H_2 build up and the burst of gas to occur preventing the cracks through the filaments corrosion product. Prevention of these cracks could limit fresh neutral pH and Cl^- rich bulk solution from entering at the filament head potentially leading to the stopping of the filaments propagation. Such a mechanism would coincide with other FFC mechanisms for Al and steel alloys where the solution at the anodic filament head is made more acidic than the bulk solution via a differential aeration cell (O_2 depletion at the filament head). The mechanism for Mg would be similar however the bulk solution in this case would be at a lower pH than the OH^- rich solution generated at the filament tail where the cathodic reaction primarily occurs. Fresh bulk solution consistently introduced at the filament head would then be required to keep the filaments propagating and limited corrosion product rupturing by H_2 gas could prevent this condition from being met.

Stage III propagation is shown in **Figure 1.20d-f** where FFC propagated between the previously corroded filaments from stage II and appear to span the width of previously corroded filaments. The large area covered by the filaments in stage III will be referred to here as a “corrosion front” as they act similar to the radial propagating corrosion fronts observed on low purity Mg when immersed in higher (> 0.1 M) concentrations of NaCl solutions [31]. This corroding front also accompanied rapid H_2 evolution produced across a more confined area necessitating the use of a lower magnification lens. The appearance of rapid H_2 evolution produced at the corrosion fronts during stage III relative to the shallow filaments of stage II prompted investigation of lateral propagation rates for each stage.

1.6.5 Filament volume dissolution rates of AZ31B at OCP

From the videos found in reference [30], **Figure 1.20**, and additional experiments, FFC propagation rates were determined for stage II, III by *ImageJ* analysis. White light interferometry measurements determined the depth of penetration for corrosion filaments. A backscattered SEM micrograph of the surface is shown in **Figure 1.21a**, with stage II, III filaments present. **Figure 1.21b** is the corresponding white light interferometry measurement of the area in **Figure 1.21a** revealing penetration depth of stages II, III filaments after the specimen was cleaned of corrosion product. The yellow pixels in the interferometry map were typically observed for areas corroded during stage III because of small high aspect ratio features present on the chromic acid cleaned surface. White light interferometry has difficulty obtaining information when sharp pit like features are present.

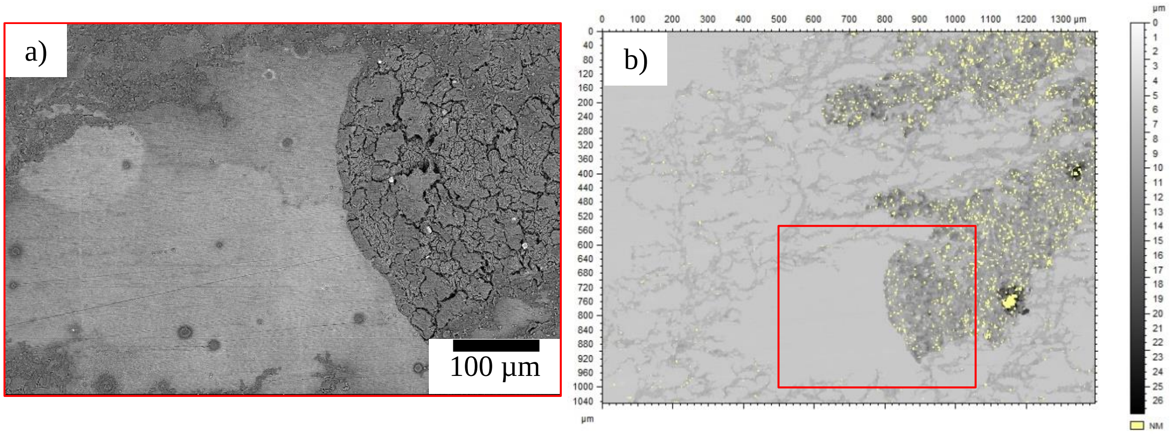

Figure 1.21: Backscattered electron micrograph of the as-received AZ31B specimen after 5 hours of immersion in 0.6 M NaCl is shown in (a). A white light interferometry topography map of the corresponding area from (a) after chromic acid cleaning is shown in (b), revealing penetration of stage II versus stage III filaments.

The propagation rates were determined for individual filaments in stage II. Each filament was found to propagate parallel to the surface at a rate $r_{II} = 1.5 \pm 0.5$ µm/s with an average width of 11 ± 4 µm and depth of 2.6 ± 0.6 μm. For stage III, the FFC propagation rates were determined by measuring the length of each propagating corroding front which moved across the surface with time, yielding a similar propagation rate in stage III with r_{III} = 1.5 ± 0.3 μm/s with an average FFC depth of 7.3 ± 3 μm. The corroding fronts are similar to the propagation observed for pure Mg when radial corrosion takes place [12, 30]. Except that, in this case, these fronts of corrosion activity are bound by the previous FFC filaments from stage II. The width of stage III corroding fronts ranged from several μm to several hundreds of μm as the spacing between stage II filaments dictated their width.

From the above analysis, a "volume loss" rate of corrosion may be tabulated for stages II and III. In stage II, an average propagation rate of a single filament was 43 $\mu m^3/s$. For stage III, a volume loss rate for a broad corroding front was determined with a width of 450 μm and found to be ~ 4,900 μm^3/second. The width chosen for stage III is from numerous video observations where between one to five corroding fronts were active on the surface after 5 hours of immersion and the combined width of the fronts was approximated at ~ 450 μm. From previous work, mass loss over a 24 hour period in 0.6 M NaCl was 0.0024 g or 0.6 μm/hr [95]. However, the depth of penetration for filaments far exceeds this upon FFC initiation after 10 minutes in stage II, at 2.6 μm, and after 5 hours the average penetration was ~ 3 μm. In contrast the penetration depth is greater than 7 μm from interferometry data in stage III. As a result, assuming uniform corrosion of Mg substrates across the entire surface can greatly underestimate the true corrosion depth.

For a single filament in stage II and the corroding fronts of stage III, an R_{FFC} can be estimated using the average lateral propagation rate of 1.5 μm/sec with equations **(5)** and **(6)** to be 0.02 $\Omega\text{-cm}^2$, assuming the Stern-Geary approach is valid. Using the average propagation rate for each stage does not account for the discrimination between the two different corrosion morphologies and depths observed. However it is possible to speculate the surface coverage (θ), or area, of active filament area and can for the first time be measured from knowledge of R_{FFC} from equations **(5)** and **(6)** and global R_p from EIS on the whole specimen:

$$\frac{1}{R_p} = \frac{\theta}{R_{FFC}} + \frac{1-\theta}{R_p^{passive\,film}} \qquad (7)$$

The θ value is the area of active global anodic region, area where intense Mg dissolution is occurring, associated with all active filaments for stage II or the area of all active corroding fronts in stage III. The $R_p^{passive\,film}$= 900 Ω-cm^2 and assumed to be constant at all times. In **Table 1.6**, the theoretical global R_p is determined by varying θ. This revealed that a surface coverage of active sites between 0.0002 and 0.0005 is required to produce a similar decrease in EIS measured R_p as observed in stage II (i.e. from 900 to 200 ohm-cm^2). For stage III, the EIS determined R_p was correlated to a slightly lower θ of around 0.00003. This approach further revealed the actively corroding area, filament head area, and the low impedance of a few rare active sites dictates the global electrochemical response of a locally corroding Mg surface. At any one time only a very small fraction of the filaments are actively corroding as supported by the videos and this could be followed over time. Moreover, it merits comment to note that the results were insensitive to plausible variations in the passive film $R_p^{passive\,film}$ impedance suggesting that the surface coverage of the actively corroding area can be accurately assessed when active sites have such a low impedance such as previously observed in the case of Al pitting [101,102]. This analysis is impactful because it indicates that FFC sites propagate at high rates, similar to pitting corrosion in other metals and that such a small area fraction is active at any one time that a reassessment of cathode area and kinetics is justified and necessary. The global EIS measured is the composite impedance of a few active sites propagating at high rates while the balance of the Mg alloy surface corrodes at a low rate. However, the global R_p measured by EIS matches mass loss and H_2 evolution even though it is a composite impedance between two distinctly different sites. The EIS-mass loss-H_2 evolution correlation is not invalid but the system is far from a uniform type corrosion.

Due to the rapid and violent evolution of hydrogen during the corrosion of AZ31B-H24, careful *in-situ* analysis is an essential element to fully understand the corrosion mechanism in operation. The results from the investigation on FFC of the AZ31B-H24 alloy will be utilized to examine the impact laser processing has on the corrosion response of the Mg alloys here.

Table 1.6: Overall or global R_p estimated by varying coverage of active corrosion sites assuming $R_{passive}$ = 900 Ω-cm^2.

Theta, θ (coverage in cm^2)	**Propagation rate estimated global R_p [Ω-cm^2]**
0	900
0.00001	621
0.00005	277 (average value in stage III)
0.0001	164
0.0002	90 (lowest value in stage II)
0.0003	62
1	0.02

1.7 Techniques to reduce the density of secondary phase particles

Many techniques have been employed to dissolve the secondary phase particles present in Mg alloys or inhibit their formation all together [26,37,38,103,104,105]. Initial studies utilized non-equilibrium techniques such as splat quenching and melt spinning to generate high cooling rates of the Mg alloys [37,38]. Rapid quench rates have been shown to prevent the formation of secondary phase particles and extend the solid solubility limit of alloying elements in Mg alloys, as well as other alloy systems [103,104,106,107,108]. In recent years, the utilization of lasers has increased due to the ability to modify the surface by inducing complete melting and subsequent rapid cooling while limiting the impact on the underlying bulk properties [104,109,110]. That said, many of these investigations have shown mixed results with respect to improving corrosion resistance as well as achieving chemical homogeneity [104,111,112]. One of the more complete studies performed by Coy et al. utilized an excimer laser to modify the AZ91D alloy leading to significant chemical homogenization at the alloys surface and an increase to the alloys corrosion resistance for ~6 hours after full immersion in 0.6 M NaCl [104]. However, the laser modification was observed to form solute bands within the melted surface. In addition, no correlation was explicitly investigated between the laser modified microstructure and the resulting corrosion response. This lack of complementary investigations, which elucidate the changes to the alloy microstructure and resulting corrosion response, identifying the microstructural factors which control the initiation and propagation of localized corrosion, has yet to be performed for laser processed Mg alloys. In addition an extensive study regarding the optimization of laser processing parameters which maximize the chemical homogeneity and explicate the homogenizing mechanisms of a Mg alloy has also yet to be performed.

1.8 Knowledge gaps

- Many of the investigations on the laser processing of Mg alloys fail to explain a mechanism for secondary phase particle dissolution in the alloy. These mechanisms will be elaborated on through careful experimental analysis with the scanning electron microscope along with support from analytical calculations.
- All investigations regarding the corrosion of excimer laser processed Mg alloys observe the initial stages of corrosion with minimal analysis of their longevity in corrosive environments. This thesis will address the corrosion response for a series of laser processed Mg alloys beyond the initiation of FFC and provide a mechanistic understanding regarding chemical homogenization and the onset of FFC. The controlled dissolution of the smaller (below 250 nm) secondary phase particles will also be investigated to describe their contribution to the corrosion process.
- There are a range of corrosion products capable of forming during the corrosion of Mg and its alloys, however, an explanation of why phases such as layered double hydroxides (LDHs) form at the surface has not be explicitly investigated. A thermodynamic approach to describe corrosion product formation for Mg alloys during atmospheric exposures will be provided along with testing of laser processed alloys to examine the impact of local composition on corrosion product formation.
- A potential use for laser processing is as a precursor to conversion coatings, utilizing it as a homogenization technique which may result in uniform deposition of the coating, minimizing coating defects. However, many of these coating techniques, such as conversion coatings/plasma electrolytic oxidation, would consume the laser processed layer and reduce the benefits of the

homogenized microstructure. An investigation will be provided regarding a physical vapor deposited (PVD) passive film onto the chemically homogenized laser processed Mg alloy with a focus on the coatings ability to compliment the homogenized surfaces reduced cathodic activity.

1.9 Thesis objectives

This thesis took a multifaceted approach to minimizing the localized corrosion and overall corrosion rate for a series of Mg alloys presented in **Table 1.2**; AZ31B-H24, AZ91D, and AM60B. The initial thrust of the work looked to homogenize the surface microstructure of each alloy through excimer laser processing. The objective was to investigate the effect laser processing has on the extent of secondary phase particle dissolution for each alloy, with a focus on the mechanism of particle dissolution. The laser processing parameters were also optimized for maximum chemical homogeneity and minimum cathodic corrosion kinetics. The AZ31B-H24 alloy was primarily used for these studies because of the abundance and size of high melting temperature constituent secondary phase particles making it the most difficult of the alloys to homogenize.

The second thrust investigated the corrosion response of the laser processed Mg alloys, observing the benefits of laser processing on the alloys through improved imaging and an improved suite of electrochemical techniques in full immersion of stagnant 0.6 M NaCl solution. The first objective was to compare the global corrosion resistance of the as-received alloys and the laser processed alloys through electrochemical measurements. The second objective observed the local corrosion behavior on each alloy surface, focusing on the initiation of FFC and the change in the corrosion product depending on the surface microstructure.

The third thrust of this thesis was to develop a coating scheme which would work with the chemically homogenized surface of the AZ31B-H24 alloy, extending the time to initiation of FFC. A coating consisting of two different oxide/hydroxide layers was developed, both of which are stable at high pH. The first layer was determined to be $MgO/Mg(OH)_2$ and the second layer was of $Gd(OH)_3$. When applied to the laser processed AZ31B alloy, the time to initiation and polarization resistance was increased 3 fold on average when immersed at its freely corroding potential in stagnant 0.6 M NaCl.

The final thrust observed an artificial atmospheric exposure of the Mg alloys using the ASTM B117 salt spray test. The atmospheric corrosion study revealed a change in the corrosion product on the laser processed alloys in the form of the more uniform coverage of a protective and stable LDH phase. This corrosion product developed primarily because of the distribution of Al and more uniform corrosion formation across the surface for all laser processed alloys.

1.10 Reference

---

1 M. James, J. M. Kihiu, and G. O. Rading: 'Automobile Weight Optimization Using Magnesium Alloy AZ31B', 2012 Mechanical Engineering Conference on Sustainable Research and Innovation, 2012.

2 D. S. Kumar, C. T. Sasanka, K. Ravindra, and K. N. S. Suman, "Magnesium and Its Alloys in Automotive Applications – A Review," American Journal of Materials Science and Technology, 2015.

3 M. Elektron. 'Magnesium Elektron Service & Innovation in Magnesium', 2016 [viewed 2016; Available from: http://www.magnesium-elektron.com/.

4 T. B. Abbott, "Magnesium: Industrial and Research Developments Over the Last 15 Years," Corrosion, 2015, 71(2), 120-127.

5 M. K. Kulekci, "Magnesium and its alloys applications in automotive industry," The International Journal of Advanced Manufacturing Technology, 2007, 39(9-10), 851-865.

6 L. A. Dobrzanski, Tanski, T., Domagala, J., Malara, S., Krol, M., "Effect of high power diode laser surface melting and cooling rate on microstructure and properties of magnesium alloys," Journal of Achievements in Materials and Manufacturing Engineering, 2009, 37(2), 238-257.

[7] M. Esmaily, J.E. Svensson, S. Fajardo, N. Birbilis, G.S. Frankel, S. Virtanen, R. Arrabal, S. Thomas, L.G. Johansson, Fundamentals and advances in magnesium alloy corrosion, Progress in Materials Science, 89 (2017) 92-193.

[8] G.L. Makar, J. Kruger, Corrosion of magnesium, International Materials Reviews, 38 (1993) 138-153.

[9] R. Allain, Fuel Economy Versus Mass, Wired.com, 2012.

[10] G. Williams, H. Neil McMurray, Localized Corrosion of Magnesium in Chloride-Containing Electrolyte Studied by a Scanning Vibrating Electrode Technique, Journal of The Electrochemical Society, 155 (2008) C340.

[11] G. Williams, R. Grace, Chloride-induced filiform corrosion of organic-coated magnesium, Electrochimica Acta, 56 (2011) 1894-1903.

[12] G. Williams, H. ap Llwyd Dafydd, R. Grace, The localised corrosion of Mg alloy AZ31 in chloride containing electrolyte studied by a scanning vibrating electrode technique, Electrochimica Acta, 109 (2013) 489-501.

[13] R. E. McNulty and J. D. Hanawalt, "Some Corrosion Characteristics of High Purity Magnesium Alloys," Journal of Electrochemical Society, 1942, 81(1), 423-433.

[14] S. Mathieu, C. Rapin, J. Steinmetz, and P. Steinmetz, "A corrosion study of the main constituent phases of AZ91 magnesium alloys," Corrosion Science, 2003, 45(12), 2741-2755.

[15] T. Zhang, Y. Li, and F. Wang, "Roles of β phase in the corrosion process of AZ91D magnesium alloy," Corrosion Science, 2006, 48(5), 1249-1264.

[16] N. Birbilis, M. A. Easton, A. D. Sudholz, S. M. Zhu, and M. A. Gibson, "On the corrosion of binary magnesium-rare earth alloys," Corrosion Science, 2009, 51(3), 683-689.

[17] Y.-l. Cheng, T.-w. Qin, H.-m. Wang, and Z. Zhang, "Comparison of corrosion behaviors of AZ31, AZ91, AM60 and ZK60 magnesium alloys," Transactions of Nonferrous Metals Society of China, 2009, 19(3), 517-524.

[18] A. D. Südholz, N. T. Kirkland, R. G. Buchheit, and N. Birbilis, "Electrochemical Properties of Intermetallic Phases and Common Impurity Elements in Magnesium Alloys," Electrochemical and Solid-State Letters, 2011, 14(2), C5.

[19] R. M. Asmussen, W. J. Binns, R. Partovi-Nia, P. Jakupi, and D. W. Shoesmith, "The stability of aluminum-manganese intermetallic phases under the microgalvanic coupling conditions anticipated in magnesium alloys," Materials and Corrosion, 2016, 67(1), 39-50.

[20] K. Gusieva, C. H. J. Davies, J. R. Scully, and N. Birbilis, "Corrosion of magnesium alloys: the role of alloying," International Materials Reviews, 2015, 60(3), 169-194.

[21] W. Zheng, Derushie, C., Zhang, R., Lo, J., "Protection of Mg Alloys for Structural Applications in Automobiles," SAE International, 2004, 25-42.

[22] J.A. Yuwono, N. Birbilis, K.S. Williams, N.V. Medhekar, Electrochemical Stability of Magnesium Surfaces in an Aqueous Environment, The Journal of Physical Chemistry C, 120 (2016) 26922-26933.

[23] M.P. Brady, G. Rother, L.M. Anovitz, K.C. Littrell, K.A. Unocic, H.H. Elsentriecy, G.L. Song, J.K. Thomson, N.C. Gallego, B. Davis, Film Breakdown and Nano-Porous Mg(OH)2 Formation from Corrosion of Magnesium Alloys in Salt Solutions, Journal of The Electrochemical Society, 162 (2015) C140-C149.

[24] M. Pourbaix, Lectures on Electrochemical Corrosion, Springer US, 2012.

[25] D.A. Jones, Principles and Prevention of Corrosion: Pearson New International Edition, Pearson Education, Limited, 2013.

---

[26] F.H. Froes, Y.W. Kim, S. Krishnamurathy, Rapid Solidification of Lightweight Metal Alloys, Materials Science and Engineering A, 117 (1989) 19-32.

[27] T.B. Massalski, H. Okamoto, P.R. Subramanian, L. Kacprzak, W.W. Scott, Binary Alloy Phase Diagrams, American Society for Metals2001.

[28] D.A. Porter, K.E. Easterling, Phase Transformations in Metals and Alloys, Third Edition (Revised Reprint), Taylor & Francis, 1992.

[29] S. Pawar, X. Zhou, G.E. Thompson, G. Scamans, Z. Fan, The Role of Intermetallics on the Corrosion Initiation of Twin Roll Cast AZ31 Mg Alloy, Journal of The Electrochemical Society, 162 (2015) C442-C448.

[30] M.A. Melia, T.W. Cain, B.F. Briglia, J.R. Scully, J.M. Fitz-Gerald, Evolution of the Corrosion Morphology on AZ31B Tracked Electrochemically and by In Situ Microscopy in Chloride-Containing Media, Jom, 69 (2017) 2322-2327.

[31] G. Williams, N. Birbilis, H.N. McMurray, Controlling factors in localised corrosion morphologies observed for magnesium immersed in chloride containing electrolyte, Faraday Discussion, 180 (2015) 313-330.

[32] Z.P. Cano, M. Danaie, J.R. Kish, J.R. McDermid, G.A. Botton, G. Williams, Physical Characterization of Cathodically-Activated Corrosion Filaments on Magnesium Alloy AZ31B, Corrosion, 71 (2015) 146-159.

[33] H.M. Krebs, A. Chirazi, L. Lechner, J. Gleb, X. Zhou, G.E. Thompson, P.J. Withers, Time-lapse Correlative 3D Imaging Applied to the Corrosion Study of AZ31 Mg Alloy in a Saline Environment, FIMPART 2015, Hyderabad, India, 2015.

[34] S.D. Cramer, A.I.H. Committee, B.S. Covino, ASM Handbook, ASM International, 2005.

[35] J.E. Gray, Luan, B., Protective coatings on magnesium and its alloys — a critical review, Journal of Alloys and Compounds, 336 (2002) 88-113.

[36] X.B. Chen, N. Birbilis, T.B. Abbott, Review of Corrosion-Resistant Conversion Coatings for Magnesium and Its Alloys, Corrosion, 67 (2011) 035005-035001 - 035005-035016.

[37] F. Hehmann, F. Sommer, H. Jones, R.G.J. Edyvean, Corrosion inhibition in magnesium-aluminium-based alloys induced by rapid solidification processing, Journal of Materials Science, 24 (1989) 2369-2379.

[38] C.B. Baliga, P. Tsakiropoulos, Development of corrosion resistant magnesium alloys Part 2 Structure of corrosion products on rapidly solidified Mg-16Al alloys, Materials Science and Technology, 9 (1993) 513-519.

[39] M.A. Melia, P. Steiner, N. Birbilis, J.M. Fitz-Gerald, J.R. Scully, Excimer Laser Surface Modification of AZ31B-H24 for Improved Corrosion Resistance, Corrosion, 72 (2015) 95-109.

[40] G.v. Baril, G. Galicia, C. Deslouis, N. Pébère, B. Tribollet, V. Vivier, An Impedance Investigation of the Mechanism of Pure Magnesium Corrosion in Sodium Sulfate Solutions, Journal of The Electrochemical Society, 154 (2007) C108.

[41] A.D. King, N. Birbilis, J.R. Scully, Accurate Electrochemical Measurement of Magnesium Corrosion Rates; a Combined Impedance, Mass-Loss and Hydrogen Collection Study, Electrochimica Acta, 121 (2014) 394-406.

[42] S. Thomas, O. Gharbi, S.H. Salleh, P. Volovitch, K. Ogle, N. Birbilis, On the effect of Fe concentration on Mg dissolution and activation studied using atomic emission spectroelectrochemistry and scanning electrochemical microscopy, Electrochimica Acta, 210 (2016) 271-284.

[43] J. Światowska, P. Volovitch, K. Ogle, The anodic dissolution of Mg in NaCl and Na2SO4 electrolytes by atomic emission spectroelectrochemistry, Corrosion Science, 52 (2010) 2372-2378.

[44] V. Shkirskiy, A.D. King, O. Gharbi, P. Volovitch, J.R. Scully, K. Ogle, N. Birbilis, Revisiting the Electrochemical Impedance Spectroscopy of Magnesium with Online Inductively Coupled Plasma Atomic Emission Spectroscopy, A European Journal of Chemical Physics and Physical Chemistry, 16 (2015) 536-539.

[45] L.G. Bland, N. Birbilis, J.R. Scully, Exploring the Effects of Intermetallic Particle Size and Spacing on the Corrosion of Mg-Al Alloys Using Model Electrodes, Journal of The Electrochemical Society, 163 (2016) C895-C906.

[46] G. Baril, Pébère, N., The corrosion of pure magnesium in aerated and deaerated sodium sulphate solutions, Corrosion Science, 43 (2001) 471-484.

[47] S. Mathieu, C. Rapin, J. Steinmetz, P. Steinmetz, A corrosion study of the main constituent phases of AZ91 magnesium alloys, Corrosion Science, 45 (2003) 2741-2755.

[48] O. Lunder, J.E. Lein, T.K. Aune, K. Nisacioglu, The Role of Mg17Al12 Phase in the Corrosion of Mg Alloy AZ91, Corrosion, 45 (1989) 741-748.

[49] G. Song, B. Johannesson, S. Hapugoda, D. StJohn, Galvanic corrosion of magnesium alloy AZ91D in contact with an aluminium alloy, steel and zinc, Corrosion Science, 46 (2004) 955-977.

[50] S. S. Jamali, ’Developing Scanning Electrochemical Microscopy Method for Studying Bio-Corrosion of Magnesium Alloys and Protective Surface Treatments, PhD, University of Wollongong, 2016.

---

[51] O. Lunder, J.E. Lein, S.M. Hesjevik, T.K. Aune, K. Nisancioglu, Corrosion morphologies on magnesium alloy AZ91, Werkstoffe und Korrosion, 45 (1994) 331-340.

[52] J.M.C. Mol, B.R.W. Hinton, D.H. Van Der Weijde, J.H.W. De Wit, S. Van Der Zwaag, A filiform corrosion and potentiodynamic polarisation study of some aluminum alloys, Journal of Materials Science, 35 (2000) 1629-1639.

[53] W.H. Slabaugh, M. Grotheer, Mechanism of Filiform Corrosion, Industrial & Engineering Chemistry, 46 (1954) 1014-1016.

[54] R.T. Ruggeri, T.R. Beck, An Analysis of Mass Transfer in Filiform Corrosion, Corrosion, 39 (1983) 452-465.

[55] A. Bautista, Filiform corrosion in polymer-coated metals, Progress in Organic Coatings, 28 (1996) 49-58.

[56] P. Schmutz, V. Guillaumin, R.S. Lillard, J.A. Lillard, G.S. Frankel, Influence of Dichromate Ions on Corrosion Processes on Pure Magnesium, Journal of The Electrochemical Society, 150 (2003) B99.

[57] N.N. Aung, W. Zhou, Effect of grain size and twins on corrosion behaviour of AZ31B magnesium alloy, Corrosion Science, 52 (2010) 589-594.

[58] H.S. Kim, G.H. Kim, H. Kim, W.J. Kim, Enhanced corrosion resistance of high strength Mg–3Al–1Zn alloy sheets with ultrafine grains in a phosphate-buffered saline solution, Corrosion Science, 74 (2013) 139-148.

[59] J. Liao, M. Hotta, S.-i. Motoda, T. Shinohara, Atmospheric corrosion of two field-exposed AZ31B magnesium alloys with different grain size, Corrosion Science, 71 (2013) 53-61.

[60] R.S. Lillard, G.F. Wang, M.I. Baskes, The Role of Metallic Bonding in the Crystallographic Pitting of Magnesium, Journal of The Electrochemical Society, 153 (2006) B358.

[61] H. Jia, X. Feng, Y. Yang, Effect of crystal orientation on corrosion behavior of directionally solidified Mg-4 wt% Zn alloy, Journal of Materials Science & Technology, (2017).

[62] G.-L. Song, Z. Xu, Crystal orientation and electrochemical corrosion of polycrystalline Mg, Corrosion Science, 63 (2012) 100-112.

[63] K. Hagihara, M. Okubo, M. Yamasaki, T. Nakano, Crystal-orientation-dependent corrosion behaviour of single crystals of a pure Mg and Mg-Al and Mg-Cu solid solutions, Corrosion Science, 109 (2016) 68-85.

[64] M. Liu, D. Qiu, M.-C. Zhao, G. Song, A. Atrens, The effect of crystallographic orientation on the active corrosion of pure magnesium, Scripta Materialia, 58 (2008) 421-424.

[65] L.G. Bland, K. Gusieva, J.R. Scully, Effect of Crystallographic Orientation on the Corrosion of Magnesium: Comparison of Film Forming and Bare Crystal Facets using Electrochemical Impedance and Raman Spectroscopy, Electrochimica Acta, 227 (2017) 136-151.

[66] D.J. Horton, A.W. Zhu, J.R. Scully, M. Neurock, Crystallographic controlled dissolution and surface faceting in disordered face-centered cubic FePd, MRS Communications, (2014) 1-7.

[67] D. Song, A. Ma, J. Jiang, P. Lin, D. Yang, J. Fan, Corrosion behavior of equal-channel-angular-pressed pure magnesium in NaCl aqueous solution, Corrosion Science, 52 (2010) 481-490.

[68] K.D. Ralston, G. Williams, N. Birbilis, Effect of pH on the grain Size Dependence of Magnesium Corrosion, Corrosion, 68 (2012) 507-517.

[69] C. op't Hoog, N. Birbilis, Y. Estrin, Corrosion of Pure Mg as a Function of Grain Size and Processing Route, Advanced Engineering Materials, 10 (2008) 579-582.

[70] G.V. Raynor, The physical metallurgy of magnesium and its alloys, Pergamon Press, 1959.

[71] I. Polmear, D. StJohn, J.F. Nie, M. Qian, Light Alloys: Metallurgy of the Light Metals, Elsevier Science, 2017.

[72] H.A. Robinson, George, P.F., Effect of Alloying and Impurity Elements in Magnesium Alloy Cast Anodes, Corrosion, 10 (1954) 182-188.

[73] J.A. Yuwono, N. Birbilis, R. Liu, Q. Ou, Q. Bao, N.V. Medhekar, Aqueous Electrochemical Activity of the Mg Surface: The Role of Group 14 and 15 Microalloying Elements, Journal of The Electrochemical Society, 164 (2017) C918-C929.

[74] N. Birbilis, G. Williams, K. Gusieva, A. Samaniego, M.A. Gibson, H.N. McMurray, Poisoning the corrosion of magnesium, Electrochemistry Communications, 34 (2013) 295-298.

[75] F. Hehmann, F. Sommer, B. Predel, Extension of Solid Solubility in Magnesium by Rapid Solidification, Materials Science and Engineering A, 125 (1990) 249-265.

[76] M. L. Technologies. 'Meridian', Meridian Lightweight Technologies 2016 [viewed 2016; Available from: http://www.meridian-mag.com/.

[77] T.B. Massalski, H. Okamoto, P.R. Subramanian, L. Kacprzak, W.W. Scott, Binary Alloy Phase Diagrams, American Society for Metals, 2001.

[78] M. Liu, P.J. Uggowitzer, A.V. Nagasekhar, P. Schmutz, M. Easton, G.-L. Song, A. Atrens, Calculated phase diagrams and the corrosion of die-cast Mg–Al alloys, Corrosion Science, 51 (2009) 602-619.

---

[79] R. Berthold, G. Kreiner, U. Burkhardt, S. Hoffmann, G. Auffermann, Y. Prots, E. Dashjav, A. Amarsanaa, M. Mihalkovic, Crystal structure and phase stability of the Φ phase in the Al–Mg–Zn system, Intermetallics, 32 (2013) 259-273.

[80] P. Liang, T. Tarfa, J.A. Robinson, S. Wagner, P. Ochin, M.G. Harmelin, H.J. Seifert, H.L. Lukas, F. Aldinger, Experimental investigation and thermodunamic calculation of the Al-Mg-Zn system, Thermochimica Acta, 314 (1998) 87-110.

[81] N. Stanford, D. Atwell, The Effect of Mn-rich Precipitates on the Strength of AZ31 Extrudates, Metallurgical and Materials Transactions A, 44 (2013) 4830-4843.

[82] N. Birbilis, R.G. Buchheit, Electrochemical Characteristics of Intermetallic Phases in Aluminum Alloys, Journal of The Electrochemical Society, 152 (2005) B140.

[83] K. Schlüter, C. Zamponi, A. Piorra, E. Quandt, Comparison of the corrosion behaviour of bulk and thin film magnesium alloys, Corrosion Science, 52 (2010) 3973-3977.

[84] S. Fajardo, G.S. Frankel, Effect of impurities on the enhanced catalytic activity for hydrogen evolution in high purity magnesium, Electrochimica Acta, 165 (2015) 255-267.

[85] R.M. Asmussen, W.J. Binns, R. Partovi-Nia, P. Jakupi, D.W. Shoesmith, The stability of aluminum-manganese intermetallic phases under the microgalvanic coupling conditions anticipated in magnesium alloys, Materials and Corrosion, 67 (2016) 39-50.

[86] R.G. Buchheit, Local Corrosion of Al-Li-Cu Alloys, Materials Science, University of Virginia, Charlottesville,VA, 1991, pp. 1-279.

[87] S. Jain, M.L.C. Lim, J.L. Hudson, J.R. Scully, Spreading of intergranular corrosion on the surface of sensitized Al-4.4Mg alloys: A general finding, Corrosion Science, 59 (2012) 136-147.

[88] S. Jain, J.L. Hudson, J.R. Scully, Effects of constituent particles and sensitization on surface spreading of intergranular corrosion on a sensitized AA5083 alloy, Electrochimica Acta, 108 (2013) 253-264.

[89] T. Ramgopal, P. Schmutz, G.S. Frankel, Electrochemical Behavior of Thin Film Analogs of $Mg(Zn,Cu,Al)_2$, Journal of The Electrochemical Society, 148 (2001) B348.

[90] R. Ambat, Aung, N.N., Zhou, W., Evaluation of microstructural effects on corrosion behaviour of AZ91D magnesium alloy, Corrosion Science, 42 (2000) 1433-1455.

[91] D. Zander, C. Schnatterer, The influence of manufacturing processes on the microstructure and corrosion of the AZ91D magnesium alloy evaluated using a computational image analysis, Corrosion Science, 98 (2015) 291-303.

[92] M. Curioni, F. Scenini, T. Monetta, F. Bellucci, Correlation between electrochemical impedance measurements and corrosion rate of magnesium investigated by real-time hydrogen measurement and optical imaging, Electrochimica Acta, 166 (2015) 372-384.

[93] Y. Yang, F. Scenini, M. Curioni, A study on magnesium corrosion by real-time imaging and electrochemical methods: relationship between local processes and hydrogen evolution, Electrochimica Acta, 198 (2016) 174-184.

[94] K.A. Unocic, H.H. Elsentriecy, M.P. Brady, H.M. Meyer, G.L. Song, M. Fayek, R.A. Meisner, B. Davis, Transmission Electron Microscopy Study of Aqueous Film Formation and Evolution on Magnesium Alloys, Journal of The Electrochemical Society, 161 (2014) C302-C311.

[95] L.G. Bland, A.D. King, N. Birbilis, J.R. Scully, Assessing the Corrosion of Commercially Pure Magnesium and Commercial AZ31B by Electrochemical Impedance, Mass-Loss, Hydrogen Collection, and Inductively Coupled Plasma Optical Emission Spectrometry Solution Analysis, Corrosion, 71 (2015) 128-145.

[96] A.S. G1, Standard Practice for Preparing, Cleaning, and Evaluating Corrosion Test Specimens, ASTM International, West Conshohocken, PA, 2011.

[97] L. Wang, T. Shinohara, B.-P. Zhang, H. Iwai, Characterization of surface products on AZ31 magnesium alloy in dilute NaCl solution, Journal of Alloys and Compounds, 485 (2009) 747-752.

[98] E. McCafferty, Sequence of steps in the pitting of aluminum by chloride ions, Corrosion Science, 45 (2003) 1421-1438.

[99] J. Soltis, Passivity breakdown, pit initiation and propagation of pits in metallic materials – Review, Corrosion Science, 90 (2015) 5-22.

[100] P.M. Natishan, E. McCafferty, The Mechanism of Blister Formation and Rupture in the Pitting of Ion-Implanted Aluminum, Journal of The Electrochemical Society, 136 (1989) 53-58.

[101] J.R. Scully, D.E. Peebles, A.D. Romig, D.R. Frear, C.R. Hills: Metallurgical Transactions A, 23, 2641, (1992).

[102] J.R. Scully, R.P. Frankenthal, K.J. Hanson, D.J. Siconolfi, J.D. Sinclair: Journal of The Electrochemical Society, 137, 1365, (1990).

[103] M. Melia, P. Steiner, N. Birbilis, J. Fitz-Gerald, J. Scully, Excimer Laser Surface Modification of AZ31B-H24 for Improved Corrosion Resistance, Corrosion, 72 (2015) 95-109.

---

[104] A.E. Coy, F. Viejo, F.J. Garcia-Garcia, Z. Liu, P. Skeldon, G.E. Thompson, Effect of excimer laser surface melting on the microstructure and corrosion performance of the die cast AZ91D magnesium alloy, Corrosion Science, 52 (2010) 387-397.

[105] L.F. Guo, T.M. Yue, H.C. Man, Excimer laser surface treatment of magnesium alloy WE43 for corrosion resistance improvement, Journal of Materials Science, 40 (2005) 3531-3533.

[106] D. Schippman, A. Weisheit, B.L. Mordike, Short Pulse Irradiation of Magnesium Based Alloys to Improve Surface Properties, Surface Engineering, 15 (1999) 23-26.

[107] T. M. Yue, J. K. Yu, Z. Mei, and H. C. Man, "Excimer laser surface treatment of Ti–6Al–4V alloy for corrosion resistance enhancement," Materials Letters, 2002, 52, 206-212.

[108] W. L. Xu, T. M. Yue, H. C. Man, and C. P. Chan, "Laser surface melting of aluminium alloy 6013 for improving pitting corrosion fatigue resistance," Surface and Coatings Technology, 2006, 200(16-17), 5077-5086.

[109] Y. Jun, G.P. Sun, S.S. Jia, Characterization and wear resistance of laser surface melting AZ91D alloy, Journal of Alloys and Compounds, 455 (2008) 142-147.

[110] J.D. Majumdar, R. Galun, B.L. Mordike, I. Manna, Effect of laser surface melting on corrosion and wear resistance of a commercial magnesium alloy, Materials Science and Engineering: A, 361 (2003) 119-129.

[111] S. Santhanakrishnan, N. Kumar, N. Dendge, D. Choudhuri, S. Katakam, S. Palanivel, H.D. Vora, R. Banerjee, R.S. Mishra, N.B. Dahotre, Macro- and Microstructural Studies of Laser-Processed WE43 (Mg-Y-Nd) Magnesium Alloy, Metallurgical and Materials Transactions B, 44 (2013) 1190-1200.

[112] P.C. Banerjee, R.K. Singh Raman, Y. Durandet, G. McAdam, Influence of Laser Processing Parameters on Microstructure and Corrosion Kinetics of Laser-Treated ZE41 Magnesium Alloy, Metallurgical and Materials Transactions A, 44 (2013) 2346-2357.

Page intentionally left blank.

Chapter 2: Al containing Mg alloy's secondary phase dissolution by excimer laser processing

2.1 Background on laser processing for Mg alloys and objectives

Researchers have sought to improve the corrosion resistance of Mg alloys by non-equilibrium, homogenization processes [1,2,3,4,5,6]. The use of high quench rate techniques such as melt spinning, laser processing, and splat cooling have been explored with mixed results [7,8,9]. Early work on the extension of the solid solubility (SS) limit of alloying elements in Mg was performed on binary Mg-X systems with such techniques [7,8,9]. The SS limit of 24 alloying elements was extended, including X = Al, Zn, and Mn. In general, non-equilibrium processed materials have shown an improvement in corrosion resistance in comparison to conventionally processed bulk material [3,4,5,6,8, 10,11,12,13,14,15,16,17,18]. However, techniques such as melt spinning and splat cooling are typically used experimentally to explore high quench rate conditions to attain extended solid solubility. In an attempt to create non-equilibrium microstructures through rapid quenching at a materials near surface regions, laser processing has been implemented to modify numerous material systems for industrial applications with the purpose of enhancing wear and corrosion resistance at the surface while retaining the underlying bulk materials properties and functionality [19,20,21,22].

The majority of the previous research on laser processing of Mg alloys has utilized continuous wave (CW) or pulsed lasers with millisecond (ms) pulse durations which result in the formation of melt depths ranging from 100 μm to 1000 μm whilst limited to quench rates of 10^5 K/s and yielding large heat affected zones on the order of 400 μm [14,23,24,25,26]. CO_2 laser irradiation of AZ31, AZ61 and WE43, all reported a melt depth of approximately 1000 μm and a decrease in corrosion rate, determined by mass loss [23]. The improved corrosion resistance was attributed to reduced grain size and a more uniform distribution of secondary phases, with minimal oxidation and loss of Mg from laser processing [23]. CW Nd:YAG surface melting of ZE41 yielded a melt depth of approximately 250 μm with little to no improvement in corrosion resistance, largely attributed to an increase in surface roughness as well as negligible improvement in corrosion observed from Zn in solid solution with Mg [24]. A decrease in corrosion resistance is frequently ascribed to the combined effects of increased surface roughness and the preferential evaporation of Mg in the modified layer [14,24,26]. In general, it also merits comment that the large heat affected zone (HAZ), when combined with the high thermal conductivity of Mg will result in a modification of the bulk mechanical properties [27,28].

Chemical homogenizing effects have been achieved through the rapid quench rates produced by nanosecond (ns) laser pulses [5,6,15,29]. In comparison to CW and ms pulse duration lasers, materials processed on the order of ns are capable of attaining quench rates on the order of 10^6 to 10^{11} K/s, which is sufficient for chemical homogenization with melt depths on the order of 500 nm to ~70 μm with a reduced heat affected zone [6,12,30,31,32,33] These melt depths result in little or no impact to the underlying bulk properties. Research in the area of ns laser processing of Mg alloys has revealed microstructures with secondary phase dissolution and a fine grained structure. Coy et al. demonstrates significant dissolution of the secondary phase, β-$Mg_{17}Al_{12}$, present in AZ91D, verified by multiple characterization techniques including cross-sectional scanning electron microscopy (SEM), X-ray diffraction (XRD), and scanning kelvin probe force microscopy (SKPFM) [5]. Similar results were obtained regarding secondary phase dissolution by ns laser processing of Mg alloys WE43 and ZE41 by Khalfaoui et al. and Guo et al., respectively [6,34]. These homogenized surfaces were shown to be largely free of segregation and secondary phases resulting in an improvement to the alloys corrosion resistance [5,6,10,35].

For a non-equilibrium processing technique to chemically homogenize the heterogeneous microstructure found in a Mg alloy, the complete melting of all phases at the alloy surface followed by rapid quenching is typically required, solidifying alloying elements into a saturated solid solution with the primary phase, in this case α-Mg. Few researchers address other dissolution mechanisms that may occur during laser processing in this time regime which can impact homogenization [5,6,34,35,36,37]. A potential mechanism which will result in significant liquid mixing during high powered laser processing is the plasma induced pressure wave which develops after ablation occurs on a materials surface [10,30,31,30,31,32,38,39]. The development of a plasma at the surface leads to an intense pressure (>20 MPa) to act on the melted surface during processing, resulting in material transport of the melted layer away from the center of the laser spot [30,31,38]. Previous studies verify the peak plasma pressure and the peak surface temperature to occur at similar times and result in the ejection of liquid material away from the center of the laser spot on the order of several µm per pulse, depending on laser fluence (energy density).

When mentioned in the Mg and Al alloy literature, the pressure wave mechanism is said to cause numerous defects such as voids and cracks [5,10]. In addition the roughening and cracking at the surface often occurs in proximity to the laser pulse overlapped regions, i.e. areas where the plasma pressure wave is primarily acting. That said, the macroscopic surface defects that develop within the modified layer is a result of the high laser fluences (energy density) typically used, leading to lessened improvement to the corrosion resistance [5,10,11,15].

The laser fluence is the primary parameter influencing the melt lifetime and heating for increased diffusion of the solute into the Mg matrix [30,32,40,41]. The selected laser fluence will determine a number of important processing conditions, namely the surface melt duration, melt depth and peak temperature. Resulting conditions often dictate how effective laser processing will be at dissolving secondary phases into the surrounding Mg matrix as well as the severity of surface defects formed. One way to increase the effective diffusion time is by increasing the irradiation dosage, pulse per area (PPA), hence increasing the total number of rapid heating and cooling events [5].

In many cases, an increase in fluence and/or PPA leads to more defects at the surface in the form of voids, cracks, and increased roughness [5,10,11,34]. For Mg alloys, the production of voids is often attributed to the peak temperature exceeding the vaporization temperature of Mg and Zn causing preferential evaporation. Relatively high laser fluences can produce temperatures on the order of 10^3 K, promoting evaporation of material from the Mg alloy. Voids have also been attributed to the trapping of gas from the atmosphere caused by surface turbulence of the melted region during laser processing [5,15,42]. If the processing fluence is high enough to cause voids, both previously described effects will be amplified with added PPA. Hence, the proper selection of laser fluence has a major impact on the corrosion performance, with lower fluences (1 J/cm^2) leading to less defects in the surface and a more increase to the corrosion resistance [12,29,33].

This chapter looks to characterize the secondary phase particle dissolution mechanisms afforded by excimer laser processing of the AZ31B-H24 alloy. This alloy was chosen for its large range of secondary phase particle size, to discern the extent of particle alteration throughout the entire surface [12,29]. First a general analytical approach will be explored to estimate the extent of secondary phase dissolution incorporating diffusional and plasma pressure effects. Second, experimental results will be provided to corroborate the analytical calculations, revealing the homogenization of the alloys microstructure with scanning electron microscopy analysis for secondary phase particles down to a resolution of 5 nm. Finally a processing parameter study will be used to explore the low fluence parameter space along with processing pressure and pulse per area (PPA). These empirical processing parameters control the lasers heat incorporation and the plasma induced pressure wave which subsequently dictates the dissolution of secondary phase particles.

Hypothesis to be tested: If an excimer laser fluence is chosen so the temperature at the surface of a Mg alloy reaches ~100^{o}C above the melting temperature of the secondary phase particle with the highest melting temperature, then through the addition of pulse per area the microstructure at the surface of the Mg alloy will become chemically homogenized.

2.2 Experimental set-up for excimer laser surface processing

2.2.1 Processing chamber design and capabilities

The processing chamber, shown in **Figure 2.1**, was utilized for all laser processing and allowed for control of the pressure, gas flow, pulse overlap, and PPA [29]. Ar gas (99.998%) was used in order to mitigate oxidation at the surface of the Mg substrates. Gas flow was controlled by a manual flow meter. Pressures below atmosphere were controlled by a roughing vacuum and a fine ball valve to allow for a graduated feed of Ar during processing with an ultimate pressure capable of 1 x 10^{-2} Torr. Pressures above atmosphere were controlled by the Ar flow rate (~20 liters per minute) and a pressure relief valve with the maximum achievable pressure being 1280 Torr. Sample translation was accomplished with a Newport linear actuator.

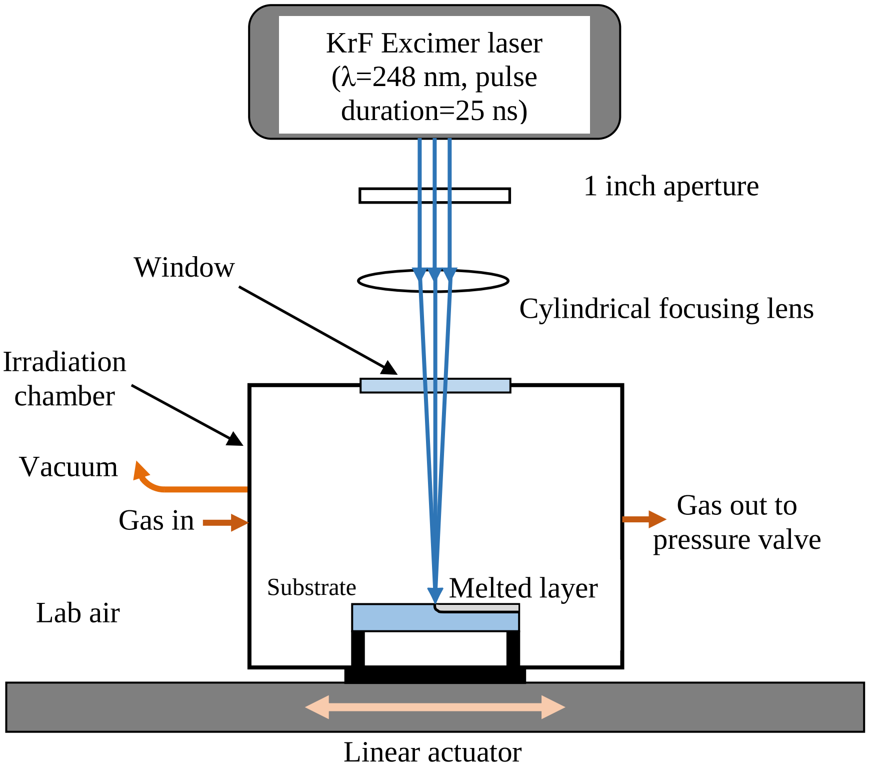

Figure 2.1: Schematic of laser processing chamber showing general flow of Ar as well as where and how pressure is controlled.

A KrF excimer laser (λ = 248 nm, pulse duration = 25 ns FWHM) was utilized with a cylindrical lens focused to a spot size of 28 mm x 1.0 mm, measured by burn paper and an optical microscope. The focal distance was fixed and the energy of the laser was varied to attain the desired laser fluence. The sample stage was translated during processing which yielded an overall effected area of 28 mm by 59 mm. The speed of translation was varied to control the pulse overlap which was consistently at 50%. The number of times a given sample region was translated in front of the laser determined the overall irradiation, known as pulse per area (PPA).

2.2.2 Choice of processing parameters

The laser fluences were carefully selected based on the ablation threshold of the AZ31B alloy so the impact of ablation on secondary phase particle dissolution could be investigated. The term "ablation threshold" here is in reference to the limiting fluence required to produce a plasma, we will not distinguish if this plasma stems from an evaporation or ablation mechanism. The ablation threshold was experimentally determined using a Q-stick™ optical emission spectrometer (OES) [43]. An AZ31B specimen was irradiated over a range of fluences in an Ar background pressure of 1 x 10^{-2} Torr, as shown in **Figure 2.2**. A fluence of 0.7 J/cm^2 was determined to be below the ablation threshold. Peaks observed in **Figure 2.2** are from the optical emission of Mg (λ = 390, 530, etc.) and background peaks from ambient lab light **[**43**]**.

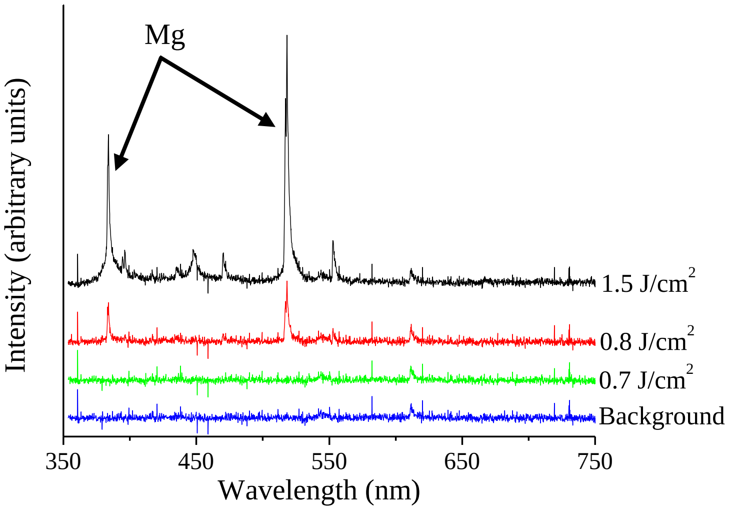

Figure 2.2: The optical emission spectra of AZ31B-H24 sample surface at a pressure of 1×10^{-2} Torr during laser processing. Peaks indicate elements present in the ablation plume (0.8 and 1.5 J/cm^2 fluences) or the spectra from ambient light entering the chamber (background and 0.7 J/cm^2 fluence).

2.2.3 Surface temperature calculation by simulated laser interactions with materials (SLIM^{TM})

To better understand the phenomena and morphologies due to laser processing, simulations to determine the surface temperature achieved during processing were performed. The SLIM software [40,41] was utilized to determine the surface temperature profiles with respect to time during the 25 ns pulse of a KrF excimer laser on a pure Mg substrate, shown in **Figure 2.3** at fluences of 0.7, 0.8, and 1.5 J/cm^2. The thermodynamic data used for the SLIM calculations are shown in **Table 2.1** as well as the melting and vaporization temperature of pertinent phases (γ-Al_8Mn_5 and β-$Mg_{17}Al_{12}$) [44,45,46,47,48]. It is important to note the values in **Table 2.1** are all for pure Mg, while the values for alloys, such as AZ31B and AZ91D, will be slightly different, in particular the properties such as thermal conductivity [49,50]. Using the simulation data as a starting point for the OES analysis, melting and ablation regimes were established, consistent with the high vapor pressure of Mg (~10 Torr at the melting temperature) and Mg high thermodynamic susceptibility to oxidize [51,52].

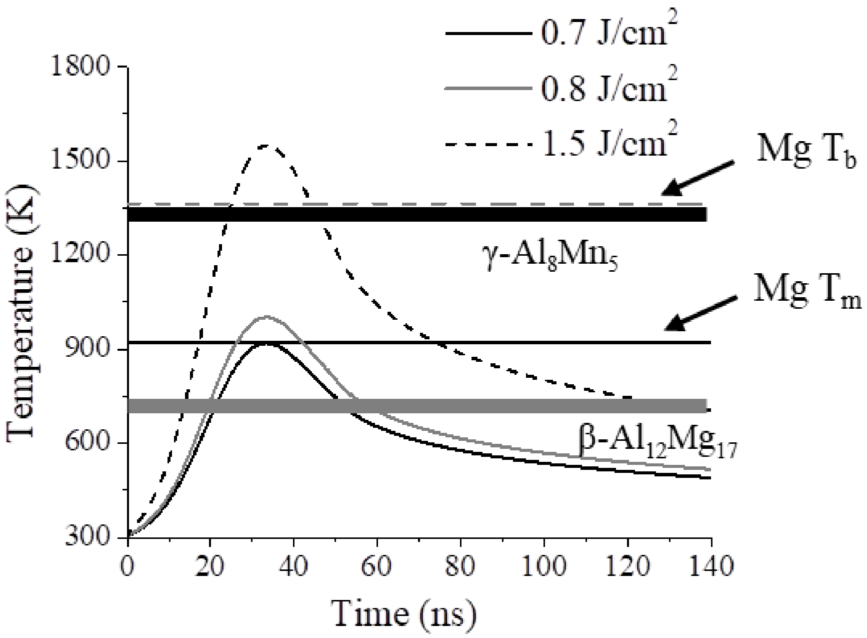

Figure 2.3: Surface temperature versus time plots produced by SLIM simulations at various KrF excimer laser fluences on a pure Mg substrate. Horizontal lines represent melting or boiling temperature of important phases.

The fluences utilized may be split into three categories to help describe and distinguish between their microstructural and corrosion modifications. For a fluence of 0.7 J/cm^2, no ablation or melting should occur. For a fluence of 0.8 J/cm^2, ablation and melting of the Mg matrix would have occurred for a very limited time based on the SLIM calculations in **Figure 2.3**. Finally for a fluence of 1.5 J/cm^2, significant ablation and melting of both the matrix and all secondary phase particles should occur.

Besides laser fluence the other processing parameters investigated were PPA and processing pressure. The PPA was chosen to investigate the impact of melt cycles on the dissolution of secondary phase particles ranging from a single pulse of the laser to 400 PPA. Varying processing pressure was utilized to reveal its impact on the plasma pressure wave.

Table 2.1: Thermodynamic data used in SLIM calculations of pure Mg and the melting temperatures of pertinent secondary phases.

Parameter	**Value**	**Unit**
Melting temperature	923	K
Boiling temperature	1380	K
Latent Heat of Melting	655.2	J/cm^3
Latent Heat of Vaporization	8,532	J/cm^3
Thermal Conductivity	1.55	W/cm.K
Reflectivity (500 nm)	0.72	
Absorption Coefficient (248 nm)	1,013,416	1/cm
Heat Capacity – Solid	$26.2\ T - 1.01 \times 10^{-3}\ T - 1.6 \times 10^{5}\ T^{-2} + 8.4 \times 10^{-6}\ T^{2}$	J/mol.K
Heat Capacity – Liquid	$213\ T - 2.1 \times 10^{-1}\ T - 3.5 \times 10^{7}\ T^{-2} + 5.6 \times 10^{-5}\ T^{2}$	J/mol.K

Secondary phase melting temperatures		
$\beta - Mg_{12}Al_{17}$	728	K
$\Phi - Mg_6(Al,Zn)_5$	663	K
$\gamma - Al_8Mn_5$	1,321	K

2.3 Analytical calculations to estimate secondary phase particle dissolution

2.3.1 Diffusion effects (random walk)

The approach for estimating diffusional effects here will be based on a first approximation from random walk processes, to estimate the diffusion of a solid into a liquid [53]:

$$d(cm) = 2.4 \cdot \sqrt{D\left[\frac{cm^2}{sec}\right] \cdot t[sec]} \tag{1}$$

Random walk diffusion was chosen based on the temperature profiles generated in **Figure 2.3**, revealing the surface of the alloy will be well above the melting temperature for pure Mg for ~ 50 ns for a fluence of 1.5 J/cm^2. The random walk process will approximate the case of the elements present in a solid, most Al-Mn secondary phase particles, diffusing into the liquid Mg with use of proper diffusivity constants. For the fluences with peak temperatures closer to the melting temperature of pure Mg, 0.7 and 0.8 J/cm^2, the random walk process will still be used, however, the diffusivity constant for solid state diffusion will be utilized.

For a majority of the secondary phases, this assumption will underestimate the melting time of the secondary phases. Specific phases such as β-$Mg_{17}Al_{12}$ or the Φ-$Mg_6(Al,Zn)_5$ phases readily melt prior to melting the Mg matrix [44,47,48]. The secondary phase particles containing only Al and Mn (and for a small fraction Fe) are of a major concern, as these phases show the lowest degree of melting and solid-liquid diffusion where the melting temperature for γ-Al_8Mn_5 is ~ 500^{o}C above pure Mg [44]. As such, the calculations presented here are limited to diffusion of Al and Mn into liquid or solid Mg depending on the fluence. In addition, the Al/Mn particles are present in two size regimes, below 10 nm and above 250 nm in radius.

The diffusivity for Al was taken from literature where the diffusivity was determined for a solid piece of Al which was allowed to diffuse into liquid Mg, determined both experimentally and computationally [54,55,56]. The diffusivity for Al into liquid Mg ranged from $D = 2.0 \times 10^{-5}$ to 2.0×10^{-4} cm^2/sec for a temperature of 1,000 K, largely dependent on the source of the diffusivity coefficient [54,55,56]. These diffusivities are similar for other solid into liquid diffusivity constants [56,57]. For the solid state case, the diffusivity of Al into solid Mg was found to approximately be 2.0×10^{-9} cm^2/sec at a temperature of 800 K, verifying that liquid Mg will enhance dissolution.

Taking equation **(1)** and the total time Mg will be liquid, estimated by the SLIM calculations to be 50 ns, the distance the solid Al or Mn was estimated to diffuse into the Mg liquid is ~24 to 76 nm (depending on the diffusivity). Therefore, as a first approximation, particles ranging from ~ 24 to 76 nm in radius should be completely dissolved via diffusion effects for the 1.5 J/cm^2 fluence. For the lower fluence range, if a temperature around 800 K is assumed to persist for 50 ns, then the solute is estimated to travel 1.2×10^{-1} nm per pulse, three orders of magnitude lower than what is to be expected when the Mg surface is liquid.

2.3.2 Plasma and recoil pressure

The plasma and recoil pressures which occur at the liquid/plasma interface contribute to material transport during laser processing [38,39]. The pressures originate as a result of ablation/evaporation of the substrate, which for the case of Mg, occurs at the onset of melting. The recoil pressure is produced in the early stages of the expanding dense vapor, often associated with the Knudsen layer, and may be estimated to be roughly half of the saturated vapor pressure [32,57]. The solution for the saturated vapor pressure is from the Calusius-Clapyron equation:

$$p_{saturated\ vapor} = p_o e^{\left[-\frac{\Lambda_b}{R}\cdot\left(\frac{1}{T}-\frac{1}{T_b}\right)\right]} \tag{2}$$

$$p_{recoil} = 0.54 \cdot p_{saturated\ vapor} \tag{3}$$

The ambient pressure, p_o, is taken as the processing pressure of 0.11 MPa, the heat of vaporization, Λ_b, for pure Mg is 128 kJ/mol, and R is the gas constant [45]. The equilibrium boiling temperature, T_b, for pure Mg is 1380 K and the value for T was taken as the maximum achievable temperature as calculated by SLIM, 1600 K. Based on these parameters, the recoil pressure, p_{recoil}, was estimated to be 0.3 MPa.

The plasma pressure is generated by the evaporated or ablated particles from the target substrate which acts on the target surface for as long as the plasma is near the surface, typically on the order of 10 ns [58,59]. The pressure is proportional to the laser irradiance, with a higher irradiance increasing the plasma pressure the surface experiences, often on the order of 10 to 100 MPa [30,31]. The value of the plasma pressure for the case of Mg was determined by the equation posed by Schaaf, which is adapted from Raizer for a laser supported combustion (LSC) wave [31,60]:

$$p_s^{LSC} = \left[1 - \frac{2W}{\gamma_o - 1}\right]\left[\frac{\gamma_o + 1}{2}\right]^{\frac{1}{3}}\left[\frac{(\gamma-1)(\gamma+1)}{(\gamma+W)(\gamma_o-1-2W)}\right]^{\frac{2}{3}} \cdot \rho_o^{\frac{1}{3}} \cdot I_o^{\frac{2}{3}} \tag{4}$$

with $W = 0.009 \cdot I_o^{\frac{2}{3}}$ as a dimensionless particle velocity and I_o in MW/cm^2. The parameters for the p_s^{LSC} calculation are $\gamma_o = 1.67$ and $\gamma = 1.2$ as the adiabatic exponents of the processing gas and metal vapor, respectively, $\rho_o = 1.78$ kg/m^3 is the gas density, and I_o (for a laser fluence of 1.5 J/cm^2) is 60,000 MW/m^2. Parameters of the gas/plasma were similar to the case in Schaaf et al. resulting in an expected plasma pressure of 49 MPa for a fluence of 1.5 J/cm^2.

At the same time, plasma and recoil pressure components are acting on the Mg surface, which will be liquid. The material transport of liquid Mg at the surface can be quantified by association with laser drilling by von Allmen et al. and Luft et al. [30,61]. The material transport of the liquid metal was treated as a non-viscous, incompressible fluid estimating the pressure distribution as a “top hat” profile as depicted in **Figure 2.4**. The radial velocity of the liquid was calculated from the volume work of the plasma and recoil pressures [31]:

$$v_{lat} = \sqrt{\frac{2 \cdot \Delta p}{\rho}} \tag{5}$$

where Δp is the sum of the recoil and plasma pressures minus the ambient pressure, and ρ is the density of the liquid being displaced, taken as 1,471 kg/m^3 for liquid Mg [62]. Consequently the velocity of the liquid Mg away from the center of the laser spot can be estimated as 250 m/s, resulting in the liquid moving 13 µm per pulse if the Mg is liquid for 50 ns.

A schematic of the material transport may be observed in **Figure 2.4** depicting the impact of the plasma pressure, as well as suggesting where the Gaussian intensity of the laser spot will be acting. **Figure 2.4** only illustrates the large Al/Mn secondary phases as these will be dominated by the plasma induced material transport. Convective forces such as the Marangoni effect were disregarded for this analysis as they have been shown to provide little impact on material transport [31].

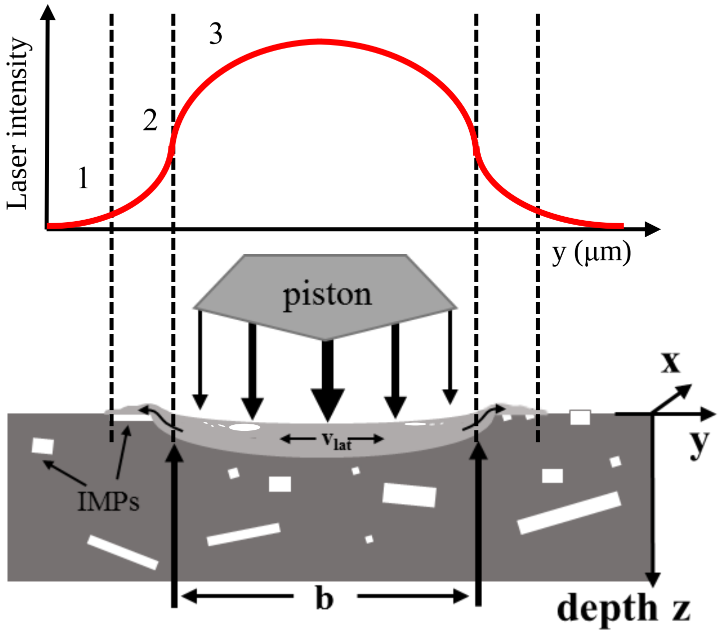

Figure 2.4: Schematic of the material transport afforded by the plasma induced pressure wave, adapted from Schaaf and von Allmen [30,31]. The expected Gaussian distribution of laser intensity plot ted above the schematic suggests what phenomena and extent of chemical homogenization may be afforded by a single laser pulse.

2.4 Experimental approach to observing influence of laser processing parameters

The goal of the experimental approach was to observe how processing parameters influenced the dissolution of the secondary phase particles present in the Mg alloys. The AZ31B-H24 specimens were prepared in two ways prior to laser processing. Primarily, the AZ31B sheet would be cut to size with a metal shear and ground to a 1200 grit finish using an ethanol based lubricant to prevent oxidation during the grinding process. This specimen would then be laser processed within 30 minutes of the final grinding procedure to minimize the time an oxide could grow on the specimen's surface. The grinding and laser processing procedures were used for the majority of the laser processing studies as well as corrosion experimentation.

The second sample preparation route was utilized to determine the extent of secondary phase particle dissolution for the smaller, below 250 nm radius, particle sizes. These specimen were polishing to a colloidal finish (~50 nm) followed by a 5 second immersion in a solution of 2% nitric acid and 98%

methanol to etch the Mg, exposing the secondary phases. This etching procedure was necessary since a specimen polished to a colloidal finish would reflect a majority of the laser light. The 1200 grit finish (~9 μm) provided a smooth enough surface so a single laser pulse would yield no scratch marks while being rough enough to absorb the laser light and promote melting.

A majority of the secondary phase particle dissolution, as well as other laser processing effects, were observed by scanning electron microscopy (SEM). An FEI Quanta 650 SEM operating at accelerating voltages ranging from 5 to 20 kV and a spot size of 4.0 was used with the secondary electron and backscatter electron (BSE) detectors. The BSE imaging mode was the primary detector used to show compositional contrast, typically observing a resolution of ~5 nm. The SEM was accompanied by an Oxford energy dispersive spectroscopy (EDS) system to quantify compositional variations of all phases present. The observation of laser processing effects to the secondary phase particle utilized an imaging technique where a registration mark was used as a reference point on a specimen so the same area of the specimen could be imaged before and after laser processing. Markings were made with a Vicker's micro-hardness indenter.

ImageJ^{TM} particle size and counting analysis was provided to verify and quantify the degree of dissolution afforded by laser processing. In general, the image processing used the SEM micrographs and converted them to binary with a thresholding method. Thresholding was performed based on interpretation of the micrographs to ensure the contrast observed was from a secondary phase and not any other feature (care was taken for laser processed specimen as ripples disrupt this thresholding procedure). After conversion to the binary format, the images were sent through the particle counting and measurement application in ImageJ^{TM} yielding their size as well as a near neighbor distance (NND) application to determine changes to secondary phase particle NND. This data was binned and plotted as a histogram to observe changes in quantity, size, and NND of secondary phase particles present before and after laser processing.

Phase analysis on a select number of samples was performed by grazing incidence X-ray diffraction (GI-XRD) utilizing a PANalytical X'Pert Pro MPD diffractometer with a Cu-K$_\alpha$ (λ=1.54 Å) source at a 0.5^o

incident angle (2.5 μm X-ray penetration depth). The volume fraction of secondary phase particles was below the detection limit for the AZ31B alloy however this technique will be used to reveal oxidation effects from laser processing as well as homogenization effects for other cast alloys which contained higher volume fractions of the β-$Mg_{17}Al_{12}$ phase.

In addition, characterization of the corrosion response was used as a metric for chemical homogenization of the microstructure. The particles of interest are known to be preferential sites for the cathodic reaction therefore changes to the cathodic reaction rate, determined by cathodic polarization measurements, will indicate qualitatively the extent of secondary phase particle dissolution afforded by laser processing. The processing parameters were optimized around the cathodic polarization measurements, with the lowest achievable cathodic current densities correlating to the "best" processing parameters.

Corrosion characterization was performed in a standard three-electrode corrosion cell with the base alloy or laser processed surface as the working electrode (1 cm^2 exposed area), a saturated calomel electrode (SCE) as the reference electrode, and a platinum mesh counter electrode. Prior to corrosion testing, the base alloy samples were ground to a 1200 grit finish while the laser processed specimens were used directly. All corrosion experiments were performed at lab temperature ~25^{o}C. A stagnant 0.6 M NaCl solution (pH=5.2) was used for open circuit potential (OCP) measurements taken for 30 minutes. After the OCP measurement a cathodic polarization measurement was taken which began by applying a voltage 20 mV above the working electrodes OCP and scanning at 1 mV/sec to -2.3 V vs. SCE.

All corrosion and microstructural changes were repeatable with at least 3 replications of a given result.

2.5 Experimental results

The as-received AZ31B-H24 microstructure is shown in **Figure 1.10**, at low (a) and high (b) magnification. The low magnification micrograph in **Figure 1.10a** primarily shows the large Al-Mn secondary phase particles, with radii larger than 125 nm, termed *tier 1* for this discussion. These larger particles, which form during casting, have the highest melting temperature of any of the secondary phases found in the Mg-Al alloys, and appear to have a random distribution, with occasional clustering. **Figure 1.10b** shows a higher magnification micrograph of a sample following a mild etch in nitric acid, highlighting the irregularly shaped Al/Zn rich phase (β-$Mg_{17}Al_{12}$ or Φ-$Mg_6(Al, Zn)_5$) found near the grain boundaries. These particles range in radius from ~ 15 nm to 250 nm and will be termed *tier 2* particles. In addition, **Figure 1.10b** shows the uniform distribution of sub-10 nm radius Al/Mn rich particles throughout the grains, magnified in the inlayed image. The sub-10 nm Al-Mn rich particles have been observed in other studies, termed *tier 3* particles here, showing similar chemistry to the *tier 1* Al-Mn particles yet formed after rolling, during the heat treatment process.

2.5.1 General homogenization and laser processing effects with a laser fluence of 1.5 J/cm^2

Studies to observe the potential for homogenization and dissolution of all secondary phase particles present in the AZ31B microstructure by laser processing was performed utilizing a single pulse at a fluence of 1.5 J/cm^2 because the simulated surface temperature rose above the melting temperature of the Al-Mn secondary phase particles. Backscattered electron (BSE) micrographs taken before and after a single laser pulse are shown in **Figure 2.5** revealing melting of all secondary phases, with particular attention to the cluster of Al-Mn particles in **Figure 2.5c**.

The dissolution of the *tier 2* and *tier 3* particles was verified in **Figure 2.5d** after laser processing, at least to the resolution limits of the SEM (~5 nm). The change to secondary phase particle populations is observed in **Figure 2.6**. Binary images generated from the BSE micrographs in **Figure 2.5a and c** clearly show a reduction in the number of sub-µm particles, from 2,201 to 317 particles after a single pulse from the laser. These binary images shown in **Figure 2.6** were analyzed using the particle counting application in ImageJ and presented as histograms binned by particle radius in **Figure 2.6c**. Overall, the quantity of secondary phase particles exposed at the AZ31B surface is reduced by 4 fold or more with the total number of particles being reduced from a total of ~2,500 for the as-received condition to ~300 after a single laser pulse. In addition, the nearest neighbor distance (NND) is also reported in **Figure 2.6d** revealing minimal change to the distribution of the NND, with the primary emphasis on the dramatic reduction in quantity of secondary phase particles. The *tier 1* particles show significant evidence of melting and coverage by a "wave" of liquid Mg, but complete dissolution was rarely observed, dependent on the size of the particle.

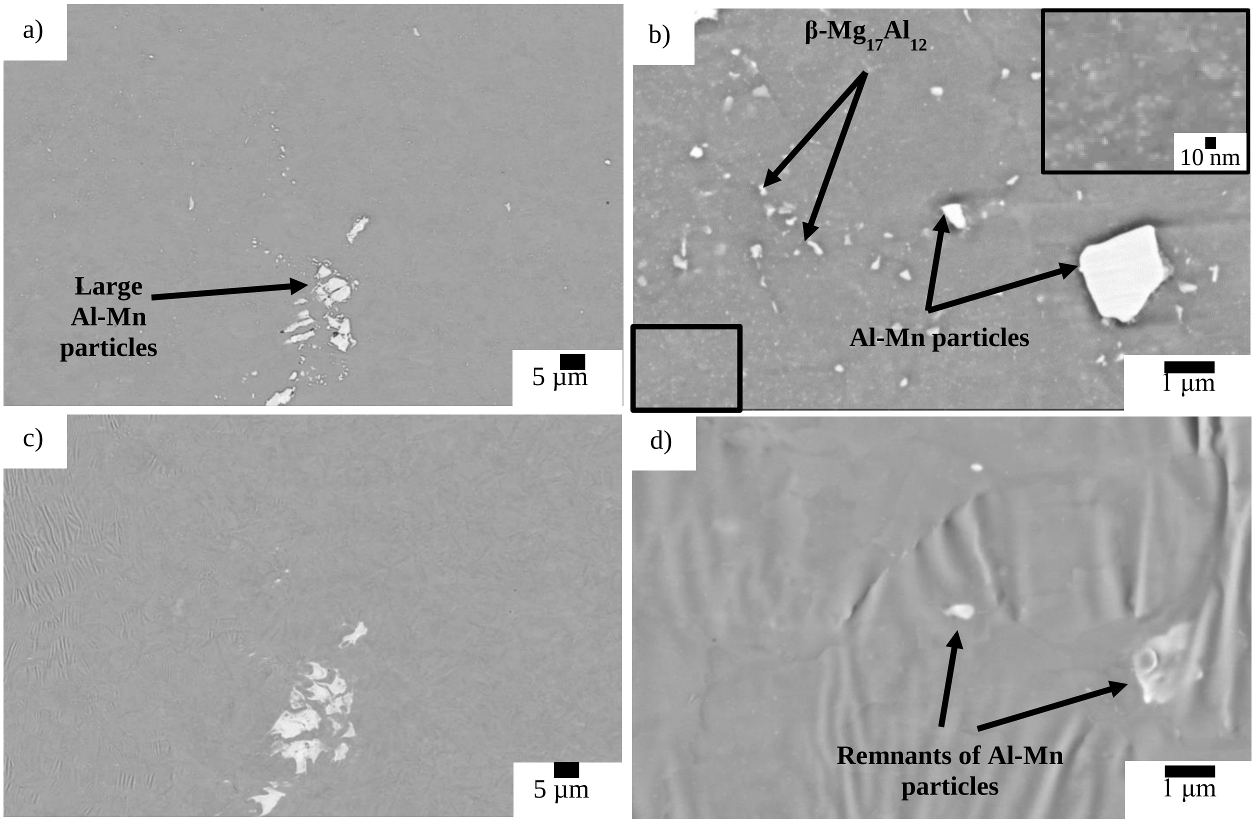

Figure 2.5: BSE micrographs taken with respect to a hardness mark reveal the dissolution of secondary phases on multiple length scales. Low magnification micrograph in a) show cluster of *tier 1* Al-Mn particles and after 1 laser pulse, c), the partial melting of these particles and disappearance of the other smaller observable particles. At higher magnification in b) smaller particles are revealed at sub-10 nm to ~200 nm, all of which are homogenized after a single laser pulse as shown in d).

The dissolution of the *tier 3* secondary phase particles in **Figure 2.5** correlate well with the calculations based solely on solid/liquid diffusion with the assumption that a particle with a radius of 24 to 76 nm can be completely dissolved. However, this diffusion case only takes into consideration the time where the secondary phase particles are solid and the Mg is liquid. The majority of the *tier 2* particles (15 to 250 nm in radius) were also observed to dissolve after one laser pulse or be covered by the Mg liquid movement caused by the plasma induced pressure wave. The composition of the *tier 2* particles was similar to that of the Φ and β phases, both of which have a T_m below that of Mg. Hence melting would occur for all of these particles along with the Mg matrix, leading to liquid mixing followed by rapid solidification.

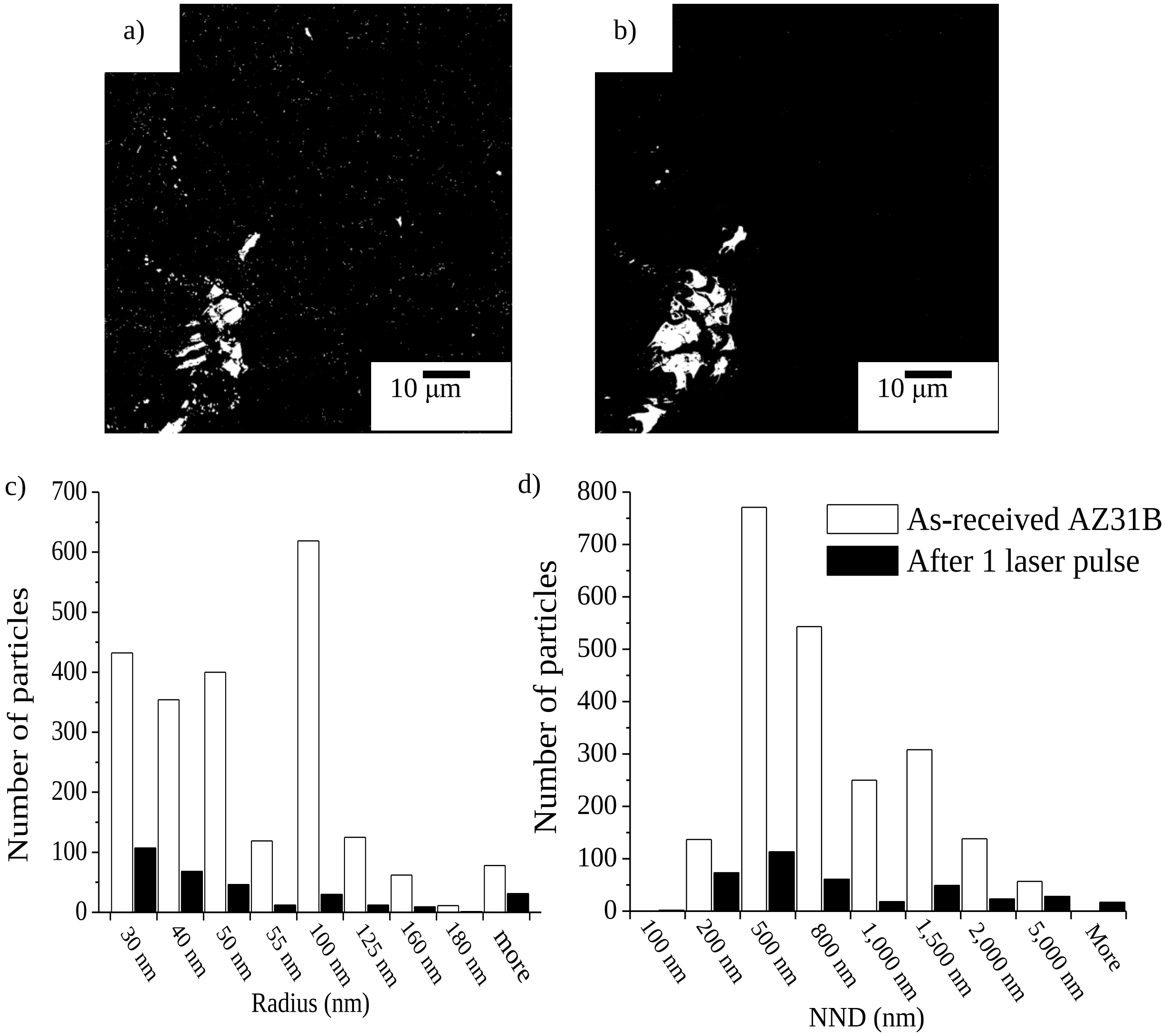

Figure 2.6: Binary images a) and b) of the low magnification micrographs from Figure 3 a) and c), respectively. ImageJ particle size, c), and near neighbor distance (NND), d), analysis of a) and b) represented as a histograms.

Evidence of a plasma induced pressure wave is shown in **Figure 2.7** which reveals the partial coverage of a large *tier 1* Al-Mn particle by Mg liquid during processing. The particle was partially covered by a 3 µm wide Mg-rich layer, covering about half of the initially exposed particle. In addition, the particle itself exhibited rounded edges after the laser pulse, verifying melting of the particle and the entire surface of the Mg alloy. The total effect of liquid mixing can further improve homogenization when coupled with the plasma induced pressure wave. Partial coverage of the *tier 1* particles was commonly observed throughout the region of the laser spot where melting occurred as shown in **Figure 2.7**. The outward material transport of the liquid Mg resulted in partial coverage of many *tier 1* particles, observed to be covered by a Mg layer ~ 3 µm wide, supporting the expected pressure wave calculations which suggested 13 µm per pulse for a fluence of 1.5 J/cm^2.

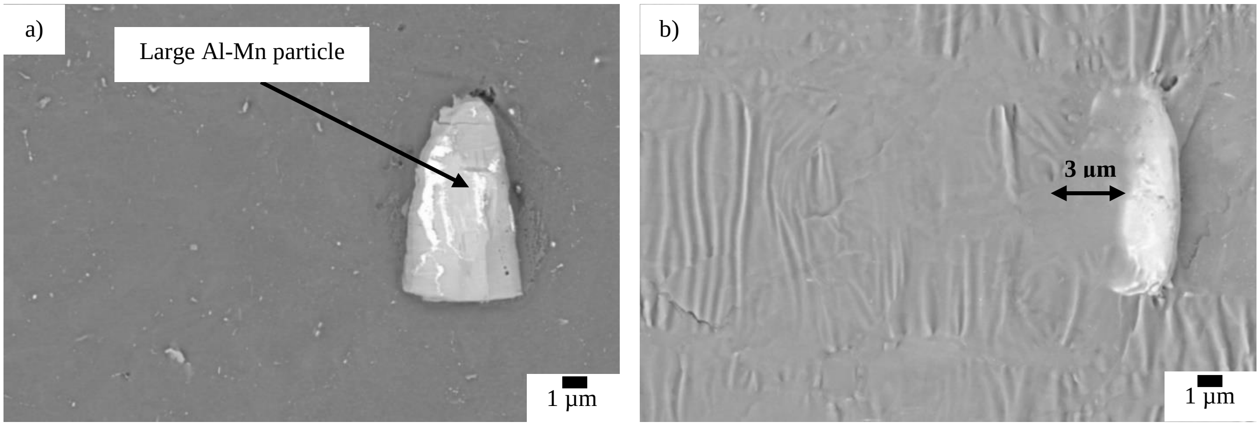

Figure 2.7: BSE micrographs taken with respect to a hardness mark reveal a large *tier 1* particle, in a), partially covered by Mg after a single laser pulse by material transport caused by the plasma induced pressure wave in b).

The combination of the experimental results, analytical results, and knowledge of laser processing provide a schematic of how secondary phase dissolution occurs at the AZ31B surface, shown in **Figure 2.8**. An outline of various regimes with respect to the Gaussian laser intensity profile is shown, revealing where and the extent to which dissolution will occur in a single pulse of the laser. At the very outer edge of the laser spot (intensity **region 1**) the *tier 2* and *tier 3* phases show signs of diffusion; however no secondary phases appear to be completely dissolved. At the center of the laser spot, **region 3**, the laser intensity is relatively uniform and at its maximum showing complete dissolution of the *tier 2* and *tier 3* particles. The *tier 1* particles with high melting temperatures show substantial signs of dissolution and melting in addition to partial coverage of Mg, which has a “wavelike” appearance.

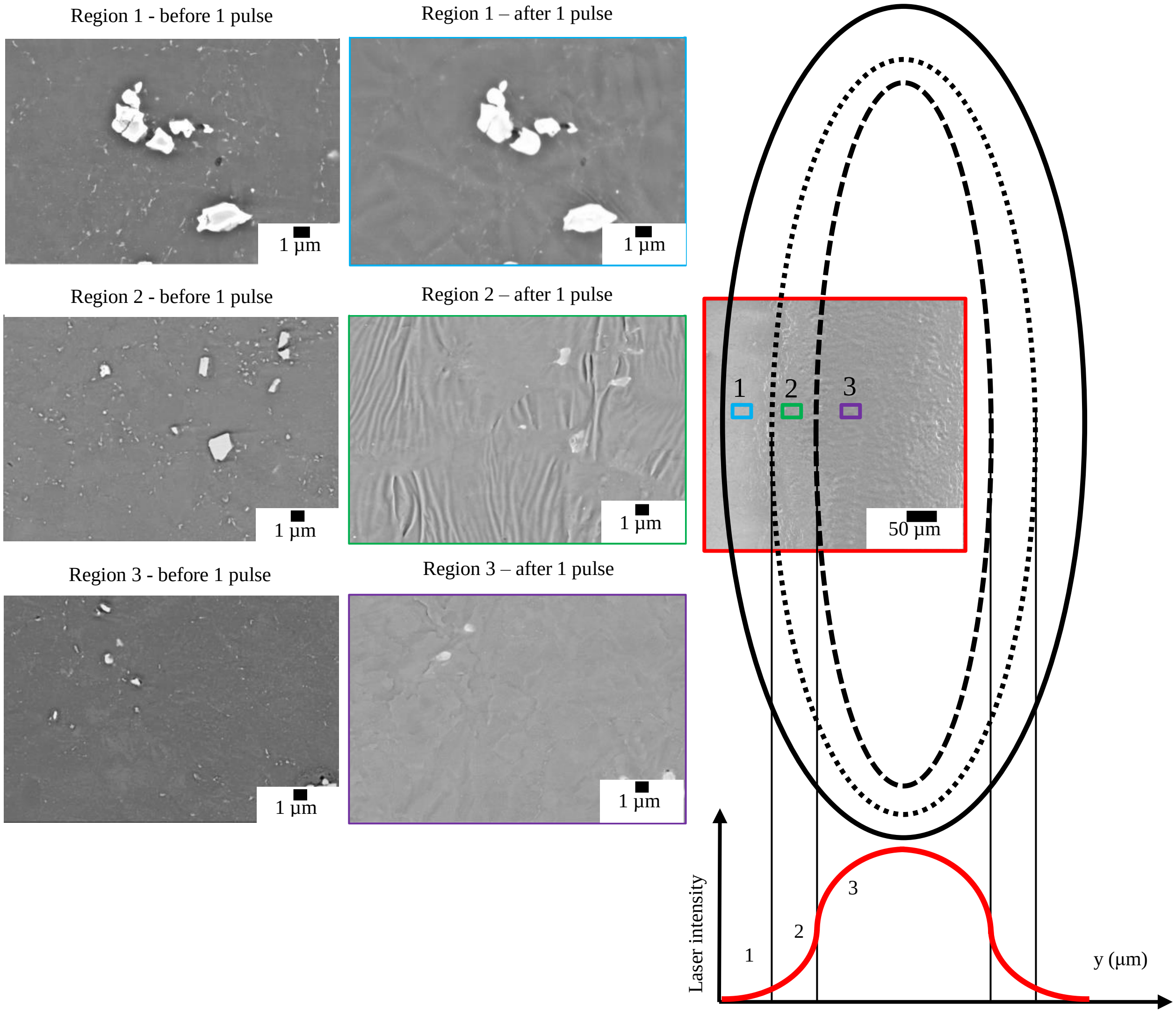

Figure 2.8: Schematic of where homogenization will take place under irradiation of a single laser pulse from an excimer laser on AZ31B with respect to the Gaussian laser intensity profile and spot size. Minimal dissolution occurs in region 1 while region 2 exhibits dissolution of the majority of smaller and medium particles in addition to with ripple formation. Region 3 reveals similar fate for *tier 2* and *tier 3* particles as in region 2 with qualitatively more melting and dissolution of the *tier 1* Al-Mn particles.

Within these two regimes there exists an intermediate region, **region 2**, where the surface changes from complete melting (**region 3**) to no melting (**region 1**). The surface shows intense ripples and wave like formations stemming from the outward motion of the liquid, propagated by the plasma-induced pressure wave followed by rapid solidification. Dissolution of the *tier 2* and *tier 3* particles were still observed under SEM. One critical difference can be observed in **region 3** where the *tier 1* particles were more indicative of their original shape yet still exhibiting partial coverage from liquid Mg.

2.5.2 Impact of pulse per area (PPA) on *tier 1* secondary phase particle dissolution and corrosion

The apparent complete dissolution of the *tier 2* and *tier 3* secondary phase particles observed in the previous section suggest that low PPA will have a significant impact on the corrosion response. That said, the *tier 1* particles are likely to persist as preferred cathodic sites as little change to their surface coverage is observed at low PPA. This section reveals how additional PPA impacts the dissolution of the *tier 1* particles present on the AZ31B-H24 surface.

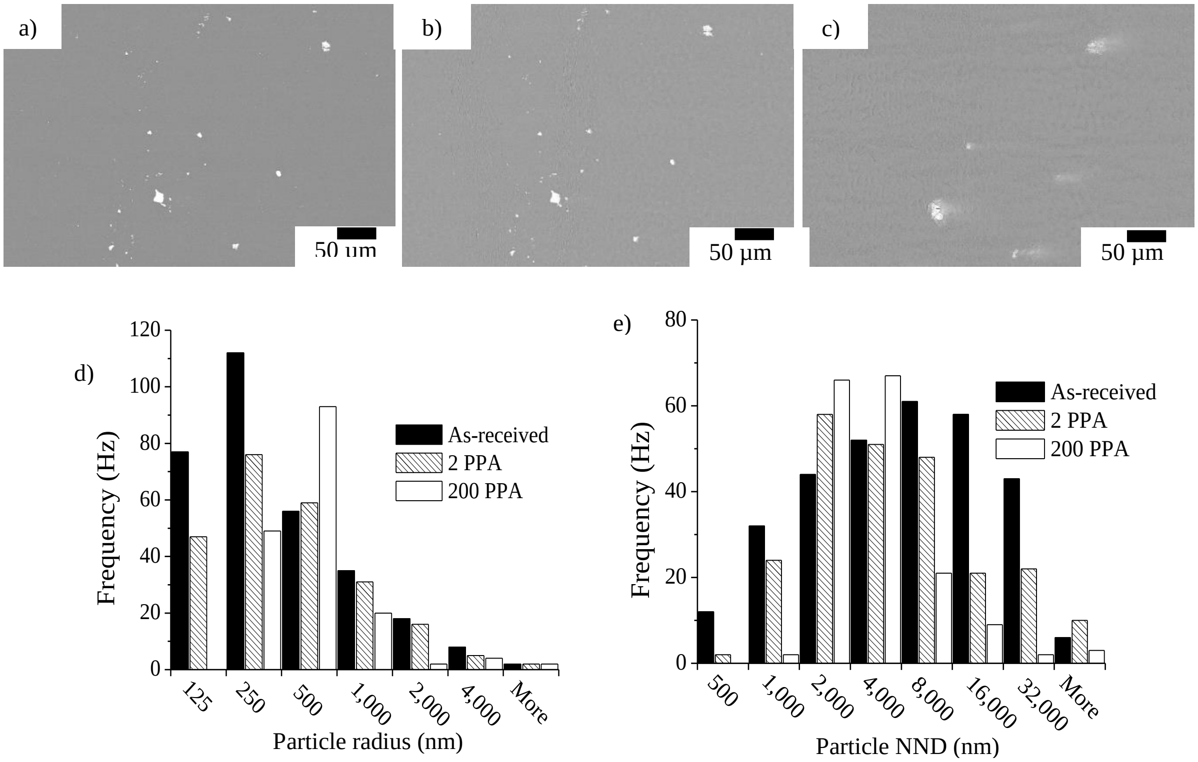

Figure 2.9: BSE micrographs of AZ31B taken with respect to a hardness mark before and after laser processing; a) as-received, b) 2 PPA, and c) 200 PPA. Particle radius (d) and NND (e) distributions for each micrograph.

Fiduciary mark SEM analysis of a polished and etched AZ31B-H24 specimen, before and after laser processing at 2 and 200 PPA is shown in **Figure 2.9**. The BSE micrograph of the as-received material in **Figure 2.9a** reveals the *tier 1* secondary phase particles, ranging in radius of 125 to 20,000 nm. After 2 PPA, **Figure 2.9b**, the diameter and distribution of the Al-Mn particles showed little change from the as-received condition, as seen in the histograms in **Figure 2.9 d and e**. After 200 PPA a more noticeable change is observed, seen in **Figure 2.9c**, where the majority of the smaller Al-Mn particles have disappeared and the larger particles have become agglomerates of smaller Al-Mn rich particles. The particle radius histogram in **Figure 2.9d** reveals an increase in quantity of particles at a radius of 500 nm in comparison to all other conditions as well as the majority of the particles having a NND between 2,000 and 4,000 nm.

The change from more randomly dispersed Al-Mn particles is observed in **Figure 2.10** where the centroids of each particle from the micrographs in **Figure 2.9** are plotted. Placing a grid on each centroid plot with 50 µm spacing and counting the particle density in each 50 by 50 µm grid provides some quantification of the clumping behavior observed after laser processing, seen in **Figure 2.10d**. The agglomeration of secondary phase particles was most obvious for the 200 PPA condition. The 200 PPA micrograph observed agglomerates of small Al-Mn rich particles to form where previous t*ier 1* particles existed. This analysis also confirms minimal change in *tier 1* particle distribution is observed when going from as-received to 2 PPA.

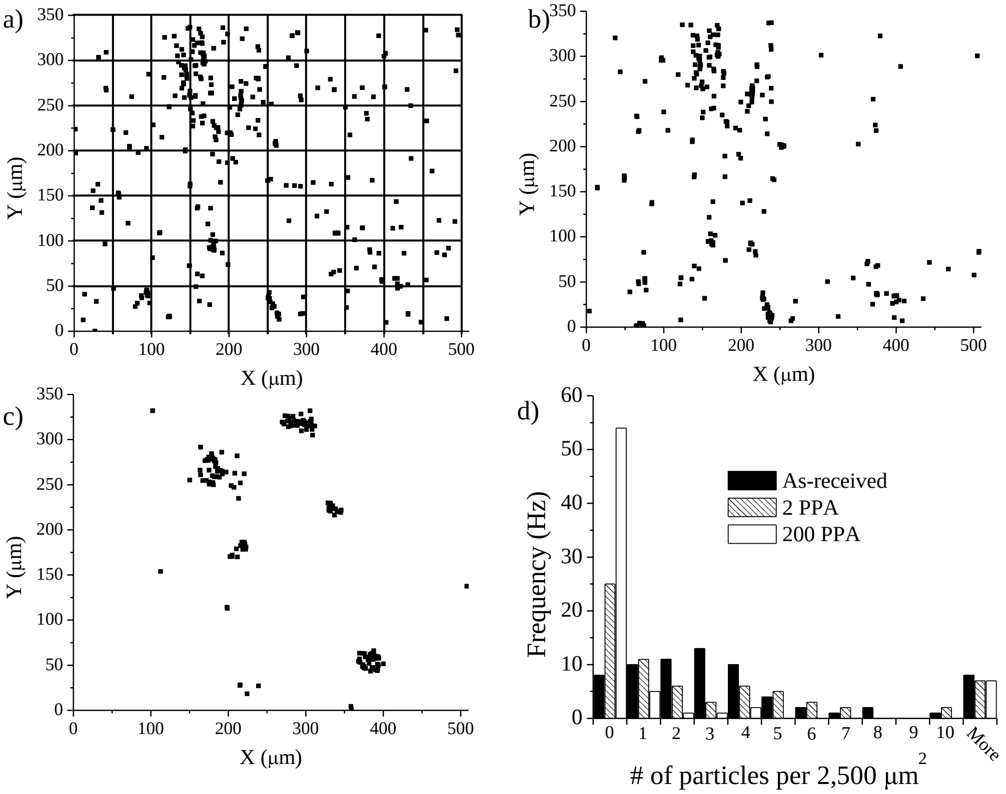

Figure 2.10: Centroids plotted from the fiduciary micrographs in **Figure 2.9** of AZ31B before and after laser processing; a) as-received, b) 2 PPA, and c) 200 PPA. After placing a grid, shown in a), on the plots the number of particles present in each area was plotted as a histogram in d).

The secondary phase particles in the *tier* 1 regime had a tendency to exhibit a mixed morphology after 200 PPA of laser processing was applied, showing partial dissolution of the secondary phase particle and some of the original particle residing near the center of the enriched region. Such regions were non-uniform throughout the thickness of the modified layer. This behavior is shown in **Figure 2.11** where the cross-section shows a partially dissolved Al-Mn particle, as well as the laser processed region to be ~5 µm thick. An enriched region spreading away from the parent particle was also observed from surface micrographs, as shown in **Figure 2.9c**. The spreading of the secondary phase particle was observed to be consistent with the mechanism of the plasma induced pressure waves, which would push the melted surface material away from the center of the incident laser beam. A depiction of how PPA influences each particle size tier is shown in **Figure 2.12**.

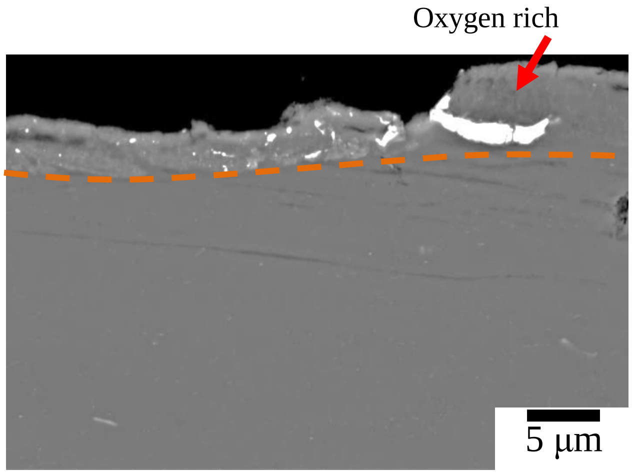

Figure 2.11: Cross-section of a AZ31B specimen after processing at a fluence of 1.5 J/cm^2, a pressure of 810 Torr, and 100 PPA using the backscattered electron detector. Observation of partially dissolved Al-Mn secondary phase particle and oxygen rich Mg covering what is left of the original particle.

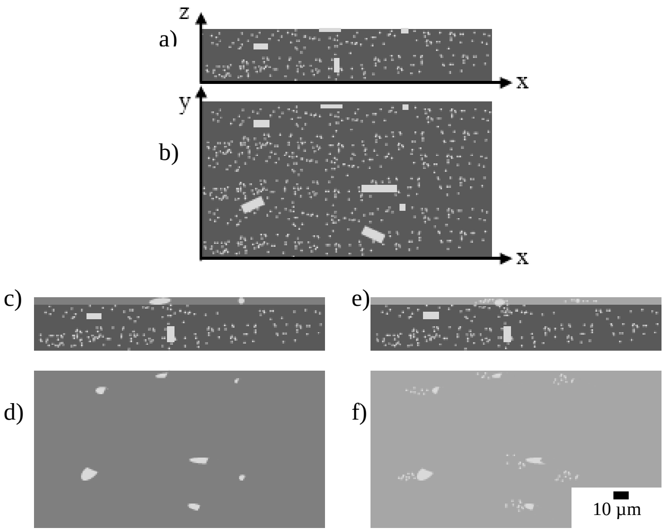

Figure 2.12: Schematic suggesting the impact PPA with a fluence of ~1.5 J/cm^2 will have on the homogenization of the AZ31B-H24 alloy microstructure. The alloy is depicted as a cross section and of the surface in a) and b) respectively. The small particles represent *tier 2* secondary phases while the larger rectangular shaped particles represent the *tier 1* Al-Mn particles. Laser processing with 2 PPA is shown in c) and d) while processing with 200 PPA is shown in e) and f).

The pronounced difference in the melting temperatures of Mg and the Al-Mn secondary phase particles results in minimal time where both are liquid, reducing their potential to physically mix via the plasma induced pressure mechanism. If the particle remains solid it can act as a barrier to the flow of the liquid

Mg surrounding it. The barrier effect can lead to liquid Mg flowing over the top of the solid particle. Covering the particle with Mg, as seen in **Figure 2.11**, will reduce their ability to act as an effective cathode during corrosion by reducing their exposed area. Partial dissolution of *tier 1* particles results in a more uniform corrosion potential at the Mg alloys surface reducing the potential difference between the cathodic secondary particle and its surrounding matrix, limiting the severity of micro-galvanic coupling.

The impact of reducing the number of secondary phase particles by increased PPA was observed via a cathodic polarization measurement. The cathodic kinetics or H_2 evolution reaction rate is directly proportional to the number and area coverage of the secondary phase particles, as the noble secondary phases are a preferred site for the H_2 evolution reaction. As shown in **Figure 2.13a**, compared to the as-received material, laser processing greatly reduces the H_2 evolution reaction rate, even at low PPA. The cathodic polarization measurements in **Figure 2.13a** are representative of what was typically observed at each processing condition. **Figure 2.13b** is a bar plot exhibiting the effect of PPA on the OCP at 30 minutes of immersion in stagnant 0.6 M NaCl solution. The OCP and cathodic polarization measurements began to show increased deviation from the mean at 400 PPA, likely from increase roughening and possibly surface defects present with the increased irradiation.

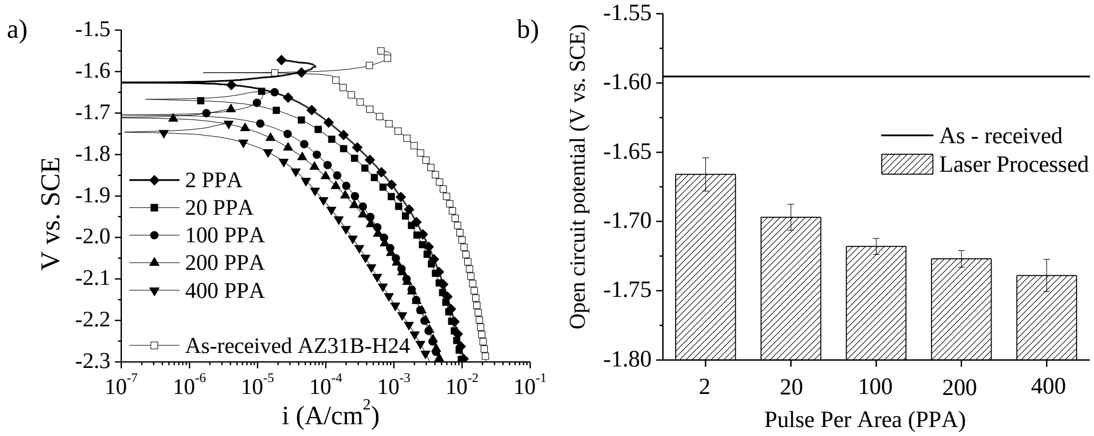

Figure 2.13: a) Cathodic polarization measurement of specimen before and after processing with a fluence of 1.5 J/cm^2, pressure of 810 Torr, and various PPA; 2, 20, 100, 200, and 400 PPA. b) Summary of change in OCP for each PPA after 30 minute stabilization in stagnant 0.6 M NaCl.

The OCP measurements of an alloy are derived from the combination of all phases present at the alloy surface. Therefore, the OCP is a galvanic coupled potential between every electrochemically active particle at the AZ31B-H24 surface with its surrounding Mg matrix, this holds for the cathodic polarization measurements as well. From **section 2.5.1**, the dissolution of all secondary phase particles below ~200 nm in radius was observed after a single laser pulse at a fluence of 1.5 J/cm^2. It follows for the 2 PPA condition, the cathodic polarization measurements revealed a reduction in current density magnitude along with the OCP becoming more negative, moving toward values of pure Mg [63].

2.5.3 Influence of laser fluence and processing pressure on microstructure and corrosion response

The results from SEM imaging taken with respect to a hardness mark are shown in **Figure 2.14** for fluences of 0.7, 0.8, and 1.5 J/cm^2 respectively. All specimens were processed with an Ar background pressure of 810 Torr and a total PPA of 100, recorded at an accelerating voltage of 5 kV. At a fluence of 0.7 J/cm^2, which is below the ablation threshold, the large Al-Mn secondary phase particles exhibited minimal size and shape changes as well as the development of cracks in close proximity to the particles. The secondary phase particles below 500 nm in radius showed signs of complete dissolution within the resolution of the SEM, circled in red. Samples processed above the ablation threshold exhibited significant dissolution of all secondary phase particles with the exception of certain *tier 1* particles above ~ 2,500 nm in radius, shown in **Figure 2.14d and f**.

The impact of processing pressure on the dissolution of the secondary phase particles is shown in **Figure 2.15** for a fluence of 1.5 J/cm^2. The 0.8 J/cm^2 fluence exhibited a similar response as 1.5 J/cm^2 and will not be shown for brevity. Also, the 0.7 J/cm^2 showed almost no dependence with respect to pressure changes so it will not be shown, results for this fluence are similar to that observed in **Figure 2.14b**. Micrographs in **Figure 2.15** were taken at two different accelerating voltages to reveal the dissolution of secondary phase particles throughout the modified layer for all pressures. At an accelerating voltage of 5 kV, the three higher pressures showed minimal contrast with respect to the location of the secondary phase particles as shown in **Figure 2.15 e, h, and k**. At 20 kV all pressures exhibited contrast where the original secondary phase particles were present. Regardless of pressure and initial particle size, each particle showed signs of significant dissolution and change in its shape.

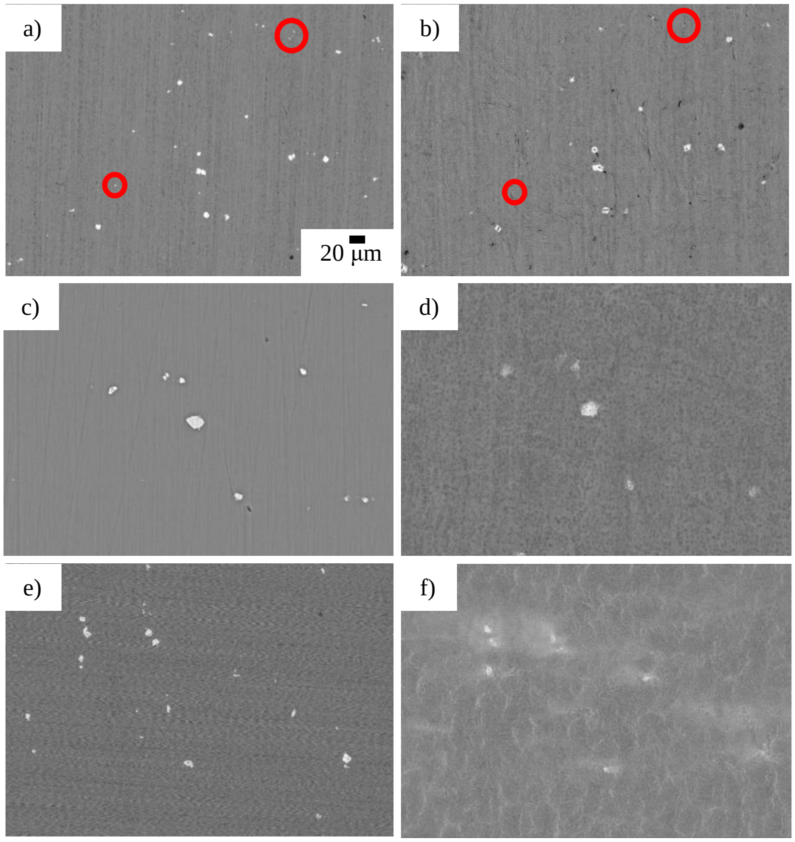

Figure 2.14: Backscattered electron micrographs of AZ31B microstructure processed at differing fluences. (a), (c), and (e) are of the microstructure prior to processing and (b), (d), and (f) are after processing at a fluence of 0.7, 0.8, and 1.5 J/cm^2, respectively. All were processed at a pressure of 810 Torr Ar and 100 PPA. An accelerating voltage of 5 kV was used.

The average change in OCP with respect to fluence and processing pressure after 30 minute immersion in 0.6 M NaCl is presented in **Figure 2.16**. Representative cathodic polarization measurements, depicted in **Figure 2.17**, reveal the general trend observed by varying fluence or processing pressure on the H_2 evolution reaction rate. At all pressures, at a fluence of 0.7 J/cm^2, the reduction in OCP was ~50 mV compared to the as-received material. The ablating fluences revealed more dependence on processing pressure with the 1 x 10^{-2} Torr condition consistently showing the lowest OCP and cathodic current densities. In addition fluences above the ablation threshold revealed a stronger dependence on background pressure and consistently an order of magnitude reduction in H_2 evolution reaction rate which correlates well with the electron microscopy.

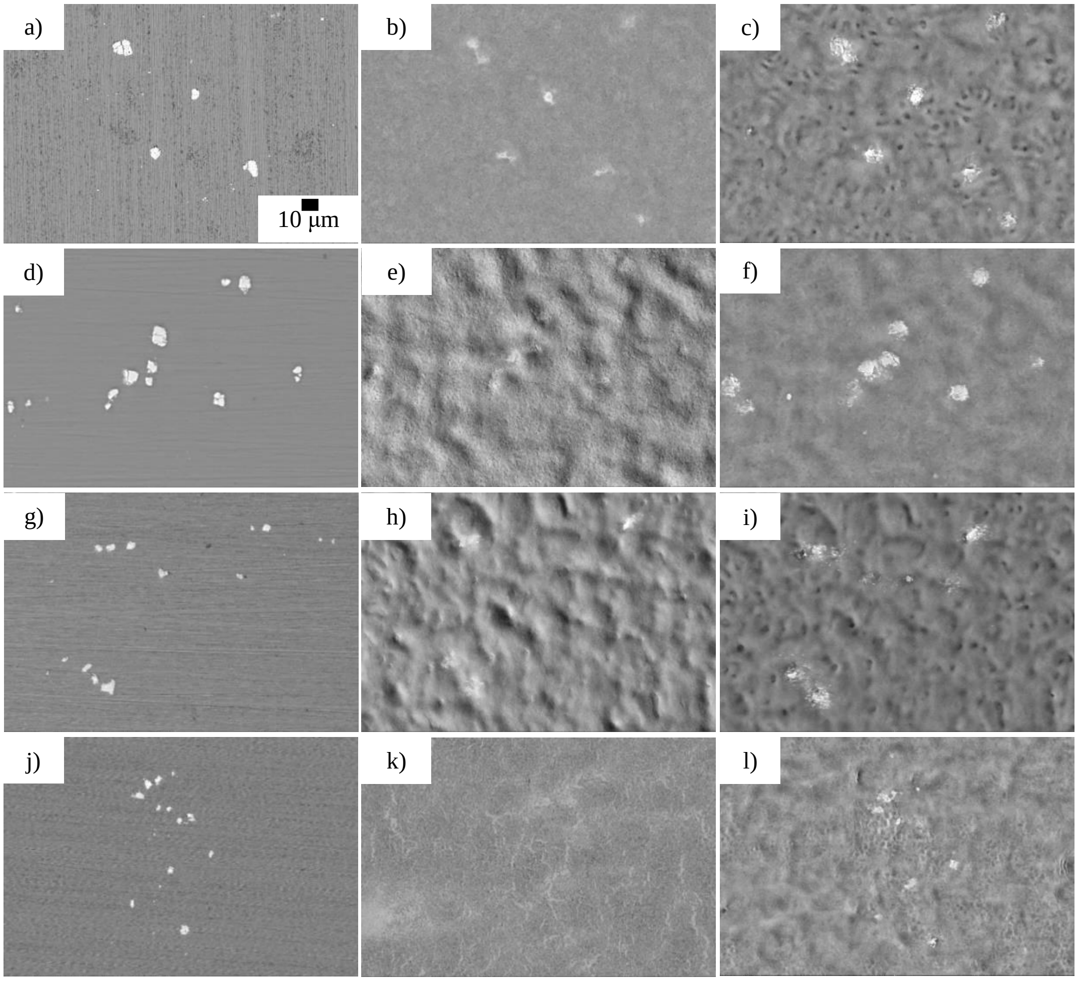

Figure 2.15: Backscattered electron micrographs of AZ31B microstructure processed at differing pressures. (a, b, c) were processed at 1 Torr, (d, e, f) were processed at 10 Torr, (g, h, i) were processed at 100 Torr, and (j, k, l) were processed at 810 Torr. (a), (d), (g), and (j) are the starting microstructure for the processed specimen. (b), (e), (h), and (k) were imaged at an accelerating voltage of 5 kV while (c), (f), (i), and (l) were imaged at an accelerating voltage of 20 kV. All were processed at a fluence of 1.5 J/cm^2 and 100 PPA.

Disregarding pressure and PPA effects, fluences which can melt and ablate reduce the presence of secondary phases at the surface of AZ31B, as observed in **Figure 2.14**. The overall difference between fluences is the amount of solute spreading observed around the larger *tier 1* particles. The secondary phase particle dissolution is due to the higher temperatures reached throughout the melted layer at 1.5 J/cm^2 leading to significant melting of the *tier 1* particles and subsequent mixing into the Mg matrix.

Compared to the *tier 2* and *tier 3* that may be present, presumed to exhibit complete dissolution after laser processing per their low melting temperatures and smaller size, the dissolution of the larger *tier 1* particles is not always complete and can come in many forms, some of which can be observed in **Figure 2.11** and **Figure 2.14f**.

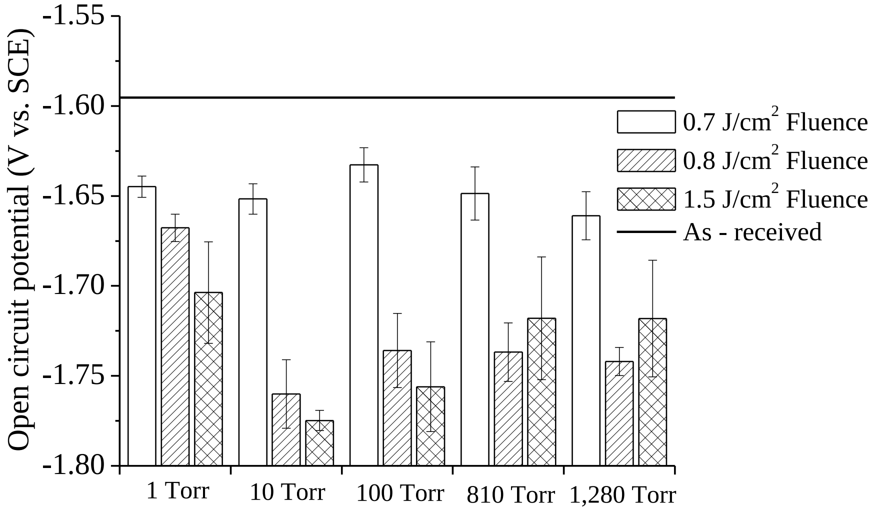

Figure 2.16: Summary of OCP after 30 minute immersion in 0.6 M NaCl. Specimen were processed at a constant PPA of 100 while the pressure and fluence were varied.

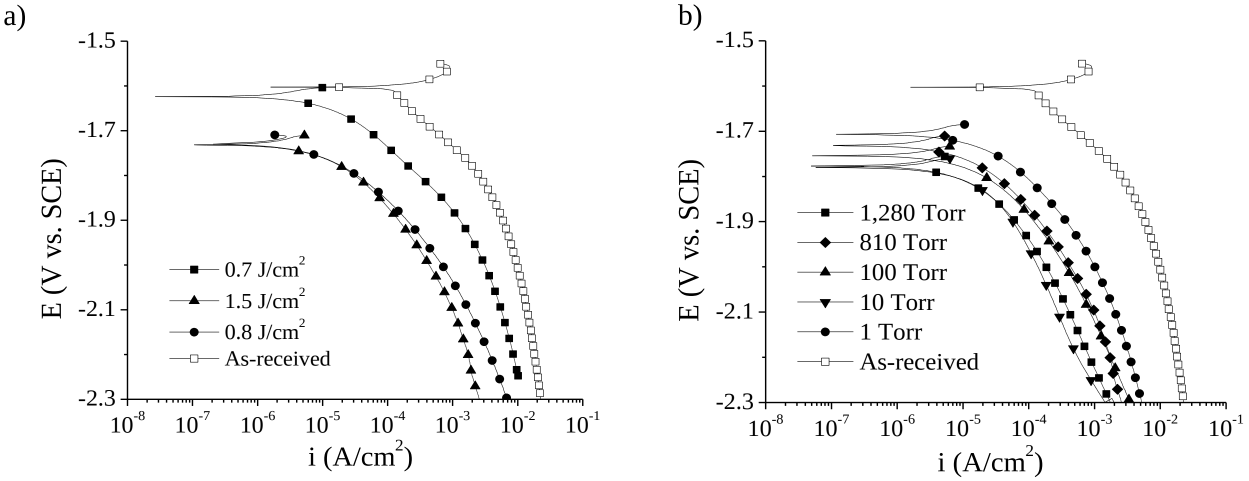

Figure 2.17: Cathodic polarization measurement of specimen before and after laser processing at varying fluence a) and varying processing pressure b). These measurements reveal how the change in one processing parameter may influence the cathodic polarization response while holding all other parameters the same.

The micrographs comparing processing pressure and accelerating voltage exhibited a capping layer, rich in Mg and O, over the entire surface with little indication of secondary phase particles at 5 kV for pressures of 1 x 10^{-2} and 1 x 10^{-1} Torr in **Figure 2.15**. The impact of this capping layer was seen by the electrochemistry measurements, with the 1 x 10^{-2} and 1 x 10^{-1} Torr specimen showing the lowest average OCP and cathodic current densities. Such a protective layer was derived from the re-deposition of ablated Mg during processing yielding a thin capping layer with every pass of the laser across the surface. This is observed to occur less at higher external pressures because ablation is being suppressed. The re-deposition of an ablated material is dictated by the Mach number [34] of the expanding ablated material and subsequently the pressure inside the chamber. This suggests the optimal re-condensation for producing the most corrosion protective film occurs at 1 x 10^{-2} Torr.

In addition, use of the lower three processing pressures appeared to reduce the overall dissolution of the large secondary phase particles in comparison to 810 Torr as more intact Al-Mn secondary phase particles were observed when utilizing an accelerating of 20 kV, revealing more information below the surface. The material transport caused by the plasma induced shock wave is dependent on irradiance and the external pressure. Reduction in one will reduce the ability for transport of the liquid Mg to cover secondary phase particles. At near atmosphere pressures (810 Torr) the material transport plays a large role in dissolving secondary phase particles, however the re-condensation of Mg from ablation is not sufficient enough to produce a capping layer. The reduction in the external pressure has the opposite effect where a capping layer can be formed but the material transport of liquid Mg is reduced.

2.5.4 TEM study and oxide formation on laser processed surfaces

Transmission electron microscopy (TEM) was performed on the as-received and the laser processed (200 PPA) AZ31B to investigate the changes to the alloys microstructure after laser processing, in particular to observe the formation of oxides throughout the processed region. The bright field micrograph of the as-received alloy in **Figure 2.18a** observes a number of the smaller ($r < 50$ nm) Al-Mn rich particles as well as a few indications of the β-phase. The laser processed material, shown in **Figure 2.18b** does not show signs of these secondary phase particles, however the laser processed layer was abundant with clusters of nm sized oxide particles, highlighted by a box in red. One of these oxide particles was imaged at high resolution, shown in **Figure 2.18c**, and were consistently shown to be ~5 nm nanocubes, suggested to be composed of MgO.

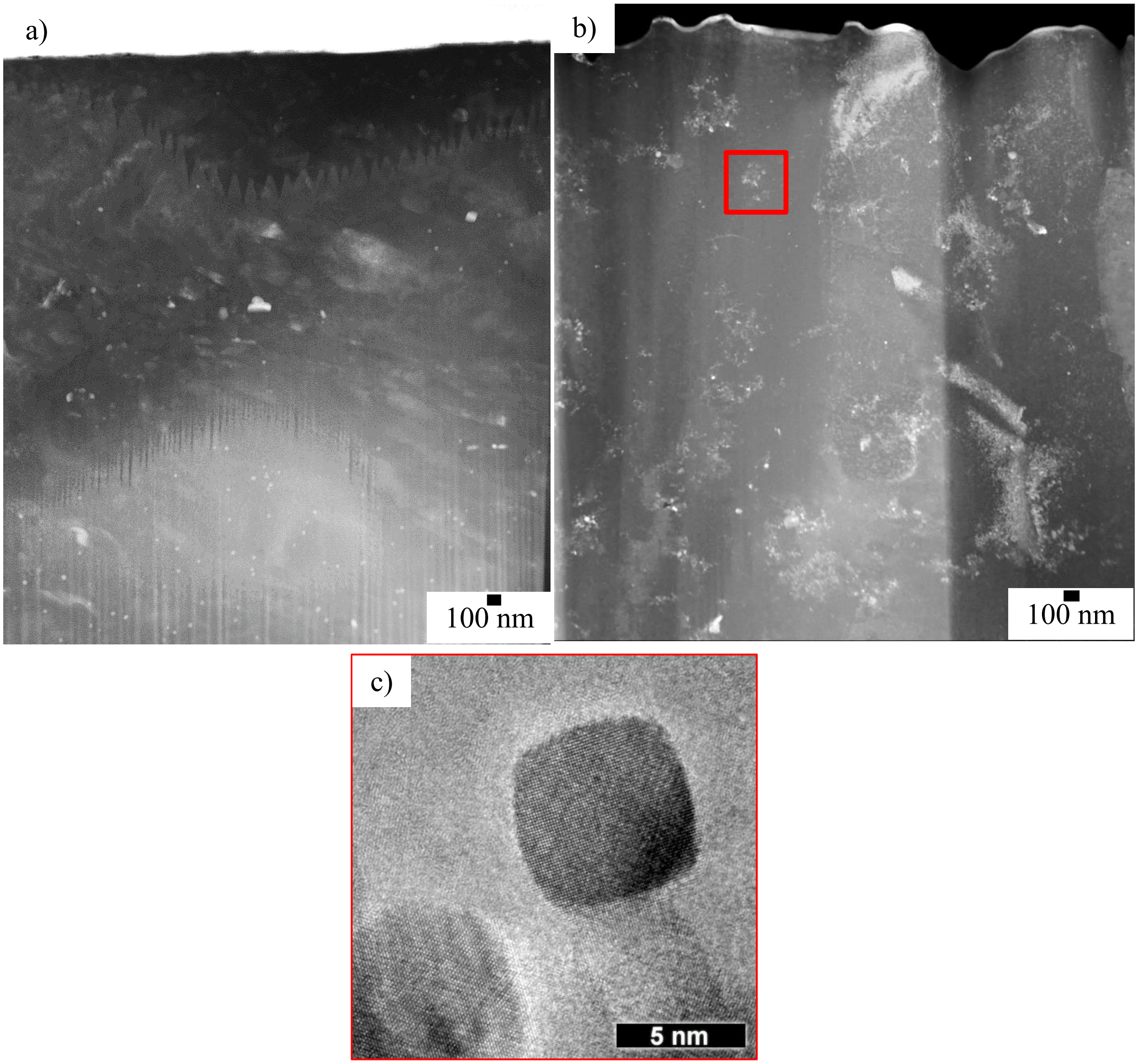

Figure 2.18: Bright field TEM micrographs from a) as-received and b) laser processed specimen which had FIB cross sections taken from their surface. The high resolution micrograph in c) is of an oxide nanocube found as clusters throughout the laser processed region, as indicated by the red box in b). TEM results were courtesy of Matt Schneider at UCF.

Observation of the laser processed surface by SEM, using the secondary electron detector is shown in **Figure 2.19**. These observations of oxide formation suggest the Ar gas cannot suppress the formation of oxides at the surface during laser processing, which is expected given the propensity both Mg and AL have to react with oxygen. In addition, it reveals the laser processed surfaces are not homogenized completely in a traditional sense. The oxides which form cover a majority of the laser processed surfaces, they penetrate into the laser processed layer, as well as the persistence of the larger Al-Mn particles which see substantial dissolution, but many are never completely dissolved into the Mg matrix. That said, the corrosion results still allow for the surface to behave as if it is electrochemically homogeneous.

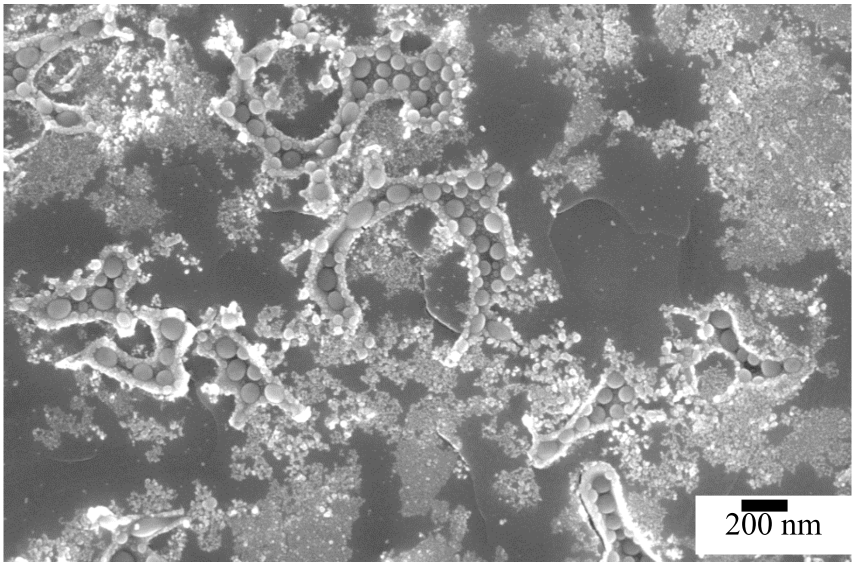

Figure 2.19: Secondary electron micrograph of laser processed AZ31B surface exhibiting network of oxide particles, likely MgO.

In order to observe the impact the oxides formed on the laser processed surfaces has on the corrosion response, a laser processed specimen was immersed in a chromic acid solution to remove the oxide found on the surface. Following the chromic acid cleaning, the laser processed and chromated specimen had its cathodic kinetics measured with an E-log(i) measurement, shown in **Figure 2.20**, revealing a further reduction in the cathodic kinetics after chromic acid cleaning. This result further suggests the dominant mechanism reducing the cathodic kinetics of the laser processed AZ31B is reduction in secondary phase particles.

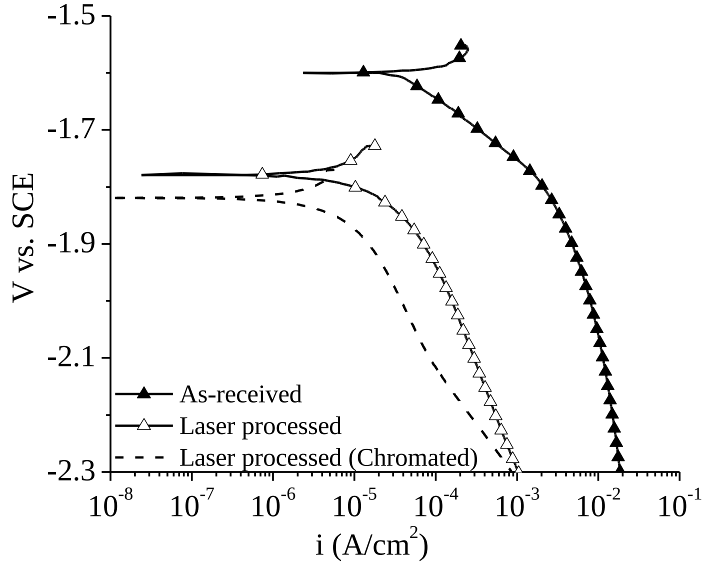

Figure 2.20: Cathodic E-log(i) measurement performed on an as-received, laser processed, and laser processed and chromated (oxide removed) AZ31B specimen after immersion in stagnant 0.6 M NaCl for 10 minutes.

2.5.5 Optimal processing parameters

The results from the processing parameter study yielded a processing window over which the rest of the Mg alloys will be processed in to ensure an optimal corrosion response. These parameters are listed in **Table 2.2**, showing there may be some variation in PPA. The choice for each parameter was largely made based on the lowest OCP and cathodic current density magnitude. That said, the use of a pressure of 810 Torr was chosen for convenience and simplicity. The true optimal pressure for the ablating fluences from a corrosion stand point was observed to be 1 x 10^{-2} Torr, however this condition required the use of a vacuum. In addition it did not optimize another parameter under consideration, the extent of homogenization of the *tier 1* particles. The reduction in cathodic kinetics and more negative OCP was partially derived from the re-deposited capping layer which would have brought in another level of complexity to the corrosion analysis.

Table 2.2: Optimized laser processing parameters for Mg alloys.

Laser processing parameter	Parameter value
Laser fluence (J/cm^2)	1.5
Pulse overlap	50 %
Processing pressure (Torr)	810 of Ar
PPA	100 to 200

2.6 Laser processing of as-cast alloys

The microstructure of the AM60B and AZ91D alloys were investigated by BSE imaging to observe the secondary phases present in each alloy before and after laser processing with an accelerating voltage of 15 kV, shown in **Figure 2.21**. The microstructures of AM60B and AZ91D are similar, but with a marked presence of the eutectic phase, β-$Mg_{17}Al_{12}$, at the grain boundaries, and 5 μm or smaller Al-Mn secondary phase particles randomly distributed throughout. In these micrographs, the bright white regions represent the Al-Mn particles and the light gray regions represent the β-$Mg_{17}Al_{12}$ phase present at the grain boundaries. The remaining dark region in the micrographs is the α-Mg matrix. Semi-quantitative EDS was utilized to suggest the aforementioned phases are β-$Mg_{17}Al_{12}$ and Al-Mn secondary phase particles as shown in **Figure 2.21c, f**. There is noticeably less β phase in the AM60B microstructure, **Figure 2.21d**, than AZ91D, **Figure 2.21a** as expected for the lower alloy content. Following laser processing, the as-cast alloys exhibited enhanced homogeneity in terms of the local surface composition. The β phase appears to be completely dissolved with the remnants of the Al-Mn secondary phase particles persisting, similar to that of the AZ31B-H24 *tier 1* particles.

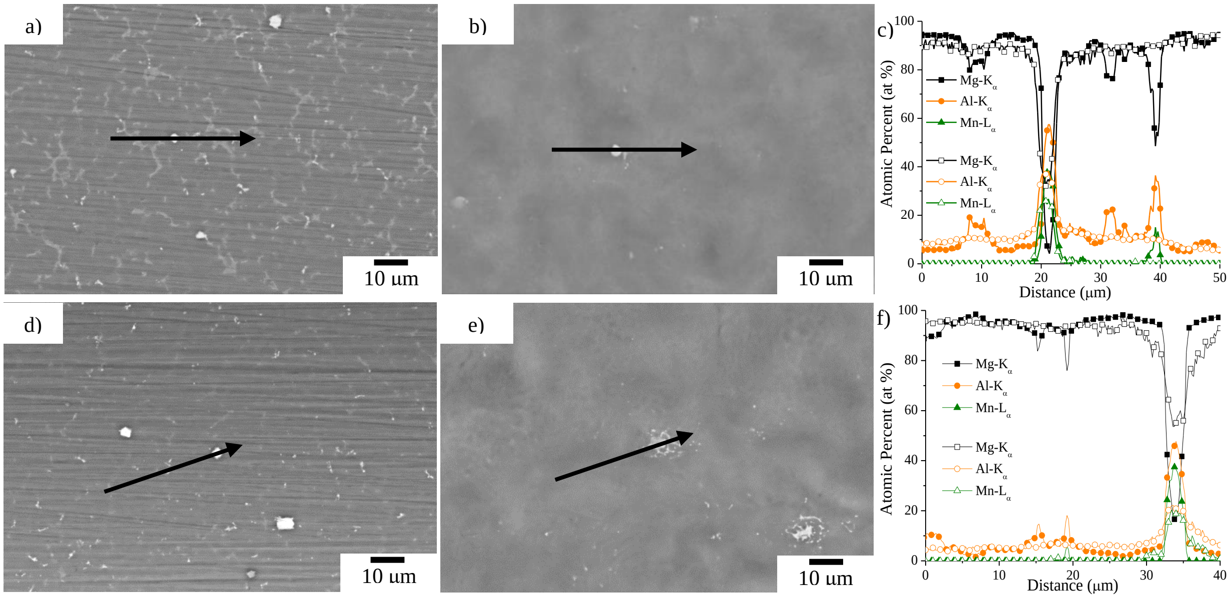

Figure 2.21: BSE micrographs taken with respect to a hardness mark of AZ91D and AM60B in the as-received condition, a) and d) respectively, and after 100 PPA of laser processing, b) and d) respectively. The black lines in each micrograph represent an EDS line profile of AZ91D and AM60B, c) and f) respectively, before and after laser processing. Solid points represent the as-received alloy and open points represent the laser processed alloy.

Micrographs and EDS line profiles of the laser processed specimens for both alloys illustrate a similar degree of dissolution and homogenization as shown in **Figure 2.21**. The EDS line profiles of the laser processed specimens reveal a homogenized Mg matrix with a relatively uniform Al content, similar to that expected for the of the as-received alloy, 6 or 9 wt%. It is also clear the size of the original particles plays a significant role in the final dissolution profile which is expected. Coarse Al-Mn particles, 5 µm in size or greater, remain with evidence of significant dissolution. In contrast, populations of Al-Mn particles, less than 1 µm in size along with the β-$Mg_{17}Al_{12}$ phase completely dissolve into the surrounding matrix. That said, the spatial resolution of EDS is on the order of 1 µm so smaller precipitates are undetectable and the exact spreading and composition of the secondary phases is not possible. A cross-section of the laser processed AM60B alloy was observed by BSE imaging in **Figure 2.22**. The thickness of the laser processed layer is shown to be ~2.5 µm as indicated by the dashed orange line as well as the lack of β phase present in that layer. To definitively prove this further work with TEM should be done to observe if there are any features such as solute bands, as others have shown [5].

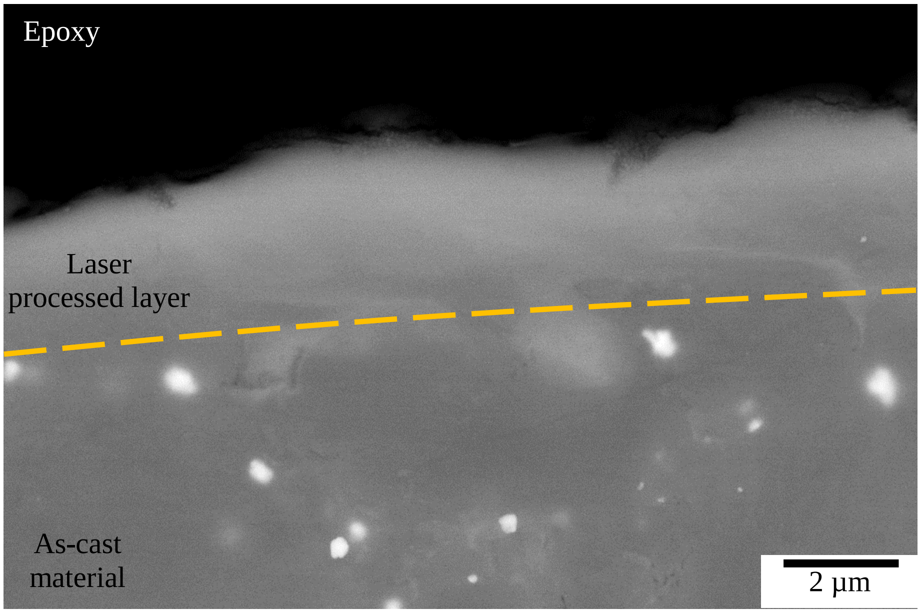

Figure 2.22: Cross-section BSE micrograph of the AM60B cast alloy after laser processing with 100 PPA. The laser processed layer reveals uniform mixing of the β phase into the Mg matrix suggesting homogenization through the 2.5 μm thick processed layer.

Grazing incidence XRD is shown for all alloys, including AZ31B-H24, in **Figure 2.23**. There is a low volume fraction of secondary phases present in the AZ31B alloy hence the only noticeable modification to the XRD spectra is the increase in MgO content of the laser processed specimen. The cast alloys in the base condition show signs of the β-$Mg_{17}Al_{12}$ phase, the largest amount observed in AZ91D. The Al-Mn particles present in all alloys are below the detection limit of the XRD machine. After laser processing, the dissolution of the β phase can be qualitatively observed via GI-XRD for the laser processed cast alloys by the reduction in size of the β phase diffraction peaks. The major peak typically observed for β is near 2θ (411) = 36^o and was reduced to the detection limit for both cast alloys after processing. In addition, the shift of the Mg peaks away from pure Mg increases after laser processing. These shifts are indicative of Al incorporation into the parent Mg phase [9].

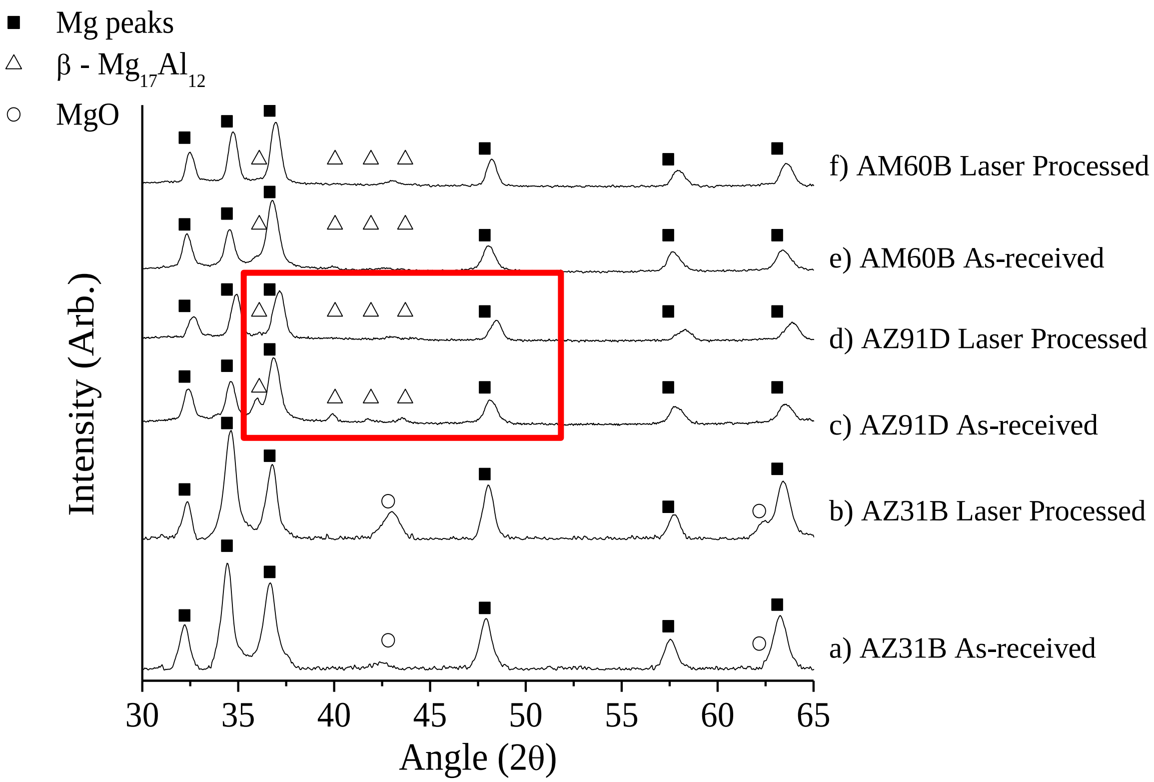

Figure 2.23: GI-XRD of alloys surfaces, before and after processing. (a, b) AZ31B-H24 base and laser processed, respectively. (c, d) AZ91D base and laser processed, respectively. (e, f) AM60B base and laser processed, respectively.

The observation of cathodic polarization measurements in **Figure 2.24** reveals a similar response for the as-cast alloys as was observed for the AZ31B-H24 alloy after laser processing. A reduction to a more negative OCP was also observed for the cast alloys and these results corroborate the choice of laser processing parameters determined from the work performed on AZ31B.

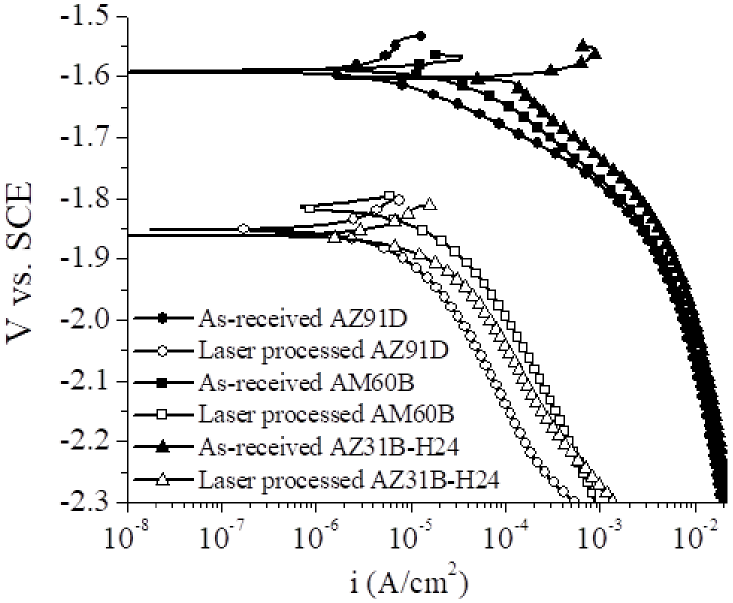

Figure 2.24: Cathodic polarization measurements for the AM60B, AZ91D, and AZ31B-H24 in the as-received and laser processed (100 PPA) condition after a 30 minute OCP and performed in stagnant 0.6 M NaCl solution.

2.7 Summary of results for laser processing

Utilization of an excimer laser process performed on a set of Mg-Al alloys was shown to melt and chemically homogenize the surface microstructure. A study of secondary phase particle dissolution was primarily performed on the AZ31B-H24 alloy which observed three *tiers* of particle radii. After a single laser pulse at a fluence of 1.5 J/cm^2 all *tier 2* and *tier 3* particles were presumed to be homogenized into the surrounding Mg matrix as they were not observable through high magnification BSE imaging. These results corroborated the analytical calculations with respect to diffusional effects and whether homogenization of the smaller particles was possible at the alloy surface. The larger and higher melting temperature *tier 1* particles showed signs of melting however complete homogenization was not observed. A secondary mechanism aiding chemical homogenization was observed through material transport of the melted surface known as the plasma induced pressure wave. The plasma induced pressure acted as a source of liquid mixing during the short melt times induced by the laser as well as created substantial motion of the liquid Mg to cover many of the *tier 1* particles that persisted as a solid phase.

The laser processing chamber was capable of controlling several parameters critical to the final laser processed surface including: processing pressure, laser fluence, processing environment, laser pulse overlap, and laser PPA. A majority of these parameters were optimized by experimental works with the goal of maximizing the chemical homogenization occurring at the alloy surface, results are presented in **Table 2.2**. Chemical homogenization was primarily observed through SEM analysis however the use of cathodic polarization ad OCP measurements corroborated the microscopy through a reduction in cathodic kinetics and a more negative OCP, representative of less active cathodic material at a materials surface. All laser processing experimentation was performed on the as-cast alloys as well, further suggesting the optimized processing parameters cause homogenization of the Mg-Al alloy microstructure.

2.8 References

---

[1] C.B. Baliga, P. Tsakiropoulos, The structure and morphology of the corrosion products formed on the surfaces of a rapidly solidified Mg-3.5Al alloy, Materials Science and Engineering, A134 (1991) 1029-1032.

[2] C.B. Baliga, P. Tsakiropoulos, Development of corrosion resistant magnesium alloys Part 2 Structure of corrosion products on rapidly solidified Mg-16Al alloys, Materials Science and Technology, 9 (1993) 513-519.

[3] K. Schlüter, C. Zamponi, J. Hapke, N. Hort, K.U. Kainer, E. Quandt, Mechanical properties and corrosion behaviour of freestanding, precipitate-free magnesium WE43 thin films, international Journal of Materials Research, 104 (2013) 286-292.

[4] K. Schlüter, C. Zamponi, A. Piorra, E. Quandt, Comparison of the corrosion behaviour of bulk and thin film magnesium alloys, Corrosion Science, 52 (2010) 3973-3977.

[5] A.E. Coy, F. Viejo, F.J. Garcia-Garcia, Z. Liu, P. Skeldon, G.E. Thompson, Effect of excimer laser surface melting on the microstructure and corrosion performance of the die cast AZ91D magnesium alloy, Corrosion Science, 52 (2010) 387-397.

[6] L.F. Guo, T.M. Yue, H.C. Man, Excimer laser surface treatment of magnesium alloy WE43 for corrosion resistance improvement, Journal of Materials Science, 40 (2005) 3531-3533.

[7] F.H. Froes, Y.W. Kim, S. Krishnamurathy, Rapid Solidification of Lightweight Metal Alloys, Materials Science and Engineering A, 117 (1989) 19-32.

[8] F. Hehmann, F. Sommer, H. Jones, R.G.J. Edyvean, Corrosion inhibition in magnesium-aluminium-based alloys induced by rapid solidification processing, Journal of Materials Science, 24 (1989) 2369-2379.

[9] F. Hehmann, F. Sommer, B. Predel, Extension of Solid Solubility in Magnesium by Rapid Solidification, Materials Science and Engineering A, 125 (1990) 249-265.

[10] A. Koutsomichalis, L. Saettas, H. Badekas, Laser treatment of magnesium, Journal of Materials Science, 29 (1994) 6543-6547.

[11] D. Schippman, A. Weisheit, B.L. Mordike, Short Pulse Irradiation of Magnesium Based Alloys to Improve Surface Properties, Surface Engineering, 15 (1999) 23-26.

[12] M. Melia, P. Steiner, N. Birbilis, J. Fitz-Gerald, J. Scully, Excimer Laser Surface Modification of AZ31B-H24 for Improved Corrosion Resistance, Corrosion, 72 (2015) 95-109.

[13] R.K. Singh, J. Narayan, A novel method for simulating laser-solid interactions in semiconductors and layered structures, Materials Science and Engineering B, 3 (1989) 217-230.

[14] D. Dube, M. Fiset, A. Couture, I. Nakatsugawa, Characterization and performance of laser melted AZ91D and AM60B, Materials Science and Engineering A, 299 (2001) 38-45.

[15] F. Viejo, A.E. Coy, F.J. Garcia-Garcia, Z. Liu, P. Skeldon, G.E. Thompson, Relationship between microstructure and corrosion performance of AA2050-T8 aluminium alloy after excimer laser surface melting, Corrosion Science, 52 (2010) 2179-2187.

[16] W. L. Xu, T. M. Yue, H. C. Man, and C. P. Chan, "Laser surface melting of aluminium alloy 6013 for improving pitting corrosion fatigue resistance," Surface and Coatings Technology, 2006, 200(16-17), 5077-5086.

[17] T. M. Yue, J. K. Yu, Z. Mei, and H. C. Man, "Excimer laser surface treatment of Ti–6Al–4V alloy for corrosion resistance enhancement," Materials Letters, 2002, 52, 206-212.

[18] T.M. Yue, L.J. Yan, C.P. Chan, C.F. Dong, H.C. Man, G.K.H. Pang, Excimer laser surface treatment of aluminum alloy AA7075 to improve corrosion resistance, Surface and Coatings Technology, 179 (2004) 158-164.

[19] Y. Jun, G.P. Sun, S.S. Jia, Characterization and wear resistance of laser surface melting AZ91D alloy, Journal of Alloys and Compounds, 455 (2008) 142-147.

[20] A.K. Mondal, S. Kumar, C. Blawert, N.B. Dahotre, Effect of laser surface treatment on corrosion and wear resistance of ACM720 Mg alloy, Surface and Coatings Technology, 202 (2008) 3187-3198.

[21] J.D. Majumdar, R. Galun, B.L. Mordike, I. Manna, Effect of laser surface melting on corrosion and wear resistance of a commercial magnesium alloy, Materials Science and Engineering: A, 361 (2003) 119-129.

[22] G. Abbas, L. Li, U. Ghazanfar, Z. Liu, Effect of high power diode laser surface melting on wear resistance of magnesium alloys, Wear, 260 (2006) 175-180.

[23] G. Abbas, Z. Liu, P. Skeldon, Corrosion behaviour of laser-melted magnesium alloys, Applied Surface Science, 247 (2005) 347-353.

[24] P.C. Banerjee, R.K. Singh Raman, Y. Durandet, G. McAdam, Influence of Laser Processing Parameters on Microstructure and Corrosion Kinetics of Laser-Treated ZE41 Magnesium Alloy, Metallurgical and Materials Transactions A, 44 (2013) 2346-2357.

---

[25] S. Santhanakrishnan, N. Kumar, N. Dendge, D. Choudhuri, S. Katakam, S. Palanivel, H.D. Vora, R. Banerjee, R.S. Mishra, N.B. Dahotre, Macro- and Microstructural Studies of Laser-Processed WE43 (Mg-Y-Nd) Magnesium Alloy, Metallurgical and Materials Transactions B, 44 (2013) 1190-1200.

[26] P.C. Banerjee, R.K.S. Raman, Y. Durandet, G. McAdam, Electrochemical investigation of the influence of laser surface melting on the microstructure and corrosion behaviour of ZE41 magnesium alloy – An EIS based study, Corrosion Science, 53 (2011) 1505-1514.

[27] A. Jain, O. Duygulu, D.W. Brown, C.N. Tomé, S.R. Agnew, Grain size effects on the tensile properties and deformation mechanisms of a magnesium alloy, AZ31B, sheet, Materials Science and Engineering: A, 486 (2008) 545-555.

[28] L. Guo, Z. Chen, L. Gao, Effects of grain size, texture and twinning on mechanical properties and work-hardening behavior of AZ31 magnesium alloys, Materials Science and Engineering: A, 528 (2011) 8537-8545.

[29] M.A. Melia, D.C. Florian, F.W. Steuer, B.F. Briglia, M.K. Purzycki, J.R. Scully, J.M. Fitz-Gerald, Investigation of critical processing parameters for laser surface processing of AZ31B-H24, Surface and Coatings Technology, 325 (2017) 157-165.

[30] M. Von Allmen, A. Blatter, Laser-Beam Interactions with Materials, 2nd ed., Springer Series in Materials Science 1987.

[31] P. Schaaf, Laser nitriding of metals, Progress in Materials Science, 47 (2002) 1-161.

[32] D.W. Bäuerle, Laser Processing and Chemistry, Springer Berlin Heidelberg 2013.

[33] M.A. Melia, M.L. Serron, D.C. Florian, J.P. Weiler, J.R. Scully, J.M. Fitz-Gerald, Excimer Laser Processing of Cast Mg-Al-Zn (AZ91D) and Mg-Al (AM60B) Alloys for Improved Corrosion Resistance, Corrosion, 72 (2016) 1580-1586.

[34] W. Khalfaoui, E. Valerio, J.E. Masse, M. Autric, Excimer laser treatment of ZE41 magnesium alloy for corrosion resistance and microhardness improvement, Optics and Lasers in Engineering, 48 (2010) 926-931.

[35] T.M. Yue, Wang, A.H., Man, H.C., Improvement in the corrosion resistance of magnesium ZK60-SiC composite by excimer laser surface treatment, Scripta Materialia, 38 (1998) 191-198.

[36] T.-C. Wu, Y.-H. Ho, S.S. Joshi, R.S. Rajamure, N.B. Dahotre, Microstructure and corrosion behavior of laser surface-treated AZ31B Mg bio-implant material, Lasers in Medical Science, 32 (2017) 797-803.

[37] C. Taltavull, B. Torres, A.J. Lopez, P. Rodrigo, E. Otero, A. Atrens, J. Rams, Corrosion behaviour of laser surface melted magnesium alloy AZ91D, Materials & Design, 57 (2014) 40-50.

[38] S.I. Anisimov, V.A. Khokhlov, Instabilities in Laser-Matter Interaction, Taylor & Francis 1995.

[39] S.I. Anisimov, Vaporization of Metal Absorbing Laser Radiation, Journal of Experimental and Theoretical Physics, 27 (1968) 182.

[40] R.K. Singh, J. Narayan, A novel method for simulating laser-solid interactions in semiconductors and layered structures, Materials Science and Engineering B, 3 (1989) 217-230.

[41] R.K. Singh, J. Viatella, Personal computer-based simulation of laser interactions with materials, Jom, 44 (1992) 20-23.

[42] D.S. Qian, Z. Liu, Comparative Study of Microstructural and Corrosion Characteristics of Excimer Laser-Melted AA2124-T4 and AA6061-T4 Alloys, Materials Science Forum, 794-796 (2014) 235-240.

[43] E. Andersson, G.A. Johannesson, Extended Analysis of the Spectrum of Mg III, Physica Scripta, 3 (1971) 203.

[44] T.B. Massalski, H. Okamoto, P.R. Subramanian, L. Kacprzak, W.W. Scott, Binary Alloy Phase Diagrams, American Society for Metals, 2001.

[45] M.M. Avedesian, H. Baker, A.S.M.I.H. Committee, ASM Specialty Handbook: Magnesium and Magnesium Alloys, ASM International ,1999.

[46] D.R. Lide, CRC Handbook of Chemistry and Physics, 85th Edition, Taylor & Francis, 2004.

[47] R. Berthold, G. Kreiner, U. Burkhardt, S. Hoffmann, G. Auffermann, Y. Prots, E. Dashjav, A. Amarsanaa, M. Mihalkovic, Crystal structure and phase stability of the Φ phase in the Al–Mg–Zn system, Intermetallics, 32 (2013) 259-273.

[48] N. Stanford, D. Atwell, The Effect of Mn-rich Precipitates on the Strength of AZ31 Extrudates, Metallurgical and Materials Transactions A, 44 (2013) 4830-4843.

[49] A. Rudajevova, M. Stanek, P. Lukac, Determination of thermal diffusivity and thermal conductivity of Mg–Al alloys, Materials Science & Engineering A, 341 (2003) 152-157.

[50] T. Ying, M.Y. Zheng, Z.T. Li, X.G. Qiao, Thermal conductivity of as-cast and as-extruded binary Mg–Al alloys, Journal of Alloys and Compounds, 608 (2014) 19-24.

---

[51] J.M. Juneja, G.N.K. Iyenhar, K.P. Abraham, Thermodynamic properties of liquid (magnesium + copper) alloys by vapour-pressure measurements made by a boiling-temperature method, Journal of Chemical Thermodynamics, 18 (1986) 1025-1035.

[52] A. Ditze, C. Scharf, Recycling of Magnesium, Papierflieger Verlag, 2008.

[53] D.A. Porter, K.E. Easterling, Phase Transformations in Metals and Alloys, Third Edition (Revised Reprint), Taylor & Francis, 1992.

[54] Y. Tang, L. Zhang, Y. Du, Diffusivities in liquid and fcc Al–Mg–Si alloys and their application to the simulation of solidification and dissolution processes, Calphad, 49 (2015) 58-66.

[55] A.S. Yue, Determination of thermal diffusion coefficient and diffusion coefficient, Journal of Crystal Growth, 42 (1977) 542-546.

[56] Y. Du, Y.A. Chang, B. Huang, W. Gong, Z. Jin, H. Xu, Z. Yuan, Y. Liu, Y. He, F.Y. Xie, Diffusion coefficients of some solutes in fcc and liquid Al: critical evaluation and correlation, Materials Science and Engineering: A, 363 (2003) 140-151.

[57] G.H. Geiger, D.R. Poirier, Transport phenomena in metallurgy, Addison-Wesley Pub. Co.,1973.

[58] S.S. Harilal, C.V. Bindhu, M.S. Tillack, F. Najmabadi, A.C. Gaeris, Internal structure and expansion dynamics of laser ablation plumes into ambient gases, AMER INST PHYSICS, 2003.

[59] C. Boulmer-Leborgne, J. Hermann, B. Dubreuil, Plasma formation resulting from the interaction of a laser beam with a solid metal target in an ambient gas, Plasma Sources Science and Technology, 2 (1993) 219.

[60] Y.P. Raizer, Subsonic Propagation of a Light Spark and Threshold Conditions for the Maintenance of Plasma by Radiation, Soviet Physics Journal of Experimental and Theoretical Physics, 31 (1970) 1148-1154.

[61] A. Luft, U. Franz, L. Emsermann, J. Kaspar, A study of thermal and mechanical effects on materials induced by pulsed laser drilling, Applied Physics A, 63 (1996) 93-101.

[62] K.C. Mills, A. Knovel, Metals, Metallurgy, Recommended Values of Thermophysical Properties for Selected Commercial Alloys, Woodhead Publishing Limited, Sawston, 2002.

[63] C. op't Hoog, N. Birbilis, Y. Estrin, Corrosion of Pure Mg as a Function of Grain Size and Processing Route, Advanced Engineering Materials, 10 (2008) 579-582.

Page intentionally left blank.

Chapter 3. Full immersion corrosion analysis of laser processed Al containing Mg alloys

3.1 Background on corrosion of laser processed and rapidly solidified Mg alloys

In general, non-equilibrium processed metal alloys have shown an improvement in corrosion resistance in comparison to conventionally processed material [1,2,3,4,5,6,7,8,9,10,11,12,13,14,15,16]. Many of the early studies on rapidly solidified Mg alloys consider binary alloys for the purpose of suppressing the formation of secondary phases, improving the alloys corrosion resistance in Cl^- containing aqueous solutions. Mg-xAl (x = 9 to 62 wt% Al) alloys received significant attention. Hehmann et al. and Baliga et al. observed reductions in the corrosion rate of the Mg-Al alloys when splat quenching or melt spinning were employed, with much of the credit given to the elimination of micro-galvanic couples [7,8,9]. Additional protection was attributed to a more stable corrosion film attributed to the high Al content often used. Work by Schluter et al. revealed PVD (10^{12} K/s) was capable of producing secondary phase-free thin films of AZ31B and AZ80, resulting in a reduction in open circuit potential (OCP) when compared to the bulk [6]. That said, the reduction in micro-galvanic couples is said to only afford the thin films a slight reduction in corrosion rate when compared to the bulk [6]. A similar reduction in corrosion potential was observed on the PVD of WE43 thin films [4,5].

In a similar fashion, a more negative corrosion potential is commonly observed for of Mg alloys processed with ns-pulse duration lasers [10]. There are few comprehensive studies on the corrosion behavior of the laser treated Mg alloys yet many present encouraging results [10,17,18,19]. An improvement in corrosion resistance was demonstrated by Khalfaoui et al. via salt-spray testing of laser processed ZE41, linking an improved corrosion resistance to the refinement of the grain structure and dissolution of secondary particles [18]. However, large craters were formed, resulting in a rough surface and cracks through to the melted layer, typically located in proximity to the pulse overlap regions. In a similar manner, Guo et al. exhibited the impact of excimer laser processing on the rare earth containing

Mg alloy, WE43 [17]. A reduction in cathodic kinetics and an increase in electrochemical impedance spectroscopy (EIS) estimated corrosion resistance was due to the alteration of electrochemically noble secondary phases present at the surface. Experiments were only carried out to 4 hours of immersion hence longevity of the processed surface is unknown. The experiments by Coy on excimer laser treatment of AZ91D reveal a largely homogenized processed layer resulting in a reduction of the OCP and corrosion current density as well as an increase in the EIS-estimated corrosion resistance [10]. Scanning kelvin probe force microscopy (SKPFM) was also employed to elucidate the relative surface potential of the laser modified region, yielding a more uniform potential than the heterogeneous bulk microstructure. That said, only a two fold increase was observed in the EIS-estimated corrosion resistance after 24 hours. The lack of longevity of the laser processed layer was primarily attributed to the voids and cracks commonly observed in the overlapped region.

Many of the investigated laser processed Mg alloys have shown improvements to corrosion however, all suffer from similar issues [10,17,18,20,21]. Namely the breakdown of the processed surface after no more than 12 hours, often attributed to surface defects produced during laser processing. Additionally, the literature understanding of the corrosion response of Mg alloys with respect to processing and surface morphology is incomplete and requires further work. Recent improvements in corrosion assessment methods by electrochemical measurement and mapping methods may illuminate the relationship between corrosion and laser processed microstructure [22,23,24,25,26,27].

This section aspires to present a comprehensive understanding of how laser processing affects the full immersion corrosion response of the AZ31B-H24, AM60B, and AZ91D alloys through newly developed corrosion experimentation. Focus will be given to time dependent electrochemical and visual measurements of the corrosion resistance and the observed time to initiation of local corrosion activity, i.e. filiform-like corrosion (FFC). The development of the corrosion product on the as-received alloys in comparison to the laser processed surfaces will also be shown. An explanation for improved corrosion resistance will be suggested, derived from the reduction in micro-galvanic coupling and formation of corrosion products that might afford protection.

Hypothesis to be tested: If the chemically homogenized surface generated by laser processing slows the general corrosion rate sufficiently, then the surface will become more uniformly covered with a protective corrosion product which will reduce the initiation and propagation of FFC.

3.2 Experimental approach for full immersion corrosion analysis

All corrosion experimentation was performed in stagnant 0.6 M NaCl with a starting pH between 5.5 and 6.2 (using Milli-Q® deionized water). Electrochemical characterization was performed in a standard three-electrode corrosion cell with a polished (1200 grit) as-received surface or the laser processed surface as the working electrode, a saturated calomel electrode (SCE) as the reference electrode, and platinum mesh counter electrode. The use of time lapse optical videos of the corroding as-received and laser processed surface was utilized as a first observation of the corrosion activity, capable of showing the time to corrosion film breakdown and qualitative changes in hydrogen evolution. Videos accompanied by open circuit potential (OCP) measurements allowed for changes in visual corrosion response to be correlated with changes in electrochemical response. Time lapse imaging and OCP verified the time to breakdown of the as-received alloys initial oxide film and the laser processed layer, providing insight for future long exposure experiments.

A more rigorous determination of corrosion rate utilized experimental procedures elaborated on by King et al. and Bland et al [25,26]. Electrochemical impedance spectroscopy (EIS) was performed for its nondestructive nature, as experiments were carried out at OCP, allowing for time dependent determination of the corrosion rate and the ability to combine several corrosion rate measurement techniques into a single experiment. The most common approach for the EIS technique is to measure the impedance as a function of frequency by applying a voltage as a sinusoidal wave, each at a successively smaller frequency, and measure the phase shift and amplitude (real and imaginary parts) of the resulting current [28,29]. EIS spectra may be modelled after an equivalent electrical circuit, with each component representing the electrical flow occurring during different phenomena arising near the material-electrolyte interface. The response corresponding to a certain phenomenon may be amplified within a specific frequency range so deciphering one from another is possible. Commonly observed phenomena at a material-electrolyte interface include a passivating corrosion film, electrochemical double layer (DL), the electrolyte itself as well as adsorption reaction rates. Each one may be represented as a frequency dependent capacitor, inductor, or resistor.

A Biologic SP-150[†] was used to perform the EIS measurements on the specimens, applying a potential equal to the specimens OCP and modulating the potential in a sinusoidal wave around the OCP at frequencies from 100,000 to 0.005 Hz at 6 points per decade with an amplitude of ±10 mV. In between EIS measurements the specimens were allowed to freely corrode at their OCP in order for time dependent corrosion rates to be observed. The frequency range was chosen so the entirety of the EIS measurement took approximately 10 minutes reducing the low frequency required to fully characterize the inductance behavior. Shorter times for the EIS measurement reduce the possibility of accelerating corrosion by applying a potential to the surface since Mg is known to be sensitive to small over-potentials [25,26].

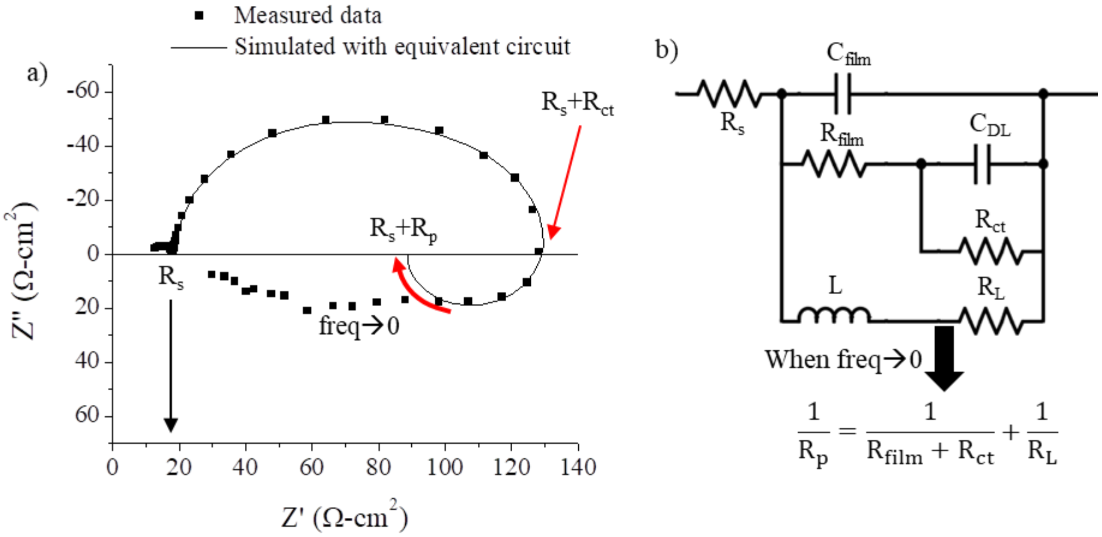

Figure 3.1: A Nyquist plot is shown in a) of an expected EIS measurement revealing graphically how to determine values such as R_s, R_{ct}, and R_p. In b) is the equivalent circuit the EIS measurements were fit to.

The impedance data was modeled after an equivalent circuit developed for ultra-high purity (UHP) Mg and extended to AZ31B-H24 containing an inset Randle's circuit in parallel with an inductor and resistor in series as seen in **Figure 3.1**. Circuit analysis was performed using the ZView[†] software. Each EIS measurement was fit to the equivalent electrical circuit model shown above with low residual noise (<1% of calculated) as performed elsewhere by the application of a Kramers-Kronig (K-K) transform [25]. K-K transforms at low frequencies sometimes appeared to deviate from the measurements. In this case the simulated spectra were extrapolated to lower frequencies by fixing the electrical circuit element values determined by the regression fit. The inductive behavior of Mg is well documented however has seen limited use in the analysis of EIS measurements until recently. The presence of an inductor accounts for the existence of active species at the surface and in the case of AZ31B-H24 can represent the cathodically active Al-Mn secondary phases.

In this study, EIS was utilized to determine the global polarization resistance (R_p) of the corroding as-received and laser processed surfaces (R_p is inversely proportional to corrosion rate). As the frequency of the EIS measurements trend toward zero, the capacitive components approach infinite impedance and the inductive components approach zero impedance, enabling simplification of the equivalent circuit to:

$$\frac{\mathbf{1}}{\boldsymbol{R_p}} = \frac{\mathbf{1}}{\boldsymbol{R_1}+\boldsymbol{R_2}} + \frac{\mathbf{1}}{\boldsymbol{R_3}} \qquad \textbf{(3.1)}$$

R_p represents the instantaneous global polarization resistance at each OCP immersion time, which is inversely proportional to the corrosion current density (i_{corr}):

$$i_{corr} = \frac{B}{R_p} \qquad \textbf{(3.2)}$$

Using 36 mV as the value for "B", the anodic charge associated with the dissolution of Mg (Q_a^{EIS}) can be estimated by integration of the EIS-estimated instantaneous corrosion rate over the time of exposure, given as [25]:

$$Q_a^{EIS} = \int i_{corr} \cdot A \cdot dt \qquad \textbf{(3.3)}$$

The anodic charge associated with the dissolution of Mg was used to observe the EIS-estimated corrosion rate with respect to time.

The EIS measurements were accompanied by gravimetric mass loss (the exposed samples which were cleaned via a chromate, 200 g/L CrO_3, cleaning solutions as per ASTM G-1[30]), along with inductively coupled plasma-optical emission spectrometry (ICP-OES) solution measurements to unambiguously measure the corrosion rate of each specimen [26,30]. These results provided an averaged corrosion rate over a 24 hour or 72 hour full immersion period in the stagnant 0.6 M NaCl solution. All corrosion tests were repeated at a minimum of 4 times with error bars representing one standard error.

The corrosion morphology was further investigated with post-mortem SEM analysis. The primary focus was on observing changes in initiation sites of FFC on the as-received material versus the laser processed material. In addition the general corrosion of the surface was investigated with an emphasis on observing changes to local degradation surround secondary phase particles or lack thereof. The corrosion product of the specimens after 24 hours of immersion in 0.6 M NaCl was also investigated utilizing grazing incidence – x-ray diffraction (GI-XRD PANalytical X'Pert Pro MPD diffractometer) with a Cu-K_α (λ=1.54 Å) source at a 1.0^o incident angle (5.0 μm x-ray penetration depth of pure Mg). Infrared spectroscopy (PerkinElmer Frontier attenuated total reflection – Fourier transform infrared (ATR-FTIR)) was used to accompany the GI-XRD results, verifying the presence of certain compounds sensitive to IR spectroscopy (such as carbonates).

A tertiary electrochemical experiment performed to investigate the galvanic coupled current density and potential of the laser processed surface coupled with the underlying as-received material used the zero resistance ammeter (ZRA) technique [31,32]. A ZRA measurement connects two specimens as if they were physically in contact with one another and exposed to the same solution while simultaneously measuring the current between the two. The samples were coupled with the laser processed specimen as the working electrode (WE) and the as-received specimen as the counter electrode (CE). In this arrangement a positive current density would indicate the laser processed specimen was the anode in the galvanic couple.

3.3 Full immersion corrosion analysis of the laser processed AZ31B-H24

3.3.1 General electrochemistry response

The open circuit potential (OCP) was recorded, shown in **Figure 3.2**, with an accompanying set of optical micrographs taken to observe the corrosion behavior as indicated by spreading of dark regions previously discussed in literature, observed in **Figure 3.3 [**20]. The as-received AZ31B-H24 alloy corroded with a black filiform-like morphology, more rigorously described in **section 1.6**, and an average OCP of -1.56 V vs. SCE as typically observed in the literature for the solution investigated [23]. Filiform-like corrosion of the as-received material initiated after 10 minutes in solution and complete surface coverage was reached at 3 hours, followed by a slight rise in the OCP and the continued growth of the corrosion filaments across the surface. In stark contrast, the laser processed samples exhibited a lower OCP than the as-received alloy as well as a delayed initiation of filiform-like corrosion for more than 19 hours in the stagnant 0.6 M NaCl solution. A steady increase in the OCP to less negative electrochemical potential values was observed for all samples prior to the breakdown of their initial corrosion product. Similar to the as-received alloy, the breakdown of laser processed samples was marked by the initiation of filiform-like corrosion accompanied by increased fluctuations in the OCP measurements. Prior to the laser processed layer's breakdown, large bubbles of H_2 were observed to slowly grow on the surface in **Figure 3.3**, some lasting for hours, suggesting a reduction in the H_2 evolution reaction rate consistent with the cathodic polarization behavior shown in **section 2.5**.

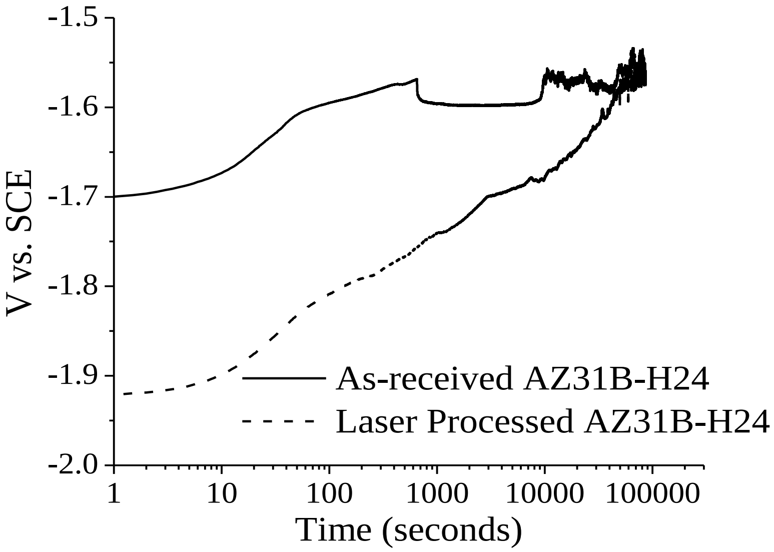

Figure 3.2: Representative OCP measurements for the as-received and laser processed AZ31B-H24 specimens on full immersion in stagnant 0.6 M NaCl solution for 24 hours.

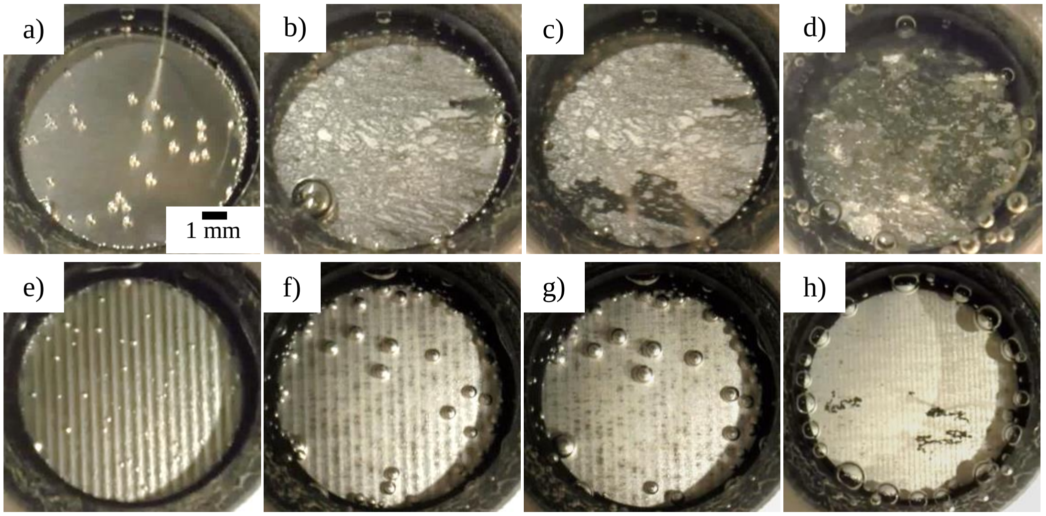

Figure 3.3: Time-lapse optical micrographs of the OCP corrosion of the as-received a) 0 sec., b) 9,600 sec., c) 19,200 sec., d) 86,400 sec. and laser processed e) 0 sec., f) 9,600 sec., g) 19,200 sec., h) 86,400 sec. AZ31B-H24 material in full immersion with stagnant 0.6 M NaCl solution.

At all freely corroding times, the EIS measurements for the laser processed samples exhibited an improvement in global R_p from the as-received material as calculated by **equation 3.1**. The impedance data, as shown in **Figure 3.4**, is representative of a typical Nyquist plot for the as-received and laser processed material after full immersion in the stagnant 0.6 M NaCl solution for 12 hours. The regression fit of the impedance measurements were made for a similar set of data after each immersion time using the equivalent circuit shown in **Figure 3.1**, each fit yielding unique values for the electrical circuit elements as seen in **Table 3.1**. While some of these tabulated values exhibit large error bars, this variability is from differences in breakdown times, often seen between 12 and 24 hours for the laser processed samples which yields a drastic reduction in R_p. The average global R_p values were plotted in **Figure 3.5** revealing the relatively stable R_p for the as-received material. Laser processed global R_p values were plotted so the specimens who observed the initiation of FFC (red dots) were distinguished from the more corrosion resistant specimens (open dots). The error bars are substantially smaller if this distinction is made in comparison to what was presented in **Table 3.1**.

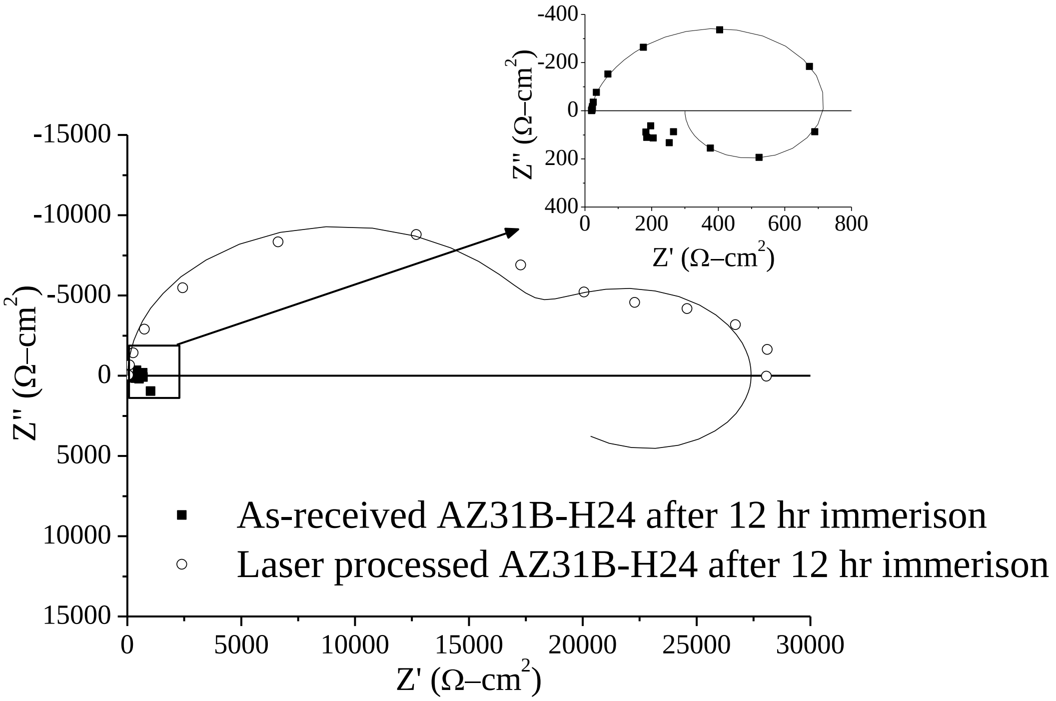

Figure 3.4: A representative Nyquist plot for the as-received and laser processed AZ31B-H24 alloy after 12 hours of full immersion in stagnant 0.6 M NaCl at the materials OCP.

Table 3.1: Equivalent circuit's component values from fitting analysis for EIS measurements of AZ31B-H24 in as-received and laser processed condition, after 1, 3, 12 and 24 hours at full immersion.

As-received	1hr	3hr	12hr	24hr
R_s (Ω-cm^2)	22 ± 1.3	22 ± 1.3	21 ± 0.9	22 ± 1.0
C_{film} (μF/cm^2)	18 ± 6.5	22 ± 8	34 ± 6.5	31 ± 5.0
R_{film} (Ω-cm^2)	430 ± 130	420 ± 120	320 ± 50	290 ± 36
C_{DL} (μF/cm^2)	58 ± 34	70 ± 32	52 ± 24	30 ± 13
R_{ct} (Ω-cm^2)	260 ± 150	390 ± 250	300 ± 85	410 ± 130
L (Ω-s-cm^2)	190 ± 65	240 ± 120	260 ± 65	590 ± 280
R_L (Ω-cm^2)	190 ± 90	270 ± 80	330 ± 85	330 ± 60
R_p (Ω-cm^2)	150 ± 65	200 ± 65	210 ± 50	220 ± 40
Laser processed	1hr	3hr	12hr	24hr
R_s (Ω-cm^2)	24 ± 1.5	25 ± 1.2	24 ± 0.90	23 ± 3.0
C_{film} (μF/cm^2)	7.0 ± 0.38	7.1 ± 0.32	7.1 ± 0.50	8.5 ± 3.3
R_{film} (Ω-cm^2)	8,100 ± 960	14,600 ± 780	14,700 ± 4,800	8,710 ± 11,200
C_{DL} (μF/cm^2)	600 ± 230	17,300 ± 16,700	900 ± 700	129,000 ± 128,000
R_{ct} (Ω-cm^2)	3,330 ± 640	5,770 ± 475	8,370 ± 1,040	3,860 ± 2,010
L (Ω-s-cm^2)	$5.4\text{x}10^6 \pm 1.4\text{x}10^6$	$3.0\text{x}10^7 \pm 1.2\text{x}10^7$	$4.8\text{x}10^7 \pm 2.0\text{x}10^7$	$2.6\text{x}10^7 \pm 2.0\text{x}10^7$
R_L (Ω-cm^2)	12,000 ± 4,000	49,600 ± 19,000	27,300 ± 11,000	9,930 ± 6,050
R_p (Ω-cm^2)	5,480 ± 1,100	13,300 ± 2,100	11,500 ± 3,800	5,510 ± 3,360

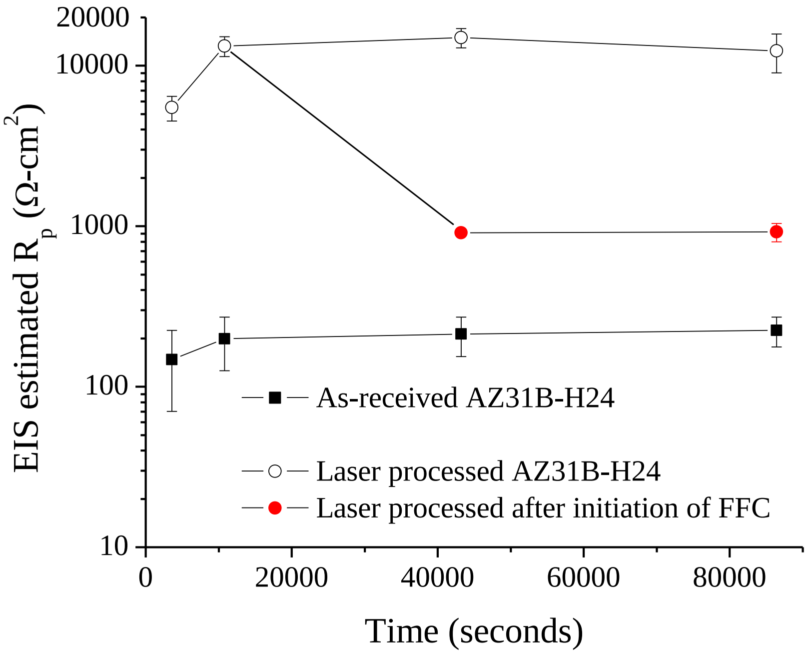

Figure 3.5: Average EIS-estimated R_p after 1, 3, 12, and 24 hours of full immersion in stagnant 0.6 M NaCl at OCP for the AZ31B-H24 as-received and laser processed material. The red circles indicate the reduction in R_p associated with the beginning of filiform-like corrosion which begins on the laser processed specimen after different immersion times. ± represents one standard error.

For the as-received alloy, the global R_p is roughly the same over time, exhibiting inductive behavior at low frequency (<1 Hz) indicated by a positive phase angle, as observed in the inlaid plot in **Figure 3.4** [25,26]. The global R_p for laser processed samples was consistently 5 to 10 times larger than the as-received alloy and exhibited an order of magnitude increase in R_p for the entire time prior to FFC initiation. The laser processed samples also displayed little to no sign of inductive behavior even when measurements reached 0.001 Hz as seen in **Figure 3.4**. After the initiation of FFC however, the laser processed impedance spectra observed an abrupt reduction in R_p along with evidence of inductive behavior similar to that of the as-received alloy.

EIS-estimated global R_p was converted to instantaneous corrosion rate through Equation (3), calculating the anodic charge associated with the dissolution of Mg (Q_a^{EIS}) as seen in **Figure 3.6**. Agreement between EIS based Q, gravimetric mass loss Q, and Q by ICP-OES solution analysis was obtained which are all statistically similar. Comparison of Q_a calculated by EIS, mass loss and ICP-OES after 24 hours at OCP reveal a similar trend as seen above, with the laser processed specimen consistently showing the smallest accumulation of anodic charge over 24 hours.

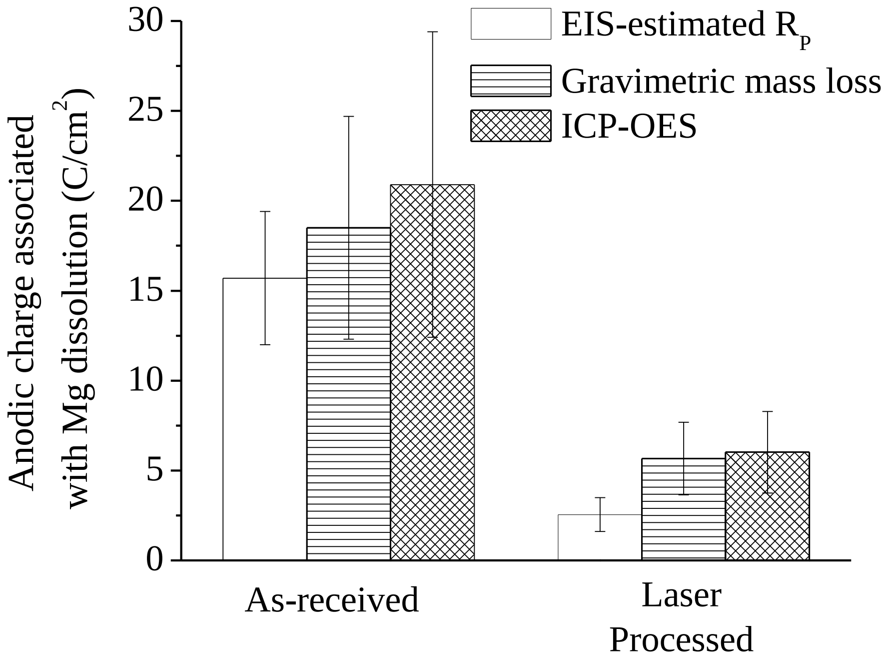

Figure 3.6: Summation of the anodic charge associated with Mg dissolution ($\boldsymbol{Q_a}$) as calculated by i_{corr} derived from EIS-estimated R_p, gravimetric mass loss, and ICP-OES after 24 hours at OCP for the AZ31B-H24 alloy immersed in stagnant 0.6 M NaCl. ± represents one standard error.

The increased R_p and reduced Q_a of the laser processed specimen as estimated by EIS measurements can be explained by the reduction of active cathodic sites present at the surface as a result of dissolution of secondary phase particles, as shown in **Chapter 2**. The reduction in corrosion rate leads to a lower coverage of absorbed intermediate filming responsible for inductive behavior and anodically induced cathodic activity. The trends observed by fits to the equivalent circuit further suggest this for the laser processed specimens which exhibited little inductive behavior at low frequencies (0.001 Hz) prior to initiation of FFC. Inductive behavior is ascribed to the surface coverage of active corroding species [25]. The partial dissolution of the cathodic particles is enough to suppress the rapid corrosion leading to the inductive behavior typically observed in Mg.

3.3.2 FFC initiation and local corrosion of laser processed specimen

Experiments were carried out to observe if there was a difference in location of initiation sites for the FFC on the as-received material versus the laser processed surface of AZ31B-H24. Specimens were immersed in stagnant 0.6 M NaCl solution until the surface was observed to breakdown, revealing immense streams of H_2 gas bubbles. BSE micrographs shown in **Figure 3.7** reveal the initiation sites for the FFC on the as-received material in a) and b) and the laser processed material in c) and d). After removal of the corrosion product for the as-received material in **Figure 3.7 b,** a cluster of *tier 1* Al-Mn secondary phase particles, which has commonly been observed as an initiation site for this alloy. On the other hand, the laser processed specimen initiated at a relatively small area in comparison to the as-received materials large circular FFC site. The laser processed specimen in **Figure 3.7** also exposed no compositional variations in the microstructure co-located at the initiation site, suggesting a secondary phase particle is not the primary cause of FFC initiation for laser processed specimens.

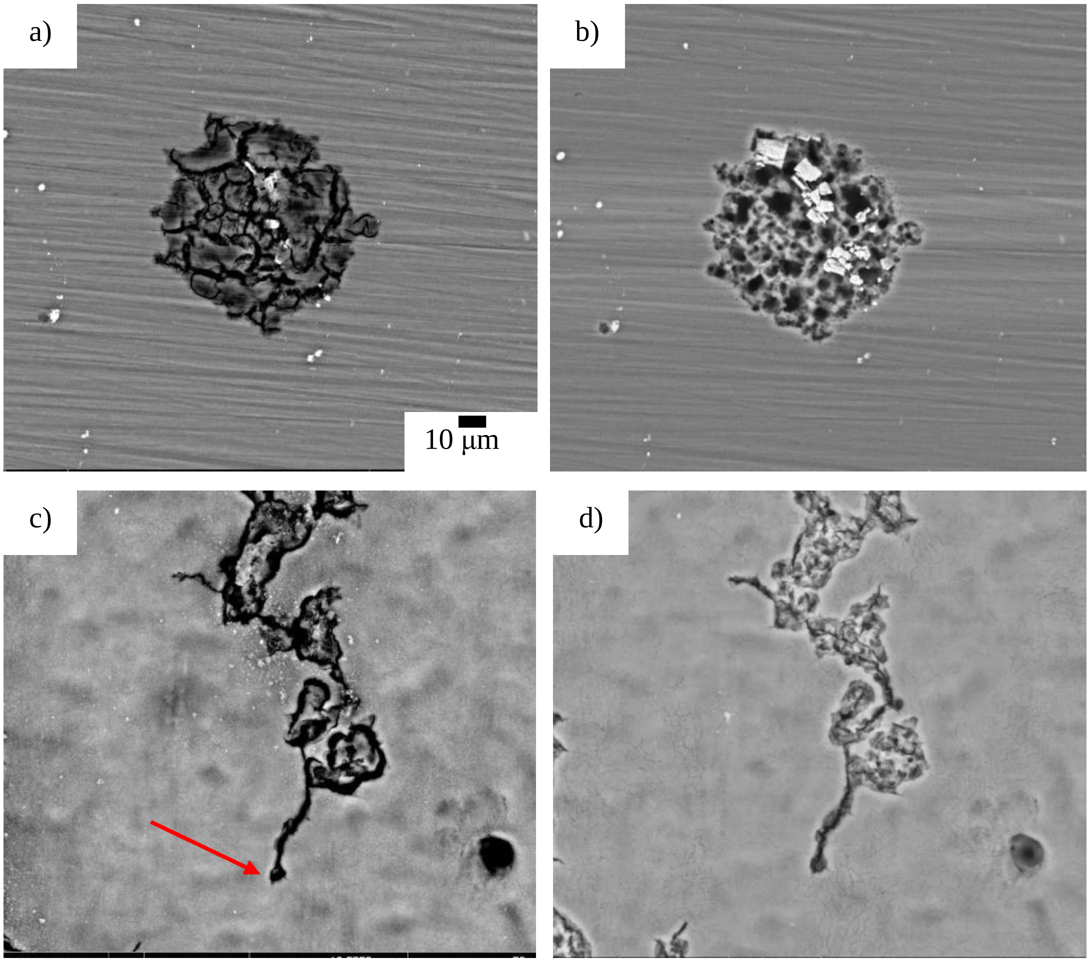

Figure 3.7: Backscattered electron micrographs of AZ31B-H24 after initiation of FFC was observed at full immersion in stagnant 0.6 M NaCl; a, b) as-received after 10 minutes and c, d) laser processed after 12 hours.

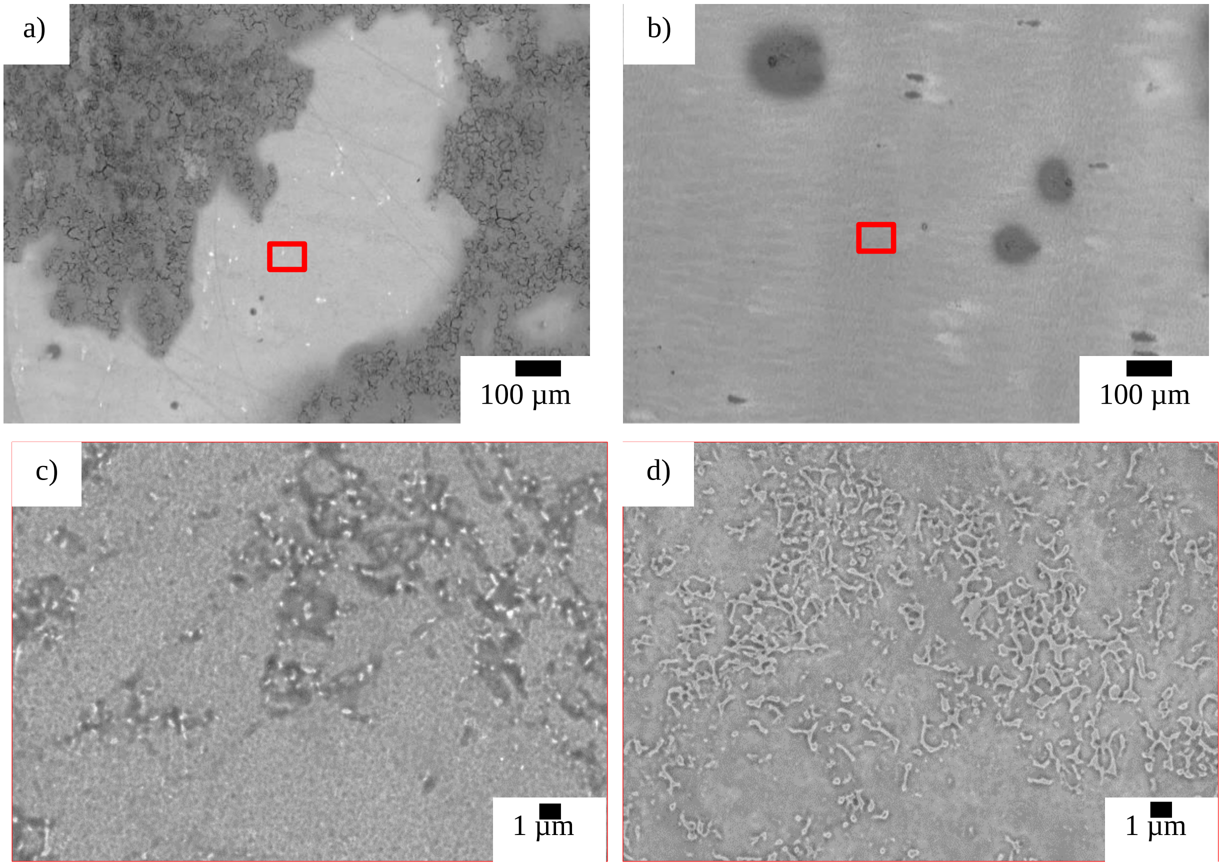

Figure 3.8: Backscattered electron micrographs of AZ31B in each condition after 3 hour immersion in 0.6 M NaCl; a, c) as-received and b, d) 200 PPA.

This fact is further corroborated by SEM micrographs comparing the as-received and laser processed material after 3 hour immersion in the stagnant 0.6 M NaCl solution as shown in **Figure 3.8**. In **Figure 3.8 a**, the dark, cracked morphology present on the as-received material is indicative of areas affected by FFC, while the lighter gray area is covered by a thin layer of $MgO/Mg(OH)_2$, typical for Mg when immersed in NaCl solutions [33,34,35]. A closer investigation of this region, **Figure 3.8 c**, reveals dark areas (local dissolution) surrounding *tier 2* secondary phase particles. The particles themselves were shown to be rich in Al and Zn from EDS analysis, suggesting the β phase, while the dark area surrounding them had a higher oxygen content than the surrounding Mg matrix.

After 3 hours immersion, the laser processed specimen showed no signs of FFC initiation, as corroborated by the OCP measurements. However the remaining Al-Mn rich regions at the surface persisted as local cathodes as seen in **Figure 3.8 b** the large dark spots on the surface, suggestive of more intense deposition of the flaky $Mg(OH)_2$ corrosion product at these regions. This flaky $Mg(OH)_2$ deposits is commonly observed because of the increased Mg dissolution near the *tier 1* particles as well as a local increase in pH caused by the H_2 evolution reaction. At higher magnification for the laser processed specimens in **Figure 3.8 d** respectively, no sign of local dissolution from *tier 2* particles was observed.

3.3.3 Alterations to corrosion product formation

The corrosion product of the AZ31B-H24 alloy was investigated via grazing incidence – x-ray diffraction (GI-XRD) after specimens were immersed in a stagnant 0.6 M NaCl solution for 24 hours, as shown in **Figure 3.9**, with standard diffraction patterns for all phases found in **Appendix 1**. The key features of these diffraction patterns is the pronounced intensity of the $Mg(OH)_2$ peaks for the as-received specimen in comparison to the laser processed specimen, suggestive of the higher coverage of FFC and general corrosion rate on the as-received alloy in comparison to the laser processed alloy [33,34,35]. In addition, the presence of a hydrotalcite-like phase for both specimen at the broad peaks at $2\theta = 11^{o}$ and 22.5^{o} is a corrosion product not commonly reported and often suggested in passing [9,33,34,35,36,37,38,39].

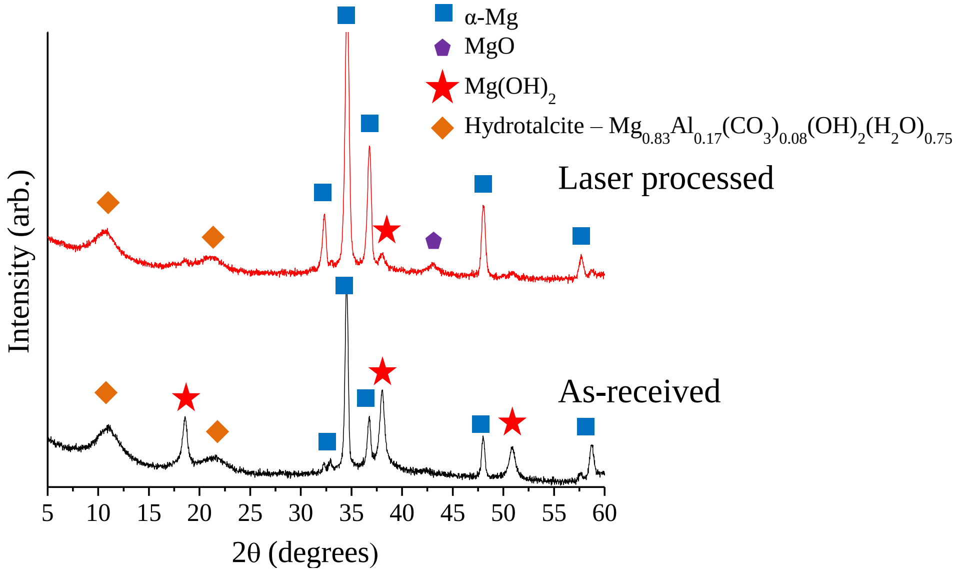

Figure 3.9: GI-XRD measurements of AZ31B-H24 corrosion product after a 24 hour full immersion in stagnant 0.6 M NaCl solution at OCP. The Cu-K_{α} (λ=1.54 Å) source was utilized at a 1.0^{o} incident angle.

This hydrotalcite phase is a layered double hydroxide (LDH) phase with the general formula of:

$$[M^{2+}_{1-x}\ M^{3+}_{x}(OH)_2]^{x+}\ [A^{n-}]_{x/n}\ .\ mH_2O.$$

where the M^{2+} and M^{3+} represent the divalent and trivalent metal ions associated with the mixed hydroxide layers [40]. In between the mixed hydroxide layers is a layer of charge compensating anions, A^{n-}, which have intercalated between the mixed metal hydroxide layers, CO_3^{2-} for hydrotalcite [40]. A schematic of a typical LDH structure is shown in , reproduced from Salomão et al. [41].

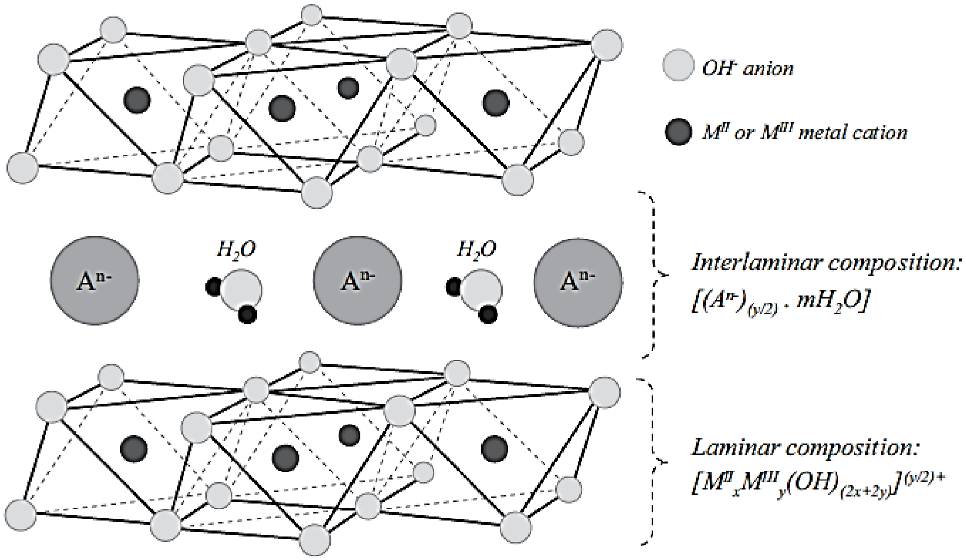

Figure 3.10: Schematic of a layered double hydroxide phase, reproduced from Salomão et al. [41].

Much of the research on LDHs pertains to their use as potential catalysts and anion exchangers, the later taking advantage of their layered structure and ability to intercalate a variety of anions (CO_3^{2-}, Cl^-, OH^-, NO_3^-, etc.) [40,42,43,44,45]. LDHs have recently seen attention for their ability to form as a corrosion inhibiting film on Mg alloys, in particular the Al containing Mg alloys after a conversion coating like process in a carbonic acid solution which was saturated with Al ions [46,47,48]. Studies on the precipitation of the Mg^{2+}/Al^{3+} LDH phases observe the typical M^{2+}/M^{3+} ratio to be 2:1 – 4:1 ($0.2 < x < 0.33$) [40]. In addition, the anion observed to be the most stable in the LDH phase is CO_3^{2-}, hence the reason the LDH phase has received attention in the Mg alloy atmospheric corrosion literature [36,37]. That said, the LDH phases include an array of other anions to be intercalated in between the hydroxide layers including Cl^- and OH^-, resulting in minimal alteration to the LDH structure making these anion differences extremely difficult to detect through XRD [40].

Numerous studies on the precipitation of the Mg^{2+}/Al^{3+} LDH phases suggest precipitation occurs when one of the metal cations (Mg^{2+}/Al^{3+}) deposits into the lattice of the other metal hydroxide ($Al(OH)_3/Mg(OH)_2$) [41,43,47,49,50]. The precipitation of these LDHs on the Mg-Al alloys under stagnant full immersion conditions, in the case here, likely occurs via a similar route with crystalline $Mg(OH)_2$ to form first at the alloy surface [47,49]. The manifestation of Al ions can occur by the alkaline corrosion of the Al rich secondary phases found throughout the Mg-Al alloy microstructure [51]. The Al ions (expected to be $Al(OH)_4^-$ because of the high pH at the Mg surface) will be localized near the alloy surface and the secondary phase particle it originated from. The $Al(OH)_4^-$ ion then deposits into the $Mg(OH)_2$ lattice above a $pH \approx 8$, which is easily achieved at the surface of a corroding Mg alloy [42,43,44,50,41].

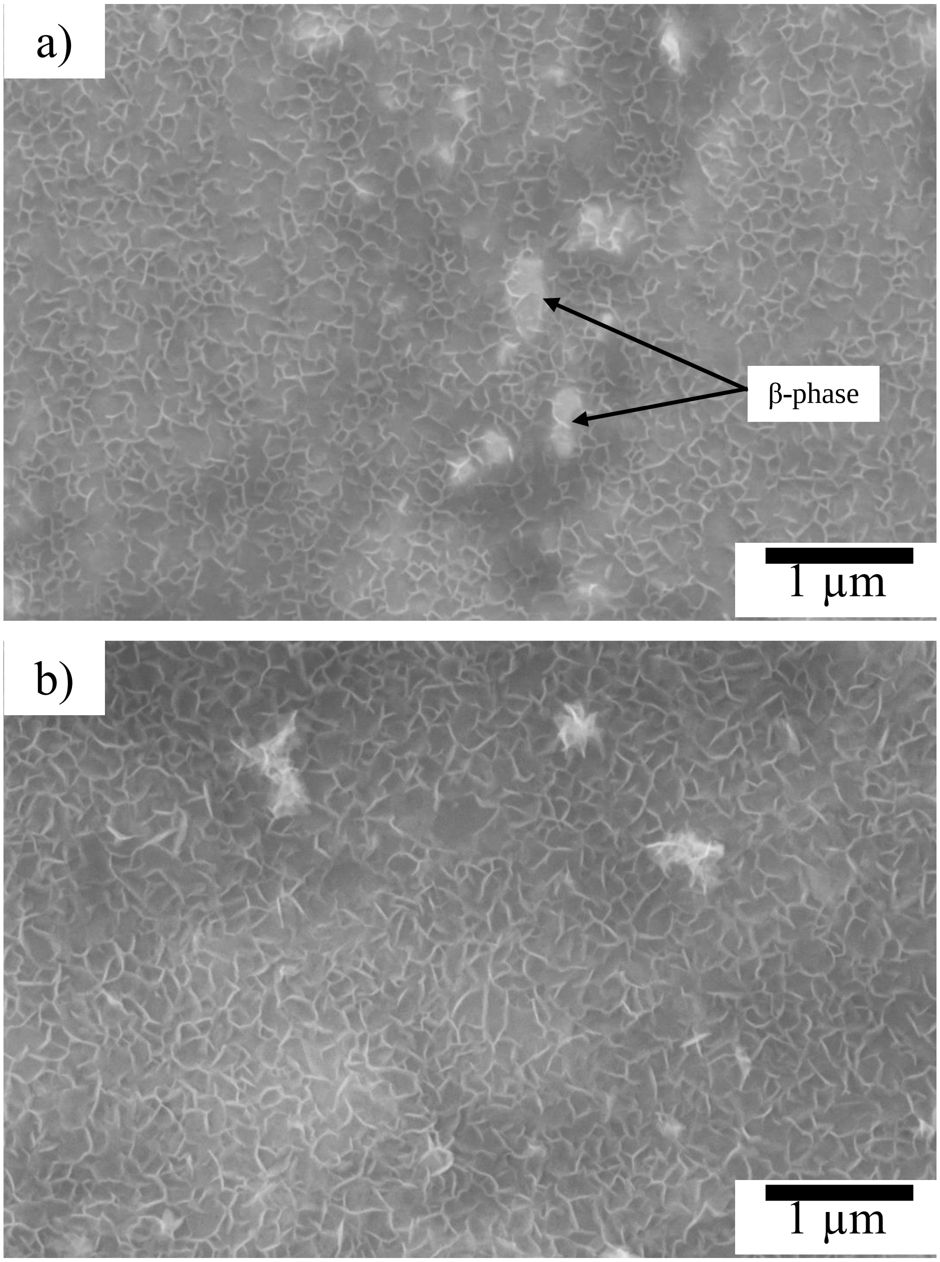

Figure 3.11: Secondary electron micrographs of the general corrosion morphology for an **a)** as-received and **b)** laser processed AZ31B-H24 specimen after a 12 hour immersion in stagnant 0.6 M NaCl.

The corrosion product morphology of an area not impacted by FFC may be observed in **Figure 3.11** for the as-received and laser processed AZ31B-H24 specimens after a 12 hour full immersion exposure in stagnant 0.6 M NaCl at OCP. **Figure 3.11** reveals both specimen have a somewhat flaky morphology, similar to the hydrotalcite conversion coatings produced in previous work where the LDH phase was purposely formed [46,47]. This corroborates the XRD results where the hydrotalcite phase was observed on the as-received and laser processed specimen with the primary difference being the large quantity of

$Mg(OH)_2$ on the as-received specimen. This $Mg(OH)_2$ is from the significant coverage of the as-received surface with FFC. Interestingly, the LDH phase appears to cover the β-phase particles present in the as-received alloy, possibly suggesting the precipitation of the LDH occurs by exceeding the LDHs solubility product in the solution directly above the alloy surface. If this is the case, then the complete coverage of the as-received and laser processed surfaces likely occurs however the initiation of FFC is still dictated by secondary phase particles and the development of micro-galvanic couples, hence the laser processed specimen will remain more resistant to corrosion than the as-received alloy.

In addition, attenuated total reflection – Fourier transform infrared (ATR-FTIR) spectroscopy was utilized to determine the anion present in the LDH phase, presented in **Figure 3.12** for both AZ31B-H24 specimen conditions after a 24 hour immersion in stagnant 0.6 M NaCl. The distinct peak at ~3,700 cm^{-1} for the as-received specimen is an indication of $Mg(OH)_2$ while the broad peak around 3,400 cm^{-1} can be attributed to OH^- stretching modes, often a sign of hydrated or hydroxide species [52,53]. The broad peaks present between 1,350 and 1,500 cm^{-1} are indicative of CO_3^{2-} bonding, suggesting the anion intercalated between the LDH is carbonate [52,53]. Standards for the compounds found using FTIR may be found in **Appendix 1**.

The existence of sufficient CO_3^{2-} in the 0.6 M NaCl solution to dramatically impact the corrosion product formation was unexpected. However, additional analysis of 300 mL of Milli-Q® deionized water (starting pH = 7.0) revealed a reduction in pH to 6.2 if left to sit in lab air for more than 5 minutes. The pH was reduced to and stabilized at 5.8 after remaining stagnant in lab air for 24 hours. This pH change is indicative of the acidification of solutions by the absorption of CO_2 from the atmosphere where the mass transfer velocity of CO_2 (g) into sea water is ~ 11 cm/hour (the height of all solutions were ~10 cm over the exposed alloy surface) [54]. The presence of CO_3^{2-} suggests hydrotalcite will be the preferred LDH phase to form. That said, it is interesting to consider the use of the LDH phase as a means of absorbing Cl^- anions from the solution as well, potentially limiting Cl^- detrimental effects on film stability, an effect controlled by the NaCl content of the solution [42,43].

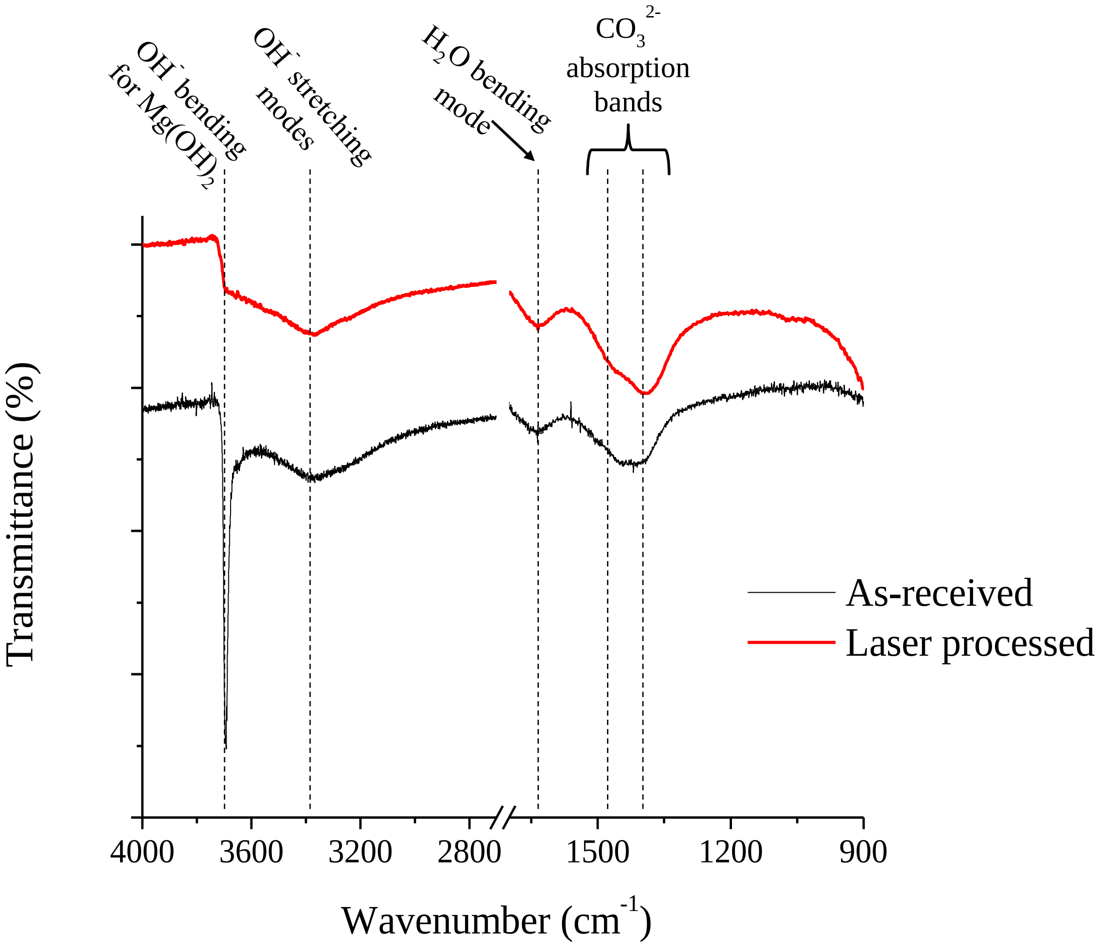

Figure 3.12: ATR-FTIR measurements of AZ31B-H24 corrosion product after a 24 hour full immersion in stagnant 0.6 M NaCl solution.

To summarize, the formation of a LDH phase was possible regardless of the AZ31B-H24 condition, observed to cover the secondary phase particles in the as-received alloy in **Figure 3.11**. Therefore suggesting the ultimate controlling factor in increasing the time to initiation of FFC is still the reduced number of micro-galvanic couples observed in the laser processed specimens.

3.3.4 Galvanic coupled behavior between as-received and laser processed surfaces

The final route to investigating the full immersion corrosion properties of the laser processed AZ31B-H24 alloy was through the zero resistance ammeter (ZRA) measurement. The galvanic coupled potential and current density between a laser processed specimen (1 cm^2), working electrode, and as-received specimen (1 cm^2), counter electrode, was obtained over a 24 hour period and observed in **Figure 3.13**. A consistently positive current density suggests the working electrode remains as the anode for the entirety of the 24 hour experiment. This result is expected since the laser processed specimens OCP was observed to have a value more negative than the OCP of the as-received alloy, suggesting its anodic behavior. A surface film with a more negative OCP than the underlying bulk material is a commonly observed coating scheme termed "cathodic protection" with the most well-known process being the galvanizing of steel [55]. Such a response suggests the laser processed layer on the AZ31B alloy may act to impede corrosion of the underlying bulk material if a scratch breaks through the entire thickness of the processed layer.

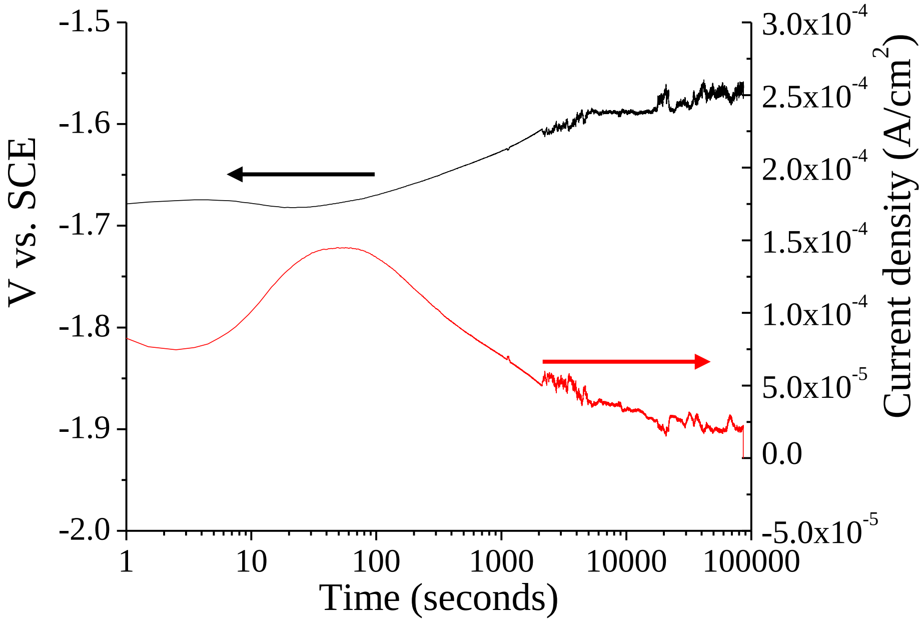

Figure 3.13: ZRA measurement with the laser processed surface as the working electrode (expected anode) and the ground as-received surface as the counter electrode (expected cathode). Both surfaces had 1 cm^2 exposed to the stagnant 0.6 M NaCl solution and were coupled for 24 hours. The red line represents the coupled current density and the black line represented the coupled potential.

To test this, specimen were prepared in their typical manner however directly before a full immersion experiment was conducted, the specimen were scratched with a diamond scribe making a 1 cm long scratch. The depth of the scratch was verified by white light interferometry to be ~15 μm deep, capable of penetrating through the entire laser processed layer down to the bulk microstructure, and ~100 μm wide. The scratched as-received and laser processed specimens were exposed to stagnant 0.6 M NaCl solution for 24 hours where the OCP was measured for that duration accompanied by time-lapse imaging. The optical micrographs observed in **Figure 3.14** reveal there was little change to the general corrosion response for either condition when compared to specimen without a scratch from **Figure 3.3**. For the as-received material, the scratch did act as a source for initiation of FFC as seen in **Figure 3.14 a**. This was not observed for the laser processed specimens were no initiation of FFC was observed for the entire 24 hour immersion time. No FFC initiation on the laser processed specimen was corroborated by the OCP measurements shown in **Figure 3.15**. While the as-received material showed a faster rise and breakdown of the surface, the laser processed specimen with the scratch persisted with an OCP more negative than the as-received material and a steady increase in potential with time. Although not at the negative potentials typically observed for a surface without a scratch, the stable OCP of the scratched laser processed specimens further suggests the laser processed layer was providing cathodic protection to the underlying bulk material exposed at the scratch.

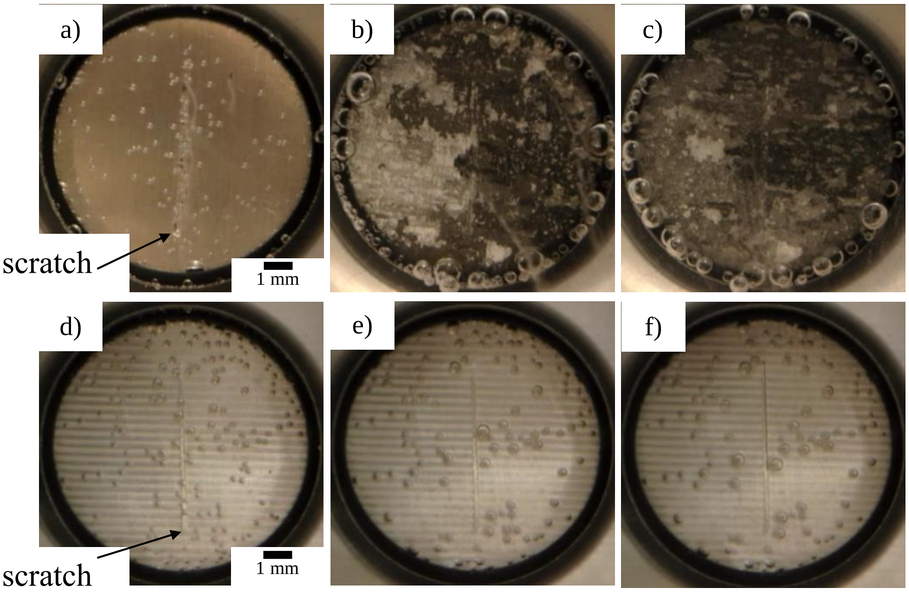

Figure 3.14: Optical micrographs taken with the Dinolite digital camera after a,d) 0 hrs., b,e) 12 hrs., and c,f) 24 hrs. of full immersion for specimen scratched with a diamond scribe in the as-received (a, b, and c) and laser processed (d, e, and f) condition. The solution used was stagnant 0.6 M NaCl solution. The scribe is at the center of each image.

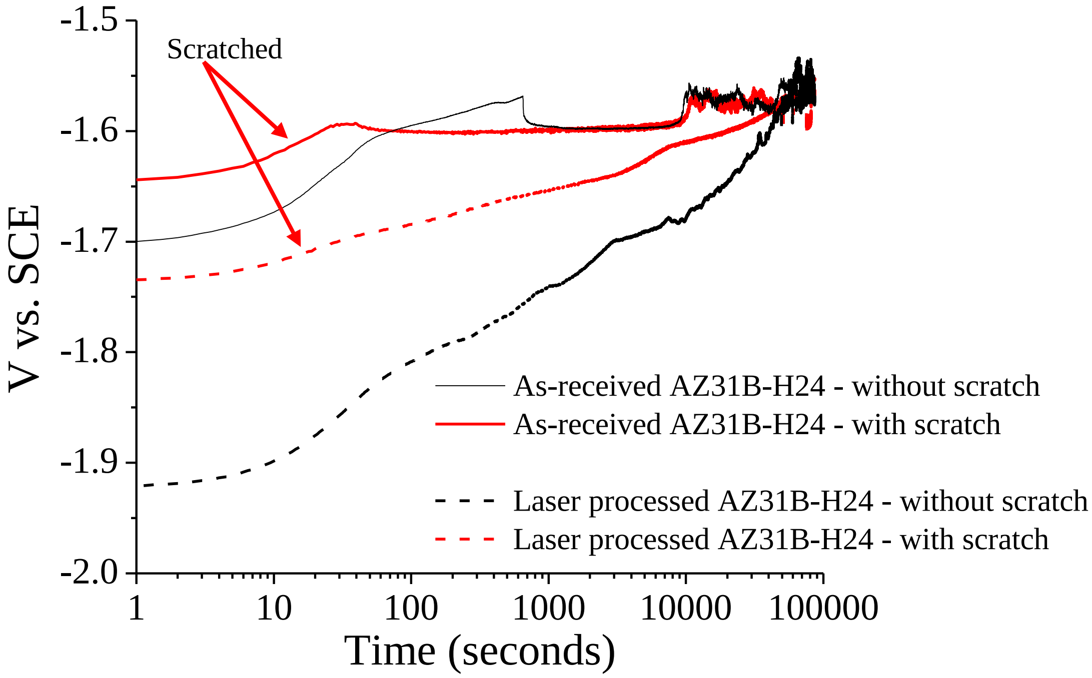

Figure 3.15: OCP measurement of the scratched AZ31B-H24 specimen during the entire 24 hour immersion. The OCP measurements from **Figure 3.2** were added for comparison.

3.4 Full immersion corrosion analysis of laser processed as-cast alloys

A set of time lapse optical micrographs were taken over 72 hours to observe the development of the corrosion product of the as-received alloy and laser processed specimens as shown in **Figure 3.16** and **Figure 3.17**. As-received specimens of AZ91D and AM60B corroded with the FFC morphology. Initiation and spreading of FFC was a stable indicator of a specimen’s surface breakdown. The as-received alloys initiated FFC after an hour of immersion in the stagnant 0.6 M NaCl solution and gradually increased in coverage, to >30% by the end of the 72 hours of immersion. In stark contrast, time lapse imaging of laser processed specimens exhibited minimal activity on the surface during the entirety of the experiment, shown in **Figure 3.16 d-f** and **Figure 3.17 d-f**. At short immersion times, the laser processed surfaces appeared covered with a high density of slow growing H_2 bubbles, eventually evolving off the surface. Filiform-like corrosion on the AM60B alloy was not observed during the 72 hour test while AZ91D exhibited FFC after 24 hours of immersion; with less than 5% coverage of the surface after

72 hours. The time-lapse imaging was accompanied by an investigation of the materials OCP as shown in **Figure 3.18**. The as-cast material in the laser processed condition observed a similar reduction in OCP at all times of immersion, consistent with the results for the AZ31B-H24 alloy and indicative of a chemically homogenized surface.

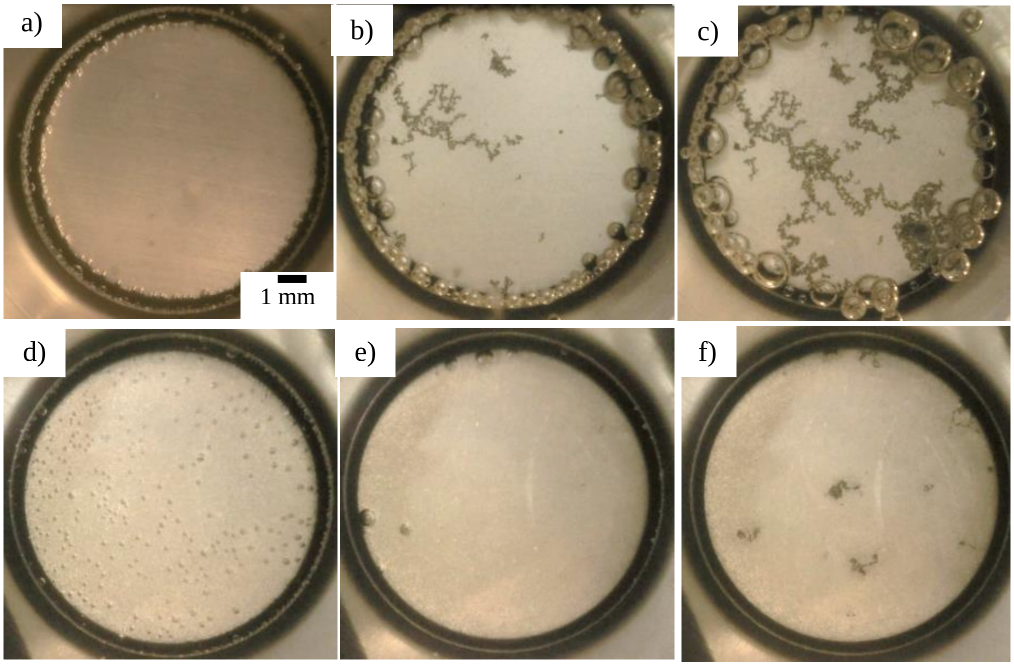

Figure 3.16: Time-lapse optical micrographs of the OCP corrosion of the as-received a) 0 sec., b) 86,400 sec., c) 292,200 sec. and laser processed d) 0 sec., e) 86,400 sec., f) 259,200 sec. AZ91D alloy in full immersion with stagnant 0.6 M NaCl solution.

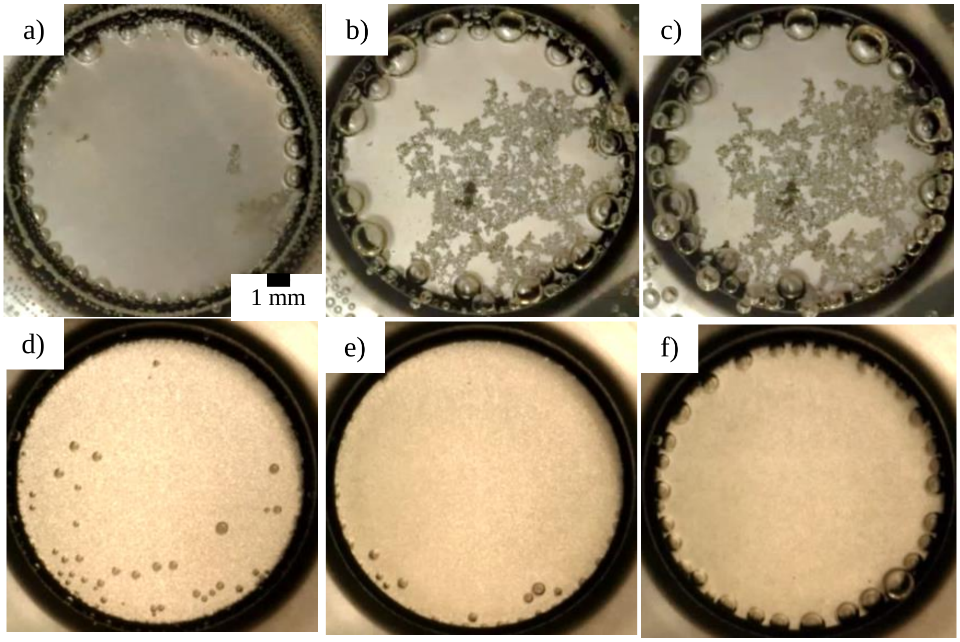

Figure 3.17: Time-lapse optical micrographs of the OCP corrosion of the as-received a) 0 sec., b) 86,400 sec., c) 292,200 sec. and laser processed d) 0 sec., e) 86,400 sec., f) 259,200 sec. AM60B alloy in full immersion with stagnant 0.6 M NaCl solution.

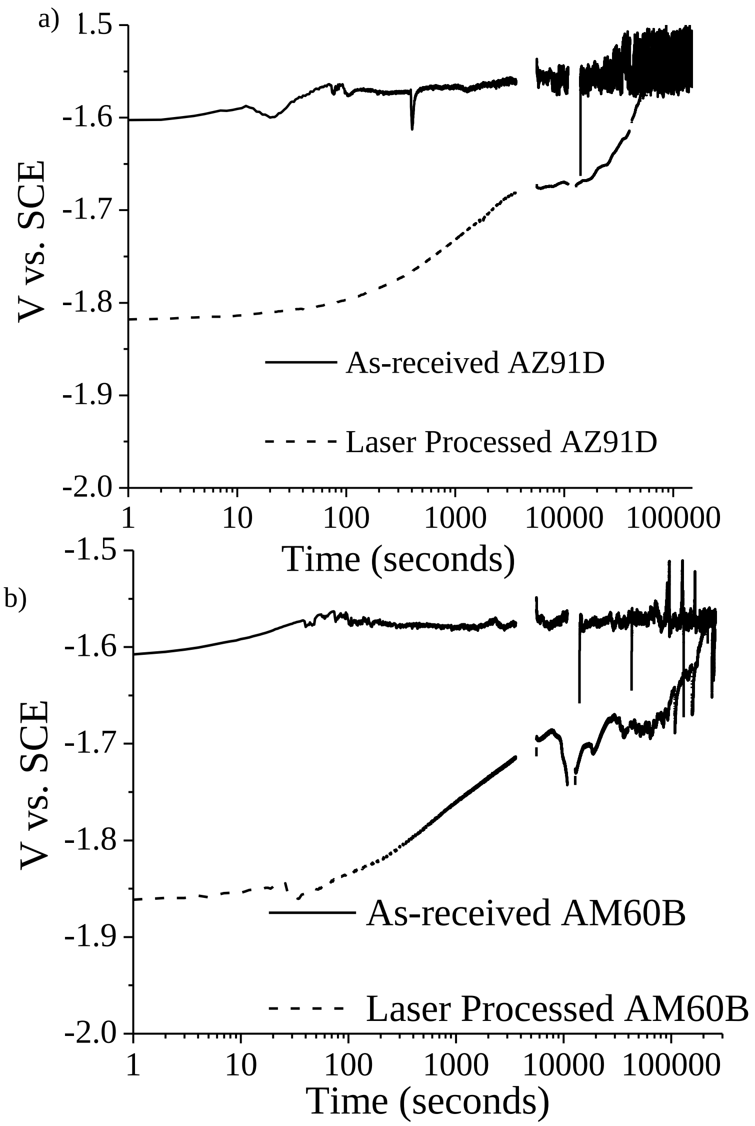

Figure 3.18: Representative OCP measurements for the as-received and laser processed a) AZ91D and b) AM60B specimens on full immersion in stagnant 0.6 M NaCl solution for 72 hours.

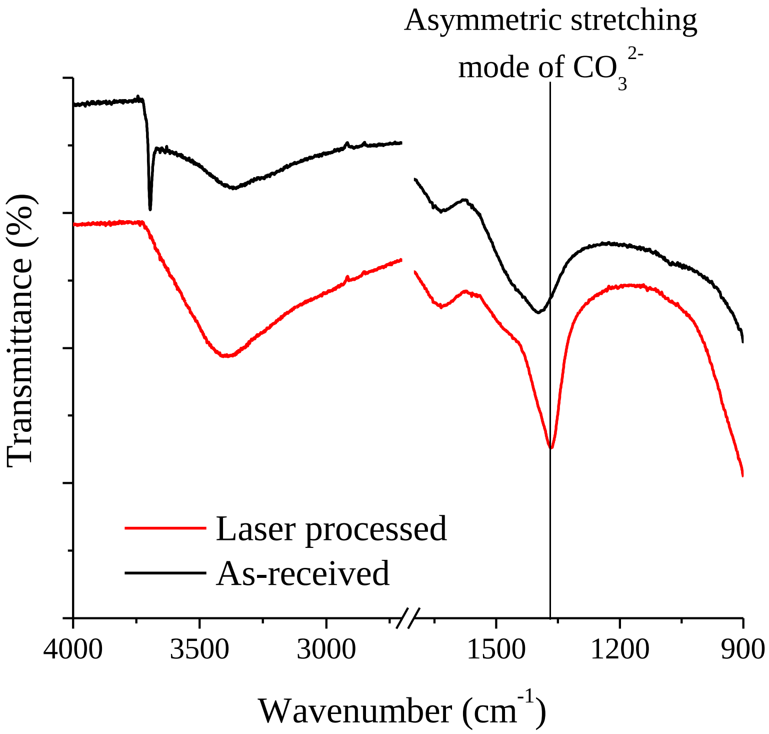

Figure 3.19: ATR-FTIR measurements of as-received and laser processed AM60B corrosion product after a 24 hour full immersion in stagnant 0.6 M NaCl solution.

Table 3.2: Corrosion products formed on Mg alloys after 24 hour immersion in stagnant 0.6 M NaCl solution. Determined by GI-XRD and ATR-FTIR.

	As-received	**Laser processed**
AZ31B-H24	LDH + $Mg(OH)_2$	LDH
AM60B	LDH + $Mg(OH)_2$	LDH
AZ91D	LDH + $Mg(OH)_2$	LDH

An increase in the Al content for both cast alloys in comparison to AZ31B-H24 suggests the precipitation of the LDH phase will be more probable since all other corrosion conditions remained the same. The concentration of Al has been observed as a controlling factor for the precipitation of the LDH phases, in particular hydrotalcite [52]. The incorporation of the Al cation into the Mg hydroxide structure is what causes the charge imbalance and allows for the anions to intercalate in between the hydroxide layers [40].

The formation of the LDH is observed by ATR-FTIR analysis for the AM60B alloy shown in **Figure 3.19** after immersion in stagnant 0.6 M NaCl for 24 hours. XRD of the cast specimen was also performed to verify the existence of the LDH phase, not shown here, revealing peaks at $2\theta = 11^o$ and 22.5^o for the AM60B and AZ91D specimens. From these analyses, the as-received AM60B and AZ91D alloys observed a similar response to the as-received AZ31B-H24 specimens, showing the LDH and $Mg(OH)_2$ while the laser processed specimen observed solely the LDH phase. A summary of the corrosion products found for all alloys is in **Table 3.2**. Interestingly, the FTIR spectra for the AM60B alloy led to a shift in one of the LDH carbonate peaks, labelled in **Figure 3.19** as an asymmetric stretching mode for CO_3^{2-}, which has been attributed with the inclusion of Al cations into the LDH structure and the stabilization of the intercalated carbonate anions [52]. This FTIR peak shift was also observed for the AZ91D alloy, not shown here. That said, the LDH was similarly observed to cover a majority of the as-received and laser processed surface meaning the increase in time to FFC initiation is still controlled by the reduction in micro-galvanic corrosion sites on the laser processed surface.

Secondary electron micrographs are shown in **Figure 3.20** of the AZ91D surface after 3 hours immersion in stagnant 0.6 M NaCl solution, revealing a similar corrosion product coverage of all secondary phases for the as-received material in **a** and **b**. These results coincide with the work performed on AZ31B in the previous section, showing the LDH corrosion product formed on all surfaces of the corroding alloy, regardless if it was homogenized or not.

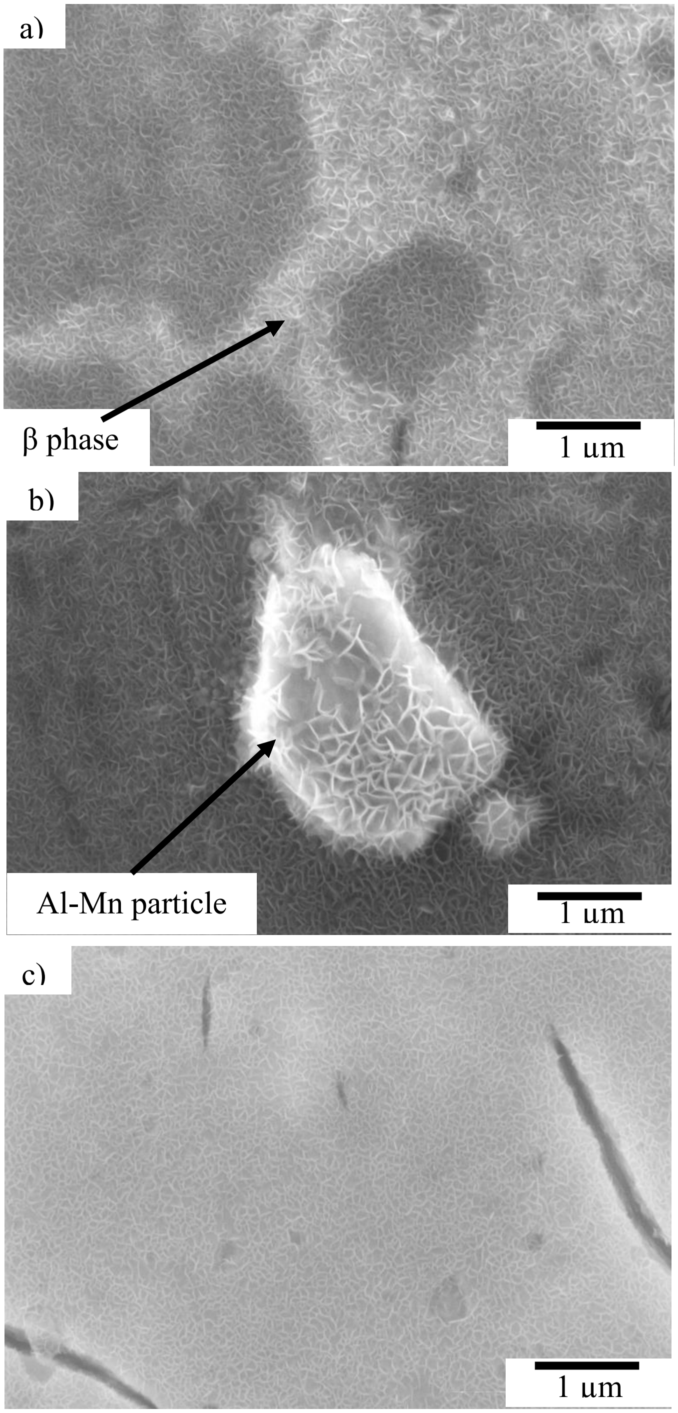

Figure 3.20: Secondary electron micrographs of the general corrosion product on AZ91D, formed on areas not yet affected by filiform-like corrosion after 3 hour immersion in stagnant 0.6 M NaCl solution, for the as-received a) and b), and laser processed c) conditions. The as-received specimen shows the corrosion product forms with a similar morphology on secondary phase particles.

Time dependent measurements from EIS validate the improvement observed by time lapse microscopy, OCP, and cathodic polarization measurements of the laser processed AM60B and AZ91D alloys. The

Nyquist plots exhibited an increased resistance to current flow for all laser processed samples during the 72 hour immersion in stagnant 0.6 M NaCl solution as shown in **Figure 3.21**. After one hour of immersion both as-cast alloys exhibited an inductive loop which coincides with the initiation of FFC which persisted for the entire 72 hour experiment. In addition to the higher magnitude of impedance values for the laser processed specimen, minimal inductance behavior was observed.

A plot summarizing the global polarization resistance (R_p) is shown in **Figure 3.22**, revealing the R_p fluctuations with time. Determination of the EIS-estimated R_p was carried out in the same manner as for the AZ31B-H24 investigation. At all immersion times, the laser processed specimens exhibited, on average, a 6 fold improvement in global R_p over the as-received specimens. The as-received specimens global R_p values showed little variation with time both ranging from 1,800 to 4,000 Ω-cm^2 while the laser processed samples ranged in R_p from 16,000 to 51,000 Ω-cm^2 for AZ91D and 8,900 to 23,000 Ω-cm^2 for AM60B. The error bars on the R_p plot stem from the variability of the laser processed specimens time for surface breakdown. The laser processed AZ91D time lapse images support the variability of the EIS experiments, exhibiting breakdown after 24 hours, whereas multiple EIS 72 hour immersion experiments showed no sign of surface breakdown. Furthermore, the Nyquist plots for laser processed samples display minimal inductive behavior, similar to laser processed AZ31B-H24, supporting the improvement due to reduced micro-galvanic couples [21].

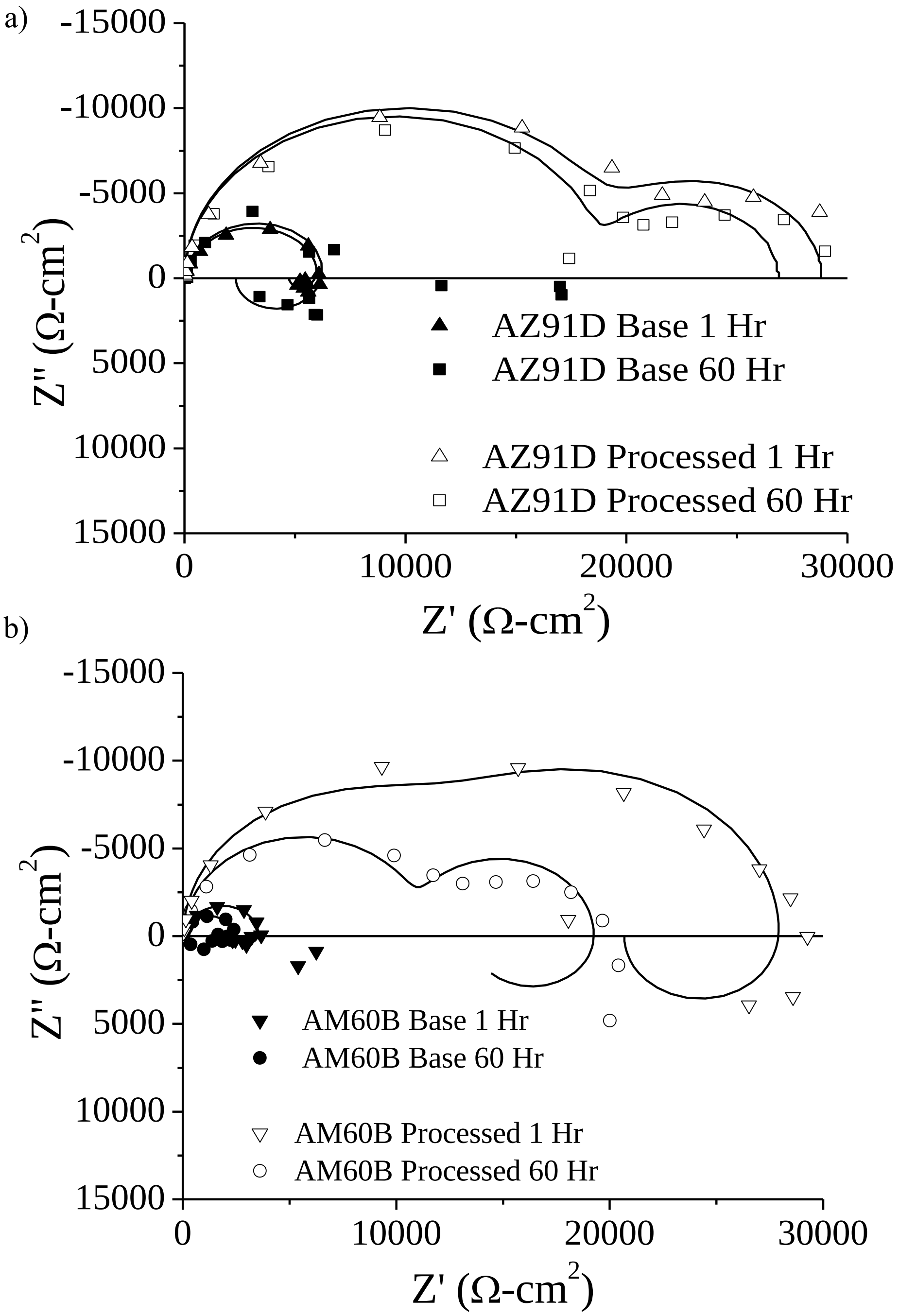

Figure 3.21: A representative Nyquist plot for the as-received and laser processed AZ91D (a) and AM60B (b) material after 1 and 60 hours of full immersion in stagnant 0.6 M NaCl at the materials OCP.

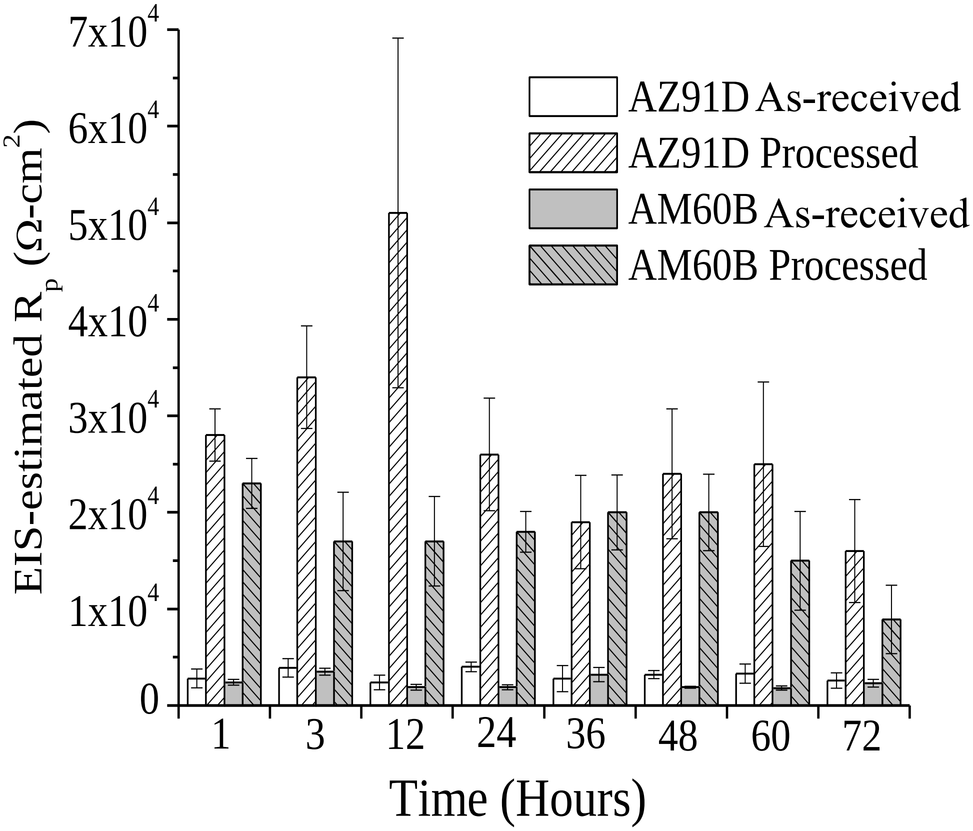

Figure 3.22: Average EIS-estimated R_p after 1, 3, 12, 24, 36, 48, 60, and 72 hours of full immersion in stagnant 0.6 M NaCl at OCP for the AZ91D and AM60B as-received and laser processed materials. ± represents one standard error.

3.5 Conclusions for corrosion analysis of laser processed Mg alloys

The chemically homogeneous microstructures produced by laser processing of the Mg alloys led to a more uniform corrosion and which suppressed the initiation of FFC and dramatically lowered the corrosion rate. A reduction in cathodic kinetics led to an increase in global R_p of laser processed AZ31B-H24, AZ91D, and AM60B alloys, primarily attributed to the reduced area of effective cathodic sites, the secondary phase particles β-$Mg_{17}Al_{12}$ and the Al-Mn particles, as shown in **Chapter 2**. In addition, the presence of a LDH phase was observed on all specimen, as-received and laser processed, and can be used as an indicator of resistance to localized corrosion since the observation of $Mg(OH)_2$ on a surface was typically associated with a substantial surface coverage of FFC. The common occurrence of the LDH phases should also be considered as a prominent corrosion product for all Al containing Mg alloys when immersed in aqueous solutions as it was observed as the primary corrosion product on the general filmed region, not where intense local corrosion had occurred (like FFC).

The time to the initiation of FFC for all laser processed alloys was extended in comparison to their as-received material, from 10 minutes for AZ31B-H24 to 18 hours for the laser processed specimen, while the cast alloys FFC initiation time increased from 1 hour to 24 hours for AZ91D and ~60 hours for AM60B. Partial dissolution of the cathodic phases is sufficient to suppress rapid corrosion caused by micro-galvanic couples hence limiting the inductive behavior observed for laser processed specimen. The absence of the inductive behavior is indicative of reduced corrosion kinetics.

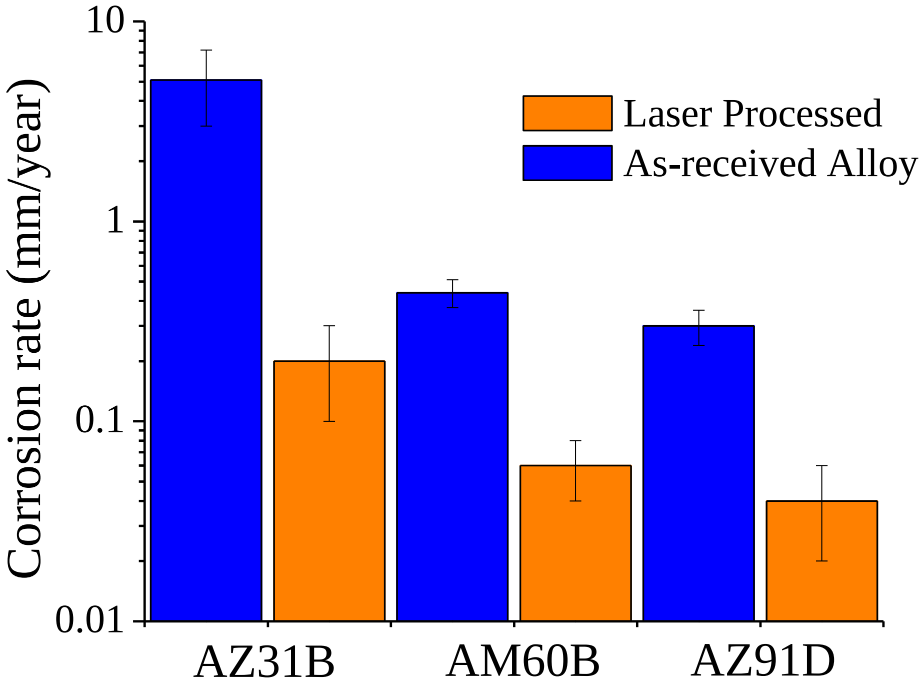

Figure 3.23: Calculation of corrosion rate, in mm per year, for all specimens investigated in **Chapter 3**. Corrosion rate was determined by conversion of the EIS-estimated R_p values using Faraday's law.

From the corrosion investigations an estimation of yearly corrosion rate for all specimens can be made utilizing the EIS-estimated global R_p values and assuming uniform corrosion. **Figure 3.23** displays the expected corrosion rate for specimen under full immersion conditions in the stagnant 0.6 M NaCl solution. In all cases, the laser processed specimens observe an 8 fold or more reduction in corrosion rate (mm per year) in comparison to their as-received counterpart.

3.6 References

---

[1] M.A. Melia, D.C. Florian, F.W. Steuer, B.F. Briglia, M.K. Purzycki, J.R. Scully, J.M. Fitz-Gerald, Investigation of critical processing parameters for laser surface processing of AZ31B-H24, Surface and Coatings Technology, 325 (2017) 157-165.

[2] M. Melia, P. Steiner, N. Birbilis, J. Fitz-Gerald, J. Scully, Excimer Laser Surface Modification of AZ31B-H24 for Improved Corrosion Resistance, Corrosion, (2015).

[3] M.A. Melia, M.L. Serron, D.C. Florian, J.P. Weiler, J.R. Scully, J.M. Fitz-Gerald, Excimer Laser Processing of Cast Mg-Al-Zn (AZ91D) and Mg-Al (AM60B) Alloys for Improved Corrosion Resistance, Corrosion, 72 (2016) 1580-1586.

[4] K. Schlüter, J. Reverey, N. Hort, C. Zamponi, E. Quandt, Mechanical Behaviour and Corrosion Performance of Thin Film Magnesium WE Alloys, Materials Science Forum, 690 (2011) 286-289.

[5] K. Schluter, C. Zamponi, J. Hapke, N. Hort, K.U. Kainer, E. Quandt, Mechanical properties and corrosion behaviour of freestanding precipitate-free magnesium WE43 thin films, Int. J. Mater. Res., 104 (2013) 286-292.

[6] K. Schlüter, C. Zamponi, A. Piorra, E. Quandt, Comparison of the corrosion behaviour of bulk and thin film magnesium alloys, Corrosion Science, 52 (2010) 3973-3977.

[7] F. Hehmann, F. Sommer, H. Jones, R.G.J. Edyvean, Corrosion inhibition in magnesium-aluminium-based alloys induced by rapid solidification processing, Journal of Materials Science, 24 (1989) 2369-2379.

[8] C.B. Baliga, P. Tsakiropoulos, The structure and morphology of the corrosion products formed on the surfaces of a rapidly solidified Mg-3.5Al alloy, Materials Science and Engineering, A134 (1991) 1029-1032.

[9] C.B. Baliga, P. Tsakiropoulos, Development of corrosion resistant magnesium alloys Part 2 Structure of corrosion products on rapidly solidified Mg-16Al alloys, Materials Science and Technology, 9 (1993) 513-519.

[10] A.E. Coy, F. Viejo, F.J. Garcia-Garcia, Z. Liu, P. Skeldon, G.E. Thompson, Effect of excimer laser surface melting on the microstructure and corrosion performance of the die cast AZ91D magnesium alloy, Corrosion Science, 52 (2010) 387-397.

[11] J.G. Hoekstra, S.B. Qadri, J.R. Scully, J.M. Fitz-Gerald, Laser Surface Modification of a Crystalline Al-Co-Ce Alloy for Enhanced Corrosion Resistance, Advanced Engineering Materials, 7 (2005) 805-809.

[12] D.S. Qian, Z. Liu, Comparative Study of Microstructural and Corrosion Characteristics of Excimer Laser-Melted AA2124-T4 and AA6061-T4 Alloys, Materials Science Forum, 794-796 (2014) 235-240.

[13] I. Nakatsugawa, R. Martin, E.J. Knystautas, Improving Corrosion Resistance of AZ91D Magnesium Alloy by Nitrogen Ion Implantation, Corrosion, 52 (1996) 921-926.

[14] Z. Xie, Z. Luo, Q. Yang, T. Chen, S. Tan, Y. Wang, Y. Luo, Improving anti-wear and anti-corrosion properties of AM60 magnesium alloy by ion implantation and Al/AlN/CrAlN/CrN/MoS_2 gradient duplex coating, Vacuum, 101 (2014) 171-176.

[15] M.S. Uddin, C. Hall, P. Murphy, Surface treatments for controlling corrosion rate of biodegradable Mg and Mg-based alloy implants, Science and Technology of Advanced Materials, 16 (2016) 053501.

[16] X.B. Chen, N. Birbilis, T.B. Abbott, Review of Corrosion-Resistant Conversion Coatings for Magnesium and Its Alloys, Corrosion, 67 (2011) 035005-035001 - 035005-035016.

[17] L.F. Guo, T.M. Yue, H.C. Man, Excimer laser surface treatment of magnesium alloy WE43 for corrosion resistance improvement, Journal of Materials Science, 40 (2005) 3531-3533.

[18] W. Khalfaoui, E. Valerio, J.E. Masse, M. Autric, Excimer laser treatment of ZE41 magnesium alloy for corrosion resistance and microhardness improvement, Optics and Lasers in Engineering, 48 (2010) 926-931.

[19] A. Singh, S.P. Harimkar, Laser Surface Engineering of Magnesium Alloys: A Review, Jom, 64 (2012) 716-733.

[20] A. Koutsomichalis, L. Saettas, H. Badekas, Laser treatment of magnesium, Journal of Materials Science, 29 (1994) 6543-6547.

[21] D. Schippman, A. Weisheit, B.L. Mordike, Short Pulse Irradiation of Magnesium Based Alloys to Improve Surface Properties, Surface Engineering, 15 (1999) 23-26.

[22] G. Williams, N. Birbilis, H.N. McMurray, Controlling factors in localised corrosion morphologies observed for magnesium immersed in chloride containing electrolyte, Faraday Discussion, 180 (2015) 313-330.

[23] G. Williams, H. ap Llwyd Dafydd, R. Grace, The localised corrosion of Mg alloy AZ31 in chloride containing electrolyte studied by a scanning vibrating electrode technique, Electrochimica Acta, 109 (2013) 489-501.

[24] M.A. Melia, T.W. Cain, B.F. Briglia, J.R. Scully, J.M. Fitz-Gerald, Evolution of the Corrosion Morphology on AZ31B Tracked Electrochemically and by In Situ Microscopy in Chloride-Containing Media, Jom, 69 (2017) 2322-2327.

---

[25] A.D. King, N. Birbilis, J.R. Scully, Accurate Electrochemical Measurement of Magnesium Corrosion Rates; a Combined Impedance, Mass-Loss and Hydrogen Collection Study, Electrochimica Acta, 121 (2014) 394-406.

[26] L.G. Bland, A.D. King, N. Birbilis, J.R. Scully, Assessing the Corrosion of Commercially Pure Magnesium and Commercial AZ31B by Electrochemical Impedance, Mass-Loss, Hydrogen Collection, and Inductively Coupled Plasma Optical Emission Spectrometry Solution Analysis, Corrosion, 71 (2015) 128-145.

[27] M. Curioni, F. Scenini, T. Monetta, F. Bellucci, Correlation between electrochemical impedance measurements and corrosion rate of magnesium investigated by real-time hydrogen measurement and optical imaging, Electrochimica Acta, 166 (2015) 372-384.

[28] E. Barsoukov, J.R. Macdonald, Impedance Spectroscopy: Theory, Experiment, and Applications, Wiley, 2005.

[29] M.E. Orazem, B. Tribollet, Electrochemical Impedance Spectroscopy, Wiley, 2017.

[30] A.S. G1, Standard Practice for Preparing, Cleaning, and Evaluating Corrosion Test Specimens, ASTM International, West Conshohocken, PA, 2011.

[31] R. Baboian, "Electrochemical Techniques for Predicting Galvanic Corrosion," ASTM STP 576 (1976): p. 5-19.

[32] ASTM-81, "Standard Guide for Conducting and Evaluating Galvanic Corrosion Tests in Electrolytes," ASTM International G71, (2014).

[33] M.P. Brady, G. Rother, L.M. Anovitz, K.C. Littrell, K.A. Unocic, H.H. Elsentriecy, G.L. Song, J.K. Thomson, N.C. Gallego, B. Davis, Film Breakdown and Nano-Porous Mg(OH)2 Formation from Corrosion of Magnesium Alloys in Salt Solutions, Journal of The Electrochemical Society, 162 (2015) C140-C149.

[34] K.A. Unocic, H.H. Elsentriecy, M.P. Brady, H.M. Meyer, G.L. Song, M. Fayek, R.A. Meisner, B. Davis, Transmission Electron Microscopy Study of Aqueous Film Formation and Evolution on Magnesium Alloys, Journal of The Electrochemical Society, 161 (2014) C302-C311.

[35] J.H. Nordlien, K. Nisancioglu, S. Ono, N. Masuko, Morphology and Structure of Water-Formed Oxides on Ternary MgAl Alloys, Journal of Electrochemical Society, 144 (1997) 461-466.

[36] M. Esmaily, J.E. Svensson, L.G. Johansson, Corrosion of Magnesium-Aluminum (Mg-Al) Alloys - An Interplay Between Al Content and CO_2, in: K. Solanki, D. Orlov, A.N. Singh, N.R. (Eds.) TMS 2017, Springer, San Diego, CA, 2017, pp. 397-403.

[37] M. Esmaily, D.B. Blücher, J.E. Svensson, M. Halvarsson, L.G. Johansson, New insights into the corrosion of magnesium alloys — The role of aluminum, Scripta Materialia, 115 (2016) 91-95.

[38] S. Mathieu, C. Rapin, J. Steinmetz, P. Steinmetz, A corrosion study of the main constituent phases of AZ91 magnesium alloys, Corrosion Science, 45 (2003) 2741-2755.

[39] R.C. Phillips, J.R. Kish, Nature of Surface Film on Matrix Phase of Mg Alloy AZ80 Formed in Water, Corrosion, 69 (2013) 813-820.

[40] V. Rives, Layered Double Hydroxides: Present and Future, Nova Science Publishers, 2001.

[41] R. Salomão, L.M. Milena, M.H. Wakamatsu, V.C. Pandolfelli, Hydrotalcite synthesis via co-precipitation reactions using MgO and Al(OH)3 precursors, Ceramics International, 37 (2011) 3063-3070.

[42] J. Lin, C. Hsia, J. Uan, Characterization of Mg,Al-hydrotalcite conversion film on Mg alloy and Cl^{-} and CO_3^{2-} anion-exchangeability of the film in a corrosive environment, Scripta Materialia, 56 (2007) 927-930.

[43] J.W. Boclair, P.S. Braterman, Layered Double Hydroxide Stability. 1. Relative Stabilities of Layered Double Hydroxides and Their Simple Counterparts, Chem. Mater., 11 (1999) 298-302.

[44] H. Tamura, J. Chiba, M. Ito, T. Takeda, S. Kikkawa, Y. Mawatari, M. Tabata, Formation of hydrotalcite in aqueous solutions and intercalation of ATP by anion exchange, Journal of Colloid and Interface Science, 300 (2006) 648-654.

[45] R.P. Bontchev, S. Liu, J.L. Krumhansl, J. Voigt, T.M. Nenoff, Synthesis, Characterization, and Ion Exchange Properties of Hydrotalcite $Mg_6Al_2(OH)_{16}(A)_x(A')_{2-x}4H_2O$ (A, A') Cl^-, Br^-, I^-, and NO_3^-, 2 x 0) Derivatives, Chem. Mater., 15 (2003) 3669-3675.

[46] J. Chen, Y. Song, D. Shan, E.-H. Han, In situ growth of Mg–Al hydrotalcite conversion film on AZ31 magnesium alloy, Corrosion Science, 53 (2011) 3281-3288.

[47] J. Chen, Y. Song, D. Shan, E.-H. Han, Study of the in situ growth mechanism of Mg–Al hydrotalcite conversion film on AZ31 magnesium alloy, Corrosion Science, 63 (2012) 148-158.

[48] J. Chen, Y. Song, D. Shan, E.-H. Han, Study of the corrosion mechanism of the in situ grown Mg–Al–CO_3^{2-} hydrotalcite film on AZ31 alloy, Corrosion Science, 65 (2012) 268-277.

[49] J.K. Lin, J.Y. Uan, Formation of Mg,Al-hydrotalcite conversion coating on Mg alloy in aqueous HCO_3^{-}/CO_3^{2-} and corresponding protection against corrosion by the coating, Corrosion Science, 51 (2009) 1181-1188.

[50] Z.P. Xu, G.Q. Lu, Hydrothermal Synthesis of Layered Double Hydroxides (LDHs) from Mixed MgO and Al2O3: LDH Formation Mechanism, Chem. Mater., 17 (2005) 1055-1062.

---

[51] L.G. Bland, N. Birbilis, J.R. Scully, Exploring the Effects of Intermetallic Particle Size and Spacing on the Corrosion of Mg-Al Alloys Using Model Electrodes, Journal of The Electrochemical Society, 163 (2016) C895-C906.

[52] J.-K. Lin, K.-L. Jeng, J.-Y. Uan, Crystallization of a chemical conversion layer that forms on AZ91D magnesium alloy in carbonic acid, Corrosion Science, 53 (2011) 3832-3839.

[53] M. Jönsson, D. Persson, D. Thierry, Corrosion product formation during NaCl induced atmospheric corrosion of magnesium alloy AZ91D, Corrosion Science, 49 (2007) 1540-1558.

[54] W. Stumm, J.J. Morgan, Aquatic Chemistry: Chemical Equilibria and Rates in Natural Waters, Wiley, 2012.

[55] S.D. Cramer, A.I.H. Committee, B.S. Covino, ASM Handbook, ASM International, 2005.

Page intentionally left blank.

Chapter 4: Development of a mixed hydroxide coating for laser processed Mg alloys

4.1 Background on conversion coatings and deposited coatings for Mg alloys

A typical coating scheme applied to Mg alloys as an initial deterrent against local corrosion initiation is known as conversion coatings (CCs) [1,2,3,4]. The application of these CCs involve a series of steps to convert the Mg alloy surface into a corrosion product which is more resistant to corrosion attack than the typical Mg alloy corrosion products (such as $Mg(OH)_2$) [1,3,5,6,7,8,9,10,11,12,13,14]. A consequence of the CC process is the requirement for the corrosion of the alloy in order to produce to precipitate a more stable corrosion product [4]. This process of CCs has been successful in improving the corrosion resistance of many Mg alloys, as well as being a major source for corrosion protection on Al and other alloy systems. The industrial standard for this realm of coatings is the hexavalent chromate CC, offering significant barrier protection, fast application, and the ability to heal a scratched portion of the coating [15,16]. That said, chromate coatings are being replaced by more environmentally friendly options as hexavalent chromium is considered a carcinogenic material and detrimental to the environment [3]. Other corrosion protection schemes used for Mg alloys are anodizing and plasma electrolytic oxidation (PEO) treatments which apply a current to the Mg substrate and actively oxidize the surface of the alloy, creating a thick (up to 38 μm), often porous oxide or phosphate coating [4,17,18,19,20]. The thicker anodized and PEO coatings have been shown to also improve wear resistance [4].

An issue regarding the application of a CC scheme to a laser processed Mg alloy stems from the necessary corrosion of the substrate to precipitate the stable corrosion product. The laser processed layer was observed to be at most 8 μm thick, with many of the CCs observing metal removal above that, even with short deposition times [4]. In order to preserve the laser processed layer, coatings applied through physical vapor deposition (PVD) techniques were investigated for their ability to add material to the surface without the metal removal required for CCs [1,21].

The investigation of PVD coatings on Mg alloys has met mixed success with regards to improving corrosion resistance via the application of oxide and metallic coatings [22,23,24,25,26,27,28,29, 30,31,32]. Utilization of metallic coatings has been shown to improve the corrosion resistance of the Mg alloy surface so long as the coating is not compromised to expose the underlying alloy [26,29,30]. If exposed, the electrochemically negative Mg alloy will galvanically couple to the metallic coating since a majority of the metals deposited are electrochemically noble (Al, Mn, Hf, etc.) with respect to the underlying Mg alloy [30,33]. This would lead to the detrimental case of a large cathode (coating) and a small anode (exposed Mg alloy). In addition, when amphoteric metals are deposited, like Al, the increase in pH from the corrosion of the underlying Mg would in turn promote the self-corrosion of Al coating itself.

The application of oxide and nitride coatings have been found to function as barrier coatings, preventing the initiation of localized corrosion for an extended period of time utilizing Al_2O_3, TiO_2, and TiN films [1,21,22,28,34]. However, one potential issue with these coatings was active protection after a scratch or defect was created in the film exposing the heterogeneous microstructure of the underlying Mg alloy, leading to rapid initiation of local corrosion. The AlN and TiN coatings produced by Altun et al. contained pinhole defects in the PVD coatings which led to the initiation of corrosion at these sites. Defects expanded at longer immersion times with eventual removal of the coating by flaking [21,22]. Research by Wu et al. also attributed the initiation of severe localized corrosion to the through-thickness defects often observed to be pinholes [26,27,28]. Similar defects are credited with causing local breakdown of the underlying Mg alloys in the case of other PVD coatings [35,36,37].

In addition, a major downfall of the electrochemical analysis for these coated Mg alloys was often the lack of long term exposures with most studies taking an E-log(i) measurement followed by SEM analysis after ~1 hour of immersion in a NaCl solution. This provided minimal information regarding how the underlying heterogeneous microstructure impacts the coatings breakdown. Additionally, there were a surprising number of studies without pretreatments to the surface, prior to the PVD coating. Pretreatment procedures are typical of CCs, utilized to chemically homogenize the surface and enhance adhesion of the coatings [38,39]. Some research has been performed on ion implantation pretreatments for PVD coatings showing better coating adhesion, however a study observing how chemical homogenization of the Mg alloy has not been performed [40,41,42,43].

This chapter will explore the use of an oxide/hydroxide coating produced by pulsed laser deposition (PLD) as an effective barrier to the initiation of localized corrosion on AZ31B-H24. These coatings were investigated to further improve the corrosion resistance afforded by the chemical homogenization of laser processing, specifically regarding the time to initiation of localized corrosion.

4.2 Experimental procedure for coatings and corrosion measurements

The Mg alloy utilized for this investigation was AZ31B-H24 in the as-received and laser processed (LP) condition. Prior to deposition, the as-received specimens were polished to a 1200 grit finish and the LP specimen were treated with the optimal laser processing parameters as shown in **Table 2.2** (200 PPA).

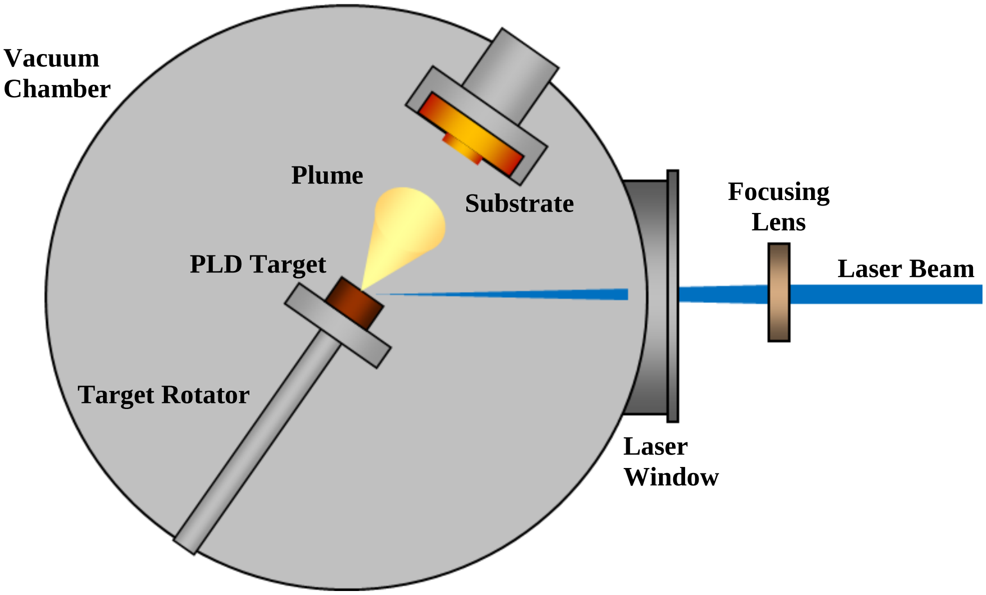

Figure 4.1: Schematic of the PLD vacuum chamber with the target (pure Mg or Gd) and substrate (as-received/laser processed AZ31B-H24 or Si wafer).

Pulsed laser deposition (PLD) was performed in a high vacuum chamber utilizing the same KrF excimer laser used for laser processing. A schematic of the target (Mg, Gd), substrate, and vacuum chamber is shown in **Figure 4.1**. The vacuum chamber was flushed two times with He gas (99.9% purity) and achieved an average ultimate pressure of 1.0 x 10^{-5} Torr. The chamber was back filled with the He gas to an average pressure of 1.4 x 10^{-1} Torr. The deposition of the pure Mg and pure Gd targets were performed at a laser fluence of 2.0 J/cm^2, at a pulse frequency of 10 Hz, at room temperature, and a deposition time of 15 minutes. A schematic of a laser processed and coated (LPC) AZ31B-H24 specimen is shown in **Figure 4.2**, revealing the multilayered coating. The majority of the characterization was performed on coated as-received specimens and LPC specimens. For simplicity, a sample denoted as "coated" will mean it has the Mg and Gd coatings on it, experiments with a single coating will be stated.

To simplify characterization, the Mg substrates were replaced with Si wafers in order to determine the thickness of the coatings as well as for phase analysis, performed by grazing incident x-ray diffraction (GI-XRD). The thickness and surface morphology of the individual Mg and Gd coatings were determined by scanning electron microscopy (SEM), utilizing the secondary and backscattered electron (BSE) detectors. Phase analysis was performed by GI-XRD utilizing a PANalytical X'Pert Pro MPD diffractometer with a Cu-K_α (λ=1.54 Å) source at a 0.5° incident angle (x-ray penetration depth of pure Mg is 2.5 μm).

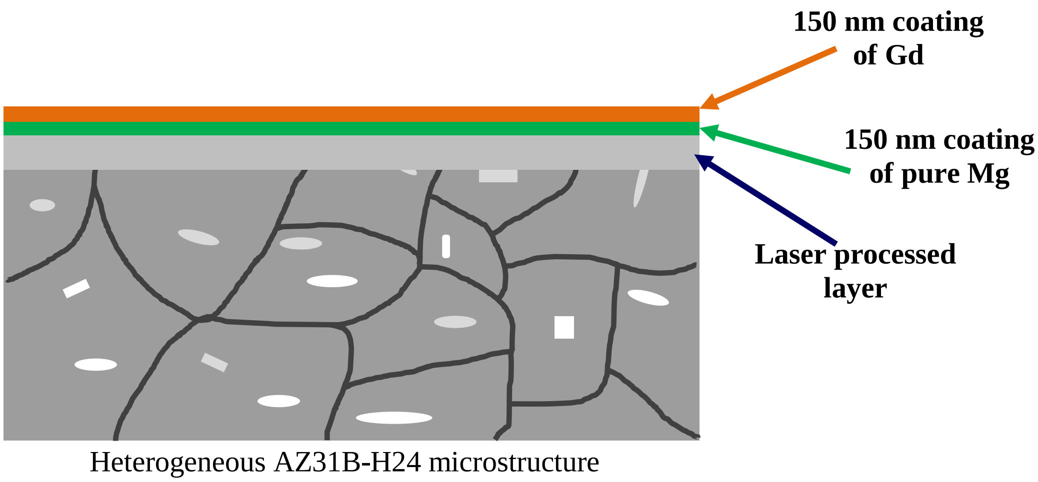

Figure 4.2: Schematic of a cross-section showing the layout of the LPC layer with the Mg and Gd coating configuration.

Similar corrosion characterization was performed as observed in **Chapter 3** under full immersion conditions with a stagnant 0.6 M NaCl solution at a starting pH between 5.5 and 6.2. A standard three-electrode corrosion cell was also utilized with the coated Mg alloy surface as the working electrode, a saturated calomel electrode (SCE) as the reference electrode, and a platinum mesh counter electrode. The corrosion of the coated specimens was initially observed with time lapse optical videos accompanied by open circuit potential (OCP) measurements. In addition, time dependent electrochemical impedance spectroscopy (EIS) was also utilized to observe the change in polarization resistance (R_p) with time using the equivalent circuit from **Figure 3.1 b**. Experiments on a separate set of specimens utilized the cathodic polarization measurements from **Chapter 2**, taken after a 30 minute OCP measurement, in order to compare coated versus uncoated. After the OCP measurement, a cathodic polarization measurement was taken which began by applying a voltage 20 mV more positive than the working electrodes OCP and scanning at 1 mV/sec to -2.3 V vs. SCE. Also, corrosion analysis of a scratched laser processed and coated specimen was performed, similar to the scratch experiments performed in **Chapter 3**, with time-lapse imaging and OCP measurements. All electrochemical measurements for the coated specimens were compared to the uncoated specimen results from **Chapters 2** and **3** with the coated results being repeatable with at least 3 replications for a given result.

4.3 Characterization of Mg/Gd coating on the AZ31B-H24 alloy

4.3.1 Individual coating morphology and phase analysis on Si wafers

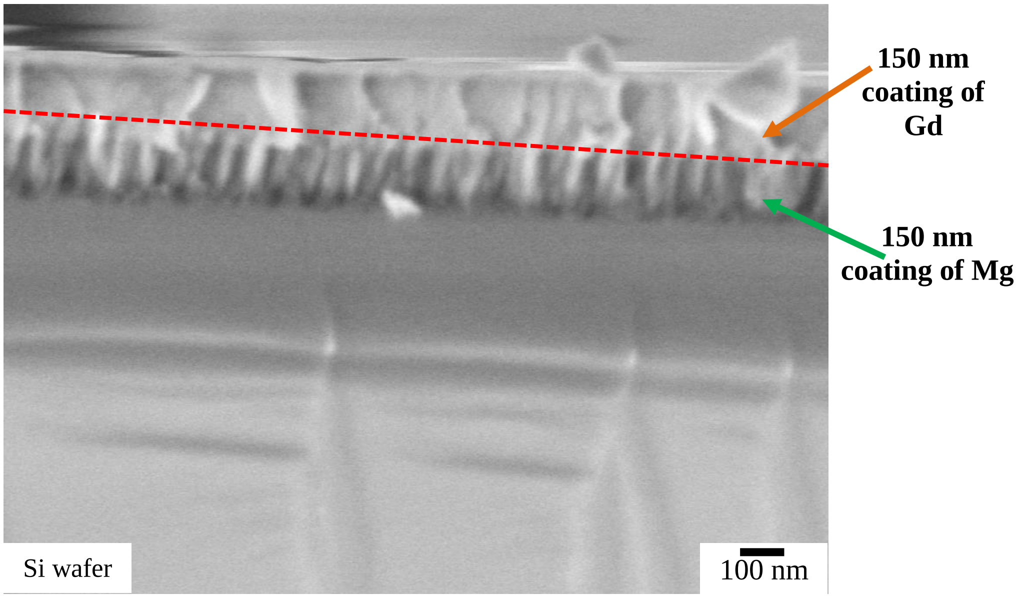

Figure 4.3: Cross-section BSE micrograph of the double layered coating deposited on a Si wafer.

The thickness of the coatings was determined through cross-section analysis of the coated Si wafers by SEM, as shown in **Figure 4.3**, with an image of the Si wafer for reference. Variation in the thickness of the coatings was observed stemming from the variation in density of particles in the ablation plume produced by the laser. In general a dense coating of Mg and Gd were observed to be ~150 nm. The surface morphology of each coating is shown in **Figure 4.4** revealing the coatings to be composed of ~20 nm diameter particles.

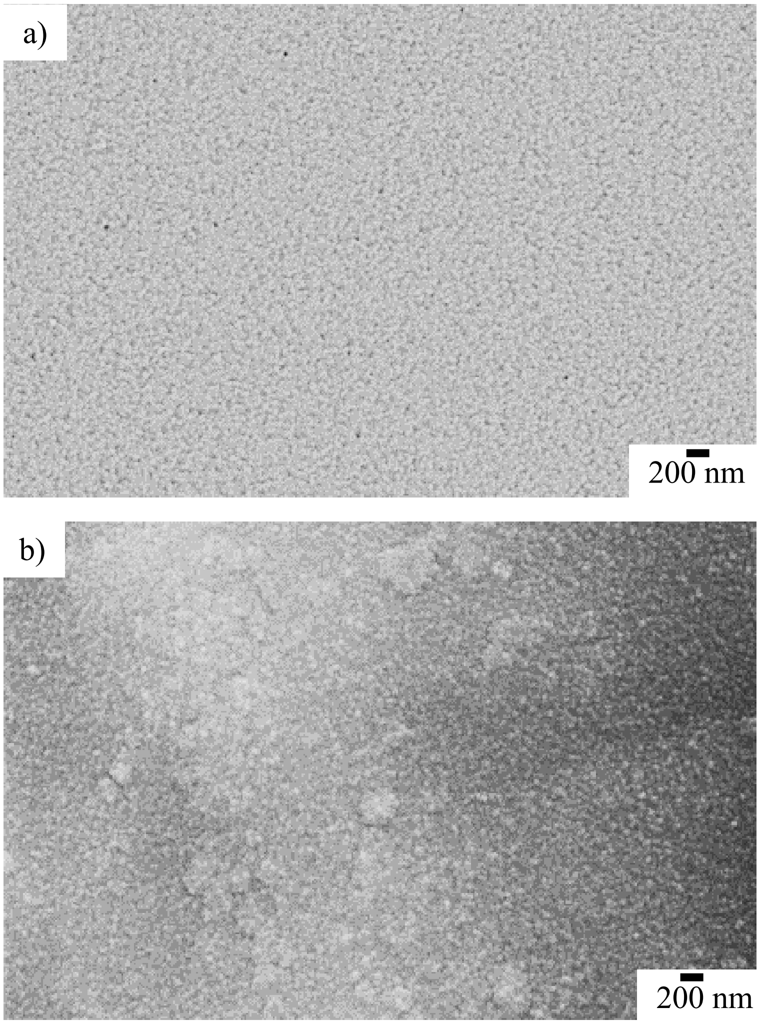

Figure 4.4: BSE micrograph of the **a)** Gd film and a secondary electron micrograph of the **b)** Mg film.

Phase analysis performed by GI-XRD of the individual coatings may be observed in **Figure 4.5**, analyzed using diffraction patterns from **Appendix 1**. The GI-XRD spectra of the Gd coating in **Figure 4.5 a** revealed a single broad peak around $2\theta = 30^o$ which correlated with the location of the primary peaks for the $Gd(OH)_3$ compound. Therefore, the PLD Gd film is suggested to be fully oxidized to the $Gd(OH)_3$ compound with a nanocrystalline grain size. The GI-XRD of the Mg film is shown to be fully oxidized, composed of $Mg(OH)_2$ and MgO in **Figure 4.5 b**. The oxide and hydroxides formed from the deposition of the pure Gd and Mg targets was expected with both elements being sensitive to oxidation when exposed to air. In addition, the vacuum chamber used was often exposed to the atmosphere leading to the adsorption of water on the inside walls of the chamber and can cause the hydroxides to form during deposition. The full oxidized coating will not galvanically couple with the underlying substrate, therefore no galvanic protection is expected.

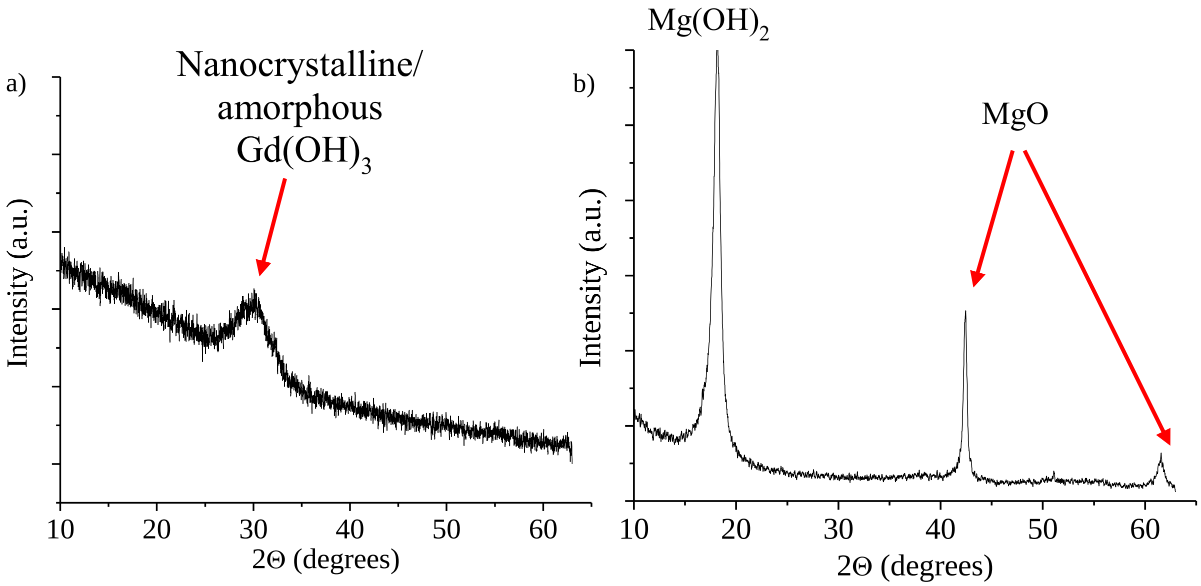

Figure 4.5: GI-XRD patterns for the **a)** Gd film and **b)** Mg film at a 0.5° incident angle.

4.3.2 Full immersion corrosion analysis of coated specimens

The initial corrosion experiments exposed samples to full immersion in a stagnant 0.6 M NaCl solution for 72 hours with optical micrographs taken at the experiments conclusion, as shown in **Figure 4.6**. The polished, as-received, and coated as-received specimens observed a similar surface coverage of black corrosion product, indicative of substantial filiform-like corrosion (FFC) coverage. A lower surface coverage of the black corrosion product was observed in the laser processed (LP) specimens compared to the as-received specimens, as shown in **Figure 4.6 c**. The initiation of FFC occurred on the laser processed and coated (LPC) specimen, in **Figure 4.6 d**, however minimal propagation of the corrosion filaments was observed.

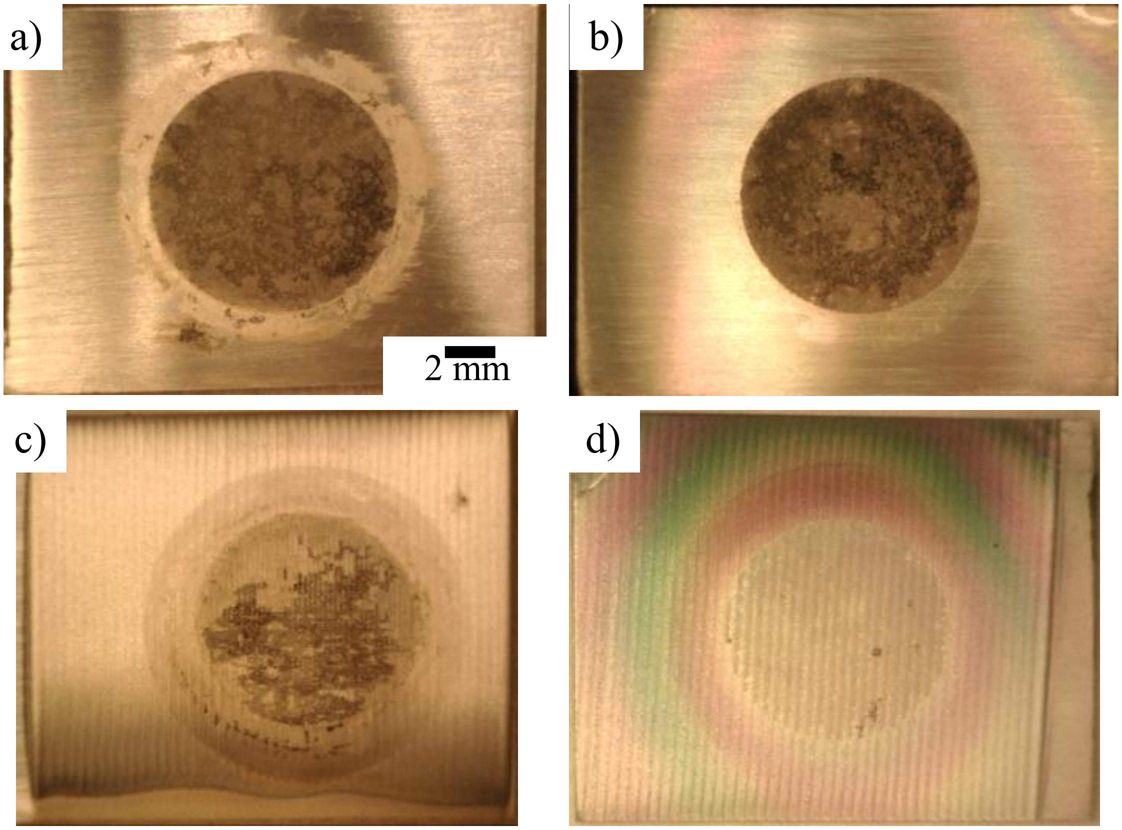

Figure 4.6: Optical micrographs of specimens after a 1 cm^2 area was exposed to stagnant 0.6 M NaCl solution for 72 hours. The **a)** as-received and **b)** coated as-received AZ31B-H24 show complete coverage with FFC in sharp contrast to **c)** LP and **d)** LPC AZ31B-H24 specimens which show minimal FFC coverage.

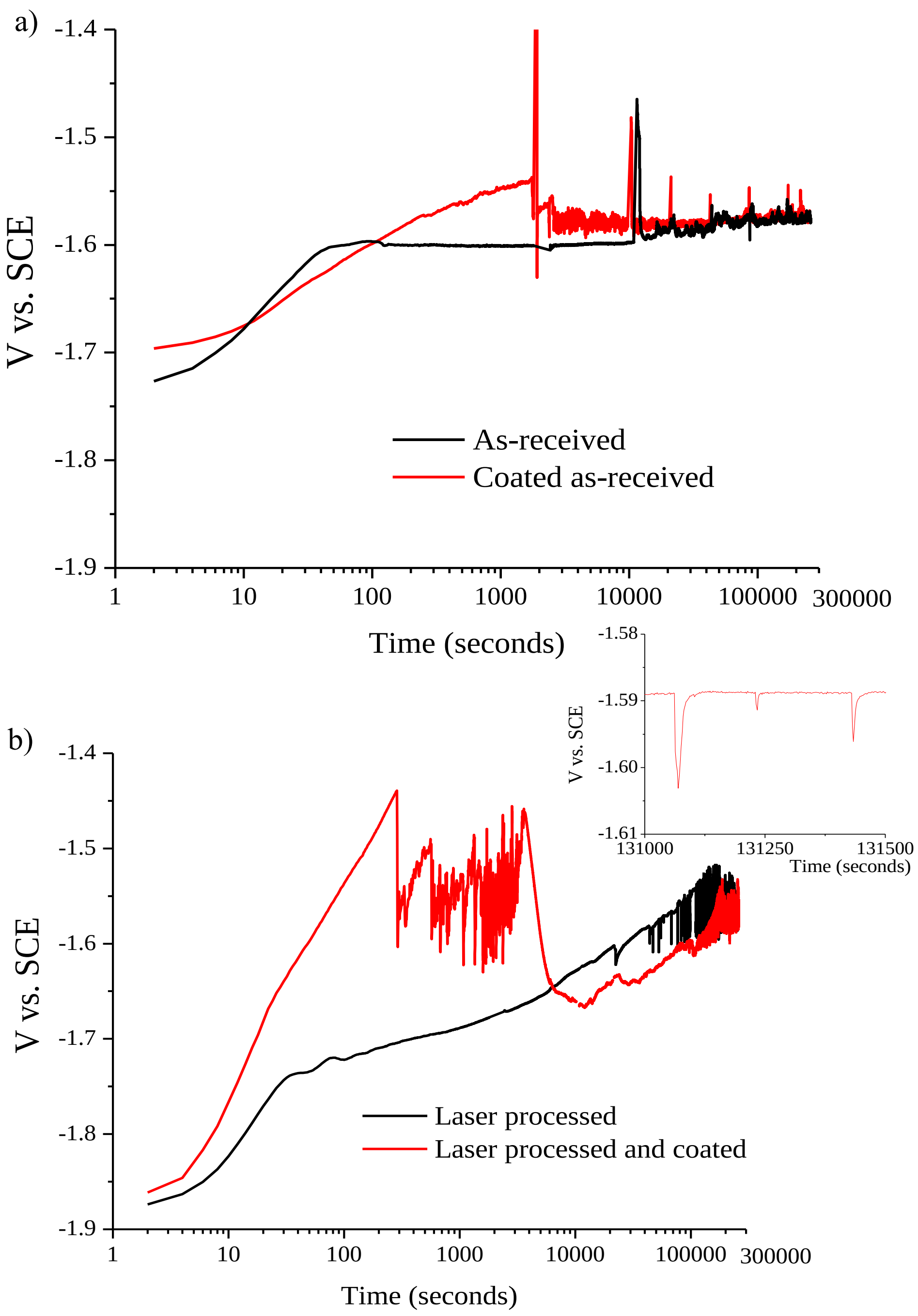

Figure 4.7: OCP measurements versus time of the **a)** as-received AZ31B-H24 substrates and **b)** LP AZ31B-H24 substrates with and without the double layered coating. An inlaid plot in **b)** shows a significant reduction in the OCP and recovery of the OCP for the LPC specimen.

The OCP was measured during the 72 hour immersion experiments, shown in **Figure 4.7**. In **Figure 4.7 a**, the OCP of the as-received specimens are shown to initiate FFC after ~100 seconds for the polished specimen, indicated by a slight reduction and subsequent stabilization of the OCP. The OCP of the coated, as-received specimen showed a steady increase for the first 2,000 seconds followed by large fluctuations in the OCP, corroborated by macroscopic videos to indicate when FFC initiated on the specimen. The stable OCP observed during stage II FFC of the polished as-received specimen did not occur for the coated as-received specimen which exhibited large fluctuations in OCP for the 72 hours experiment.

Figure 4.7 b shows the OCP for the LP specimens with and without the coating where interestingly, the OCP of the LPC specimen increased dramatically and revealed fluctuations in potential of ~100 mV for the first hour of immersion followed by a stabilization and reduction in OCP to ~ -1.7 V vs. SCE. This increase in OCP at the start of experiments involving the LPC specimens did not occur for all similar experiments; most progressed similar to the standalone LP with a gradual increase in OCP for the duration of the experiment. The OCP of the LP specimen was stable and gradually increased with time for the first 24 hours before fluctuating (±30 mV) around a potential of -1.57 V vs. SCE, indicating the initiation of FFC. Prior to the initiation of FFC on these specimens, occurring ~60 hours into the measurement for the LPC specimen, sharp reductions in the OCP followed by the exponential increase in OCP were observed, shown in the inlaid plot in **Figure 4.7 b**. The severe drop and recovery of the OCP is indicative of the local breakdown and re-passivation of a surface film, commonly observed on Al and stainless steel alloys [44,45,46].

The cathodic polarization measurements taken after a 30 minute immersion in stagnant 0.6 M NaCl solution are shown in **Figure 4.8**. These results show the coated specimens reduction in corrosion current density in comparison to their respective starting condition, without the coating. A shift to the left in these polarization measurements signifies a reduction in corrosion rate for the coated specimens. The lowest current densities were observed for the LPC specimens.

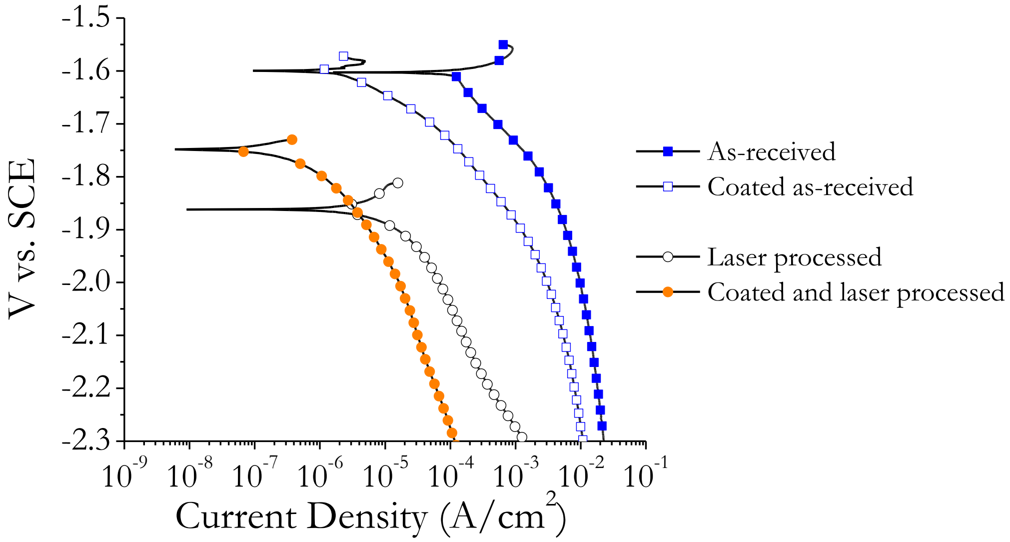

Figure 4.8: Cathodic polarization measurements of the as-received, coated as-received, LP, and LPC AZ31B-H24 specimens after a 30 minute OCP measurement in stagnant 0.6 M NaCl solution.

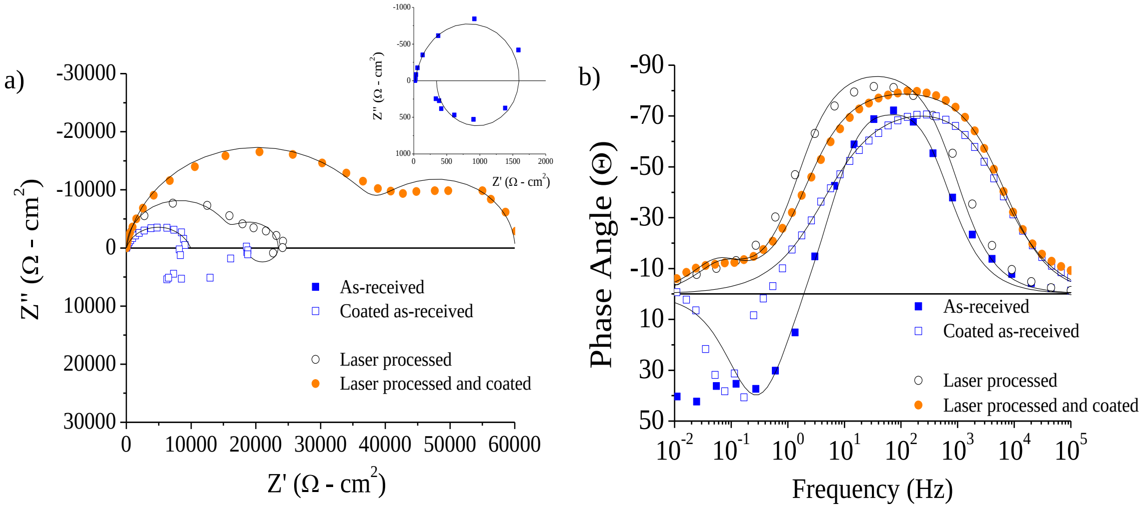

Figure 4.9: The representative EIS measurements presented as **a)** Nyquist and **b)** Bode-Phase plots for all investigated AZ31B-H24 specimens after a 3 hour immersion in stagnant 0.6 M NaCl solution.

The electrochemical impedance spectroscopy (EIS) measurements performed at OCP for all specimens periodically through the 72 hour immersion experiments are presented in **Figure 4.9** and **Figure 4.10**. In **Figure 4.9**, representative spectra are shown, taken after 3 hours of immersion in the stagnant 0.6 M NaCl solution with the symbols representing the raw data and the lines representing the fitted data from the

ZView^{TM} fitting procedure. The Nyquist plots observed in **Figure 4.9 a** reveal the 3 fold increase in impedance values for the LPC specimen in comparison to the LP specimen. In addition, both LP conditions observed two capacitive loops and minimal to no sign of an inductive loop. The coated as-received spectra observed a single capacitive loop with significant scatter of the data at low frequencies where an inductive loop would likely to be observed. Correlation with the OCP and macroscopic optical images suggest this spectra for the coated as-received specimen occurred after initiation of FFC, however there were likely very few active filaments leading to the large impedance values. In comparison, the as-received EIS response in the inlaid plot of **Figure 4.9 a** exhibits the typical low magnitude of impedance observed for Mg alloys along with a large inductive loop.

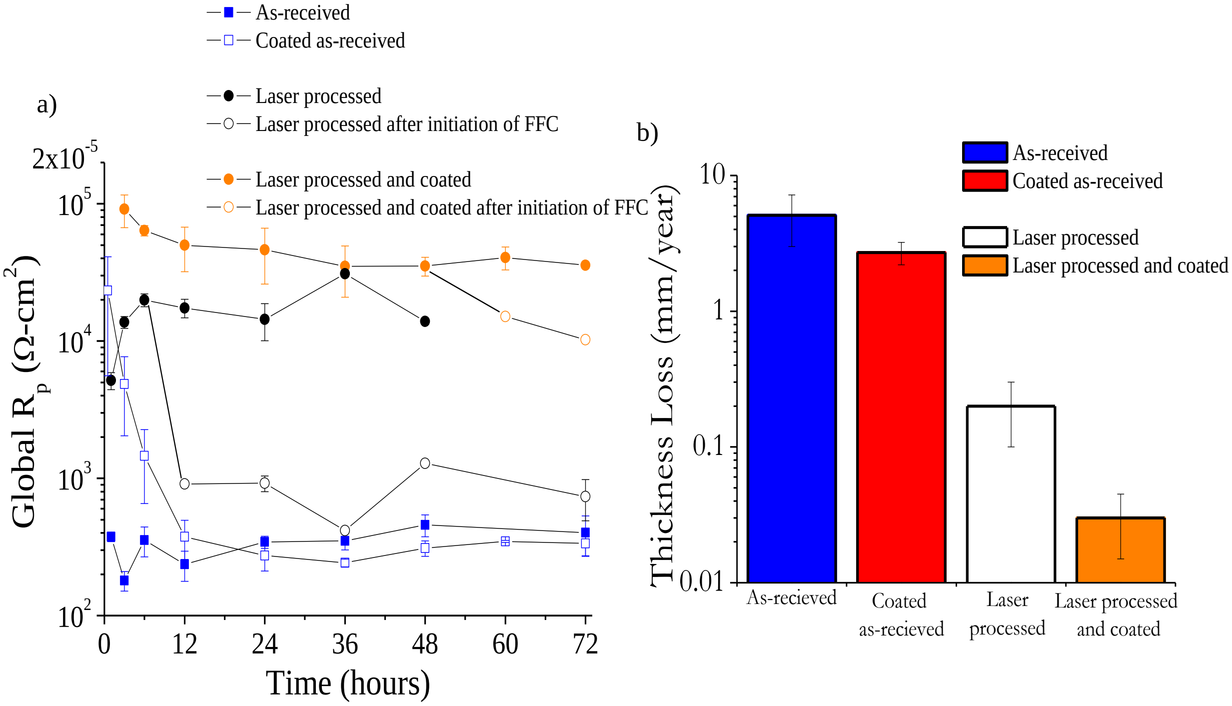

Figure 4.10: a) The time-dependent evolution of global R_p over the 72 hour OCP immersion in a stagnant 0.6 M NaCl solution for all AZ31B-H24 specimens, also revealing the change in global R_p for the LP after FFC initiation. **b)** The corrosion rate (mm/year) estimated by the accumulation of the 72 hour OCP-EIS measurements**.**

The EIS data was further analyzed to investigate the change in global polarization resistance (R_p) with respect to time for all specimens, shown in **Figure 4.10 a**, along with the EIS estimate corrosion rate derived from the 3 day EIS experiments, observed in **Figure 4.10 b**. Over the 72 hour full immersion experiment, the LPC specimens observed a one to two order of magnitude increase in global R_p, in comparison to the as-received and coated as-received specimens. At the beginning of the experiment, the LPC specimens exhibited a global R_p of ~100,000 Ω-cm^2, followed by steady decay of that R_p with time to ~30,000 Ω-cm^2 after 72 hours. The LP specimens global R_p began at ~4,000 Ω-cm^2 and, in contrast to the LPC specimens, observed an increase in global R_p over the first 12 hours of immersion, likely from the growth of a protective corrosion product. However, the initiation of FFC was observed to occur on LP specimens after 12 to 36 hours of immersion while the initiation of FFC on the LPC specimens did not occur until after 60 hours of immersion. In stark contrast, the as-received specimens observed lower global R_p values in comparison to the LP specimens for the duration of the experiments, with the exception of the coated as-received specimen starting at a global R_p of ~5,000 Ω-cm^2 followed by a rapid decrease in magnitude at longer immersion times. After 12 hours of immersion, the as-received specimens and the coated as-received specimens observed similar global R_p values.

The corrosion rates determined from the EIS estimated global R_p values in **Figure 4.10 b** reveal similar trends to those observed for the time dependent global R_p values. The as-received and coated as-received exhibit similar corrosion rates and in comparison, the LP specimens observed an order of magnitude reduction in corrosion rate. The LPC specimen observed an additional reduction in corrosion rate, however, after initiation of FFC where the global R_p was shown to reduce by up to an order of magnitude, seen in **Figure 4.10 a**. Hence the extrapolation of the EIS measurements to determine the average corrosion rate for a year is not an accurate representation of a full year of corrosion in this solution.

To investigate how the LPC specimen protected against external defects, a diamond scribe was used to scratch through to the as-received alloy of a LPC AZ31B-H24 specimen, which was then immersed in stagnant 0.6 M NaCl for 24 hours, similar to the experiments performed in **Chapter 3**. The results for the scratched specimen are presented in **Figure 4.11** revealing the OCP measurements in **Figure 4.11 a** to have a similar trend as the scratched as-received specimen. This result coincides with the observation of FFC to initiate within the scratch of the LPC specimen after ~ 1 minute of immersion in the solution from the time-lapse micrographs in **b** through **d**. That said, the propagation of the FFC was short lived, stopping after the scratched region was covered with the filaments of corrosion from stage II FFC and not extending into the LPC region. In contrast, the scratched LP specimen from **Chapter 3** showed FFC initiation after ~18 hours of full immersion with no FFC observed at early times within the scratch, similar to a non-scratched LP specimen, further suggestive of its galvanic protection. At longer immersion times, the initiation and propagation of new FFC within the scratch and the LPC region was not observed, demonstrating the protective nature of the LPC specimen even with a major defect.

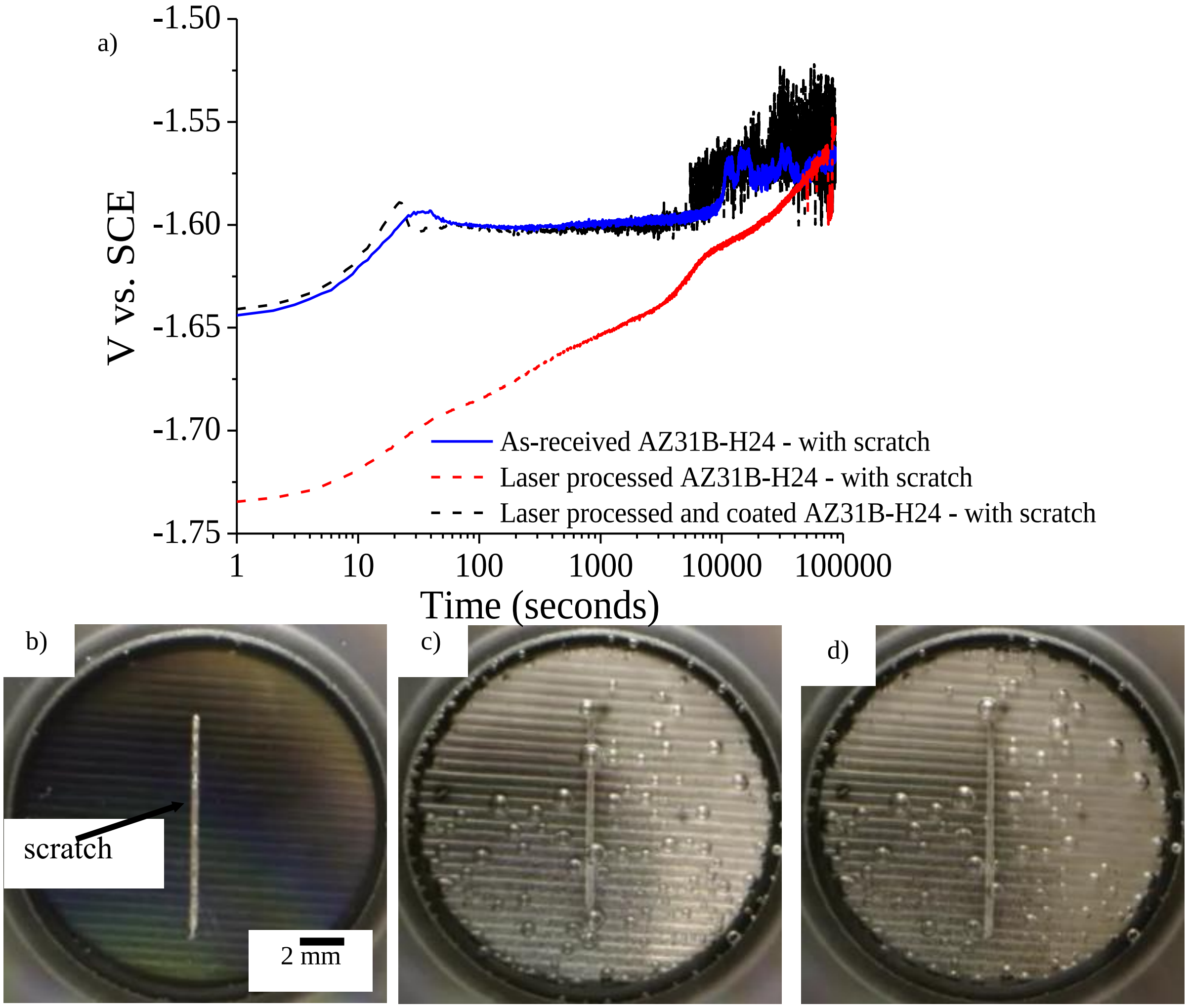

Figure 4.11: OCP measurement of the scratched, LPC AZ31B-H24 substrate during the entire 24 hour immersion shown in **a)**. The OCP from similar scratched experiments for the as-received and LP specimen are included in **a)** for comparison, from **Figure 3.14**. Optical micrographs taken with the Dinolite digital camera for the scratched LPC specimen after b) 0 hrs., c) 12 hrs., and d) 24 hrs. of full immersion in stagnant 0.6 M NaCl solution. The scribe is at the center of each image.

4.4 Discussion of Mg/Gd coating of AZ31B-H24 results

The choice of the specific coating materials, pure Mg and pure Gd, was decided based on the stability of their aqueous corrosion products at high pH, shown for Gd in **Figure 4.12** and Mg in **Figure 1.3**. The resulting films were completely oxidized, preventing the possibility for the coatings to act as sacrificial protection; similar to Mg rich primers [47,48,49,50,51,52,53]. That said, the possibility for the MgO film to act as an inhibitor to corrosion is high as the conversion of MgO to $Mg(OH)_2$ has been shown to help fill the pores/defects of a coating while simultaneously changing the solution chemistry to something more alkaline, making metallic Mg less likely to corrode [54].

The nano-crystalline $Gd(OH)_3$ film was utilized as a capping layer and acted as a protective film to corrosion attack, impeding the penetration of solution to the underlying $MgO/Mg(OH)_2$ film and alloy substrate. The extent of this protection was dependent on the state of the underlying alloy substrate, since time to initiation for FFC was at least an order of magnitude faster for the coated as-received specimens in comparison to the LPC specimens as shown in **Figure 4.7**. This result suggests that the $Gd(OH)_3$ film was permeable and permitted movement of solution to the underlying substrate, similar to other defects found in PVD coatings [35,36,37].

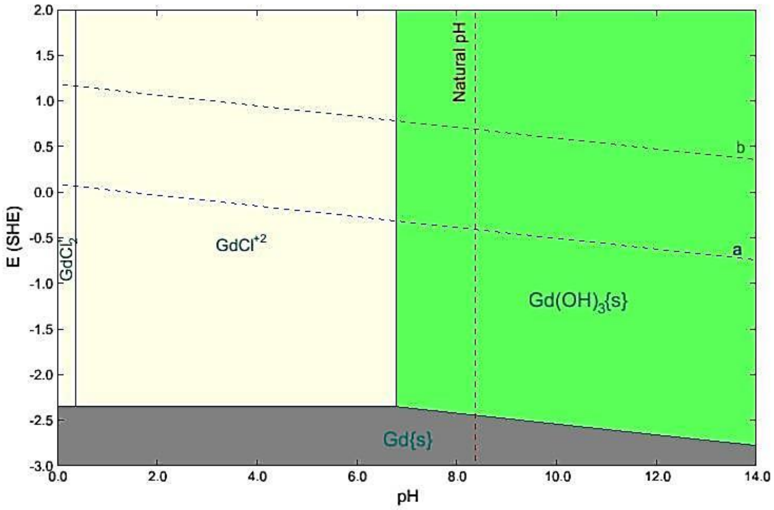

Figure 4.12: Pourbaix diagram of metallic Gd in a solution of 0.6 M NaCl and $Gd(OH)_3$ generated by the OLI software, $[Gd^{3+}] = 10^{-2}$ M.

To investigate the local breakdown of the $Gd(OH)_3$ film, backscattered (BSE) micrographs of a LPC specimen were taken after a 72 hour full immersion experiment at OCP, observed in **Figure 4.13**. The low magnification micrograph in **Figure 4.13 a** revealed a large black area to the right and was determined to be a large filament of corrosion, typical for these specimens after 72 hours of immersion albeit showing minimal area coverage. Interestingly, the FFC region does not show signs of the $Gd(OH)_3$ film (white contrast) covering the corrosion filaments, meaning the film was destroyed or broke off during the propagation of the corrosion filament. A lack of $Gd(OH)_3$ film was likely caused by the violent eruption of H_2 gas at the filament head and was similarly observed on the coated as-received specimens.

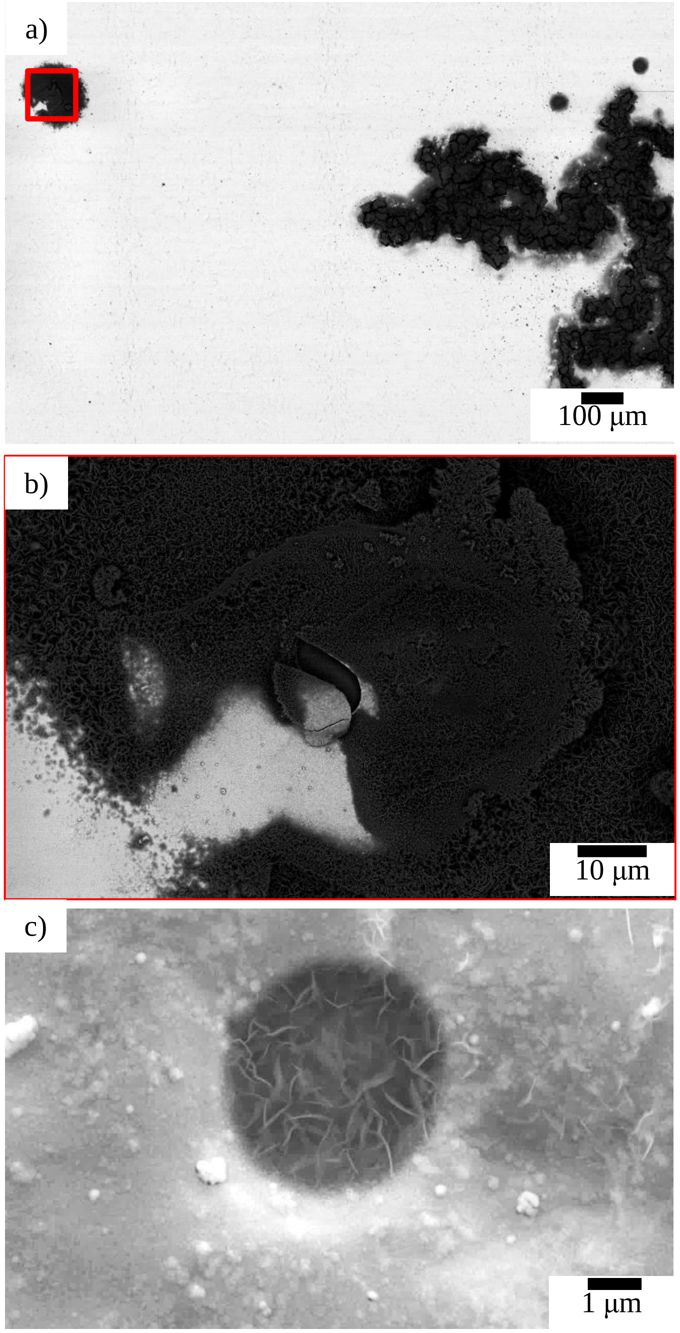

Figure 4.13: SEM micrographs of a LPC AZ31B-H24 specimen's surface after a 72 hour immersion experiment in stagnant 0.6 M NaCl. A BSE micrograph, shown in **a)** at low magnification and **b)** at higher magnification revealing FFC and rupture of the $Gd(OH)_3$ film. A secondary electron micrograph, shown in **c)**, of an area suspected to be a site of "re-passivation".

In the top left of **Figure 4.13 a** another black region was observed, however the typical FFC morphology was not detected. The region pointed out in **a** was imaged at higher magnification, shown in **Figure 4.13 b**, where a portion of the $Gd(OH)_3$ film was observed to be broken off from the as-deposited film, ~10 μm in diameter, leaving a hole in the $Gd(OH)_3$ film. The rupturing of the $Gd(OH)_3$ film may stem from numerous sources, one being the degradation of the film by prolonged exposure to the aggressive Cl^- ions, destabilizing the film [55,56,57]. Another source may be the penetration of solution through the porous film to the underlying LP alloy leading to corrosion of Mg and subsequent evolution of H_2 gas from the cathodic reaction [55]. A buildup of H_2 gas below the $Gd(OH)_3$ film would lead to tensile stresses acting on the film and eventual rupturing of the film at a critical stress, similar to the bursting of Al_2O_3 blisters on Al [55,58,59].

The H_2 gas rupture mechanism of the $Gd(OH)_3$ film fits well per the observed difference in initiation time of FFC for the coated as-received and LPC coated specimens. The delamination of the coating from the as-received AZ31B-H24 substrate was observed in **Figure 4.14** after immersion in the 0.6 M NaCl solution for ~2 hours. The existence of the locally raised coating is indicative of pinholes within the $Gd(OH)_3$ film allowing for the localized corrosion to the underlying substrate, typical for the coatings. If the solution penetrated through to the as-received microstructure of AZ31B-H24, there will be an abundance of local cathodes to produce H_2 gas, leading to a rapid buildup of tensile stresses and rupture of the $Gd(OH)_3$ film. No locally raised regions of the $Gd(OH)_3$ film was observed for the LPC AZ31B-H24 specimen. Instead the chemically homogenized LP surface prevented the rapid generation of H_2 gas limiting the potential for film rupture and prolonging the integrity of the $Gd(OH)_3$ film.

The higher magnification micrograph in **Figure 4.13b** revealed an area on the LPC specimen that ruptured the $Gd(OH)_3$ film and was surrounded with a substance having a flaky morphology and a lower atomic number than the $Gd(OH)_3$ film, indicative of $Mg(OH)_2$. This suggests that the ~10 μm wide exposed area of LP material was sufficiently large to allow for active corrosion and cause a local increase in Mg^{2+} and OH^- ions which led to the precipitation of the flaky $Mg(OH)_2$ product.

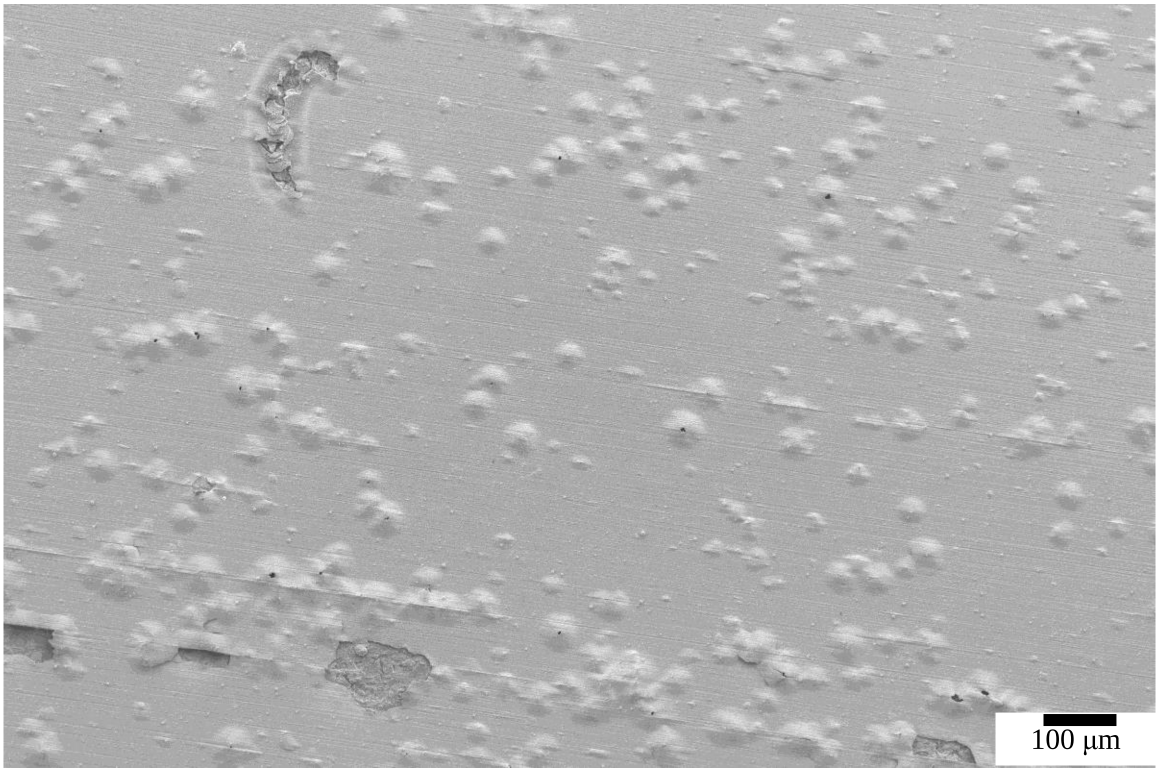

Figure 4.14: Secondary electron micrograph of a coated as-received AZ31B-H24 substrate after a 2 hour immersion in stagnant 0.6 M NaCl solution. Delamination of the coating can be observed, likely at pinholes in the $Gd(OH)_3$ coating.

These large ruptures of the $Gd(OH)_3$ film likely occurred around the time period when large fluctuations were observed in the OCP, around 200,000 seconds. Prior to these large rupturing events, sharp reductions in the LPC OCP were observed followed by exponential recovery back to the original OCP, indicative of breakdown of the film followed by a "re-passivation" phenomenon occurring at the surface [44,45,46]. These sharp reductions in OCP began around 100,000 seconds, occurring 1,000 seconds or more apart from each other, with longer immersion times exhibiting an increase in frequency, as shown in the inlaid plot in **Figure 4.7 b**. This local breakdown of the as-deposited films led to the exposure of the LP surface to solution for the first time since the specimen was immersed. Therefore, a reduction in OCP was observed because the OCP of a freshly LP AZ31B specimen is more negative than -1.6 V vs. SCE. The "re-passivation" phenomenon occurs when the OCP returns to the potential observed prior to the sharp reduction. The exact mechanism of "re-passivation" is unknown however it is speculated that the area of the ruptured $Gd(OH)_3$ film and subsequent exposed LP surface was small enough to be covered by the deposition of $Mg(OH)_2$. The $Mg(OH)_2$ can be generated from the corrosion of the underlying LP AZ31B surface and local increase in Mg^{2+} and OH^- ions, or the conversion of the mixed $MgO/Mg(OH)_2$ film completely to $Mg(OH)_2$. The conversion of MgO to $Mg(OH)_2$ is a thermodynamically favorable reaction in full immersion conditions [60,61]. Previous work on anodic oxide coatings containing MgO have credited this hydration conversion as a source of pore blocking because the molar volume of $Mg(OH)_2$ is larger than the molar volume of MgO, observing an increase in film resistance [20,54]. In addition, complete conversion of the $MgO/Mg(OH)_2$ to $Mg(OH)_2$ was observed via GI-XRD for a LP specimen which had been coated with $MgO/Mg(OH)_2$ and immersed in stagnant 0.6 M NaCl solution for 1 hour.

Existence of a potential “re-passivated” region is shown in **Figure 4.13c**, which exhibits an area of ~3 μm in diameter covered by what is speculated to be $Mg(OH)_2$. Similar dark circular spots were observed throughout the LPC specimens surface after 72 hours of immersion, some showing the familiar flaky $Mg(OH)_2$ and others revealing thinning and cracks in the $Gd(OH)_3$ film. Regardless, the “re-passivation” of the double layered coating on the LP specimen was possible. The same “re-passivation” effect was not observed for the coated as-received specimens because FFC and coating delamination dominated the corrosion response, rupturing the majority of the $Gd(OH)_3$ film after 24 hours of immersion.

4.5 Summary of the Mg/Gd coating of AZ31B-H24 results

A coating scheme to prolong the time to initiation of FFC on the AZ31B-H24 alloy under full immersion conditions was successfully developed and combined with laser pretreatment, extending the time to initiation of FFC for AZ31B-H24 to ~72 hours. The coating included an initial layer of $MgO/Mg(OH)_2$ followed by a capping layer of nanocrystalline $Gd(OH)_3$. When deposited onto LP AZ31B-H24 specimens, the global R_p increased by two orders of magnitude relative to the as-received alloy. At long immersion times, 72 hours, the global R_p of the LPC specimens reduced but never returned to the R_p of the as-received alloy.

The protection against artificial defects was also tested for the LPC AZ31B-H24 specimen by the application of a scratch through to the underlying substrate. Stage II FFC was observed to initiate quickly within the scratched region, covering the scratch entirely with corrosion filaments. That said, propagation of the filaments was stopped by the LPC region of the substrate and initiation of new FFC was not observed for the rest of the 24 hour experiment. In addition, the LPC specimens observed a pit initiation and “re-passivation” like phenomena never before observed for coatings applied to Mg alloys. This “re-passivation” phenomenon is hypothesized to be caused by the exposure of the fresh LP alloy surface or the $MgO/Mg(OH)_2$ film to the corrosion media for the first time leading to the production of $Mg(OH)_2$ which helps fill the broken down area of the $Gd(OH)_3$ film.

4.6 References

---

[1] J.E. Gray, Luan, B., Protective coatings on magnesium and its alloys — a critical review, Journal of Alloys and Compounds, 336 (2002) 88-113.

[2] X.B. Chen, N. Birbilis, T.B. Abbott, A simple route towards a hydroxyapatite–Mg(OH)2 conversion coating for magnesium, Corrosion Science, 53 (2011) 2263-2268.

[3] X.B. Chen, N. Birbilis, T.B. Abbott, Review of Corrosion-Resistant Conversion Coatings for Magnesium and Its Alloys, Corrosion, 67 (2011) 035005-035001 - 035005-035016.

[4] S.D. Cramer, A.I.H. Committee, B.S. Covino, ASM Handbook, ASM International, 2005.

[5] A.S. Akhtar, Surface Science Studies of Conversion Coatings on 2024-T3 Aluminum Alloy, Chemistry, The University of British Columbia, Vancouver, 2008, pp. 1-198.

[6] S.B. Brachetti-Sibaja, M.A. Domínguez-Crespo, A.M. Torres-Huerta, W. de la Cruz-Hernández, E. Onofre-Bustamante, Bath Conditions Role in Promoting Corrosion Protection on Aluminum Alloy using Rare Earth Conversion Coatings, Journal of The Electrochemical Society, 159 (2012) C40.

[7] G.M. Brown, K. Shimizu, K. Kobayashi, G.E. Thompson, G.C. Wood, The Development of Chemical Conversion Coatings on Aluminum, Corrosion Science, 34 (1993) 253-256.

[8] K.Z. Chong, T.S. Shih, Conversion-coating treatment for magnesium alloys by a permanganate–phosphate solution, Materials Chemistry and Physics, 80 (2003) 191-200.

[9] X. Chen, G. Li, J. Lian, Q. Jiang, Study of the formation and growth of tannic acid based conversion coating on AZ91D magnesium alloy, Surface and Coatings Technology, 204 (2009) 736-747.

[10] X.-B. Chen, X. Zhou, T.B. Abbott, M.A. Easton, N. Birbilis, Double-layered manganese phosphate conversion coating on magnesium alloy AZ91D: Insights into coating formation, growth and corrosion resistance, Surface and Coatings Technology, 217 (2013) 147-155.

[11] L. Jianrui, G. Yina, H. Weidong, Study on the corrosion resistance of phytic acid conversion coating for magnesium alloys, Surface and Coatings Technology, 201 (2006) 1536-1541.

[12] J.K. Lin, J.Y. Uan, Formation of Mg,Al-hydrotalcite conversion coating on Mg alloy in aqueous HCO3−/CO32− and corresponding protection against corrosion by the coating, Corrosion Science, 51 (2009) 1181-1188.

[13] H. Ardelean, I. Frateur, P. Marcus, Corrosion protection of magnesium alloys by cerium, zirconium and niobium-based conversion coatings, Corrosion Science, 50 (2008) 1907-1918.

[14] A.S. Hamdy, I. Doench, H. Möhwald, Smart self-healing anti-corrosion vanadia coating for magnesium alloys, Progress in Organic Coatings, 72 (2011) 387-393.

[15] J. Zhao, L. Xia, A. Sehgal, D. Lu, R.L. McCreery, G.S. Frankel, Effects of chromate and chromate conversion coatings on corrosion of aluminum alloy 2024-T3, Surface and Coatings Technology, 140 (2001) 51-57.

[16] J. Zhao, G.S. Frankel, R.L. McCreery, Corrosion Protection of Untreated AA-2024-T3 in Chloride Solution by a Chromate Conversion Coating Monitored with Raman Spectroscopy, Journal of Electrochemical Society, 145 (1998) 2258-2264.

[17] R. Arrabal, E. Matykina, F. Viejo, P. Skeldon, G.E. Thompson, Corrosion resistance of WE43 and AZ91D magnesium alloys with phosphate PEO coatings, Corrosion Science, 50 (2008) 1744-1752.

[18] M. Mohedano, C. Blawert, M.L. Zheludkevich, Cerium-based sealing of PEO coated AM50 magnesium alloy, Surface and Coatings Technology, (2015).

[19] C.E. Barchiche, E. Rocca, J. Hazan, Corrosion behaviour of Sn-containing oxide layer on AZ91D alloy formed by plasma electrolytic oxidation, Surface and Coatings Technology, 202 (2008) 4145-4152.

[20] S.J. Xia, V.I. Birss, R.G. Rateick, Anodic oxide film formation at magnesium alloy WE43, in: V.I. Birss, L.D. Burke, A.R. Hillman, R.S. Lillard (Eds.) Electrochemical Society, Orlando, FL, 2003, pp. 270-280.

[21] H. Altun, S. Sen, The effect of PVD coatings on the corrosion behaviour of AZ91 magnesium alloy, Materials & Design, 27 (2006) 1174-1179.

[22] H. Altun, H. Sinici, Corrosion behaviour of magnesium alloys coated with TiN by cathodic arc deposition in NaCl and Na2SO4 solutions, Materials Characterization, 59 (2008) 266-270.

[23] W. Dai, G. Wu, A. Wang, Preparation, characterization and properties of Cr-incorporated DLC films on magnesium alloy, Diamond and Related Materials, 19 (2010) 1307-1315.

[24] P.C. Wang, T.C. Cheng, H.C. Lin, M.J. Chen, K.M. Lin, M.T. Yeh, Effects of pre-sputtered Al interlayer on the atomic layer deposition of Al2O3 films on Mg–10Li–0.5Zn alloy, Applied Surface Science, 270 (2013) 452-456.

[25] G. Wu, W. Dai, H. Zheng, A. Wang, Improving wear resistance and corrosion resistance of AZ31 magnesium alloy by DLC/AlN/Al coating, Surface and Coatings Technology, 205 (2010) 2067-2073.

---

[26] G. Wu, K. Ding, X. Zeng, X. Wang, S. Yao, Improving corrosion resistance of titanium-coated magnesium alloy by modifying surface characteristics of magnesium alloy prior to titanium coating deposition, Scripta Materialia, 61 (2009) 269-272.

[27] G. Wu, X. Wang, K. Ding, Y. Zhou, X. Zeng, Corrosion behavior of Ti–Al–N/Ti–Al duplex coating on AZ31 magnesium alloy in NaCl aqueous solution, Materials Characterization, 60 (2009) 803-807.

[28] G. Wu, X. Zeng, W. Ding, X. Guo, S. Yao, Characterization of ceramic PVD thin films on AZ31 magnesium alloys, Applied Surface Science, 252 (2006) 7422-7429.

[29] G. Wu, X. Zeng, G. Yuan, Growth and corrosion of aluminum PVD-coating on AZ31 magnesium alloy, Materials Letters, 62 (2008) 4325-4327.

[30] D. Zhang, B. Wei, Z. Wu, Z. Qi, Z. Wang, A comparative study on the corrosion behaviour of Al, Ti, Zr and Hf metallic coatings deposited on AZ91D magnesium alloys, Surface and Coatings Technology, 303 (2016) 94-102.

[31] M. Daroonparvar, M.A.M. Yajid, H.R. Bakhsheshi-Rad, N.M. Yusof, S. Izman, E. Hamzah, M.R. Abdul Kadir, Corrosion resistance investigation of nanostructured Si- and Si/TiO_2-coated Mg alloy in 3.5% NaCl solution, Vacuum, 108 (2014) 61-65.

[32] M. Daroonparvar, M.A.M. Yajid, N.M. Yusof, H.R. Bakhsheshi-Rad, E. Hamzah, Microstructural characterisation of air plasma sprayed nanostructure ceramic coatings on Mg–1%Ca alloys (bonded by NiCoCrAlYTa alloy), Ceramics International, 42 (2016) 357-371.

[33] G. Song, B. Johannesson, S. Hapugoda, D. StJohn, Galvanic corrosion of magnesium alloy AZ91D in contact with an aluminium alloy, steel and zinc, Corrosion Science, 46 (2004) 955-977.

[34] P.C. Wang, T.C. Cheng, H.C. Lin, M.J. Chen, K.M. Lin, M.T. Yeh, Effects of pre-sputtered Al interlayer on the atomic layer deposition of Al2O3 films on Mg–10Li–0.5Zn alloy, Applied Surface Science, 270 (2013) 452-456.

[35] Z. Shi, G. Song, A. Atrens, Influence of anodising current on the corrosion resistance of anodised AZ91D magnesium alloy, Corrosion Science, 48 (2006) 1939-1959.

[3636] Z. Shi, G. Song, A. Atrens, Influence of the β phase on the corrosion performance of anodised coatings on magnesium–aluminium alloys, Corrosion Science, 47 (2005) 2760-2777.

[37] H. Hoche, C. Rosenkranz, A. Delp, M.M. Lohrengel, E. Broszeit, C. Berger, Investigation of the macroscopic and microscopic electrochemical corrosion behaviour of PVD-coated magnesium die cast alloy AZ91, Surface and Coatings Technology, 193 (2005) 178-184.

[38] Y.H. Huang, Y.L. Lee, C.S. Lin, Acid Pickling Pretreatment and Stannate Conversion Coating Treatment of AZ91D Magnesium Alloy, Journal of The Electrochemical Society, 158 (2011) C310.

[39] S. Maddela, M.J. O'Keefe, Y.-M. Wang, H.-H. Kuo, Influence of Surface Pretreatment on Coating Morphology and Corrosion Performance of Cerium-Based Conversion Coatings on AZ91D Alloy, Corrosion, 66 (2010) 115006-115001 - 115006-115008.

[40] R. Xu, X. Yang, X. Zhang, M. Wang, P. Li, Y. Zhao, G. Wu, P.K. Chu, Effects of carbon dioxide plasma immersion ion implantation on the electrochemical properties of AZ31 magnesium alloy in physiological environment, Applied Surface Science, 286 (2013) 257-260.

[41] X.B. Tian, C.B. Wei, S.Q. Yang, R.K.Y. Fu, P.K. Chu, Corrosion resistance improvement of magnesium alloy using nitrogen plasma ion implantation, Surface and Coatings Technology, 198 (2005) 454-458.

[42] Z. Xie, Z. Luo, Q. Yang, T. Chen, S. Tan, Y. Wang, Y. Luo, Improving anti-wear and anti-corrosion properties of AM60 magnesium alloy by ion implantation and Al/AlN/CrAlN/CrN/MoS2 gradient duplex coating, Vacuum, 101 (2014) 171-176.

[43] X. Wang, X. Zeng, G. Wu, S. Yao, Y. Lai, Effects of tantalum ion implantation on the corrosion behavior of AZ31 magnesium alloys, Journal of Alloys and Compounds, 437 (2007) 87-92.

[44] G. Berthomé, B. Malki, B. Baroux, Pitting transients analysis of stainless steels at the open circuit potential, Corrosion Science, 48 (2006) 2432-2441.

[45] H.S. Isaacs, C. Scheffey, R. Huang, The Location of Events Producing Potential Transients During Pitting of Freely Corroding Al and Its Alloys, ECS Transactions, 11 (2008) 1-12.

[46] H.S. Isaacs, Y. Ishikawa, Current and Potential Transients during Localized Corrosion of Stainless Steel, Journal of The Electrochemical Society, 132 (1985) 1288-1293.

[47] X.B. Chen, T. Cain, J.R. Scully, N. Birbilis, Technical Note:Experimental Survey of Corrosion Potentials for Rare Earth Metals Ce, Er, Gd, La, and Nd as a Function of pH and Chloride Concentration, Corrosion, 70 (2014) 323-328.

[48] S. Shen, Y. Zuo, The improved performance of Mg-rich epoxy primer on AZ91D magnesium alloy by addition of ZnO, Corrosion Science, 87 (2014) 167-178.

---

[49] A.D. King, J.R. Scully, Sacrificial Anode-Based Galvanic and Barrier Corrosion Protection of 2024-T351 by a Mg-Rich Primer and Development of Test Methods for Remaining Life Assessment, Corrosion, 67 (2011) 055004-055001 - 055004-055022.

[50] D. Battocchi, A.M. Simões, D.E. Tallman, G.P. Bierwagen, Electrochemical behaviour of a Mg-rich primer in the protection of Al alloys, Corrosion Science, 48 (2006) 1292-1306.

[51] A.D. King, B. Kannan, J.R. Scully, Environmental Degradation of a Mg-Rich Primer in Selected Field and Laboratory Environments: Part 1—Without a Topcoat, Corrosion, 70 (2014) 512-535.

[52] S.S. Pathak, M.D. Blanton, S.K. Mendon, J.W. Rawlins, Investigation on dual corrosion performance of magnesium-rich primer for aluminum alloys under salt spray test (ASTM B117) and natural exposure, Corrosion Science, 52 (2010) 1453-1463.

[53] A. Simões, D. Battocchi, D. Tallman, G. Bierwagen, Assessment of the corrosion protection of aluminium substrates by a Mg-rich primer: EIS, SVET and SECM study, Progress in Organic Coatings, 63 (2008) 260-266.

[54] R.J. Santucci, B. Kannan, J.R. Scully, Electrochemical Diagnostic Cycle Testing of Magnesium and Magnesium Oxide-Pigmented Primers on AA2024-T351, Corrosion, 74 (2018) 96-111.

[55] E. McCafferty, Sequence of steps in the pitting of aluminum by chloride ions, Corrosion Science, 45 (2003) 1421-1438.

[56] J. Soltis, Passivity breakdown, pit initiation and propagation of pits in metallic materials – Review, Corrosion Science, 90 (2015) 5-22.

[57] E. McCafferty, Semiconductor aspects of the passive oxide film on aluminum as modified by surface alloying, Corrosion Science, 45 (2003) 301-308.

[58] P.M. Natishan, E. McCafferty, The Mechanism of Blister Formation and Rupture in the Pitting of Ion-Implanted Aluminum, Journal of The Electrochemical Society, 136 (1989) 53-58.

[59] R.L. Ryan, E. McCafferty, Rupture of an Oxide Blister, Journal of The Electrochemical Society, 142 (1995) 2594-2597.

[60] O. Fruhwirth, G.W. Herzog, I. Hollerer, A. Rachetti, Dissolution and hydration kinetics of MgO, Surface Technology, 24 (1985) 301-317.

[61] S.O. Baumann, J. Schneider, A. Sternig, D. Thomele, S. Stankic, T. Berger, H. Grönbeck, O. Diwald, Size Effects in MgO Cube Dissolution, Langmuir, 31 (2015) 2770-2776.

Page intentionally left blank.

Chapter 5: Salt spray testing of laser processed Mg alloys

5.1 Background on atmospheric and salt spray corrosion testing of Mg alloys

Many real world applications for Mg alloys will implement them in corrosive environments similar to atmospheric corrosion conditions [1,2,3]. Atmospheric corrosion is unique from typical full immersion environments because of the thin films of aqueous solutions shown to develop on a materials surface which will range in salt concentrations depending on humidity up to super saturated conditions [4,5,6,7,8,9,10,11,12]. In addition there are a vast number of ionic species commonly found in rain or marine solutions not considered in the full immersion NaCl type tests conducted in this thesis work [13,14,15]. The utilization of full immersion corrosion testing was primarily implemented because a large reservoir of corroding solution exhibits well understood interactions with a materials surface in comparison to the thin films of aqueous solutions formed during atmospheric testing, simplifying the corrosion response [16,17,18,19].

In addition, field testing often requires years to perform with minimal utilization of electrochemical measurement techniques [2,3,5,20,21]. For this reason, artificial atmospheric corrosion conditions are often generated using salt spray machines or humidity controlled chambers to produce the thin film solution conditions commonly observed during real atmospheric corrosion. The incorporation of elevated temperatures and wetting and drying cycles lead to accelerated corrosion rates and varying salt concentrations associated with atmospheric cycles [3,4,13,15,22]. Substantial research has also been dedicated to the influence of other gaseous species and sources of degradation on the atmospheric of a material, such as O_3, SO_x, NO_y, and UV radiation [23,24,25]. The exact replication and acceleration of atmospheric corrosion is extremely difficult with many investigations dedicated to it, primarily concerned with the atmospheric corrosion of Al and steel alloys in marine conditions [4,12,13].

In comparison, Mg and their alloys have been incorporated into very few atmospheric corrosion experiments [3,5,6,7,26,27,28,29,30,31]. A major finding and constant theme of the Mg atmospheric corrosion investigations is the role of dissolved CO_2 gas on corrosion product formation and the subsequent corrosion rate of the Mg alloys [3,26,29]. Studies by Lindstrom, Jönsson, and Esmaily, have observed the benefits of CO_2 gas on the atmospheric corrosion response for a number of Al containing Mg alloys [3,26,29]. In general, for accelerated atmosphere experiments were the CO_2 gas content was controlled to below 1 ppm using a NaCl containing salt spray solution on commercial purity Mg and the AZ91 alloy, the gravimetric mass loss was observed to increase 4 fold in comparison to gravimetric mass loss of specimen under the same conditions without controlling the CO_2 content, typically between 350 to 400 ppm CO_2 [32]. The reasoning behind the dramatic improvement in corrosion resistance has widely been attributed to the formation of new carbonate containing corrosion products which are stable at a lower pH than $Mg(OH)_2$ [29,32,33]. A number of carbonate phases have been reported using Fourier transform infrared spectroscopy and x-ray diffraction techniques for the atmospheric corrosion of pure Mg as well as the Al containing Mg alloys, with the most commonly observed to be hydromagnesite ($Mg_5(CO_3)_4(OH)_2.4(H_2O)$) [5,26,29]. All of the carbonate rich Mg phases are believed to be more protective than the $Mg(OH)_2$ because of their stability at more acidic pH, around pH = 8.5 [33]. The formation of layered double hydroxide (LDH) phases has also been observed to form during the atmospheric corrosion, and full immersion, of Al containing Mg alloys, in both CO_2 and CO_2 free environments [3,34,35,36]. However, the role of the naturally formed LDH phases during the corrosion of these alloys has not been described.

The final experimental chapter of this thesis will look to observe the effect of accelerated atmospheric corrosion experiments on the as-received and laser processed condition of the AZ31B-H24, AM60B, and AZ91D alloys, utilizing the ASTM B117 standard test [13]. The focus will be on the corrosion rate after a 21 day exposure to the salt spray experiment and the resulting corrosion products formed. The constant replacement of the salt spray electrolyte on the specimen's surface will affect corrosion rate and corrosion product formation, minimizing the effect of stagnant solution conditions.

Hypothesis to be tested: Exposing the laser processed specimen to a corrosive environment for longer term exposures will enhance the localized corrosion on the laser processed specimen, increasing the corrosion rate in comparison to the studies performed in full immersion.

5.2 Experimental setup

Samples of the AZ31B-H24, AM60B, and AZ91D alloys were cut from plate using a Mager cut off saw to a size of 50 mm x 20 mm for the purposes of being able to fit within the laser processing chamber. The AZ31B-H24 specimens were prepared in 3 conditions; as-received, laser processed (LP), and laser processed and coated (LPC) with a Mg/Gd film. The as-cast alloys, AM60B and AZ91D, were prepared in the as-received and LP conditions only. As-received specimens were polished to a 1200 grit finish with an ethanol based lubricant and Buehler^{TM} SiC paper. The laser processing parameters were identical for all alloys as described in **Table 2.2**; as the optimal processing parameters. In order to ensure uniformity, after 100 PPA the specimens were flipped 180 degrees and the remaining 100 PPA were applied. The coating procedure from **chapter 4** was also identical for the AZ31B-H24 LP specimen used here. Similar nomenclature will be used to describe these specimens. All specimens were prepared a day before the start of the artificial atmospheric test, weighed using a Mettler-Toledo^{TM} analytical balance, and stored in a vacuum sealed desiccator. Prior to placement in the salt spray chamber the back side of each specimen was covered with electrochemical tape to prevent corrosion, the sides of all samples were exposed. Three of each sample condition was prepared for replication purposes.

For the salt spray test, a Q-LAB Q-FOG CCT cyclic corrosion tester, shown in **Figure 5.1a**, was utilized and the procedure for the ASTM B117 standard was followed [13]. Prior to testing, water was used to measure the solution deposition rate inside the Q-FOG tester and controlled to within the 1 to 2 mL per hour standard for B117. The solution used for testing was 5 wt% NaCl (0.9 M NaCl, pH ~ 6.5) and was prepared in 40 L containers. The pH of the solution was measured at room temperature (22^{o}C), and the experiment was performed at a temperature of 35^{o}C. The CO_2 (g) content within the chamber was not monitored and will be estimated to be the current atmospheric level of ~400 ppm as has been reported in recent climate studies [37,38,39]. The B117 standard does not employ wetting and drying cycles or any addition of pollutants and other potential atmospheric effects, such as UV radiation or O_3. Therefore the major difference from full immersion will be the constant spray of electrolyte which will lead to a thinner film of solution on the specimen than usual as well as the continuous replacement of the surface with fresh solution.

Figure 5.1: Picture of the Q-FOG salt spray chamber is shown in a) with the inside of the chamber and the sample orientation observed in b).

Specimens were placed in the chamber as shown in **Figure 5.1b**, with sufficient spacing and at approximately a 70 degree angle to the base of the chamber. Specimens were exposed in the Q-FOG tester for a total of 21 days and with removal at 1, 5, and 14 days to take macroscopic digital images of each sample, observing the change in corrosion with time. Prior to imaging, the specimens were not dried or rinsed off with water. After the last day of testing, the specimens were removed from the Q-FOG chamber, rinsed with deionized water, dried with a jet of air, and imaged with the digital camera. All specimens were stored in a vacuum sealed desiccator after imaging and subsequent characterization techniques. Mass gain and mass loss was performed on all specimens to determine the corrosion product build up and corrosion rate of each specimen. The corrosion product was removed using the ASTM G-1 standard with a chromic acid solution [40].

Prior to corrosion product removal, the specimens were characterized to determine the composition and phase of the corrosion products developed over the 3 week salt spray test. Phase analysis was performed by grazing incidence x-ray diffraction (GI-XRD PANalytical X'Pert Pro MPD diffractometer) with a Cu-K_α (λ=1.54 Å) source at a 1.0° incident angle (5.0 μm x-ray penetration depth of pure Mg). Infrared spectroscopy (PerkinElmer Frontier attenuated total reflection – Fourier transform infrared (ATR-FTIR)) was used to accompany the GI-XRD results, verifying the presence of certain compounds sensitive to IR spectroscopy (such as carbonates).

5.3 Results from salt spray tests and corrosion product phase analysis

5.3.1 General corrosion behavior and corrosion rate

The surface of the as-received AZ31B-H24 alloy after 1 day of exposure revealed dark filament like corrosion products, thought to be filiform-like corrosion (FFC), covering a majority of the surface, shown in **Figure 5.2.** After 5 days localized black corrosion product was observed with subsequent days leading to more local black corrosion areas and the remaining area covered in a white corrosion product. This white corrosion product was expected to be $Mg(OH)_2$.

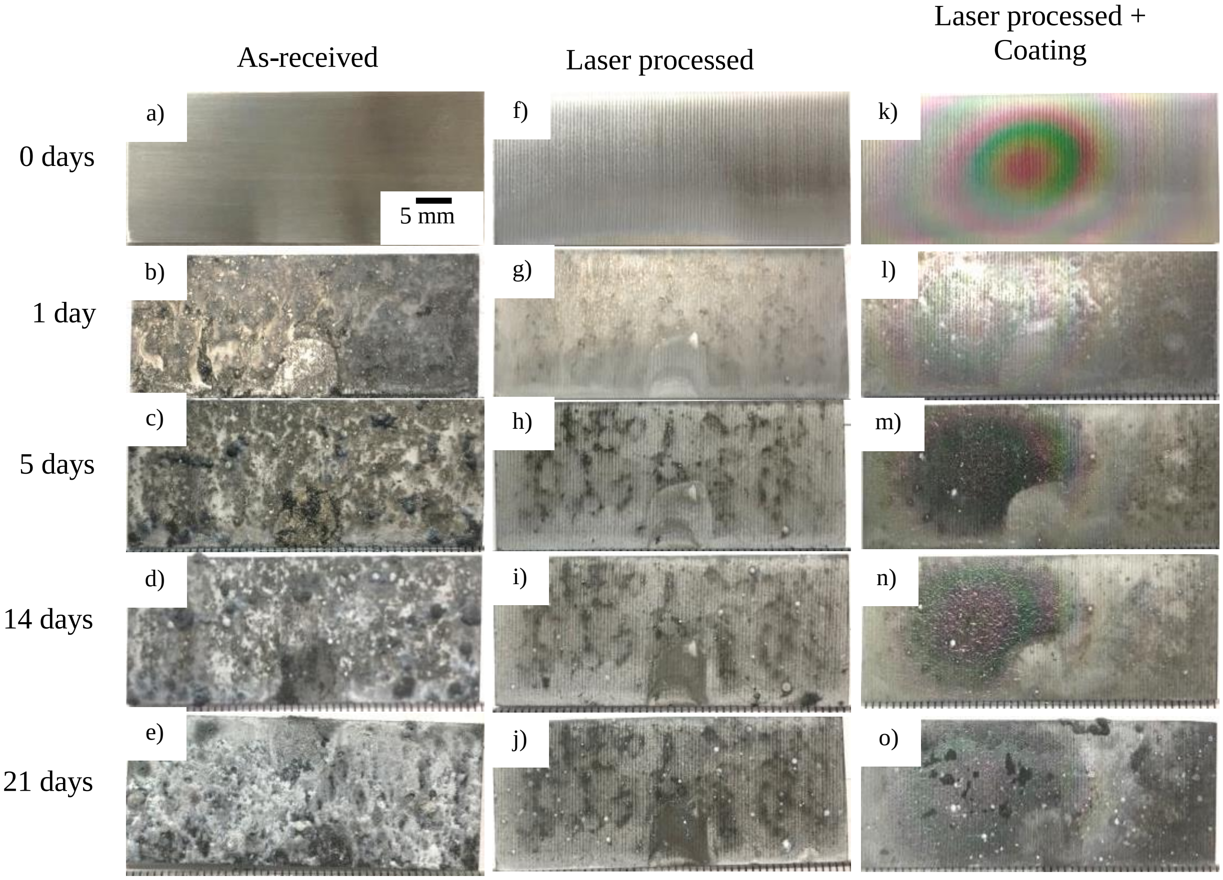

Figure 5.2: Digital images of the AZ31B-H24 alloy after the specified time of exposure to the B117 salt spray experiment for the as-received (a – e), LP (f – j), and LPC (k – o) conditions.

For the LP AZ31B-H24 specimens, shown in **Figure 5.2 f-j**, black corrosion product was not observed until day 5 and with a lower coverage density than the as-received specimens. At longer times the black corrosion product areas remained and new white circular spots began populating the surface, again suspected of being $Mg(OH)_2$. The LPC AZ31B-H24 specimens evolved in a similar manner to the LP specimens, not showing the black corrosion product and filament-like corrosion until day 21, as observed in **Figure 5.2 k-o**. The circular white spots were first observed after 5 days and coincided with the delamination of the coating from the surface. After 21 days the double layered Mg/Gd coating was flaking off from the surface and filamentous corrosion could be observed.

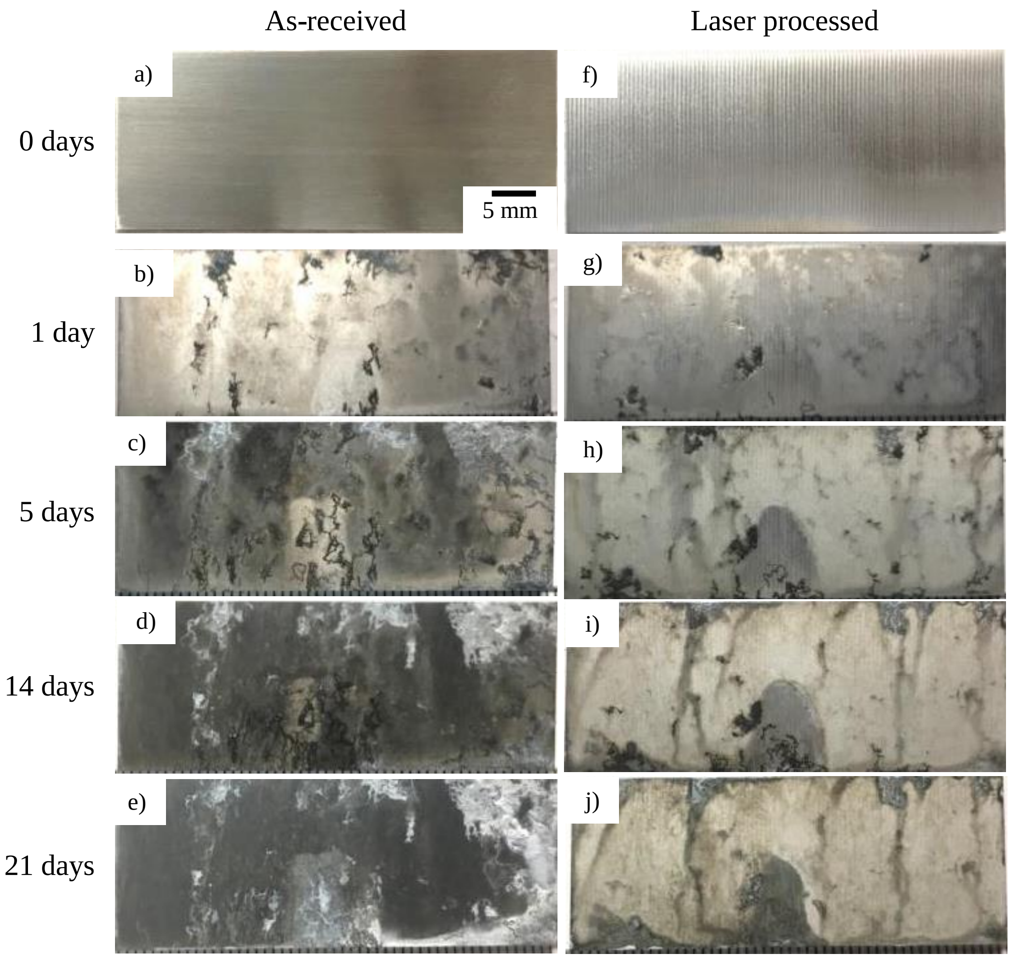

Figure 5.3: Digital images of the AM60B alloy after the specified time of exposure to the B117 salt spray experiment for the as-received (a – e) and LP (f – j) conditions.

The AM60B and AZ91D alloys corrosion over time for the as-received and LP conditions is shown in **Figure 5.3** and **Figure** 5.4. The general corrosion product covering the surface for AM60B and AZ91D alloys in the as-received condition became dark in color after ~5 days in comparison to the starting polished condition. In contrast, the general corrosion product formed on the LP cast alloys remained a beige/silvery color for the longevity of the experiment. For the case of AM60B in **Figure 5.3**, the as-received and LP condition developed the FFC morphology (black corrosion product) after 1 day of exposure in the salt spray chamber. At longer times these filaments traversed the AM60B surface for both conditions with the as-received showing more coverage by day 21. The FFC morphology was only observed on the as-received specimens of AZ91D. A few circular areas of local corrosion developed on the LP AZ91D alloy with no other local corrosion observed to initiate in the center of the specimen, some filaments of corrosion were observed to initiate on the top edge of the sample (not LP) and propagate into the LP region.

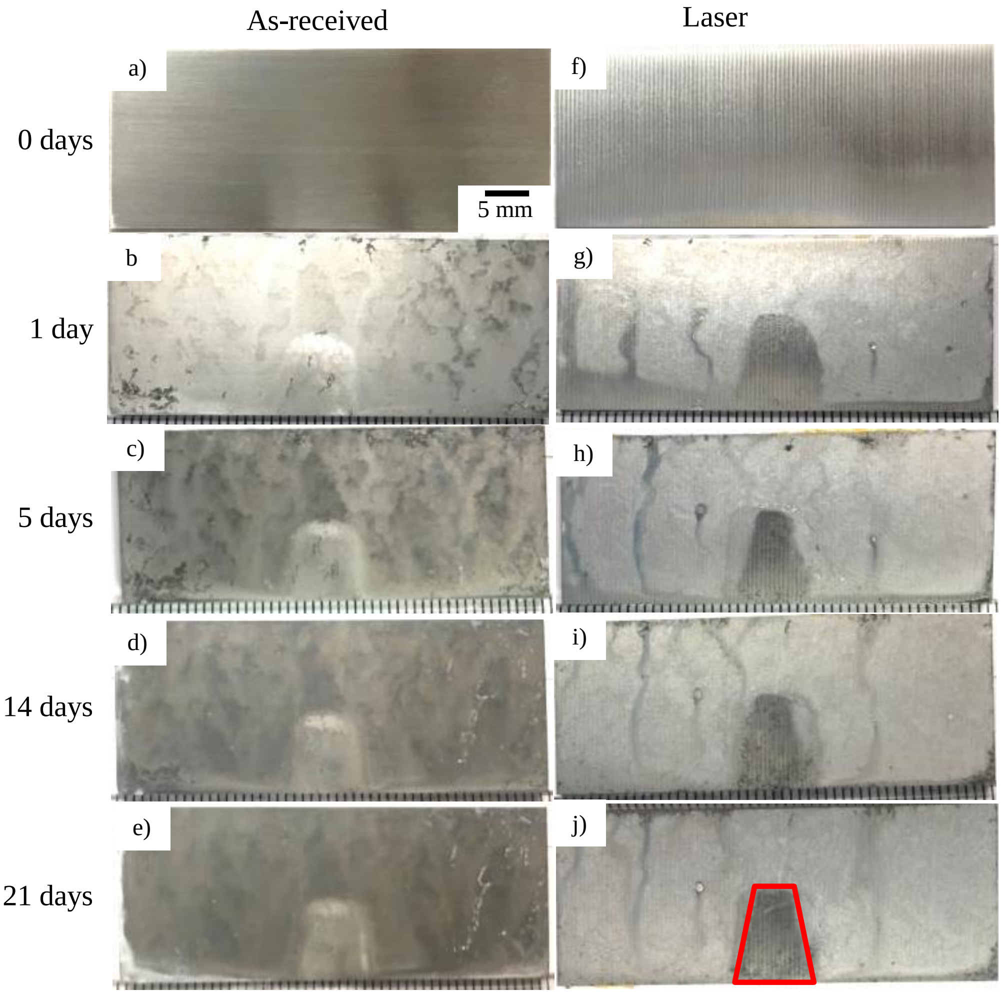

Figure 5.4: Digital images of AZ91D B117 salt spray exposure for the as-received (a – e) and LP (f – j) conditions. The red trapezoid in (j) outlines the water mark of the specimen mount.

The edge effects for the AZ91D specimens were prominent on all alloys with a majority of the localized corrosion for the LP, or LPC samples stemming from an edge. An additional irregularity in the specimens was the watermark made by the mounting bracket in the chamber for each sample, outlined in red from **Figure 5.4 j**. This area exhibited different corrosion product coverage than the rest of the sample surface. In some cases, specifically **Figure 5.3 g**, initiation of FFC was observed to occur at this differing corrosion product interface.

The averaged corrosion rate, presented as thickness loss per year, of each specimen is observed in **Figure 5.5** revealing a 3 fold reduction in expected corrosion rate for the modified AZ31B-H24 specimens, and slight reductions in corrosion rates for the cast alloys. These corrosion rates were determined from mass loss for the entire exposed surface, including the sides of each specimen, which for all conditions were left in the as-received state. Interestingly, the LP materials observed a small reduction in corrosion rate in comparison to their full immersion results, possibly stemming from the higher NaCl concentration utilized here. In addition to high chloride content, the initiation of FFC occurred on all specimens except for LP AZ91D and this localized corrosion may also have led to the minimal difference in global corrosion rates. The FFC will corrode at high rates regardless of a surface being LP or not, hence the initiation of FFC after 1 to 5 days allows for substantial propagation of the corrosion filaments over the 21 day exposure. It is important to note the sides of all specimen were exposed and remained in the as-received condition, possibly skewing the corrosion rate results.

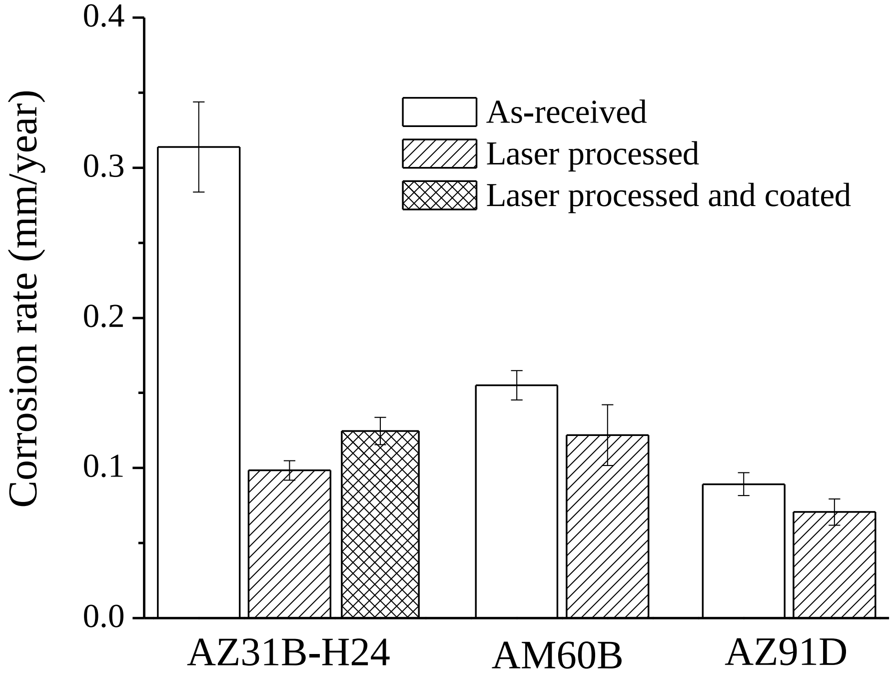

Figure 5.5: Corrosion rate in terms of average thickness loss per year (mm/year) calculated from gravimetric mass loss data after chromic acid cleaning of the B117 salt spray experiments assuming uniform corrosion of the entire exposed area.

5.3.2 Corrosion product phase analysis

Representative GI-XRD patterns are shown for each specimen condition in **Figure 5.6, Figure** 5.7**,** and **Figure** 5.8, for the AZ31B-H24, AM60B, and AZ91D alloys, respectively. Standards for XRD phase analysis can be found in **Appendix 1**. From the digital micrographs in **Figure 5.2**, **Figure** 5.3, and **Figure** 5.4, all of the specimens in the as-received condition were expected to have thicker and more intense corrosion product peaks than the modified surfaces. The as-received AZ31B-H24 specimens primary corrosion products were observed to be hydromagnesite ($Mg_5(CO_3)_4(OH)_2(H_2O)_4$) and brucite $Mg(OH)_2$ which have been observed in previous studies [20,26,29]. Additional peaks were observed at 2θ = 11 ^{o}, 22.5 ^{o}, and 45.5 ^{o}, indicative of a layered double hydroxide (LDH) phase, suspected to be meixnerite ($Mg_6Al_2(OH)_{18}•4(H_2O)$) or hydrotalcite ($Mg_{0.83}Al_{0.17}(CO_3)_{0.08}(OH)_2(H_2O)_{0.75}$) as described in **Chapter 3** [3,28,41,42,43,44]. The LP AZ31B-H24 condition observed less diffraction peaks than the as-received condition with the presence of two broad peaks at the LDH peak locations. The LPC specimen in **Figure 5.6** only observed peaks from α-Mg, likely from the surface still being partially covered by the nanocrystalline $Gd(OH)_3$ coating. It is suspected from the digital micrographs that the corrosion product under the coating was similar to the LP AZ31B-H24 results.

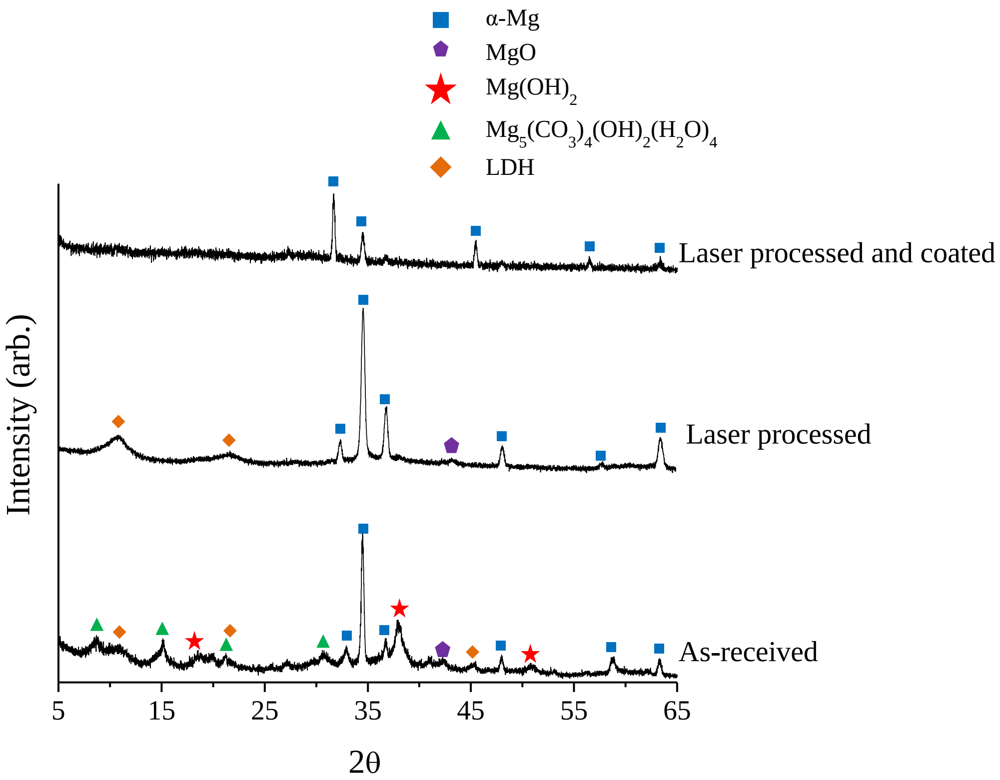

Figure 5.6: GI-XRD measurements of AZ31B-H24 corrosion product after a 21 day exposure to the B117 salt spray. The Cu-K_α (λ=1.54 Å) source was utilized at a 1.0° incident angle.

The as-received AM60B specimen in **Figure 5.7** observed similar corrosion products to the as-received AZ31B-H24 specimen. The most abundant corrosion products appeared to be the $Mg(OH)_2$ and the LDH phases with lower intensity peaks of the hydromagnesite phase. AM60B in the LP condition was similar to the LP AZ31B with the primary corrosion product being the LDH phase, although one peak for $Mg(OH)_2$ was also observed. The as-received and LP AZ91D specimens observed solely the LDH diffraction peaks, as shown in **Figure 5.8**. The intensity of the LDH peaks for the as-received specimen was greater than the LP condition, suggesting the corrosion product was thicker for the as-received material and possibly the reasoning for the darker surface observed in **Figure 5.4**.

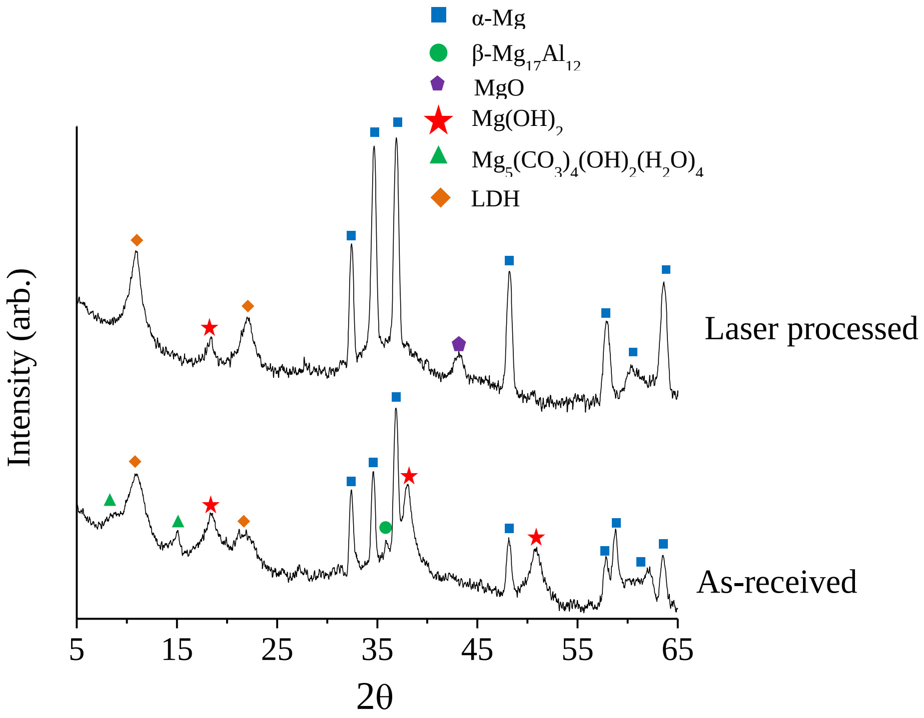

Figure 5.7: GI-XRD measurements of the AM60B corrosion product after a 21 day exposure to the B117 salt spray. The Cu-K_α (λ=1.54 Å) source was utilized at a 1.0° incident angle.

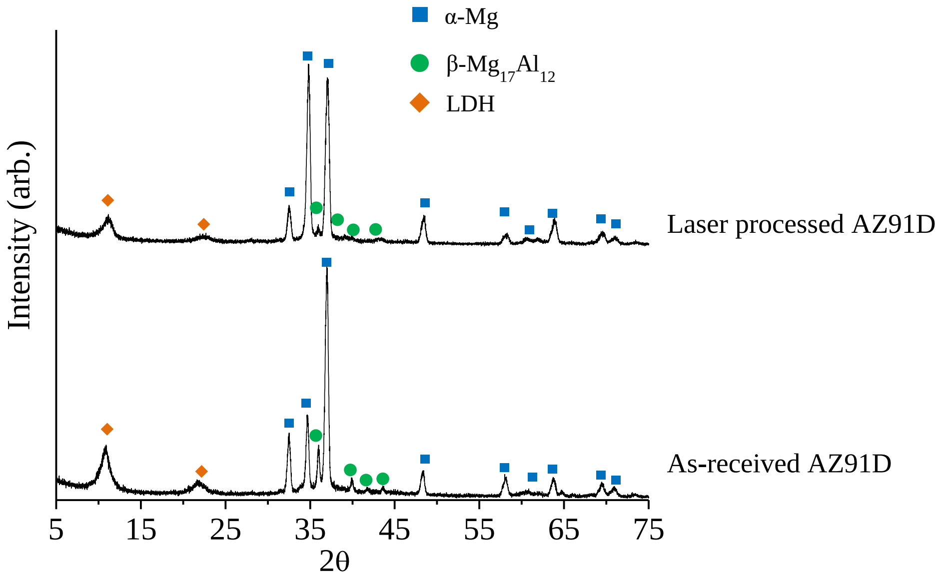

Figure 5.8: GI-XRD measurements of AZ91D corrosion product after a 21 day exposure to the B117 salt spray. The Cu-K_α (λ=1.54 Å) source was utilized at a 1.0° incident angle.

In a similar fashion to the GI-XRD analysis, attenuated total reflection – Fourier transform infrared (ATR-FTIR) was performed to verify the corrosion products on each specimen's surface after the B117 salt spray exposures. FTIR spectra were taken for all specimens prior to corrosion and revealed no response from the ATR-FTIR measurement, shown as a green line in **Figure 5.9** for a polished AZ31B-H24 surface. Identification of the FTIR peaks was performed through a detailed literature search which yielded standard FTIR spectra for the observed phases, found in **Appendix 1**. The ATR-FTIR spectra from the AZ31B-H24 specimens are presented in **Figure 5.9** and showed peaks corresponding to CO_3^{2-} and OH^- containing compounds [45]. More specifically, the CO_3^{2-} absorption bands at ~1,420 cm^{-1} and ~1,480 cm^{-1} are indicative of the hydromagnesite phase, previously observed to form during atmospheric corrosion of the pure Mg and the AZ91D alloy by Jonsson et al. [26,29]. The shoulder at ~2,980 cm^{-1} is a H_2O - CO_3^{2-} bridging mode further verifying the presence of hydromagnesite as a main corrosion product. The distinct peak at ~3,700 cm^{-1} is an indication of $Mg(OH)_2$ while the broad peak around 3,400 cm^{-1} can be attributed to OH^- stretching modes, often a sign of hydrated or hydroxide species. The peaks present for the LP and LPC specimens were less distinct with a broad peak present between 1,350 and 1,500 cm^{-1} suggesting the presence of CO_3^{2-} bonding. This broad peak may be attributed to the LDH phase which can be rich in CO_3^{2-} bonds but the indistinct peak has been attributed to a less crystalline structure and a lack of incorporation of Al cations into the LDH structure [45]. This is in strong correlation with the XRD patterns from **Figure 5.6** where the broad peaks derived from the LDH phase. In general, the AM60B ATR-FTIR investigation yielded results similar to the AZ31B-H24 specimens. The peaks corresponding to hydromagnesite were again clearly observed for the as-received AM60B specimen, shown in **Figure 5.10**, while the LP specimen had less distinct CO_3^{2-} peaks.

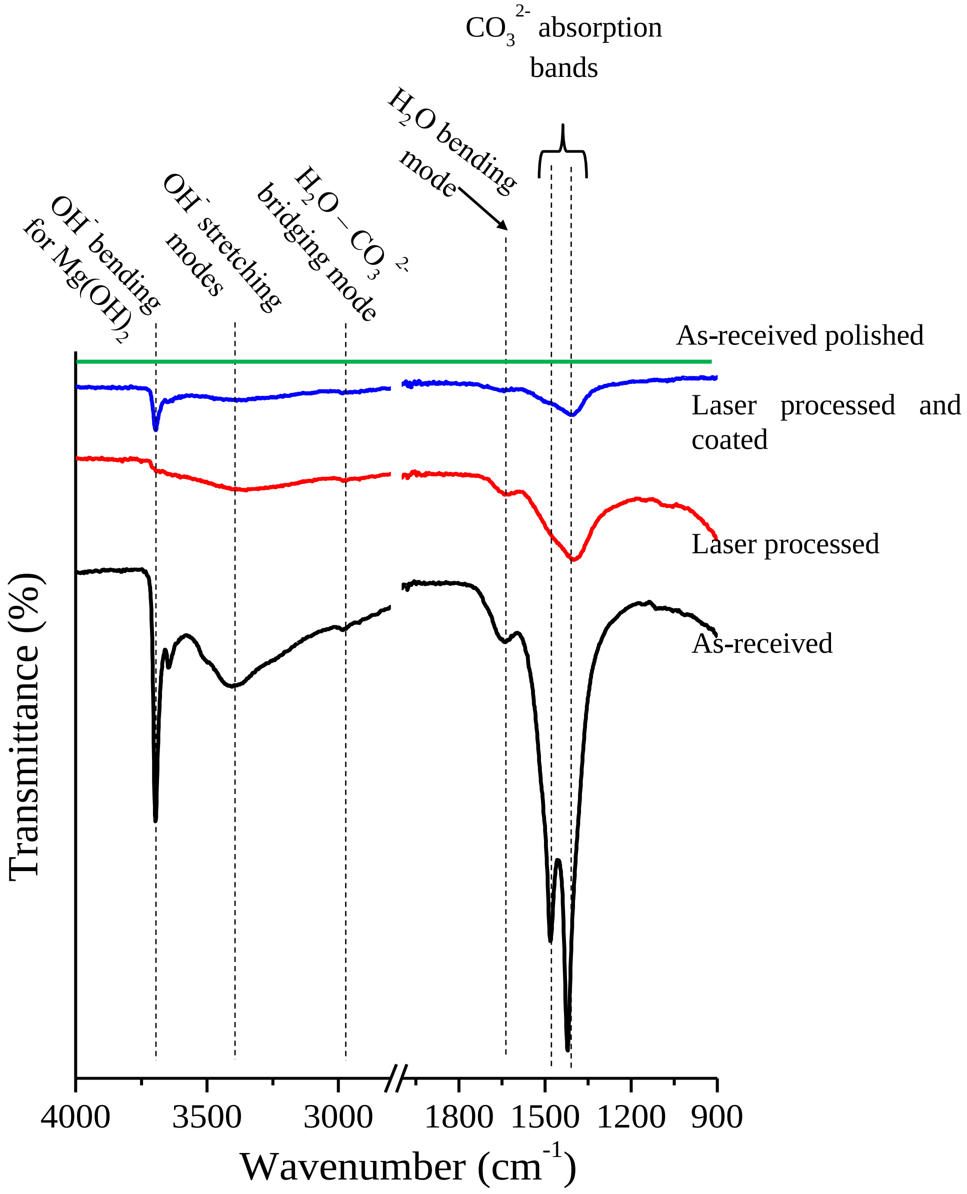

Figure 5.9: ATR-FTIR measurements of AZ31B-H24 corrosion product after a 21 day exposure to the B117 salt spray.

The ATR-FTIR spectra for the AZ91D specimens, shown in **Figure 5.11**, were slightly different from the lower Al containing alloys, as both specimens exhibited only the formation of the LDH phase as a corrosion product from GI-XRD. The existence of the CO_3^{2-} asymmetric stretching peak at ~1,370 cm^{-1} was a clear indication of the hydrotalcite (CO_3^{2-}) phase, characteristic of the CO_3^{2-} intercalation between the hydroxide sheets of the LDH when the Al content was sufficiently high [45,46]. From a study by Lin et al. on the precipitation of (Mg + Zn)/Al hydrotalcite, the broadening/indistinct CO_3^{2-} peak is characteristic of the hydrotalcite existing as an amorphous structure when the LDH phase is depleted in Al, comparable to the LP AZ31B-H24, LP AM60B, and as-received AZ91D spectra. Interestingly, the peak at 1,370 cm^{-1} becomes more distinct and intense for the LP AZ91D specimen suggesting the chemically homogenized surface allowed for a more crystalline hydrotalcite (CO_3^{2-}) phase to form.

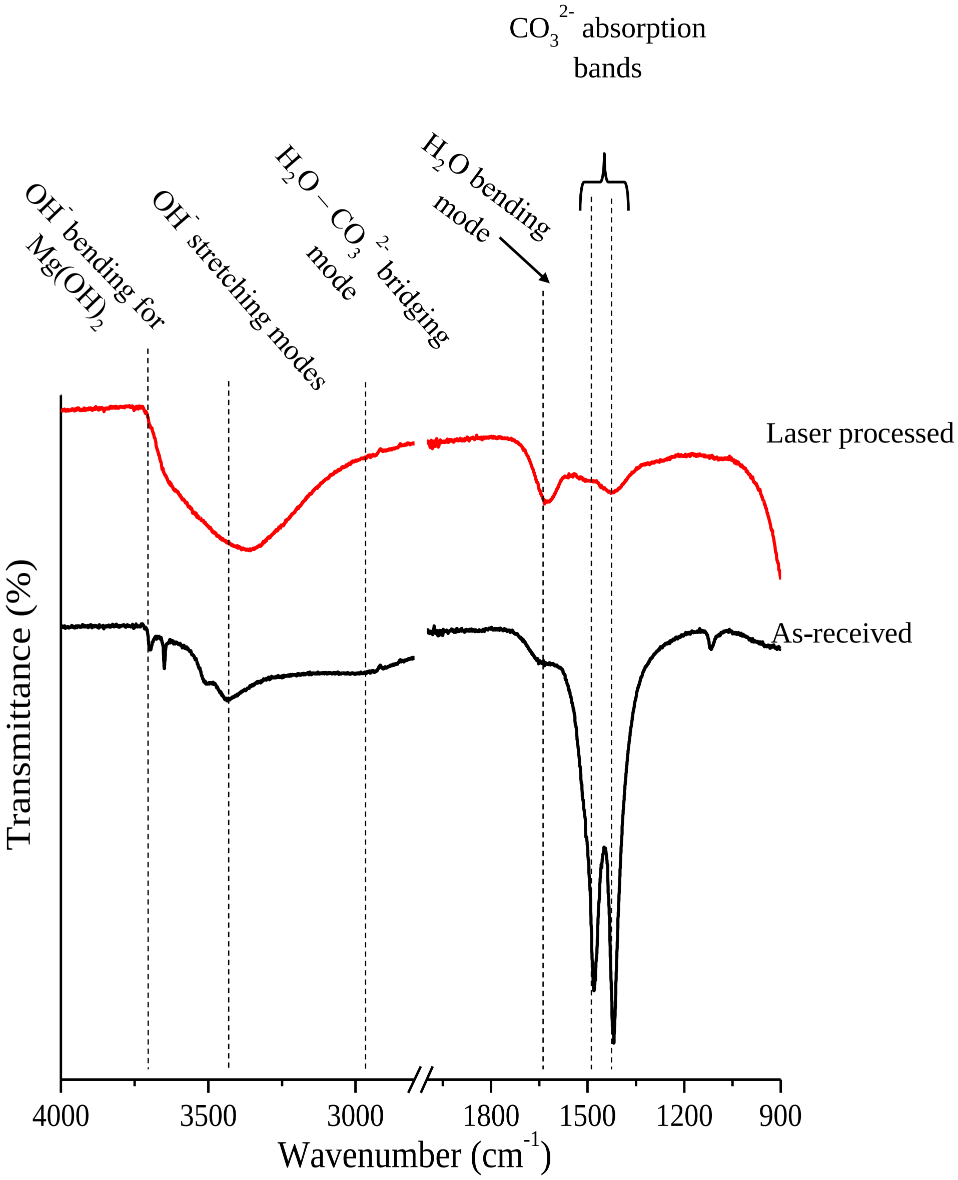

Figure 5.10: ATR-FTIR measurements of AM60B corrosion product after a 21 day exposure to the B117 salt spray.

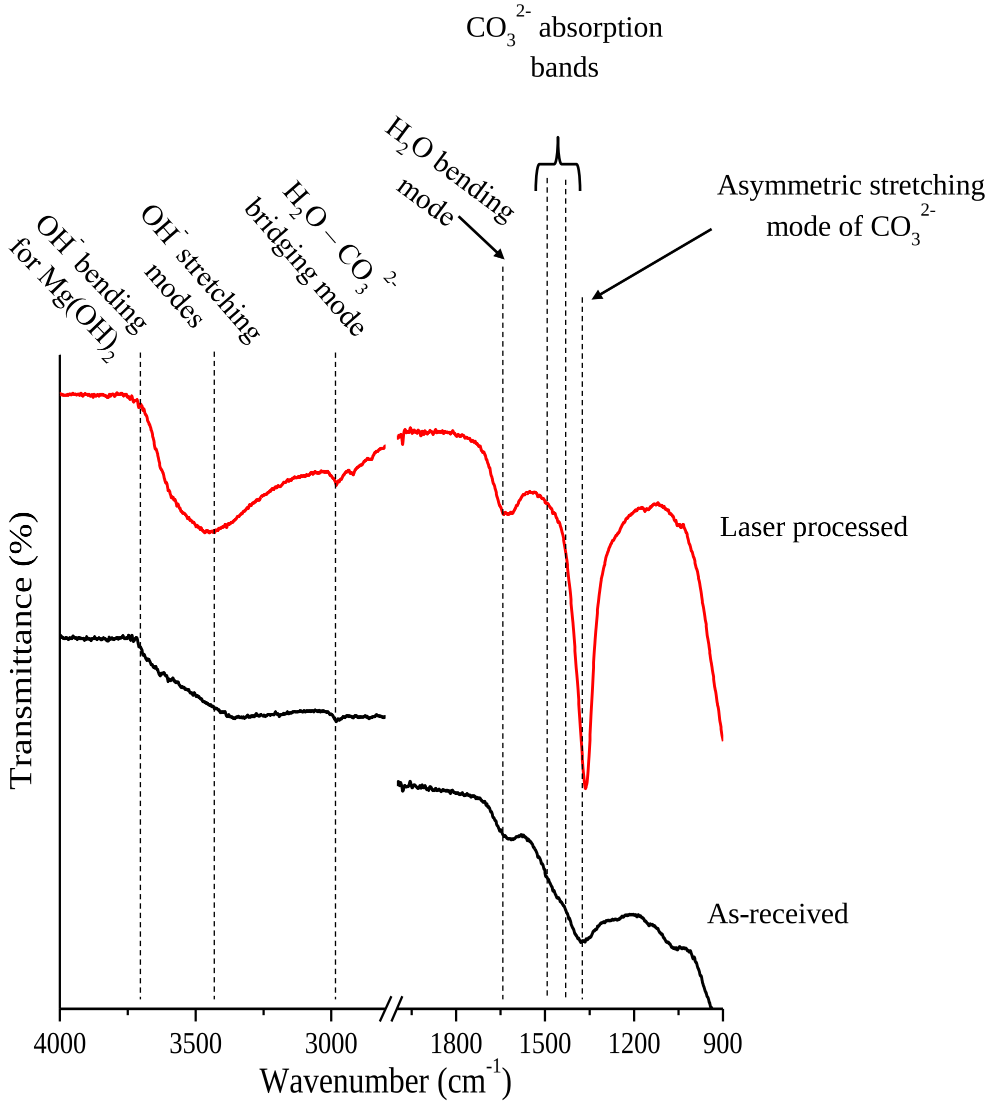

Figure 5.11: ATR-FTIR measurements of AZ91D corrosion product after a 21 day exposure to the B117 salt spray.

5.4 Discussion of salt spray results

5.4.1 Corrosion rate as determined by ASTM B117 salt spray exposures

The most unexpected result from the salt spray exposures was the 3 fold reduction in corrosion rate observed for the LP AZ31B-H24 specimens and the statistically insignificant change in corrosion rate of the cast alloys when the full immersion experiments suggested longer term protection (estimated from 3 day immersion). The reduction in micro-galvanic couples for the LP specimens likely remains as the primary mechanism for increasing the corrosion resistance, suggested from C**hapter 3**. In addition, the reappearance of the LDH corrosion product was observed for all specimens also similar to the full immersion experiments; further suggesting LDHs are one of the primary corrosion products on all Al containing Mg alloys when immersed in aqueous solutions.

The lessened reduction in corrosion rate observed on the LP specimen may be a culprit of the thin electrolyte films which developed during exposure to salt spray conditions, capable of limiting the galvanic coupled current between local cathodes and their surrounding anode [8,10,11,16,17]. Substantial research has went into quantifying these thin film electrolyte effects with some success, suggesting full immersion conditions take place with an electrolyte of ~300 μm [9]. The electrolyte thickness around which the corrosion response of an alloy is influenced is on a similar length scale as the throwing power calculations from **Figure 1.14**. If a thin electrolyte is present on a corroding surface, similar to the B117 experiment, then the available cathodic current to initiate and propagate localized corrosion may be limited, hence minimizing the typically observed impact from micro-galvanic couples in full immersion conditions. An inherent reduction in available cathodic current caused by a thin electrolyte will diminish the local corrosion impact from micro-galvanic couples for the as-received and LP specimens, minimizing the increase to corrosion resistance for the LP specimens. Consequently, the reduced gravimetric mass loss rate observed for all of the as-received specimens was expected.

The increase in NaCl concentration from 0.6 M to 0.9 M NaCl may have also played a role in the diminished improvement to the LP specimen. The more concentrated 0.9 M NaCl may have reduced the time to initiation of localized corrosion on the LP specimen in comparison to the full immersion experiments, where the onset of FFC was observed to reduce the polarization resistance of the LP specimen 5 fold.

Another influential factor the B117 exposures will show is the constant spray of fresh solution onto the surface for the entirety of the experiment. In stark contrast to the stagnant full immersion experiments, constantly replenishing the surface with fresh electrolyte will lead to the ions generated by corrosion

(Mg^{2+} and Al^{3+}/$Al(OH)_4^-$) to leave the surface, giving the alloys less time to form the LDH corrosion product if the LDH precipitates directly from solution. That said, the major barrier to initiating localized corrosion is still the reduction in cathodic particles on the LP specimen.

5.4.2 Preferred corrosion product formation during the B117 salt spray exposures

An additional factor influencing the corrosion resistance for all specimen conditions was the development of carbonate containing corrosion products that are more stable than MgO/$Mg(OH)_2$. From the GI-XRD and ATR-FTIR analysis, the three most abundant corrosion products to occur on all specimens were brucite ($Mg(OH)_2$), hydromagnesite ($Mg_5(CO_3)_4(OH)_2(H_2O)_4$), and the LDH phase. The detected corrosion products for each as-received and LP conditions are summarized in **Table 5.1**, with the accompanying non-metallic phases observed prior to the salt spray exposure.

Table 5.1: Corrosion products formed on Mg alloys after 0 and 21 day exposure to B117 salt spray. Determined by GI-XRD and ATR-FTIR.

	As-received		**Laser processed**	
	0 days	**21 days**	**0 days**	**21 days**
AZ31B-H24	MgO	LDH + $Mg(OH)_2$ + Hydromagnesite	MgO	LDH
AM60B	None	LDH + $Mg(OH)_2$ + Hydromagnesite	MgO	LDH
AZ91D	None	LDH specifically hydrotalcite (CO_3^{2-})	MgO	LDH specifically hydrotalcite (CO_3^{2-})

In previous work on the atmospheric corrosion of Mg and its alloys, the carbonate rich phases are abundant and typically credited with the improvement in corrosion resistance observed in comparison to full immersion experiments [3,5,26,29]**.** The carbonate rich phases commonly observed have a range in levels of hydration from the dehydrated phase in magnesite ($MgCO_3$) to the hydrated phases of nesquehonite ($Mg(HCO_3)(OH)\bullet 2(H_2O)$) and hydromagnesite. Previous studies by Esmaily and Jonsson predicted the thermodynamic probability and showed experimentally the formation of hydrated Mg carbonate phases in preference to magnesite, typically observing hydromagnesite [26,28]. The formations of all Mg carbonate phases are predicated on the absorption of CO_2 gas from the atmosphere into the corroding solution, which wets the surface of the alloy.

The LDH phase has been shown to form specifically on Al containing Mg alloys [3,32,35,43,47]. The expected LDH phases are meixnerite and hydrotalcite and have the general formula of [41]:

$$[M^{2+}_{1-x}\ M^{3+}_{x}(OH)_2]^{x+}\ [A^{n-}]_{x/n}\ .\ mH_2O$$

where the M^{2+} and M^{3+} represent the divalent and trivalent metal ions associated with the mixed hydroxide layers. In between the mixed hydroxide layers is a layer of charge compensating anions, A^{n-}, which can be intercalated in between the hydroxide layers, CO_3^{2-} for hydrotalcite and OH^- for meixnerite. An explanation of how these LDH phases can form on the Al containing Mg alloys was given in **section 3.3.3** and will apply here.

In order to discern the probability for precipitation of the expected corrosion products from experiments, a thermodynamic treatment of their equilibrium reactions was performed to generate stability diagrams. The corrosion products considered were:

Brucite	$Mg(OH)_2$
Hydromagnesite	$Mg_5(CO_3)_4(OH)_2(H_2O)_4$
LDH - Hydrotalcite (CO_3^{2-})	$Mg_3Al_{1.019}(CO_3)_{0.472}(OH)_{8.133}\ .\ 2.53H_2O$
LDH - Hydrotalcite (Cl^-)	$Mg_2Al(OH)_6Cl$
LDH - Meixnerite	$Mg_6Al_2(OH)_{18}\ .\ 4H_2O$

The approach analyzed the change in the compounds reaction stability over a range of pH values with respect to a change in Mg^{2+} present in solution. The Mg^{2+} ion was utilized for its commonality between all the reactions. The same set of equations were also varied with respect to the CO_2 (aq) concentration present in the solution as CO_3^{2-}, showing the dependence for hydromagnesite, and hydrotalcite (CO_3^{2-}).

The equilibrium equations used for the calculations of these stability diagrams are listed below, with in depth derivations found in **Appendix 2** [48,49,50,51,52]. Additionally the aluminate ion ($Al(OH)_4^-$) was substituted for the Al^{3+} because these phases are stable at high pH:

$$Mg(OH)_2 \leftrightarrow Mg^{2+} + 2OH^- \quad K_{sp} = 10^{-11.16} \tag{5.1}$$

$$\boldsymbol{log[Mg^{2+}] = 16.8 + 2pH}$$

$$2Mg^{2+} + Al^{3+} + Cl^- + 6OH^- \leftrightarrow Mg_2Al(OH)_6Cl \qquad K_{sp} = 10^{52.12} \tag{5.2}$$

$$\mathbf{log}[\boldsymbol{Mg^{2+}}] = \boldsymbol{6.46 - pH} \qquad [Cl^-] = 0.9\ \mathrm{M} \text{ and } [Al(OH)_4^-] = 1 \times 10^{-4}\ \mathrm{M}$$

$$3Mg^{2+} + 1.019Al^{3+} + 0.472CO_3^{2-} + 8.133OH^- + 2.53H_2O \leftrightarrow Mg_3Al_{1.019}(CO_3)_{0.472}(OH)_{8.133} \cdot 2.53H_2O \ K_{sp} = 10^{68.9} \tag{5.3}$$

$$\boldsymbol{log[Mg^{2+}] = 11.84 - \frac{4.98}{3}\,pH} \qquad [Al(OH)_4^-] = 1 \times 10^{-4}\ \mathrm{M}$$

$$Mg_5(CO_3)_4(OH)_2 \cdot 4H_2O + 2H^+ \leftrightarrow 5Mg^{2+} + 4CO_3^{2-} + 6H_2O(l) \quad K_{sp} = 10^{-12.1} \tag{5.4}$$

$$\boldsymbol{log[Mg^{2+}] = 14.86 - 2pH}$$

$$6Mg(OH)_2 + 2Al(OH)_3 + 4H_2O \leftrightarrow Mg_6Al_2(OH)_{18} \cdot 4H_2O \qquad K_{sp} = 10^{10.1} \tag{5.5}$$

$$\boldsymbol{log[Mg^{2+}] = 11.92 - \frac{5}{3}pH} \qquad [Al(OH)_4^-] = 1 \times 10^{-4}\ \mathrm{M}$$

The results of these equations are presented in **Figure 5.12** with the plot in **a)** showing the corrosion products dependence with respect to pH and [Mg^{2+}] concentration at a constant $P_{CO2}= 10^{-3.5}$ atm content and **b)** revealed the corrosion products dependence with respect to pH and P_{CO2} at a constant $[Mg^{2+}]=10^{-4}$ M. In all cases, the area of the plots in the lower left represent where the Mg^{2+} will be stable while the upper right of the plots represent where the corrosion product under consideration will be stable. Therefore the most stable phase with respect to pH and Mg^{2+} content at the atmosphere's level of P_{CO2}

will be hydromagnesite [26,28]. The inlaid plot in **Figure 5.12 a** reveals how a variation in pH by ~0.2 will change the preferred corrosion product from hydromagnesite to meixnerite and hydrotalcite (CO_3^{2-}). The plot in **Figure 5.12 b** reveals the sensitivity of the hydromagnesite phase to P_{CO2} content and reveals the hydrotalcite (CO_3^{2-}) followed by the meixnerite phase becomes more stable than the hydromagnesite phase after a small reduction ($10^{-3.5}$ to $10^{-3.1}$ atm) in P_{CO2}. Regardless of the phase, all carbonate containing corrosion products and LDH phases will be more stable than $Mg(OH)_2$ on its own. It is also interesting to note the meixnerite phase will have no dependence on P_{CO2} content and was found to be more stable, in general, than the hydrotalcite (Cl^-) and hydrotalcite (CO_3^{2-}) phase.

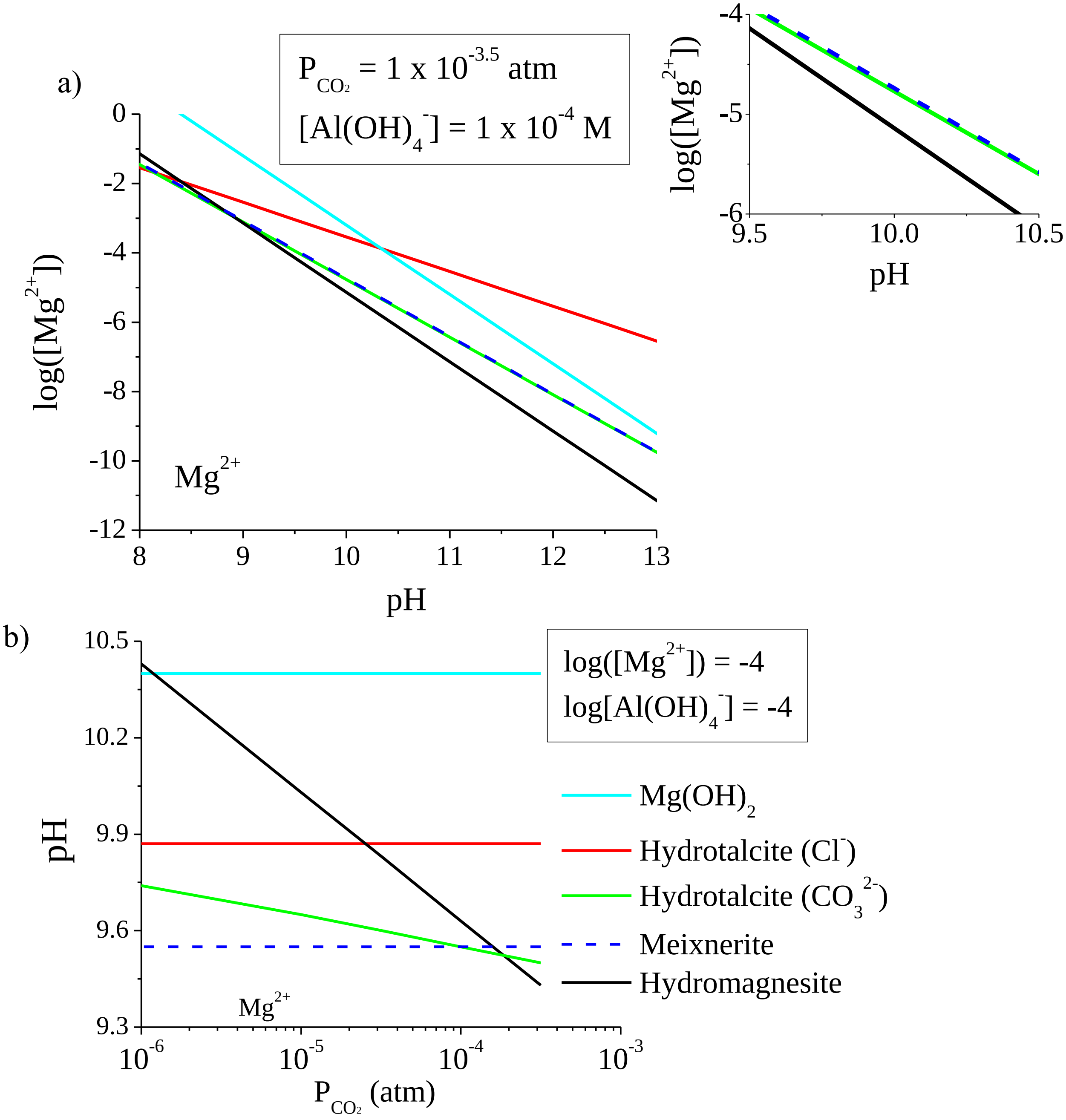

Figure 5.12: Plots for the thermodynamic stability of the experimentally observed corrosion products of the Mg alloys after salt spray exposure for **a)** pH versus Mg^{2+} concentration at a constant $P_{CO2} = 1 \times 10^{-3.5}$, and **b)** P_{CO2} versus pH at a constant $[Mg^{2+}] = 1 \times 10^{-4}$ M. Other constants are $[Cl^{-}] = 0.9$ M and $[Al(OH)_4^{-}] = 1 \times 10^{-4}$ M.

The thermodynamic analysis in conjuncture with the experimental results in **section 5.3** helps describe the interplay between the corrosion products formed on each Al containing Mg alloy. For the AZ91D alloy, the only detectable corrosion product was the LDH phase and from FTIR, in **Figure 5.11**, it was verified by the asymmetric stretching mode for CO_3^{2-} to be the hydrotalcite (CO_3^{2-}) phase. The previous explanation of the LDH formation under full immersion conditions from **section 3.3.3** applies here with sufficient Al ions required for the precipitation of the hydrotalcite (CO_3^{2-}) phase. An additional complexity for the salt spray exposures is the cycling of electrolyte on the alloy surface indicating less time for the electrolyte to produce sufficient Al ions for the LDH precipitation, assuming the expected precipitation path way is by aluminate ion incorporation into the $Mg(OH)_2$ structure. However, the abundance of Al present in the AZ91D alloy made it possible for the Mg^{2+}/Al^{3+} ratio to be met and allowed for the hydrotalcite (CO_3^{2-}) precipitation.

The as-received AZ31B-H24 and AM60B showed hydromagnesite and $Mg(OH)_2$ as the most abundant corrosion products, with signs of a LDH phase. The LDH phase was observed for both alloys from GI-XRD however the asymmetric peak at 1,370 cm^{-1} was not observed by FTIR, suggesting the CO_3^{2-} absorption peaks were primarily from hydromagnesite, in **Figure 5.6**, **Figure** 5.7, **Figure** 5.9, and **Figure** 5.10. This suggests the LDH phase formed was most likely meixnerite, correlating well with the expected thermodynamic stability from **Figure 5.12** where hydromagnesite was found to be stable at lower pH and high P_{CO2} values than hydrotalcite (CO_3^{2-}). If we assume a majority of the CO_3^{2-} was used for the formation of hydromagnesite, then the Al cations present in solution could lead to the formation of meixnerite and the observed XRD peaks at $2\theta = 11^o$ and 22.5^o in **Figure 5.6** and **Figure** 5.7. The LP AM60B and LP AZ31B-H24 observed GI-XRD peaks indicative of LDH as their only corrosion product. However, the asymmetric peak from FTIR for the hydrotalcite (CO_3^{2-}) phase was not observed for the LP AM60B and AZ31B-H24 surfaces, in **Figure 5.9** and **Figure** 5.10, suggesting meixnerite or possibly a non-crystalline LDH phase with a mixed intercalated anion of OH^- and CO_3^{2-} [45].

Irrespective of the exact compound of LDH which develops, the formation as an abundant corrosion product across the corroding surface has been shown regardless of the Al containing Mg alloy and regardless of the chemical homogeneity present at the alloys surface. The chemical homogenization provided by laser processing helps suppress the formation of other potential corrosion products like hydromagnesite and $Mg(OH)_2$ by limiting the intense localized corrosion typical for these alloys. A reduction in localized corrosion slows the general corrosion rate of the alloy, limiting the increase in pH and Mg^{2+} concentration of the corroding electrolyte, both of which are necessary for the precipitation of the corrosion products.

Overall, the work of this thesis suggests all Al containing Mg alloys are capable of forming a LDH phase, even in aggressive corrosive electrolytes like 0.9 M NaCl and without a chemically homogeneous microstructure. A special conversion coating process is not required for the precipitation of a LDH phase on these alloys. That means future analysis of Al containing Mg alloys should consider LDH phase production, in particular when localized corrosion (like FFC) is not observed.

The formation of LDH phases for the purpose of improved corrosion resistance has gained significant attention recently and has been billed as an environmentally friendly conversion coating. That said, a conversion coating process could be tailored to optimize the formation of the most stable LDH phase (containing CO_3^{2-}) likely increasing the time to initiation of FFC on the LP Mg alloys further [42,43].

5.5 Summary of B117 results

The artificial atmospheric exposure test, ASTM B117, has been utilized to observe the accelerated atmospheric corrosion behavior of the LP Al containing Mg alloys used in this thesis. In comparison to their as-received alloy condition, LP of the alloys improved the corrosion resistance of all alloys albeit less dramatically than predicted by full immersion experiments. Analysis of corrosion product after a 21 day salt spray exposure revealed the precipitation of hydromagnesite, $Mg(OH)_2$, and a LDH phase, with a summary of what corrosion products were observed on what specimen in **Table 5.1**. Corroboration of the detected corrosion products was performed by thermodynamic stability diagrams which suggest the precipitation of hydromagnesite, hydrotalcite (CO_3^{2}), and meixnerite were all more likely than $Mg(OH)_2$.

In addition the LDH phases become more thermodynamically favorable to form than hydromagnesite at lower P_{CO2} levels.

5.6 References

---

[1] T.B. Abbott, Magnesium: Industrial and Research Developments Over the Last 15 Years, Corrosion, 71 (2015) 120-127.

[2] T.L. Jones, Labukas, J.P., Placzankis, B.E., Kondoh, K., Ballistic and Corrosion Analysis of New Military-Grade Magnesium Alloys AMX602 and ZAXE1711 for Armor Applications, U.S. Army Research Laboratory, Aberdeen Proving Ground, MD, 2012, pp. 1-50.

[3] M. Esmaily, J.E. Svensson, S. Fajardo, N. Birbilis, G.S. Frankel, S. Virtanen, R. Arrabal, S. Thomas, L.G. Johansson, Fundamentals and advances in magnesium alloy corrosion, Progress in Materials Science, 89 (2017) 92-193.

[4] J. Alcántara, D.d.l. Fuente, B. Chico, J. Simancas, I. Díaz, M. Morcillo, Marine Atmospheric Corrosion of Carbon Steel: A Review, Materials, 10 (2017) 406.

[5] J. Liao, M. Hotta, Atmospheric corrosion behavior of field-exposed magnesium alloys: Influences of chemical composition and microstructure, Corrosion Science, 100 (2015) 353-364.

[6] Z. Cui, X. Li, K. Xiao, C. Dong, Atmospheric corrosion of field-exposed AZ31 magnesium in a tropical marine environment, Corrosion Science, 76 (2013) 243-256.

[7] N. LeBozec, M. Jönsson, D. Thierry, Atmospheric Corrosion of Magnesium Alloys: Influence of Temperature, Relative Humidity, and Chloride Deposition, Corrosion, 60 (2004) 356-361.

[8] E. Schindelholz, B.E. Risteen, R.G. Kelly, Effect of Relative Humidity on Corrosion of Steel under Sea Salt Aerosol Proxies: I. NaCl, Journal of The Electrochemical Society, 161 (2014) C450-C459.

[9] X. Zhang, S. Yang, W. Zhang, H. Guo, X. He, Influence of outer rust layers on corrosion of carbon steel and weathering steel during wet–dry cycles, Corrosion Science, 82 (2014) 165-172.

[10] B.E. Risteen, E. Schindelholz, R.G. Kelly, Marine Aerosol Drop Size Effects on the Corrosion Behavior of Low Carbon Steel and High Purity Iron, Journal of The Electrochemical Society, 161 (2014) C580-C586.

[11] C.-Q. Cheng, L.-I. Klinkenberg, Y. Ise, J. Zhao, E. Tada, A. Nishikata, Pitting corrosion of sensitised type 304 stainless steel under wet–dry cycling condition, Corrosion Science, 118 (2017) 217-226.

[12] F. Mansfeld, J.V. Kenkel, ELECTROCHEMICAL MONITORING OF ATMOSPHERIC CORROSION PHENOMENA, Corrosion Science, 16 (1976) 111-122.

[13] S.D. Cramer, A.I.H. Committee, B.S. Covino, ASM Handbook, ASM International, 2005.

[14] D.A. Jones, Principles and Prevention of Corrosion: Pearson New International Edition, Pearson Education, Limited, 2013.

[15] N.V.d. Steen, H. Simillion, D. Thierry, H. Terryn, J. Deconinck, Comparing Modeled and Experimental Accelerated Corrosion Tests on Steel, Journal of The Electrochemical Society, 164 (2017) C554-C562.

[16] A. Nishikata, Y. Ichihara, Y. Hayashi, T. Tsuru, Influence of Electrolyte Layer Thickness and pH on the Initial Stage of the Atmospheric Corrosion of Iron, Journal of Electrochemical Society, 144 (1997) 1244-1252.

[17] T. Zhang, C. Chen, Y. Shao, G. Meng, F. Wang, X. Li, C. Dong, Corrosion of pure magnesium under thin electrolyte layers, Electrochimica Acta, 53 (2008) 7921-7931.

[18] Y.L. Cheng, Z. Zhang, F.H. Cao, J.F. Li, J.Q. Zhang, J.M. Wang, C.N. Cao, A study of the corrosion of aluminum alloy 2024-T3 under thin electrolyte layers, Corrosion Science, 46 (2004) 1649-1667.

[19] P. Khullar, J.V. Badilla, R.G. Kelly, Cathodic Control of Intergranular Corrosion Propagation in Al-Mg Alloys Under Thin Film Conditions, Corrosion, 72 (2016) 1223-1225.

[20] J. Liao, M. Hotta, S.-i. Motoda, T. Shinohara, Atmospheric corrosion of two field-exposed AZ31B magnesium alloys with different grain size, Corrosion Science, 71 (2013) 53-61.

[21] D. Xia, S. Song, W. Jin, J. Li, Z. Gao, J. Wang, W. Hu, Atmospheric corrosion monitoring of field-exposed Q235B and T91 steels in Zhoushan offshore environment using electrochemical probes, Journal of Wuhan University of Technology-Mater. Sci. Ed., 32 (2017) 1433-1440.

[22] M.-C. Zhao, P. Schmutz, S. Brunner, M. Liu, G.-l. Song, A. Atrens, An exploratory study of the corrosion of Mg alloys during interrupted salt spray testing, Corrosion Science, 51 (2009) 1277-1292.

[23] C. Leygraf, I.O. Wallinder, J. Tidblad, T. Graedel, Atmospheric Corrosion, Wiley, 2016.

[24] D. Liang, H.C. Allen, G.S. Frankel, Z.Y. Chen, R.G. Kelly, Y. Wu, B.E. Wyslouzil, Effects of Sodium Chloride Particles, Ozone, UV, and Relative Humidity on Atmospheric Corrosion of Silver, Journal of The Electrochemical Society, 157 (2010) C146.

[25] S. Zakipour, J. Tidblad, C. Leygraf, Atmospheric Corrosion Effects of SO2, NO2, and O3, Journal of Electrochemical Society, 144 (1997) 3513-3517.

---

[26] M. Jönsson, D. Persson, D. Thierry, Corrosion product formation during NaCl induced atmospheric corrosion of magnesium alloy AZ91D, Corrosion Science, 49 (2007) 1540-1558.

[27] M. Jönsson, D. Persson, R. Gubner, The Initial Steps of Atmospheric Corrosion on Magnesium Alloy AZ91D, Journal of The Electrochemical Society, 154 (2007) C684.

[28] M. Esmaily, P. Malmberg, M. Shahabi-Navid, J.E. Svensson, L.G. Johansson, A ToF-SIMS investigation of the corrosion behavior of Mg alloy AM50 in atmospheric environments, Applied Surface Science, 360 (2016) 98-106.

[29] R. Lindström, J.E. Svensson, L.G. Johansson, The Influence of Carbon Dioxide on the Atmospheric Corrosion of Some Magnesium Alloys in the Presence of NaCl, Journal of The Electrochemical Society, 149 (2002) B103.

[30] M. Shahabi-Navid, M. Esmaily, J.E. Svensson, M. Halvarsson, L. Nyborg, Y. Cao, L.G. Johansson, NaCl-Induced Atmospheric Corrosion of the MgAl Alloy AM50-The Influence of CO_2, Journal of The Electrochemical Society, 161 (2014) C277-C287.

[31] S. Feliu Jr, M.C. Merino, R. Arrabal, A.E. Coy, E. Matykina, XPS study of the effect of aluminium on the atmospheric corrosion of the AZ31 magnesium alloy, Surface and Interface Analysis, 41 (2009) 143-150.

[32] M. Esmaily, J.E. Svensson, L.G. Johansson, Corrosion of Magnesium-Aluminum (Mg-Al) Alloys - An Interplay Between Al Content and CO_2, in: K. Solanki, D. Orlov, A.N. Singh, N.R. (Eds.) TMS 2017, Springer, San Diego, CA, 2017, pp. 397-403.

[33] M. Pourbaix, Lectures on Electrochemical Corrosion, Springer US, 2012.

[34] M. Esmaily, M. Shahabi-Navid, J.E. Svensson, M. Halvarsson, L. Nyborg, Y. Cao, L.G. Johansson, Influence of temperature on the atmospheric corrosion of the Mg–Al alloy AM50, Corrosion Science, 90 (2015) 420-433.

[35] C.B. Baliga, P. Tsakiropoulos, Development of corrosion resistant magnesium alloys Part 2 Structure of corrosion products on rapidly solidified Mg-16Al alloys, Materials Science and Technology, 9 (1993) 513-519.

[36] S. Mathieu, C. Rapin, J. Steinmetz, P. Steinmetz, A corrosion study of the main constituent phases of AZ91 magnesium alloys, Corrosion Science, 45 (2003) 2741-2755.

[37] NOAA, Trends in Atmospheric Carbon Dioxide, U.S. Department of Commerce, https://www.esrl.noaa.gov/gmd/ccgg/trends/, 2017.

[38] B. Vasel, B. Hall, B. Johnson, K. Lantz, A. Reiser, C. Schultz, P. Sheridan, J. Singewald, D. Stanitski, P. Tans, Global Monitoring Division Summary Report No. 28, in: B. Vasel (Ed.) Earth System Research Laboratory Global Monitoring Division, Boulder, Co, 2016, pp. 1-143.

[39] A.D. King, B. Kannan, J.R. Scully, Environmental Degradation of a Mg-Rich Primer in Selected Field and Laboratory Environments: Part 1—Without a Topcoat, Corrosion, 70 (2014) 512-535.

[40] A.S. G1, Standard Practice for Preparing, Cleaning, and Evaluating Corrosion Test Specimens, ASTM International, West Conshohocken, PA, 2011.

[41] V. Rives, Layered Double Hydroxides: Present and Future, Nova Science Publishers, 2001.

[42] J. Chen, Y. Song, D. Shan, E.-H. Han, Study of the in situ growth mechanism of Mg–Al hydrotalcite conversion film on AZ31 magnesium alloy, Corrosion Science, 63 (2012) 148-158.

[43] J.K. Lin, J.Y. Uan, Formation of Mg,Al-hydrotalcite conversion coating on Mg alloy in aqueous HCO3−/CO32− and corresponding protection against corrosion by the coating, Corrosion Science, 51 (2009) 1181-1188.

[44] Z.P. Xu, G.Q. Lu, Hydrothermal Synthesis of Layered Double Hydroxides (LDHs) from Mixed MgO and Al2O3: LDH Formation Mechanism, Chem. Mater., 17 (2005) 1055-1062.

[45] J.-K. Lin, K.-L. Jeng, J.-Y. Uan, Crystallization of a chemical conversion layer that forms on AZ91D magnesium alloy in carbonic acid, Corrosion Science, 53 (2011) 3832-3839.

[46] M.A. Aramendia, Y. Aviles, V. Borau, J.M. Luque, J.M. Marinas, J.R. Ruiz, F.J. Urbano, Thermal decomposition of Mg/Al and Mg/Ga layered-double hydroxides: a spectroscopic study, Journal of Materials Chemistry, 9 (1999) 1603-1607.

[47] R.C. Phillips, J.R. Kish, Nature of Surface Film on Matrix Phase of Mg Alloy AZ80 Formed in Water, Corrosion, 69 (2013) 813-820.

[48] H. Tamura, J. Chiba, M. Ito, T. Takeda, S. Kikkawa, Y. Mawatari, M. Tabata, Formation of hydrotalcite in aqueous solutions and intercalation of ATP by anion exchange, Journal of Colloid and Interface Science, 300 (2006) 648-654.

[49] J.W. Boclair, P.S. Braterman, Layered Double Hydroxide Stability. 1. Relative Stabilities of Layered Double Hydroxides and Their Simple Counterparts, Chem. Mater., 11 (1999) 298-302.

[50] W. Stumm, J.J. Morgan, Aquatic Chemistry: Chemical Equilibria and Rates in Natural Waters, Wiley, 2012.

[51] K. Rozov, U. Berner, C. Taviot-Gueho, F. Leroux, G. Renaudin, D. Kulik, L.W. Diamond, Synthesis and characterization of the LDH hydrotalcite–pyroaurite solid-solution series, Cement and Concrete Research, 40 (2010) 1248-1254.

---

[52] Y. Xiong, Experimental determination of solubility constant of hydromagnesite (5424) in NaCl solutions up to 4.4m at room temperature, Chemical Geology, 284 (2011) 262-269.

Page intentionally left blank.

Chapter 6: Summary and future work

This thesis investigated the impact excimer laser processing has on the chemical homogenization of three Mg alloys (AZ31B-H24, AM60B, and AZ91D) and elaborates on the key mechanisms for promoting the dissolution of secondary phase particles by laser processing; solid-liquid diffusion and liquid mixing aided by the plasma pressure wave. Laser processing was most successful at dissolving secondary phase particles at or below a radius of 250 nm. The larger, often higher melting temperature phases composed of Al and Mn, were seldom completely dissolved. That said, the resulting material transport generated by the plasma pressure wave led to significant coverage of the larger particles with liquid Mg, minimizing their impact as effective cathodes during corrosion. The exploration of laser processing parameters (fluence, pulse per area, and pressure) helped optimize the laser treatment for chemical homogenization and the reduction in the corrosion rate of these alloys in chloride containing aqueous solutions.

The corrosion response for all laser processed alloys exhibited an increase in initiation time of filiform-like corrosion (FFC). Typical FFC initiation times for the as-received alloys immersed in stagnant 0.6 M NaCl was 10 and 60 minutes for the wrought and cast alloys, respectively. The initiation times were extended to 1,440 and 3,600 minutes for the laser processed wrought and cast alloys, respectively. This increase in FFC initiation time has never been observed for these alloys without the application of a coating. Time dependent electrochemical impedance measurements demonstrated an order of magnitude increase in global polarization resistance for the laser processed alloys in comparison to their as-received condition, which persisted until FFC was initiated. In addition, a laser processed AZ31B-H24 specimen which was scratched through to the underlying bulk material exhibited similar delay of FFC initiation, similar to a scratch protective coating such as galvanizing.

Another critical finding in this section showed that all specimens were capable of forming a LDH phase as a corrosion product. The somewhat uniform coverage of the LDH phase on all alloy surfaces, as-received and laser processed, suggest the suppression of FFC initiation is mostly controlled by the lack of secondary phase particles present at the laser processed surface. The LDH phase may be more stable and precipitate at a lower pH than $Mg(OH)_2$, the corrosion product commonly considered to form, however the intensity of the micro-galvanic couples generated by the as-received alloys heterogeneous microstructures leads to the initiation of FFC regardless of the corrosion product.

The time to FFC initiation was further increased after the application of a multilayered coating on a laser processed AZ31B-H24 specimen, composed of $MgO/Mg(OH)_2$ and $Gd(OH)_3$. The coating acted primarily as a passive layer, preventing the corrosive media from reaching the underlying AZ31B-H24. As the coating began to degrade, a re-passivating like phenomenon occurred, which was paramount in extending the time for FFC initiation of the laser processed AZ31B-H24 alloy to 4,320 minutes versus 1,440 minutes.

Finally, accelerated atmospheric corrosion exposures were performed on all Mg alloys examined in this study utilizing the ASTM B117 standard experiment. Overall, the gravimetric mass loss results determined a reduction in corrosion rate for all laser processed specimens in comparison to their as-received condition. The stability of these LDH phases (hydrotalcite/meixnerite) was verified through thermodynamic calculations and found to be more likely to form than $Mg(OH)_2$ and hydromagnesite (at $P_{CO_2} < 1x10^{-4}$ atm). The LDHs were more readily detected on the laser processed specimens, a result of the less intense and lower coverage of localized corrosion.

Future work: There have been a number of projects spawned from my thesis work with the potential for many more. The studies investigating a change in electrochemical response (impedance) in correlation with the changing corrosion morphology is an area of great interest, found in **section 1.6**. Preliminary results have suggested the corrosion mechanism controlling stage II FFC is different than stage III from a change in time impedance time constants. It is hypothesized that the shift from stage II to stage III FFC will modify the source of the “remote anodic current” which is a controlling factor in the propagation of the corrosion filaments. Results of impedance measurements taken at anodic potentials has observed the existence of several inductive loops for the AZ31B specimen while immersed in NaCl solutions, with the time constants for these inductive loops changing upon the shift from stage II to stage III FFC. The use of rotating disc electrode experiments would accompany these impedance experiments to control the mass transport of Cl^- ions to the materials surface, assumed to be a critical factor of the initiation and propagation of FFC, and likely an integral part of the corrosion mechanism.

This thesis hypothesized the improvement to the corrosion resistance of laser processed specimens was dictated by the mitigation of micro-galvanic coupling while the formation of a LDH phase was observed to form on all surfaces, regardless of their microstructure. Investigations are required to define the stability and precipitation route of the LDH formed on the Mg alloy surfaces, in particular for the case of a solution without CO_3^{2-} present (does CO_2 play a leading role in the LDH formation?). A primary study would utilize a pure Mg substrate and observe the corrosion products formed when immersed in solutions of varying pH, Al ion content (Al^{3+} / $Al(OH)_4^-$), and CO_3^{2-} content. From a more practical application, the AZ91D alloys with their abundant Al content appeared to form the LDH easily, and experiments could be devised to observe this precipitation reaction, possibly using an *in situ* electrochemical cell in a TEM. Studies without CO_3^{2-} present in the solution could determine if the meixnerite phase is the likely alternative to hydrotalcite, and if it will form in Cl^- containing solutions as well. In a similar vein, the possibility for the LDH to absorb Cl^- ions could be investigated, even in the presence of CO_3^{2-} which is prescribed as the most stable anion to intercalate into the LDH structure.

The analytical calculations performed to describe the laser processing study could be applied to a number of other Mg or Al alloys, such as WE43B, with a different set of secondary phase particles and allow for similar chemical homogenization of the surface microstructure. Characterization of these new laser processed alloys could critically look at the dissolution of prominent secondary phases and the resulting corrosion product.

The use of excimer laser processing of Mg alloy weld zones is hypothesized to mitigate the macroscale galvanic corrosion between weld zones for autogenously and heterogeneously welded material. Preliminary work has shown the ability of laser processing to mitigate the galvanic coupling between autogenous weld zones, however the current studies were performed for the ideal situation of a polished surface. Corrosion experiments are currently being prepared for autogenously and heterogeneously welded AZ31B plate with and without a laser treatment, utilizing an atmospheric corrosion exposure. The chemically homogeneous microstructures produced by laser processing are expected to equalize the corrosion potential at each weld zone, reducing the driving force for galvanic coupling. Another route for this work could observe the impact laser processing has on dissimilar welds between Mg and Al alloys, potentially creating a less abrupt chemical gradient leading to a less severe galvanic coupling. Additional atmospheric exposures could also be pursued with the inclusion of drying and wetting cycles or a more realistic salt solution to sea water. Specimens could also be sent to the Kennedy space center (or Birdwood) for actual outdoor corrosion exposure.

Future work regarding the Mg/Gd coated specimens should include pretreatment experiments of the coatings themselves using phosphate based solutions. The phosphate phases formed by Mg and Gd are vastly superior in thermodynamic stability with respect to these elements hydroxide phases. A laser processing pretreatment should still be applied as a reduction in the general corrosion rate will still be beneficial. Additionally, if conversion of the coating can yield a Mg or Gd phosphate, then the protection afforded in NaCl containing solutions should exceed what was previously observed, where this conversion like step occurred in the NaCl solution.

Finally, it is hypothesized the multilayered Mg/Gd coating will dramatically improve the corrosion resistance and cell viability of a Mg alloy utilized as an implant because the Gd portion of the coating will convert to the very stable Gd phosphate, slowing the corrosion of the underlying Mg alloy and allow it to form its own stable phosphate corrosion product. Additional studies are in progress to observe the laser processed and the coated specimen’s cell viability, cell adherence, and corrosion rate while immersed in minimum essential media (MEM). A patent has been applied for with regards to this coating and laser processing strategy for Mg alloys used as implants.

Page intentionally left blank.

Appendix 1: Standard measurements for ATR-FTIR and XRD.

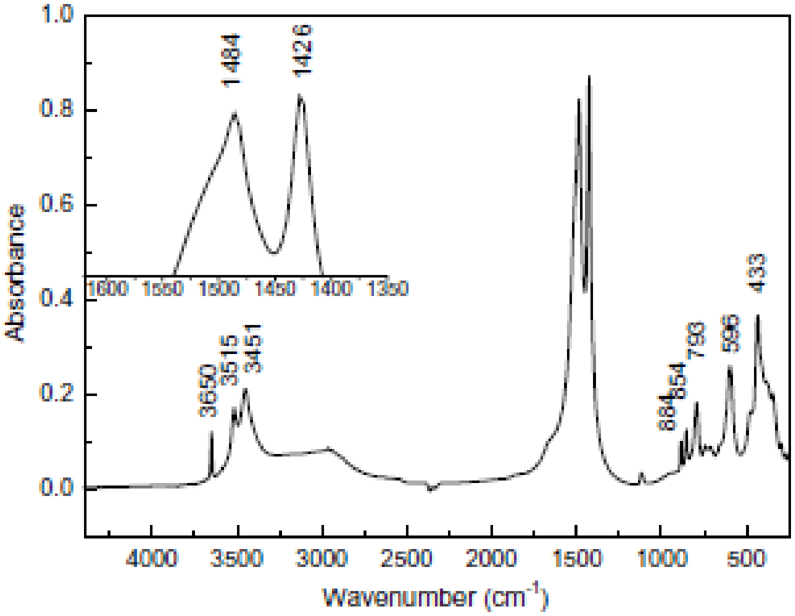

IR absorption spectra for hydromagnesite, in top left is zoomed in on the CO_3^{2-} asymmetric bending peaks.

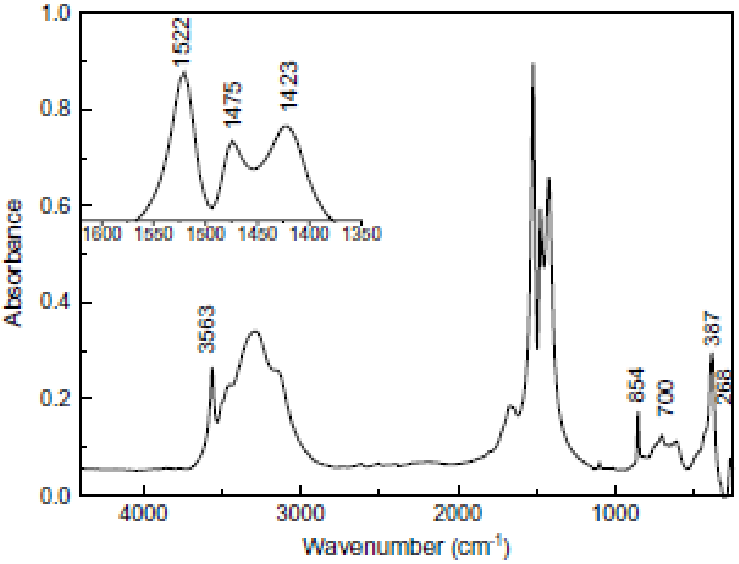

IR absorption spectra for nesquehonite, in top left is zoomed in on the CO_3^{2-} asymmetric bending peaks.

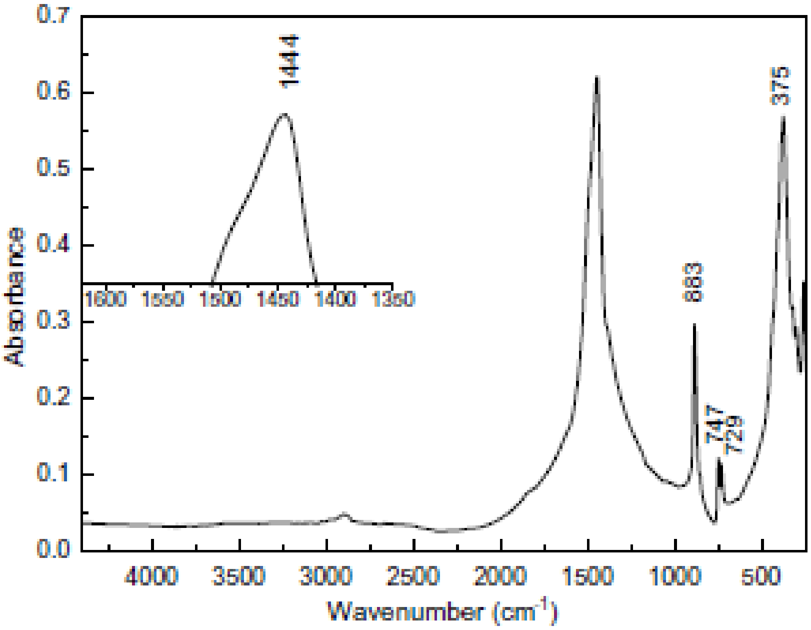

IR absorption spectra for magnesite, in top left is zoomed in on the CO_3^{2-} asymmetric bending peak.

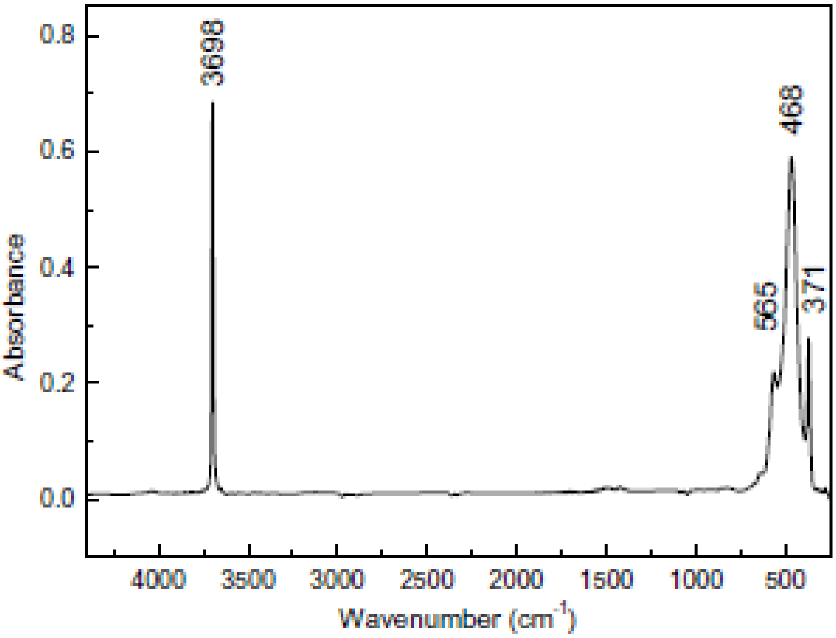

IR absorption spectra for brucite ($Mg(OH)_2$).

M. Jonsson, D. Persson, D.Thierry, “Corrosion product formation during NaCl induced atmospheric corrosion of magnesium alloy AZ91D”, Corrosion Science, 2007, vol. 49, 1540-1558.

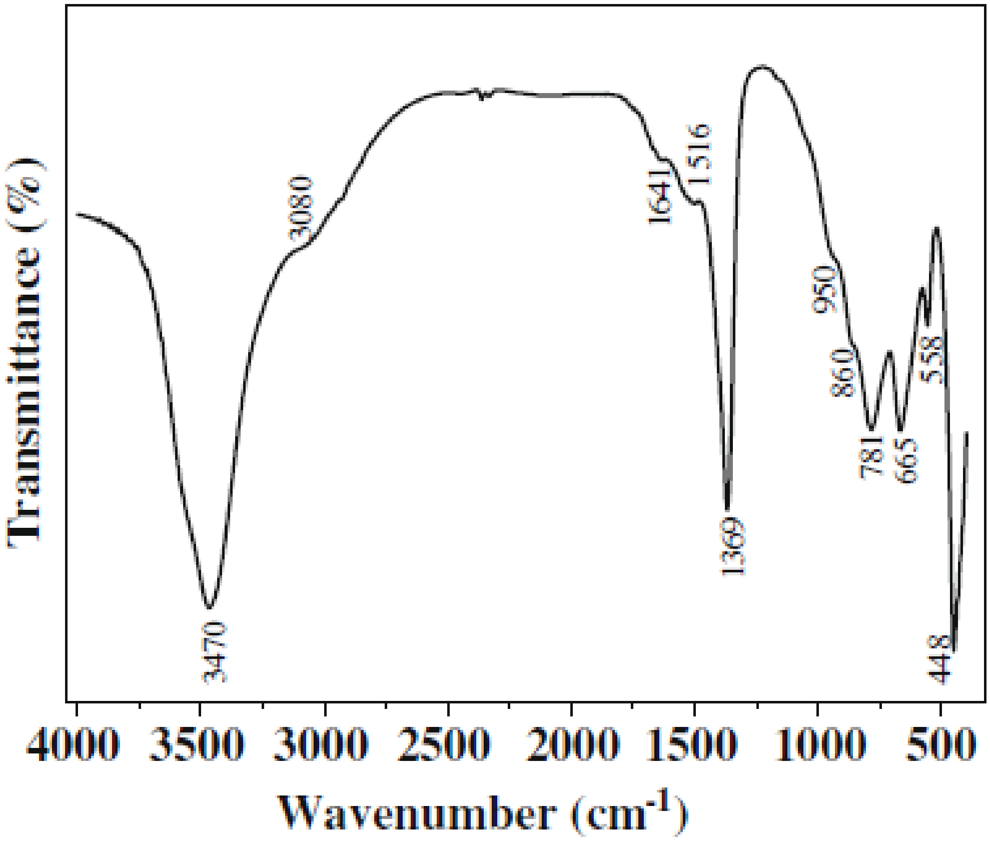

IR absorption spectra for Mg,Al – hydrotalcite formed on a AZ91D alloy by immersion in a CO_2 saturated water solution for 2 hours followed by immersion in a carbonic acid containing solution at a pH of 11.5 for 2 hours.

J.K. Lin, J.Y. Uan, Formation of Mg,Al-hydrotalcite conversion coating on Mg alloy in aqueous HCO_3^- /CO_3^{2-} and corresponding protection against corrosion by the coating, Corrosion Science, 2009, vol. 51, 1181-1188.

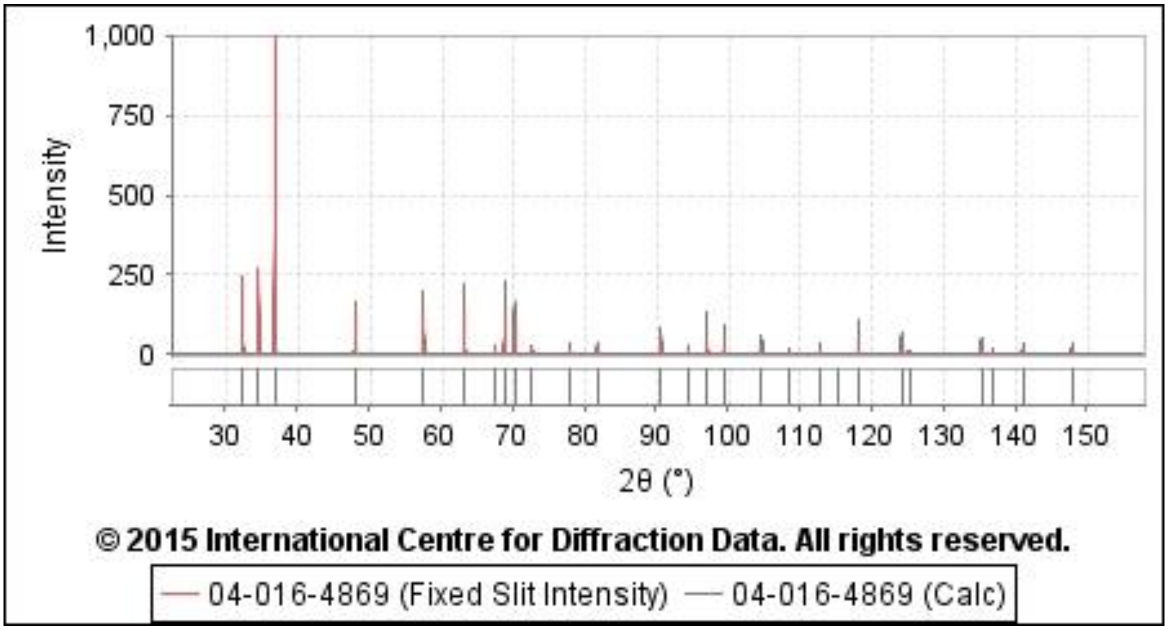

Standard XRD pattern for α-Mg

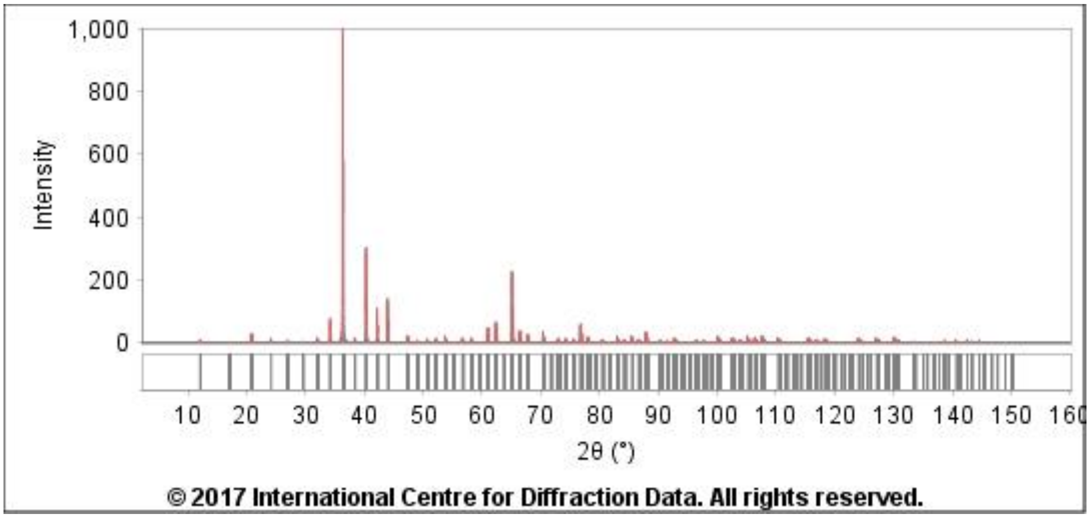

Standard XRD pattern for β-$Mg_{17}Al_{12}$.

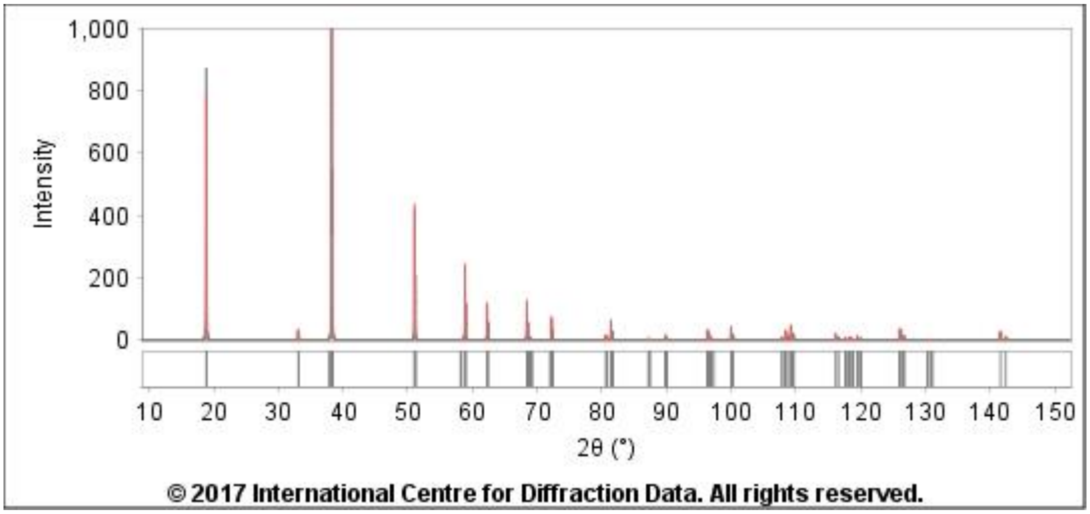

Standard XRD pattern of $Mg(OH)_2$ – brucite.

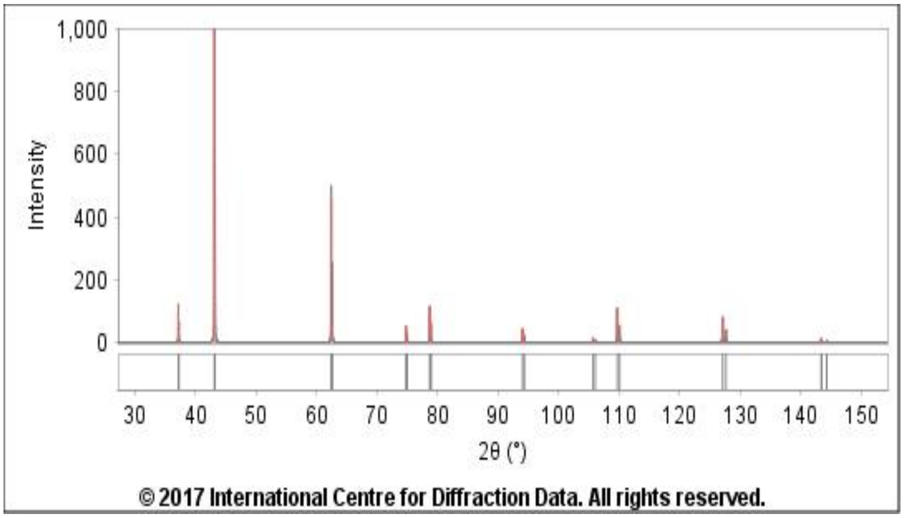

Standard XRD pattern of MgO.

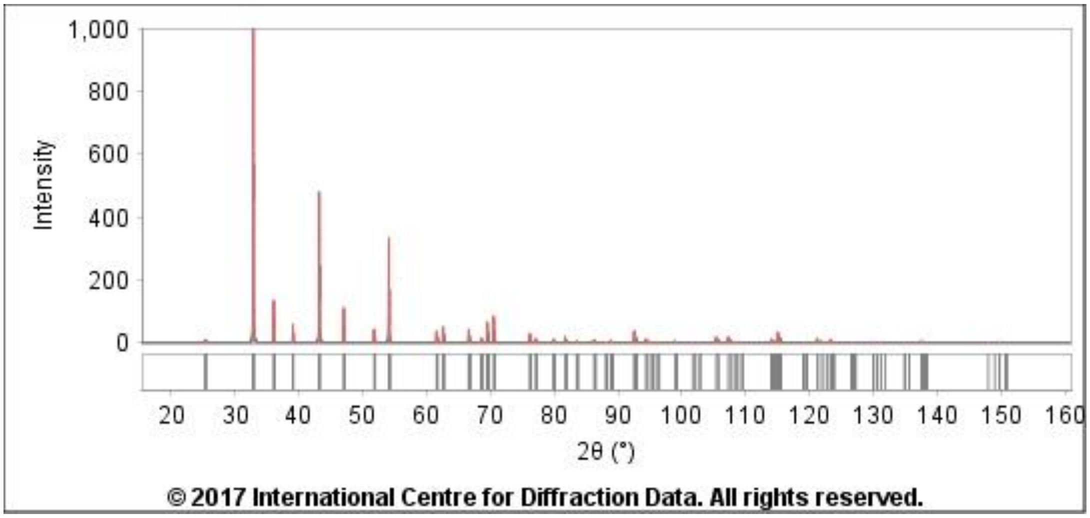

Standard XRD pattern of $MgCO_3$ – magnesite.

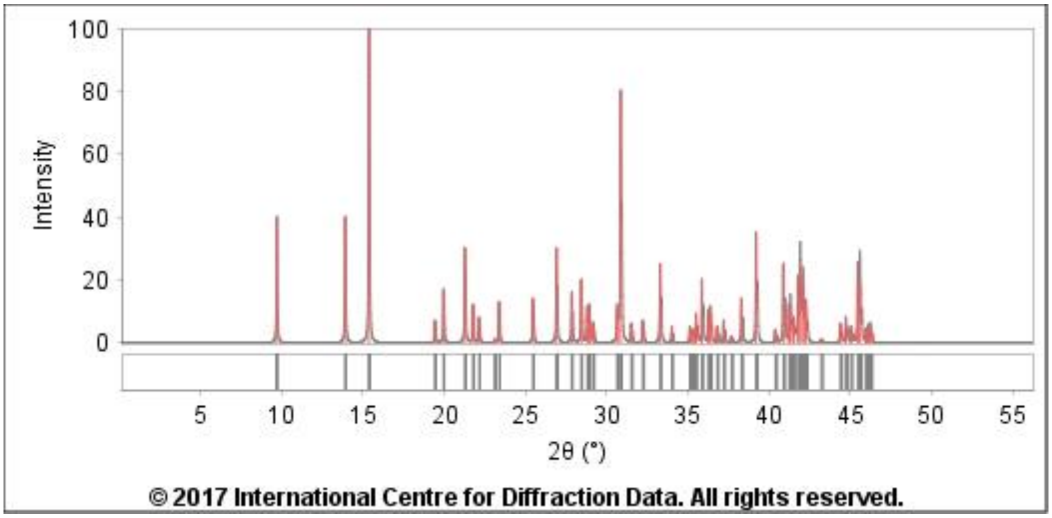

Standard XRD pattern of $Mg_5(CO3)_4(OH)_2 . 4H_2O$ – hydromagnesite.

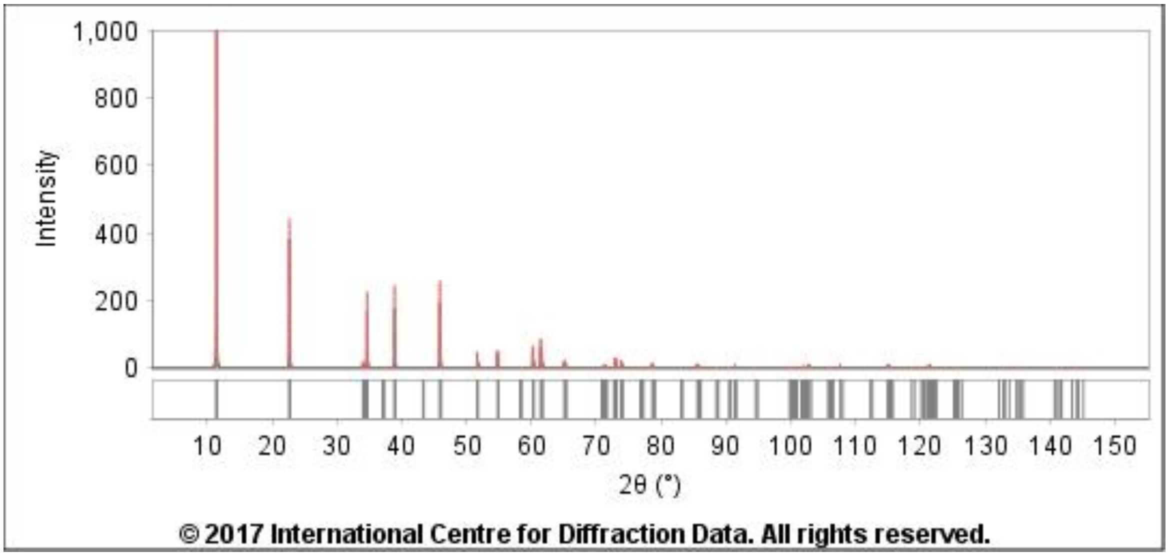

Standard XRD pattern for most hydrotalcite like phases (or layered double hydroxides) – $Mg_{0.83}Al_{0.17}(CO_3)_{0.08}(OH)_2 . 0.75 (H_2O)$

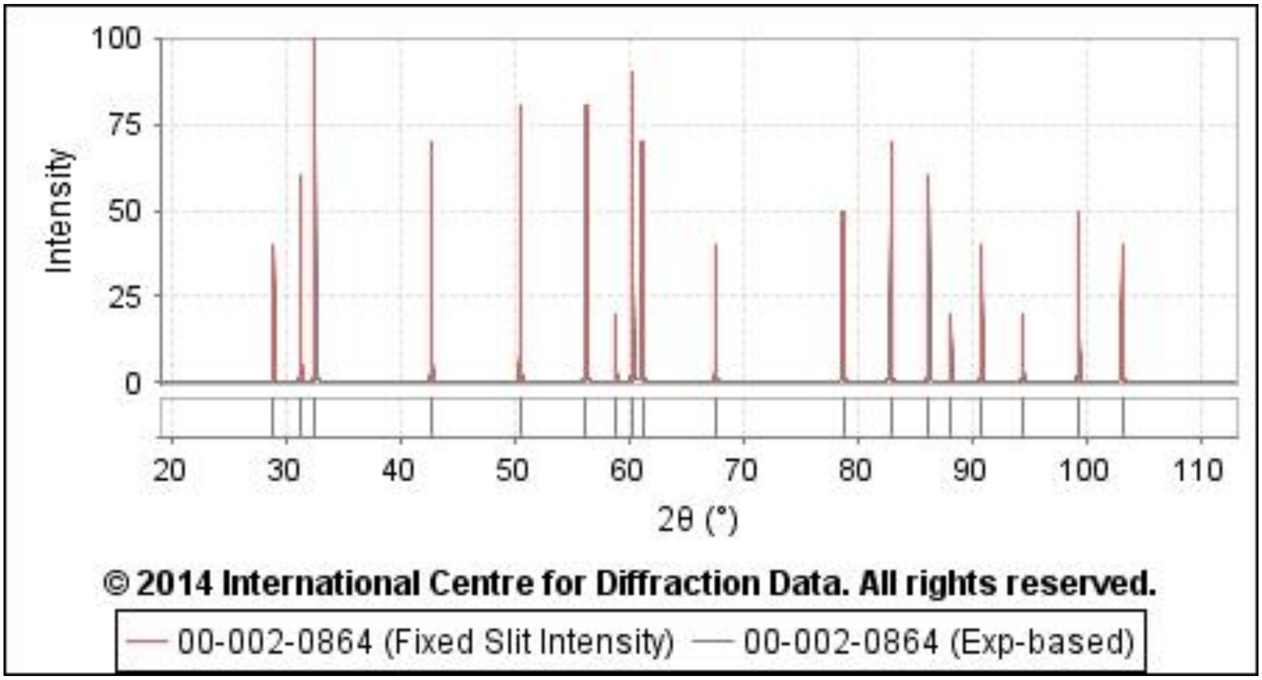

Standard XRD pattern for pure Gd.

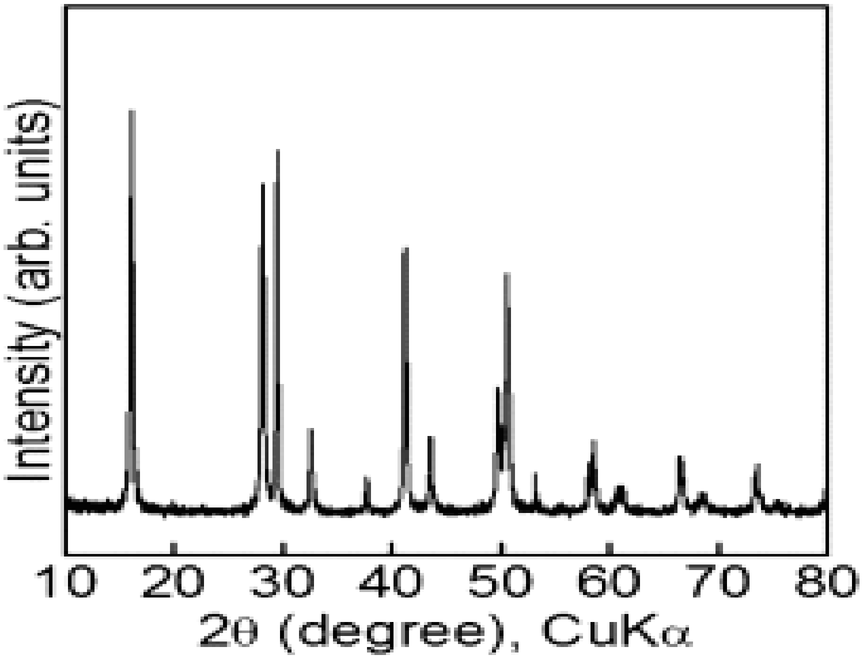

Standard XRD pattern (JCPDS 83-2037) for $Gd(OH)_3$ from:

Y. Kobayashi, H. Morimoto, T. Nakagawa, Y. Kubota, K. Gonda, N. Ohuchi, Fabrication of gadolinium hydroxide nanoparticles using ion-exchange resin and their MRI property, Journal of Asian Ceramic Societies, 4 (2016) 138-142.

Page intentionally left blank.

Appendix 2: Calculation of solubility equations

Variation of $Mg(OH)_2$ precipitation with pH:

$$Mg(OH)_2 \leftrightarrow Mg^{2+} + \ 2OH^- \ \ K_{sp} = 10^{-11.16}$$

$$10^{-11.16} = \frac{[Mg^{2+}][OH^-]^2}{[Mg(OH)_2]}$$

$$-11.16 = log[Mg^{2+}] + 2log[OH^-]$$

$$-11.16 = \ log[Mg^{2+}] - 28 + 2pH$$

$$log[Mg^{2+}] = 16.8 + 2pH$$

To substitute in for Al^{3+} making it pH dependent:

$$Al(OH)_3 \ \leftrightarrow \ Al^{3+} + 3OH^- \ \ K_{sp} = 10^{-32.7}$$

$$10^{-32.7} = [Al^{3+}][OH^-]^3$$

$$-32.7 = \ log[Al^{3+}] + 3log[OH^-]$$

$$-32.7 - 3pOH = \ log[Al^{3+}]$$

$$log[Al^{3+}] = \ -32.7 + 42 - 3pH$$

The value for $Mg(OH)_2$ and $Al(OH)_3$ precipitation could be found in multiple sources and were taken from Tamura et al. here.

Al corrodes and $Al(OH)_3$ can dissolve at high pH values and form the aluminate ion, commonly an ion used in the formation of hydrotalcite:

$$Al^{3+} + 4OH^- \leftrightarrow \ Al(OH)_4{}^- \qquad\qquad K_{sp} = 10^{33}$$

$$10^{33} = \frac{[Al(OH)_4{}^-]}{[Al^{3+}][OH^-]^4}$$

$$33 = \log[Al(OH)_4{}^-] - log[Al^{3+}] - 4log[OH^-]$$

$$log[Al^{3+}] = \ \log[Al(OH)_4{}^-] - 33 + 56 - 4pH$$

$$log[Al^{3+}] = \ \log[Al(OH)_4{}^-] + 23 - 4pH$$

Assumed $[Al(OH)_4{}^-] = 1x10^{-4}\ M$ although this is pH dependent

Hydrotalcite (Cl$^-$)

$$2Mg^{2+} + Al^{3+} + Cl^- + 6OH^- \leftrightarrow Mg_2Al(OH)_6Cl \qquad K_{sp} = 10^{52.12}$$

$$10^{52.12} = \frac{Mg_2Al(OH)_6Cl}{[Mg^{2+}]^2[Al^{3+}][Cl^-][OH^-]^6}$$

$$10^{52.12} = \frac{Mg_2Al(OH)_6Cl}{[Mg^{2+}]^2[Al^{3+}][Cl^-][OH^-]^6}$$

$$Mg_2Al(OH)_6Cl = 1$$

$$52.12 = -2\log[Mg^{2+}] - log[Al^{3+}] - log[Cl^-] - 6log[OH^-]$$

$$log[Al^{3+}] = \log[Al(OH)_4{}^-] + 23 - 4pH$$

$$-log[OH^-] = pOH = 14 - pH$$

$$52.12 = -2\log[Mg^{2+}] - \log[Al(OH)_4{}^-] - 23 + 4pH - log[Cl^-] + 84 - 6pH$$

$$2\log[Mg^{2+}] = 8.88 - 2pH - log[Cl^-] - \log[Al(OH)_4{}^-]$$

$$\log[Mg^{2+}] = 4.44 - pH - \frac{1}{2}log[Cl^-] - \frac{1}{2}\log[Al(OH)_4{}^-]$$

$$[Cl^-] = 0.9M$$

The value and equation used for this study was taken from Boclair and Braterman.

Meixnerite:

$$Mg_6Al_2(OH)_{18} \cdot 4H_2O \leftrightarrow 6Mg(OH)_2 + 2Al(OH)_3 + 4H_2O \qquad K_{sp} = 10^{-10.1}$$

$$(Mg(OH)_2 \leftrightarrow Mg^{2+} + \ 2OH^- \ K_{sp} = 10^{-11.16})^6$$

$$(Al(OH)_3 \ \leftrightarrow \ Al^{3+} + 3OH^- \ K_{sp} = 10^{-32.7})^2$$

$$Mg_6Al_2(OH)_{18} \cdot 4H_2O \leftrightarrow 6Mg^{2+} + 2Al^{3+} + 18OH^- + 4H_2O \quad K_{sp} = 10^{-142.46}$$

$$10^{-142.46} = \frac{[Mg^{2+}]^6[Al^{3+}]^2[OH^-]^{18}[H_2O]^4}{Mg_6Al_2(OH)_{18} \cdot 4H_2O}$$

$$-142.46 = 6log[Mg^{2+}] + 2log[Al^{3+}] + 18log[OH^-]$$

$$log[Al^{3+}] = \ \log[Al(OH)_4{}^-] + 23 - 4pH$$

$$-142.46 = 6log[Mg^{2+}] + 2\log[Al(OH)_4{}^-] + 46 - 8pH - 252 + 18pH$$

$$log[Mg^{2+}] = 10.59 - \frac{5}{3}pH - \frac{1}{3}\log[Al(OH)_4{}^-]$$

The K_{sp} was derived from Gibb’s free energy of formation data from “Review of the synthesis of LDH”.

Needed to put CO_3^{2-} in terms of pH:

$$CO_2(g) \leftrightarrow CO_2(aq) \quad K_H^{CO_2} = 10^{-1.5}$$

$$CO_2(aq) = H_2CO_3^*$$

$$[H_2CO_3^*] = P_{CO_2} * K_H^{CO_2}$$

$$P_{CO_2} = 10^{-3.5} \; to \; 10^{-3.4} \; atm$$

$$[H_2CO_3^*] = 10^{-3.5} * 10^{-1.5} = 10^{-5}$$

This value can vary depending on the partial pressure of CO_2 in the atmosphere.

$$H_2CO_3^* \leftrightarrow H^+ + HCO_3^- \quad K_{sp} = 10^{-6.3}$$

$$HCO_3^- \leftrightarrow H^+ + CO_3^{2-} \quad K_{sp} = 10^{-10.3}$$

Therefore:

$$H_2CO_3^* \leftrightarrow 2H^+ + CO_3^{2-} \quad K_{sp} = 10^{-16.6}$$

The general formula for CO_3^{2-} in terms of pH is:

$$10^{-16.6} = \frac{[CO_3^{2-}][H^+]^2}{[H_2CO_3^*]}$$

$$-16.6 = log[CO_3^{2-}] + 2log[H^+] - log(10^{-5})$$

$$log[CO_3^{2-}] = -21.6 + 2pH$$

This formula will be plugged into equations with CO_3^{2-} in them and the CO_2 (g) content will be varied by changing the $[H_2CO_3^*]$ concentration. The values in this section were taken from the Aquatic Chemistry book.

Derivation of hydrotalcite ($CO_3^{2})^{-}$:

$$3Mg^{2+} + 1.019Al^{3+} + 0.472CO_3^{2-} + 8.133OH^- + 2.53H_2O \\ \leftrightarrow Mg_3Al_{1.019}(CO_3)_{0.472}(OH)_{8.133} \cdot 2.53H_2O\ K_{sp} = 10^{68.9}$$

$$10^{68.9} = \frac{Mg_3Al_{1.019}(CO_3)_{0.472}(OH)_{8.133} \cdot 2.53H_2O}{[Mg^{2+}]^3[Al^{3+}]^{1.019}[CO_3^{2-}]^{0.472}[OH^-]^{8.114}[H_2O]^{2.53}}$$

$$[Mg_3Al_{1.019}(CO_3)_{0.472}(OH)_{8.133} \cdot 2.53H_2O] = 1$$

$$[H_2O] = 1$$

$$68.9 = -3log[Mg^{2+}] - 1.019log[Al^{3+}] - 0.472log[CO_3^{2-}] - 8.114log[OH^-]$$

$$log[Al^{3+}] = \log[Al(OH)_4{}^-] + 23 - 4pH$$

$$log[CO_3^{2-}] = -21.6 + 2pH$$

$$-log[OH^-] = pOH = 14 - pH$$

$$68.9 = -3log[Mg^{2+}] - 1.019(\log[Al(OH)_4{}^-] + 23 - 4pH) - 0.472(-21.6 + 2pH) \\ + 8.114(14 - pH)$$

$$3log[Mg^{2+}] = 31.4542 - 1.019\log[Al(OH)_4{}^-] + 11.246pH$$

$$log[Mg^{2+}] = 10.48 - \frac{5}{3}pH - \frac{1.019}{3}\log[Al(OH)_4{}^-]$$

The values for this hydrotalcite were taken from Rosov et al. It coincided with similar values obtained by Sato et al. considering the variation in stoichiometry.

Derivation of hydromagnesite ($Mg_5(CO_3)_4(OH)_2 . 4H_2O$) – the primary corrosion product commonly found for Mg-Al alloys during atmospheric corrosion, K_{sp} value is from experiments on naturally occurring hydromagnesite by Xiong:

$$Mg_5(CO_3)_4(OH)_2 \cdot 4H_2O + 10H^+ \leftrightarrow 5Mg^{2+} + 4CO_2(g) + 10H_2O(l) \quad K_{sp} = 10^{60.3}$$

This equation was made to incorporate CO_3^{2-} and became:

$$Mg_5(CO_3)_4(OH)_2 \cdot 4H_2O + 2H^+ \leftrightarrow 5Mg^{2+} + 4CO_3^{2-} + 6H_2O(l) \quad K_{sp} = 10^{-12.1}$$

$$10^{-12.1} = \frac{[Mg^{2+}]^5[CO_3^{2-}]^4[H_2O]^6}{[Mg_5(CO_3)_4(OH)_2 \cdot 4H_2O]\,[H^+]^2}$$

$$[Mg_5(CO_3)_4(OH)_2 \cdot 4H_2O] = 1$$

$$[H_2O]^6 = 1$$

$$-12.1 = 5log[Mg^{2+}] + 4log[CO_3^{2-}] - 2log[H^+]$$

$$log[CO_3^{2-}] = -21.6 + 2pH$$

$$-12.1 = 5log[Mg^{2+}] - 86.4 + 8pH + 2pH$$

$$log[Mg^{2+}] = 14.86 - 2pH$$

Other potentially relevant equations to consider:

$Mg_2(OH)_3Cl \;.\; 4H_2O + 3H^+ \Leftrightarrow 2Mg^{2+} + Cl^- + 7H_2O$ $\qquad K_s^o = 10^{26}$